NANOTECHNOLOGY FOR SOLAR-HYDROGEN PRODUCTION

VIA PHOTOELECTROCHEMICAL WATER-SPLITTING:

DESIGN, SYNTHESIS, CHARACTERIZATION, AND

APPLICATION OF NANOMATERIALS AND QUANTUM DOTS

A Dissertation

by

NASER D. ALENZI

Submitted to the Office of Graduate Studies of
Texas A&M University
in partial fulfillment of the requirements for the degree of

DOCTOR OF PHILOSOPHY

December 2010

Major Subject: Petroleum Engineering

NANOTECHNOLOGY FOR SOLAR-HYDROGEN PRODUCTION

VIA PHOTOELECTROCHEMICAL WATER-SPLITTING:

DESIGN, SYNTHESIS, CHARACTERIZATION, AND

APPLICATION OF NANOMATERIALS AND QUANTUM DOTS

A Dissertation

by

NASER D. ALENZI

Submitted to the Office of Graduate Studies of
Texas A&M University
in partial fulfillment of the requirements for the degree of

DOCTOR OF PHILOSOPHY

Approved by:

Co-Chairs of Committee,	Christine Ehlig-Economides
	Zhengdong Cheng
Committee Members,	Jun Kameoka
	Qi Ying
Head of Department,	Stephen A. Holditch

December 2010

Major Subject: Petroleum Engineering

ABSTRACT

Nanotechnology for Solar-hydrogen Production via Photoelectrochemical Water-splitting: Design, Synthesis, Characterization, and Application of Nanomaterials and Quantum Dots. (December 2010)

Naser D. Alenzi, B.Sc.; M. Sc., Kuwait University

Co-Chairs of Advisory Committee: Dr. Christine Ehlig-Economides
Dr. Zhengdong Cheng

Hydrogen production by water-splitting using solar energy and nanostructure photocatalysts is very promising as a renewable, efficient, environmentally clean technology. The key is to reduce the cost of hydrogen production as well as increase the solar-to-hydrogen conversion efficiency by searching for cost-effective photocatalytic materials. In this dissertation, energy efficiency calculation was carried out based on hydrogen production observation to evaluate the nanomaterials activity. The results are important to gain better understanding of water-splitting reaction mechanism. Design, synthesis, characterization/properties and application of these nanomaterials was the road-map to achieve the research objectives. The design of TiO_2 is selected based on unique photocatalytic and photovoltaic properties and high stability in aqueous solution. Various structures of nanocomposites TiO_2 were designed according to their characteristics and potential activity. TiO_2 with quantum dots, nanocomposites thin film, nanofibers, nanorods, nanowires (core/shell), nanotubes, nanopowders, nanoparticles, and nanosphere decorated with low cost metals, sensitized with dye, and doped with

nitrogen are designed. Green physical and chemical synthesis methods such as sol-gel techniques, autoclave, microwave, electrospinning, wet impregnation, hydrothermal, chemical vapor deposition, template-based fabrication (porous anodic aluminium oxide membrane), drop casting, dip coating, wet coating were used to synthesize and fabricate the nanomaterials and quantum dots.Both bottom-up and top-down synthesis techniques were used. The ability to control and manipulate the size, shape/geometry, crystal structure, chemical compositions, interaction and interface properties of these materials at nano-scale during the synthesis enable to enhance their thermal, optical, chemical, electrical, …etc properties. Several characterization techniques such as XRD, XPS, EDS, SEM, UV-visible spectra, and optical microscopic and digital camera were also obtained to characterize the properties and confirm to achieve the desired design. The application or processing to test the activity of these nanomaterials for hydrogen production by water-splitting was conducted through extensive experimental program. It was carried out in a one photo-single column experimental set-up to detect hydrogen evolution. A high throughput screening process to evaluate single photo reduction catalysts was established here for simplicity, safety, cost-effective and flexibility of testing nanomaterials for water photoreduction reactivity and hydrogen generation. Therefore, methanol as electron donor or oxidation agent was mixed with water in equal volume ratio in order to prevent the oxygen evolution and only measured the time course of hydrogen production. The primary objectives of this study is to investigate the following (1) The structure-properties relationship through testing quantum dots, nanocomposites thin film, nanofibers, nanorods, nanowires (core/shell), nanotubes,

nanopowders, nanoparticles, nanospheres of TiO_2 decorated with metals, dye sensitization, and nitrogen-doping. (2) The role of adding electron donors/relays to solution and their effect on semiconductor surface-electrolyte interface under constant conditions such as KI, Mv^{+2}, NaCl, $NaHCO_3$, sea and pure water. (3) Band gap and defect engineering by cation and anion doping. (4) Quantum dots and dye sensitization effect. The nanomaterials activity evaluated based on observed hydrogen production rate (μmol/h/g) experimentally and based on the energy efficiency (%) calculation.

Major findings in this dissertation are (1) A high throughput screening process to evaluate single photoreduction catalysts for solar-hydrogen production by water-splitting was established. (2) nanofibers structure of TiO_2 doped with nitrogen, sensitized with dye (Rose Bengal Sodium) and quantum dots ($CuInS_2$), and decorated with metals (Ag) showed the high solar-to-hydrogen conversion efficiency and high hydrogen production rate (3) Simple, safe, inexpensive, robust, efficient and green physical and chemical synthesis methods were used to prepare the nanomaterials and quantum dots. (4) Gaining insight and better understanding of water-splitting reaction mechanism by (a) Studying the structure-properties relationship of nanomaterials (b) Studying the role of additives on surface-interface chemistry of semiconductor and electrolyte (c) Knowing how to reduce the electron-hole recombination reactions to enhance quantum efficiency (d) Extending the absorption of nanomaterials to harness the visible light of solar spectrum radiation by doping and defect chemistry.

DEDICATION

I dedicate this dissertation to my parents

ACKNOWLEDGEMENTS

NOMENCLATURE

m = weight

ρ = density

V = volume

A = area

L = thickness

$\varepsilon_\circ$ = energy efficiency

ΔG° = Gibbs free energy = 237.2 KJ/mole

R_{H_2} = hydrogen production rate (mole/hour)

P_t = Power intensity (W/m^2), for UV light = 100 (W/m^2), for sunlight = 240 (W/m^2),

[Texas, College Station, Latitude: 30.6277778, Longitude: -96.3341667, 30° 37'
40" N / 96° 20' 3" W]

QE = Quantum efficiency

λ = Wavelength, nm

UV = Ultraviolet light

υ = frequency

h = Planck constant = 6.62606896(33)×10^{-34} J.s

N_A = Avogadro constant $\approx 6.022 \times 10^{23}$ mol^{-1}.

c = speed of light = 299792458 m/s

TABLE OF CONTENTS

VII   NANOFIBERS AS EFFECTIVE SUPPORTER FOR TiO$_2$
       NANOCOMPOSITES PHOTOCATALYST SYSTEM
       INCLUDING QUANTUM DOTS AND DYE SENSITIZATION 216

       Overview 216
       Introduction 217
              Nanofibers by electrospinning 218
              Ag/TiO$_2$ nanofibers, Cu^{+2}and CuO/TiO$_2$ nanopowders @
              (PVP) nanofibers 220
              Fe^{+3}/TiO$_2$ nanoparticles @ silica nanofiber 220
              Quantum dots and dye sensitization solar cell (e.g. DSSC),
              dye sensitization onto Ag/TiO$_2$ nanofiber and Quantum dots
              "CuInS$_2$" injected inside Ag/TiO$_2$ nanofiber 221
       Design and synthesis 222
              Ag/TiO$_2$ nanofibers as "one-step".. 222
              Cu^{+2} and CuO/TiO$_2$ nanopowders inside PVP nanofiber 225
              Cu^{+2} and CuO/TiO$_2$ nanopowders inside silica nanofiber
              and Cu^{+2} and CuO/TiO$_2$ nanoparticles "one-step" inside
              silica nanofiber 226
              Ag/CuInS$_2$/Dye (R.B.S)/TiO$_{2-x}$.N$_x$ injected into silica
              nanofiber.. 228
              Fe^{+3}/TiO$_2$ nanoparticles inside silica nanofiber.......................... 228
       Characterization 229
       High throughput screening process of H$_2$ production measurement.... 242
       Results and discussion of application for H$_2$ production 243
              H$_2$ production of Ag/ TiO$_2$ nanofiber as "one-step" under
              UV light.. 245
              H$_2$ production of Cu^{+2} and CuO/TiO$_2$ nanopowders inside
              PVP nanofiber under UV light and sunlight 246
              H$_2$ production of Cu^{+2} and CuO/TiO$_2$ nanopowders inside
              silica nanofiber under sunlight 248
              H$_2$ production of Ag/CuInS$_2$/Dye (R.B.S)/TiO$_{2-x}$.N$_x$ inside
              silica nanofiber under Sunlight 249
              H$_2$ production of Fe^{+3}/TiO$_2$ nanoparticles inside silica
              nanofibers under sunlight.. 250
              H$_2$ production of Cu^{+2} and CuO/TiO$_2$ nanopowders
              "one-step" inside silica nanofiber under sunlight....................... 251
       Conclusions 252

LIST OF FIGURES

FIGURE   Page

FIGURE   Page

FIGURE   Page

FIGURE										Page

LIST OF TABLES

CHAPTER I

INTRODUCTION

Energy, electricity and fuels, drive our daily life. Water desalination plants, food industries, health communities and consumer products factories, all are energy-dependent. The processes of energy production and consumption have negative impact on our environment. Fossil fuels as the current energy sources have two critical problems. First, they are limited (nonrenewable) and second they are not environmentally clean. The greenhouse gas emissions (e.g. CO_2) produced during the combustion of fossil fuels to generate energy are considered one of the reasons for global warming and climate change [1]. The climate change due to increase in the temperature on earth surface affected every aspect of the life on the planet. Accordingly, engineers and scientists have a crucial role to search for clean, efficient, economic and renewable sources of energy to overcome the energy and the environment challenges. Natural resources are the only resources that provide renewable and environmentally benign energy sources. Solar, wind, water (wave, tidal, hydroelectric) and geothermal are the four primary renewable sources of energy that could provide the energy for the entire world if cost-effective technologies are developed. Sunlight and (sea) water are renewable, clean, and natural resources and could be the permanent solution of energy production by producing solar-hydrogen fuel. In addition, sunlight and water are open

_____

This dissertation follows the style of *Nature*.

and free access resources internationally, that solves social, economical, political and any other related issues to energy production and protects the environment.

HYDROGEN

Hydrogen is colorless and highly flammable gas. Hydrogen as an energy carrier is considered to be one of the promising future energy carriers. It has higher energy content per weight (142 MJ/kg) than methane and gasoline [2]. In fact, it is the most abundant element on the earth since it is available in water and hydrocarbons (bonded with elements by all kind of chemical bonding such as ionic and covalent bonding). However, it is not available in its rich energy state. Hydrogen also can be stored, unlike electricity, and used in the time and place needed. Hydrogen has stationary and portable energy applications. These applications include fuel cell and as transportation fuel to power vehicles. Fuel is any high energy substance that can be consumed to generate useful work [3]. A fuel cell is an electrochemical device that convert chemical reaction energy into electrical energy (uses hydrogen and oxygen to generate electricity and it is physically and chemically similar to a battery but using an input fuel [3]. Hydrogen is environmentally friendly fuel because no greenhouse gases are emitted during it combustion and only water as by-product. In addition, the demand of hydrogen for bio-refinery, food industries, and oil-refinery, petrochemical and pharmaceutical industries is growing up rapidly. In summary, hydrogen is the fuel of the future because of the following reasons [4,5]: (1) Clean Energy (production, storage, conversion, transportation, and usage is environmentally benign). (2) Most abundant element in the universe. (3) Lightest fuel. (4) Richest in energy per unit mass. (5) Can be stored easily in gas, liquid

or metal hydride forms. (6) Can be produced by water (renewable fuel). (7) It can be transported via pipelines or tankers. (8) Direct conversion into: thermal, mechanical and electrical energy.

HYDROGEN PRODUCTION PROCESSES

Hydrogen has a great advantage than any other fuels because it can be produced from hydrocarbons and water resources using all available energy resources. Hydrogen can be produced from hydrocarbons (crude oil, natural gas, biomass) and coal, by using reforming process (Figure 1.1). Currently, most of the world's hydrogen production is from natural gas steam reforming [6] [7,8]. Natural gas is a finite source and natural gas steam reforming is not environmentally clean process and consumes a lot of energy. Hydrogen can also be produced by splitting water (electrolysis) [6] [7] (Figure 1.2). The electricity used to split water can be generated from fossil fuels, solar, wind, hydroelectric, and geothermal, nuclear energies. Water electrolysis process is not efficient because the input energy required is much more than the output energy [6]. Therefore, economical and environmental obstacles make the hydrogen production from these technologies an unpractical option [3].

In contrast, photoelectrochemical water splitting (PEC) is a very promising process to produce hydrogen. Using sunlight and (sea) water to produce hydrogen as the most available natural resources on the earth is considered to be the most optimal solution of energy and environment challenges. Both the sun and the (sea) water are efficient, renewable, environmentally clean and abundant to majority of the people on the earth. However, a cost-effective methods need to be developed to enhance the

catalytic activity of photo catalyst materials and optimum process design to be mature commercial technology for hydrogen production.
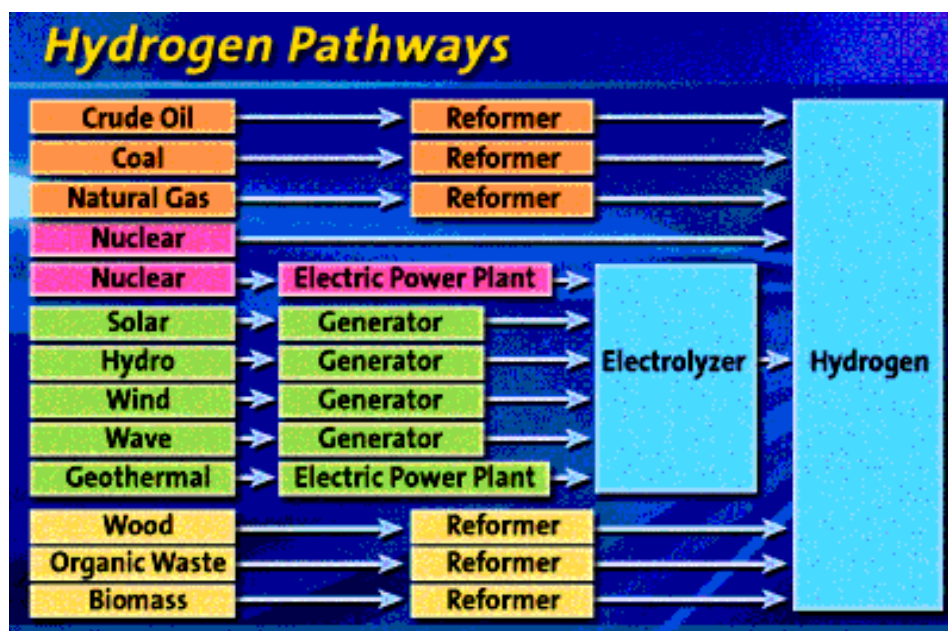
Figure 1.1 Hydrogen production pathways [9].
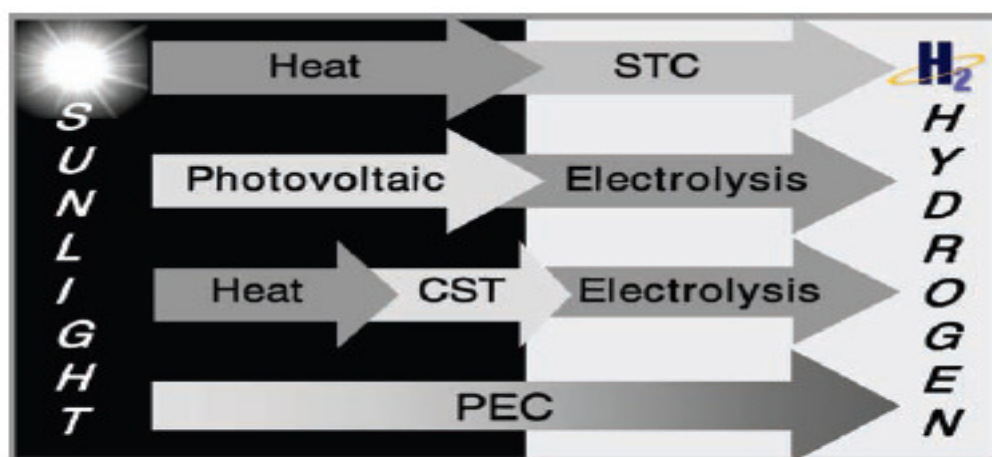
Figure 1.2 Solar to hydrogen conversion pathways, STC is solar thermochemical, CST is concentrating solar thermal, and PEC is photoelectrochemical [10].

PHOTOELECTROCHEMICAL WATER-SPLITTING

Splitting seawater into hydrogen and oxygen gases using sunlight is very straightforward method from clean, sustainable, renewable and free natural resources on earth. A breakthrough in novel multifunctional materials or photocatalyst (speed up the rate of reaction without being consumed in the reaction) is the key to develop this technology. Through nanoscience and nanotechnology, it is possible to promote the stability and efficiency of these materials by enhancing their properties (chemical, optical, electronic…etc). The ability to manipulate the materials at nano, molecular or even atomic scales enables designer to effectively design and synthesize these materials. The tremendous advance that happened recently in the probe scanning microscopic, characterization techniques, and nanolithography technologies are the base of nanotechnology applications.

The basic principles steps of photoelectrochemical water-splitting mechanism (Figure 1.3) are (1) sunlight harvesting if the photon energy is larger than band gap energy of the semiconductor (2) photogenerated electron-hole separation. (3) Electrons trapping at metal surface (4) Protons transfer to photocathode surface. (5) Water adsorbed species reduced and oxidized by electrons and hole, respectively to produce hydrogen and oxygen. Reduction reactions occurred at metal surface and oxidation reactions occurred at semiconductor surface.
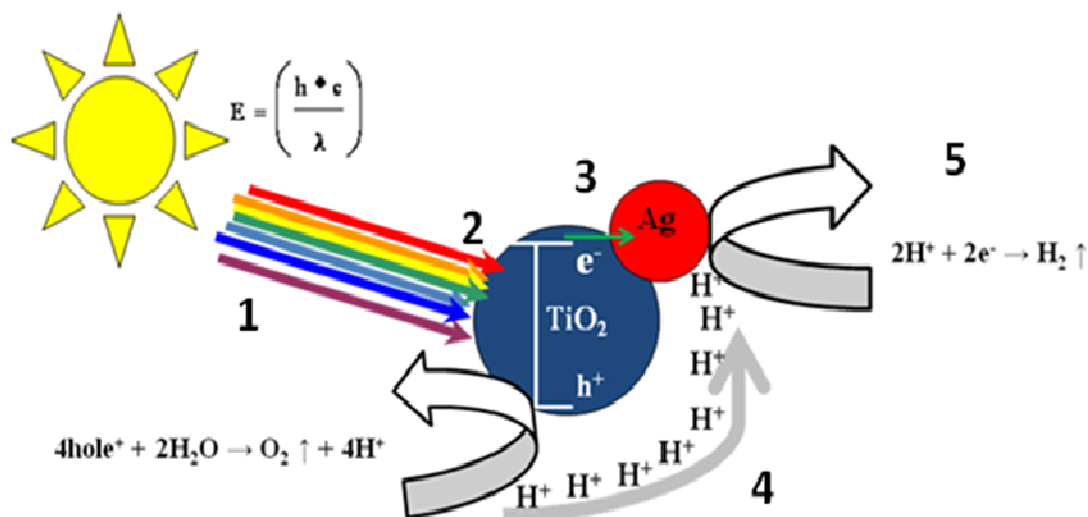
Figure 1.3 Schematic diagram illustrates the basic principles of photoelectrochemical water-splitting using photocatalytic nanomaterials and solar energy.

Accordingly, to split water into H_2 and O_2 using photocatalytic nanomaterials and solar energy, there are three main obstacles need to be overcome: (1) narrowing the bang gap to harness the visible light of solar energy spectrums [11], (2) increasing the efficiency of charge separation, and (3) reducing the recombination reaction of O_2 and H_2 to avoid water formation [12]. First two obstacles are highly dependent on the structure, properties and their relationship of the photocatalyst. The third obstacle is depend on the cocatalyst (usually metal or metal oxide) that used to reduced and oxidized the adsorbed species of water on photocatalys surface to generate H_2 and O_2 [13]. The cocatalysts are embedded onto photocatalyst surface as dispersion of nanoparticles to increase the surface area, to provide more active sites, more electron-hole pair per photon, and to reduce the activation energy for gas production [13]. Several

semiconductors with n-type and p-type in various forms such as powder suspensions have been extensively used to harvest solar energy and split water for hydrogen production [14-25] [26,27] [28,29]. Since the discovery in 1972 of Fujishima and Honda using Pt and TiO_2, over 130 materials have been tested. So far, no material capable of splitting water under UV or visible light with energy efficiency closer to theoretically maximum solar to hydrogen conversion efficiency [30] [31] has been found. The current energy efficiency reported [32] [33] is very low and need enormous research and development to be economically competitive to fossil fuels. Also, long term stability of the photocatalyst is still unknown. The electronic properties (band gap and band edge positions corresponding to water oxidation and reduction potential energy) are very important for photocatalysts selection for water-splitting reactions. By reviewing the periodic table of elements, it demonstrated that metal oxides with d^0 or d^{10} electronic configuration are the suitable photocatalyst for overall water splitting [13]. TiO_2 is a well known semiconductor for its high photocatalytic activity, photovoltaic, and high stability in aqueous solution [34]. It has an UV responsive band gap energy (Eg=3.2 eV for anatase crystal structure) with broad applications such as a photocatalyst for pollutants degradation, dye-sensitized solar cells, lithium batteries and gas sensors [35] [36] [34] [37] [38]. The band gap energy of TiO_2 can be modified to be responsive to visible solar spectrum by several approaches, such as nitrogen doping. Visible response photocatalyst is targeted to maximize the utilization of solar energy (visible light region is contributing to large portion of sunlight spectrum). A high efficient and high stable visible-light-driven photocatalyst with band edge potentials suitable for overall water splitting (minimum

energy required is 1.23 eV) is the target band gap energy level. Based on very recent literature reviews [39], designing a photocatalyst composed of quantum dots, TiO_2, nitrogen doping, and metals is the cutting-edge research for water-splitting under solar energy.

The goal of the study is to seek the possibility of using nanostructures of TiO_2 embedded with metal and quantum dots to harvest visible solar light in order to improve their quantum and energy efficiencies The road map to achieved the main goal is as follows: (1) Design, synthesis, and characterization of TiO_2 nanocomposites for solar-hydrogen production from photoelectrochemical water-splitting. (2) Application of TiO_2 nanocomposites by testing their photocatalytic activity performance using simple, inexpensive and high throughput screening process. Experiments were conducted in the laboratory and under natural sunlight with high accuracy detection of hydrogen production rate. (3) Calculate the energy efficiency % based on observations results. It is important to mention that the TiO_2 nanocomposite is used for hydrogen production from water-splitting reactions, therefore, methanol as hole scavenger (electron donor) will be added to water to be oxidized by hole to prevent the O_2 evolution (methanol act as water photooxidation agent). As a result, a single-photoanode experiment (one column) will be possible to use in the laboratory with hydrogen gas as main product to test.
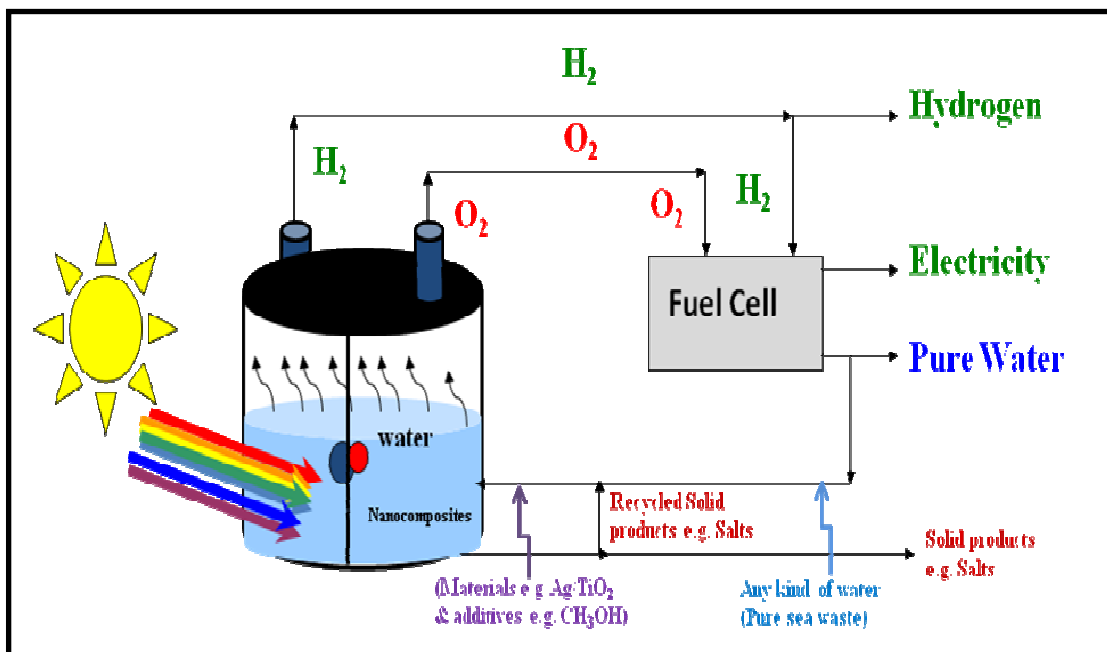
Figure 1.4 Solar water-splitting connected with fuel cell to produce hydrogen, electricity, and pure water. Photocatalyst is the key to advance these applications.

This model of experiment is providing simple, low cost, and flexible to test large numbers of nanomaterials, high throughput screening process and also safe experimental technique. The results should guide to better understanding of the photoelectrochemical redox water-splitting reaction mechanism and which lead to develop photocatalyst system for hydrogen production high in term of superb stability and activity. The role of many parameters such as the weight of photocatalyst, the land area required, the power intensity, the photocatalyst properties and structure should be quantitatively and qualitatively analyzed.This will facilitate better design of superb effective photocatalyst along with theoretical prediction of materials properties using computer modeling and simulation.

If hydrogen could be produced from water-splitting to supply the fuel cell, which converts the hydrogen and oxygen into electricity and pure water, completely clean, efficient, and renewable energy source during the production and combustion would be achieved (Figures 1.4 & 1.5). Hydrogen fuell cell works based on O_2 and H_2 recombination reaction to generate electricity. Hydrogen fuel for hydrogen fuell cell can be produced from water-splitting reaction. This water cycle is promising approach as future energy carrier if solar to hydrogen conversion efficiency of water-splitting reaction and fuel cell technology is well-developed (Figure 1.6).
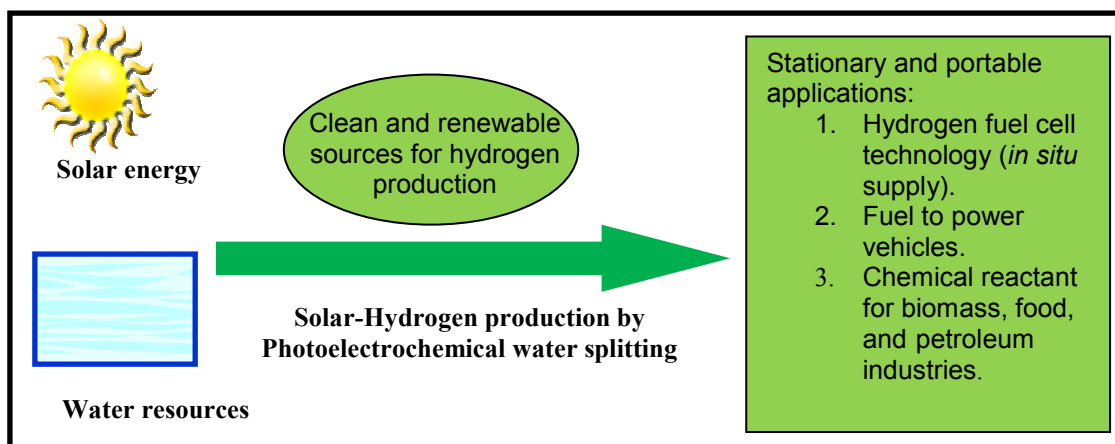
Figure 1.5 Hydrogen can be produced from water-splitting using solar energy then used as an energy carrier to generate electricity or as chemical in the industries.
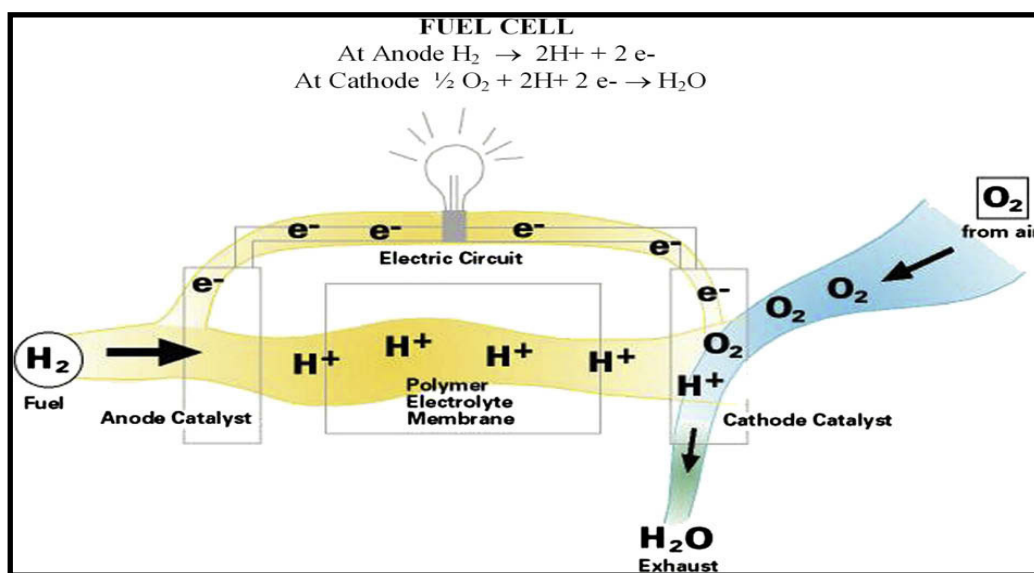
Figure 1.6 Hydrogen fuel cell principal. The only byproduct (exhausted water) could be split to generate hydrogen and oxygen gases which used as input fuels for this technology [4].

Photoelectrochemical water-splitting can be simply described that when light or solar irradiation is exposed to a system of photocatalyst immersed in water, the energy conversion of photon to electrical then to chemical energy will lead to split water into O_2 and H_2 [40]. Since Fujishima and Honda discovered the concept in 1972, hydrogen production rate has been too low in commercial scale to supply the fuel cell. The reported efficiency is still too low due to low materials activity [41]. Searching for effective, stable, and inexpensive photocatalyst, the maximum efficiency reported since 1972 to 2005 is around 18% where the maximum efficiency could be achieved theoretically is around 30% [10]. Two main technical problems related to the materials must be solved to extent the efficiency. First, the ineffective performance to absorb light in the visible light region (λ=400-800 nm). The visible light region approximately consists of 43% of solar energy (Figure 1.7) [42].
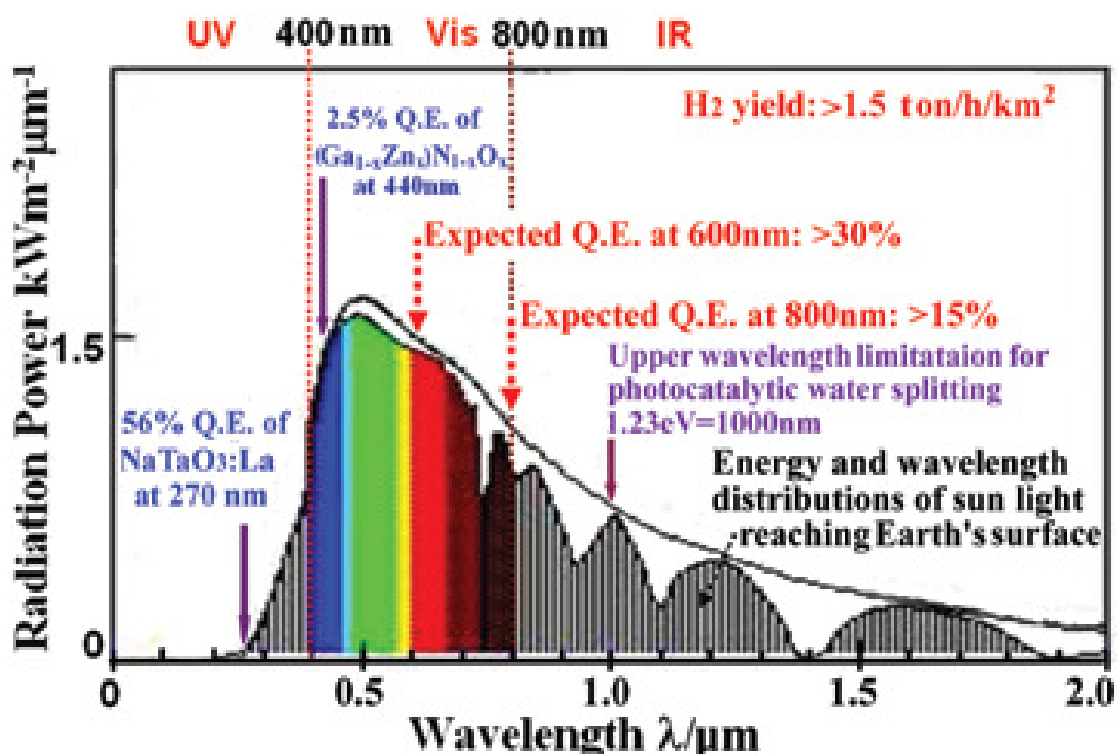
Figure 1.7 The maximum power radiation of sunlight lies at visible wavelength range of (λ= 400-800 nm) [42].

Second, the high probability of the fast electron-hole recombination reaction is more than the carriers charge separation reaction because of low activity of photocatalyst and additives to suppress this phenomena. To be effective, the semiconductor band gap should be tuned to cover the visible- light wavelength. Also, the photocatalyst must effectively catalyze the water separation reaction by enhancing the charge separation. The potential difference to split water is 1.23 eV (λ= 1008 nm) (Figure 1.8) [42] [43]. Therefore, an integration material system must include combination of materials that simultaneously solve all these technical challenges.
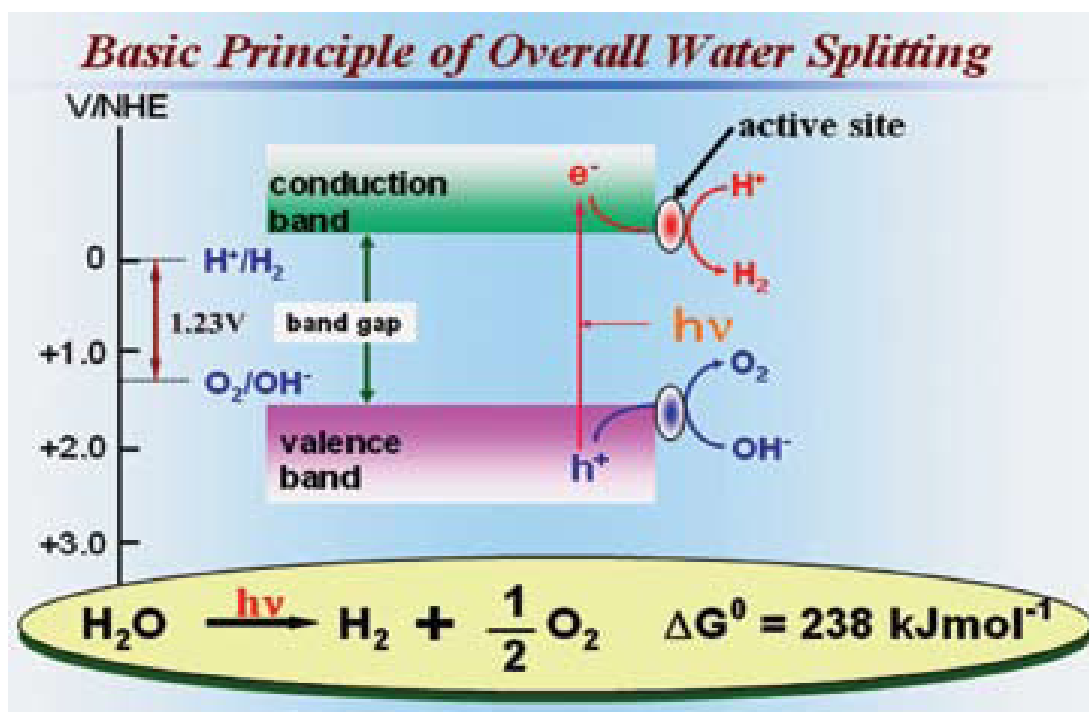
Figure 1.8 Minimum potential energy required to split water is 1.23 e V [42].

Osterloh (2008) [12] summarized all the studies and research results regarding materials-related issues. This review showed that TiO_2 is a strong candidate for this process because of its stability, thermal properties, and resistance to corrosion. Hoffmann (1995) [44] discussed the technical details of using TiO_2 as a semiconductor photocatalyst. Ni (2007) [45] presented an overview about all possible ways to use TiO_2 to enhance a photocatalytic water-splitting reaction such as electron donor additives, ion doping, and the composite semiconductor.

According to recommendations and conclusions from these recent literature reviews, more attention should be paid to modifying the activity of a stable semiconductor because stability is likely to be a preferable criterion for commercialization. The hydrogen production rate (efficiency) and the long term activity (stability) are the two important parameters for the evaluation. Therefore, this dissertation will attempt to extend the benefits from recent progress in nanotechnology and advanced materials science to develop doped metal-TiO_2 nanocomposite. Nanoparticles have more surface area to weight ratio, more surface energy, and large contribution of surface atoms; therefore, they show different thermal, mechanical, and electronic properties than the bulk material. It is important to mention that the band edge positions of pure TiO_2 is not appropriate for water redox reactions based on potential energy diagram of the H_2/H_2O and O_2/H_2O redox (Figure 1.9) [46]. When metals are doped on the surface of a semiconductor, these energy impurities will affect the crystal locations that caused change in the quantum dots confinement. The change of a crystal lattice configuration by lattice defect chemistry and by rearranging the oxygen stoichiometry will reengineer the band gap energy of the semiconductor. A different configuration may reduce the band gap energy to harvest the visible-light. Therefore, the success to excite, generate and separate charge carriers is essential to enhance the quantum efficiency and consequently the solar to hydrogen conversion efficiency. Nanocomposite metal-TiO_2 has high surface energy which enhances the charge separation by reducing the chance to be a recombination center [45] [47]. This will allow using a highly active metal such as platinum with less weight [48]. The work of Matsuoka

et al. (2007) [49] demonstrates that the preparation methods are important for metals or ion doping on semiconductors.
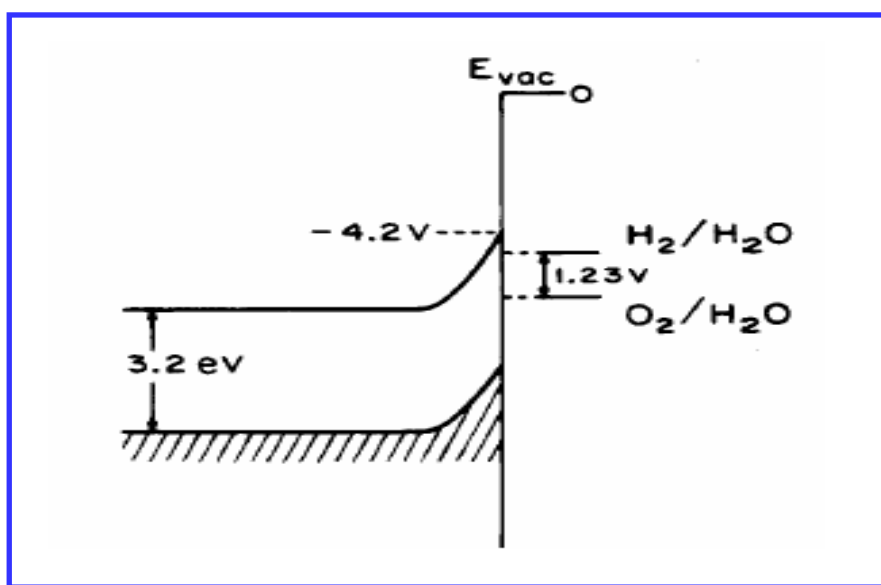
Figure 1.9 TiO_2 band-edge position compared to H_2/H_2O and O_2/H_2O redox position [46].

Figure 1.10 shows the effort has been made to search for best candidate materials for this technology since establishment the concept in 1972. Among those effort to develop the materials performance, dye sensitizer is highly recommended to improve the absorption of full spectrum solar irradiation [45] [50]. The effect of dye on TiO_2 particles is to drive the water-splitting reaction under visible light [51]. Reduction and oxidation agents are also important to limit electron-hole pair recombination. Adding the additives to water electrolyte solution in the presence of TiO_2 nanoparticles is also recommended [45]. The mechanism also received attention to better understand the water splitting reaction.

For example, Matsuoka et al. (2007) [49] well presented the mechanism as shown in Figure

1.11.
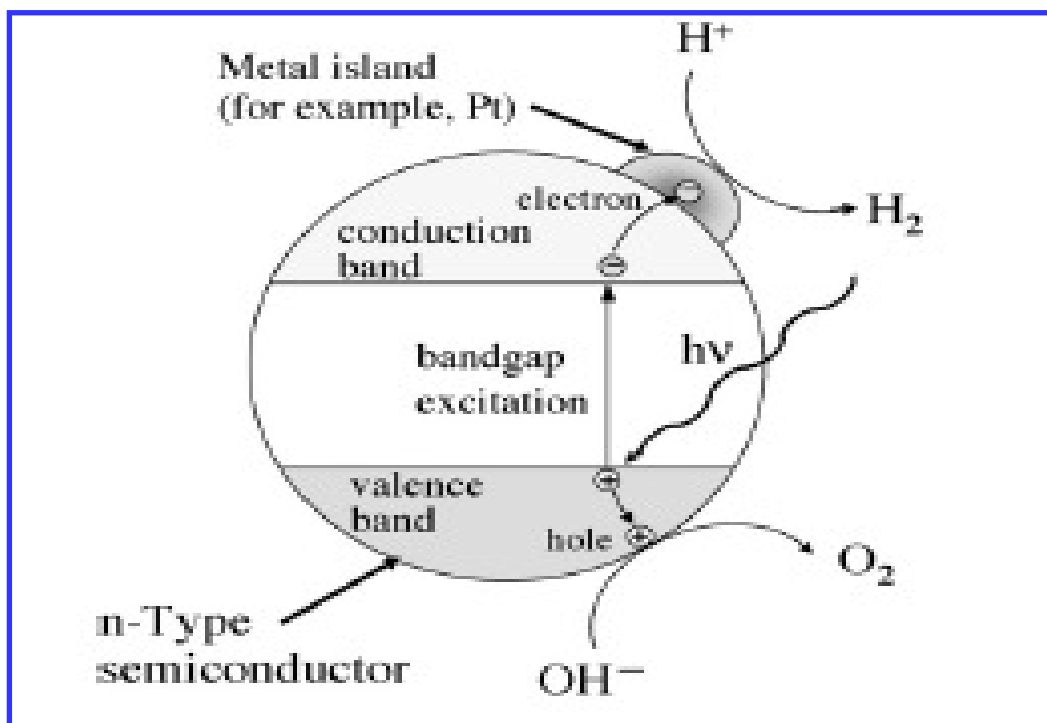
Figure 1.10 Electron-hole recombination reactions that must be minimized [49].
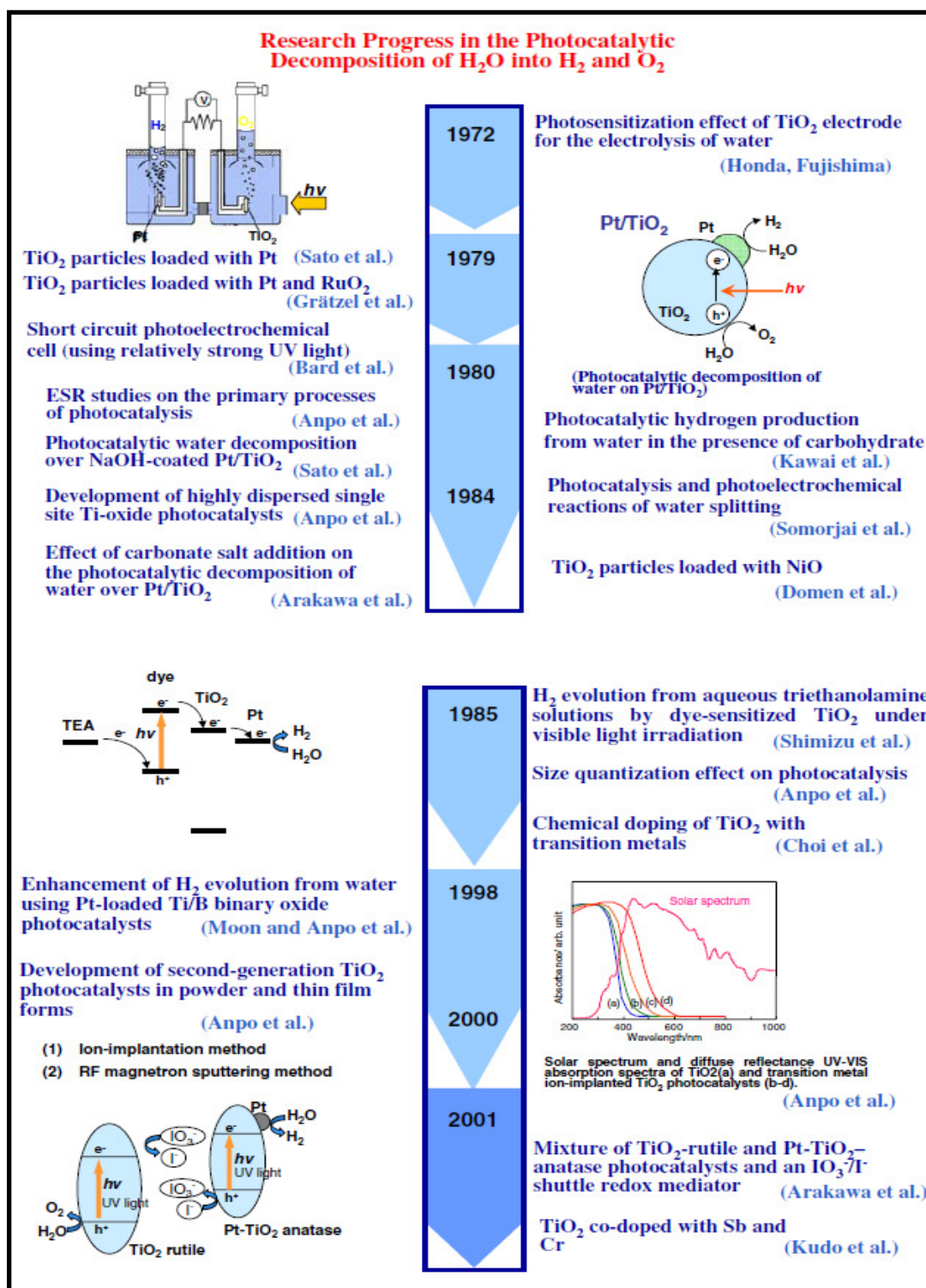
Figure 1.11 Background summaries of water-splitting research and development [30].
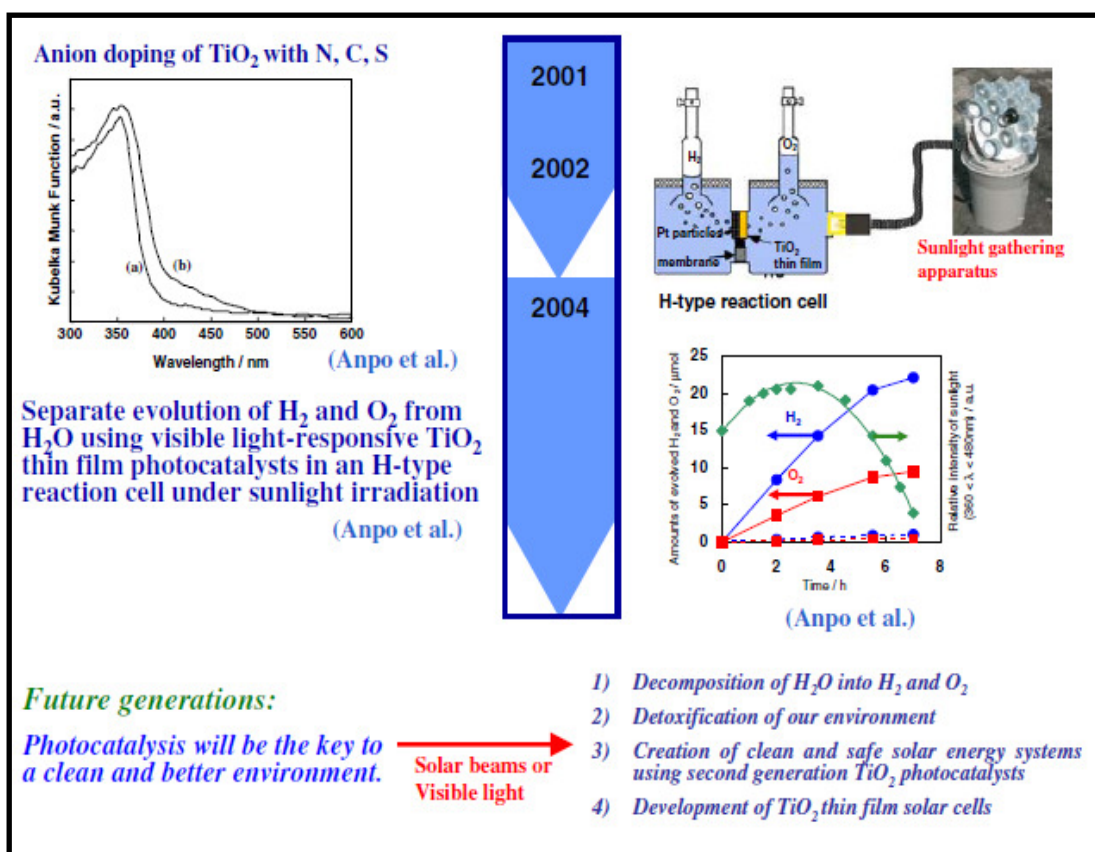
Figure 1.11 continued.

The water-splitting experiments can be conducted in the laboratories and under sunlight by closed circuit photoelectrochemical as shown in Figure 1.12. Upon excitation, the electrons flow through the external circuit to the Pt cathode where water species are reduced to hydrogen gas and the holes remain in the TiO_2 anode to oxidized water species to oxygen gas. An externally applied electrical potential (> 0.25 eV) may be necessary but this is much smaller than that required in water electrolysis (> 1.23 eV) [46, 52].
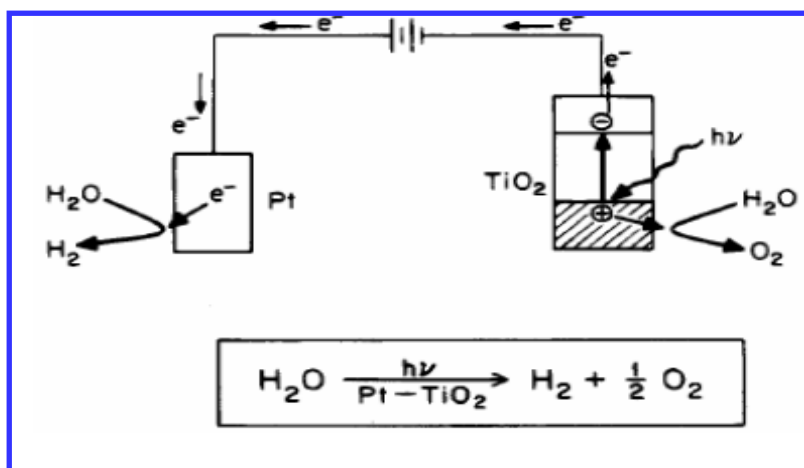
Figure 1.12 Closed circuit photoelectrochemical water-splitting cell [46] [52] .

In another approach, a composite semiconductor system ($Pt/RuO_2/TiO_2$) can be used for water-splitting system as a short-circuited cell. Pt/TiO_2 acts as cathode for water reduction reaction to generate hydrogen by photogenerated electrons and RuO_2/TiO_2 acts as anode for water oxidation reaction to generate oxygen by photogenerated holes. Figure 1.13 illustrates the mechanism [46] [52].
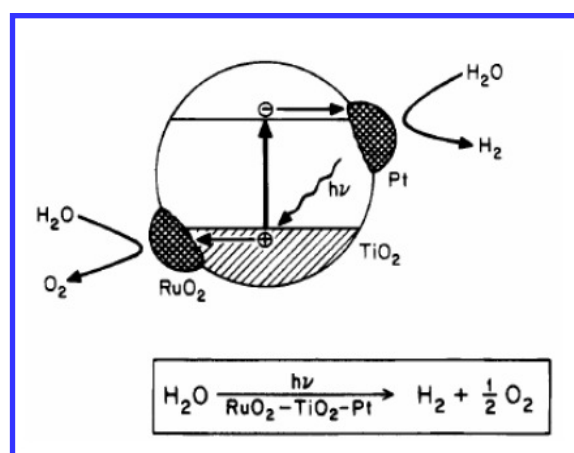
Figure 1.13 Composite semiconductor system for water-splitting cell [46] [52].

However, the oxygen and hydrogen evolution together in one system require a special experimental set-up for safety (avoid explosion) and for effective gases separation. Therefore, a simple technique can be used in this case by adding sacrificial agent, also called electron donors or hole scavengers as shown in Figure 1.14. The sacrificial species are used to remove one of the photodecomposition products so that the reaction equilibrium is shifted toward further decomposition. The sacrificial agent may be oxidized by holes to stop oxygen production or reduced by electrons to stop hydrogen production. The research in this dissertation following this approach by adding methanol as electron donor to water in order to shift the reaction toward hydrogen production and study the photocatalytic activity of water reduction reaction [46] [52].
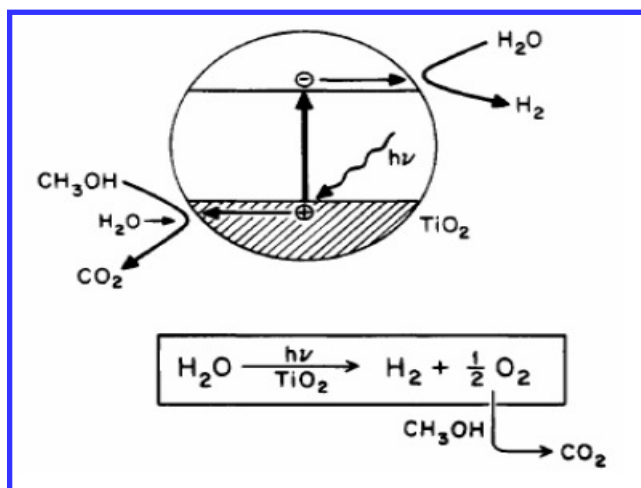
Figure 1.14 Methanol as electron donor added to water for water-splitting redox reactions [46] [52].

In conclusion, hydrogen production by water-splitting using solar energy is a great and promising method for future energy because both (sea) water and sunlight are clean, renewable, free natural resources. In addition, this technology is quite simple and can be used in small and large scales. To be mature commercially, a huge research and development include theoretical and experimental research to search for best materials based on their efficiency and stability is required. The research should cover the following items (1) the relationship between the materials properties and their structures, composition, size…etc. (2) bulk properties and interface properties at the solid / solid interfaces (grain boundaries) and solid / liquid interfaces (electrode / electrolyte) (3) harnessing full spectrum of solar radiation and excitation of electron–hole pair (more electron-hole pairs for single photon energy) (4) efficient charge separation and reduce recombination reaction of electron-hole or photo-generated oxygen and hydrogen gases (5) electrode (semiconductor) surface charge potential and transfer (6) generation of electron volts required for water-splitting (1.23 eV) [30].

SEMICONDUCTORS; TITANIUM DIOXIDE

Semiconductor is a material that has electrical conductivity between conductor and insulator. The electronic structures are characterized by a filled valence band, and an empty conduction band. If the valence band cannot be completely filled with electrons, no band gap will be present and a material is called metal. If the valence band is completely filled with electrons and has quit small band gap (<5 eV) the material called semiconductor, and if the band gap is large (>5 eV) the material called insulator. In solid

states physics, electrical conductivity occurs only when the electrons in partially-filled (valence) band excited into higher unfilled bands (conduction) either thermally and/or optically (Figure 1.15). When a photon with an energy of hv matches or larger the band gap energy, Eg of the semiconductor, an electron is jumped from the valence band to the conduction band leaving a hole according to Planck-Einstein equation. Electrons and holes can react with electron donors or acceptors adsorbed on the semiconductor surface. Upon excitation, the fate of the separated electron and hole can follow several pathways. (A) Electron-hole pair recombines at the surface (B) Electron-hole pair recombines in the volume of the semiconductor particle or with the release of heat. (C) Electrons jump to semiconductor surface and reduced by electron acceptor (metal). (D) The hole remains at other semiconductor surface to oxidize an electron donor (e.g. RuO_2 or alcohols). The probability of all these pathways are highly depend on the band edges positions (conduction and valence bands) and the redox potential levels of the adsorbate species [46][52].
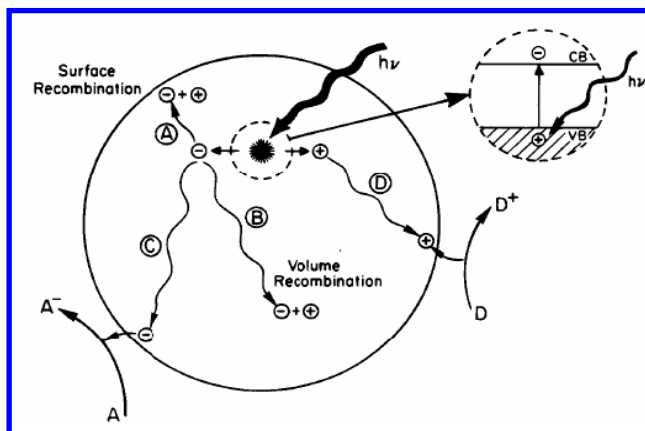
Figure 1.15 In Solid state physics, possible electron-hole pair pathways upon photo excitation [46][52].

The relevant potential level of the acceptor species is thermodynamically required to be below (more positive than) the conduction band potential of the semiconductor. The potential level of the donor needs to be above (more negative than) the valence band position of the semiconductor in order to donate an electron to the vacant hole. The Energies for various semiconductors in aqueous electrolytes at pH = 1 and the band edge positions of several semiconductors are showed in Figure 1.16 [46] [52].
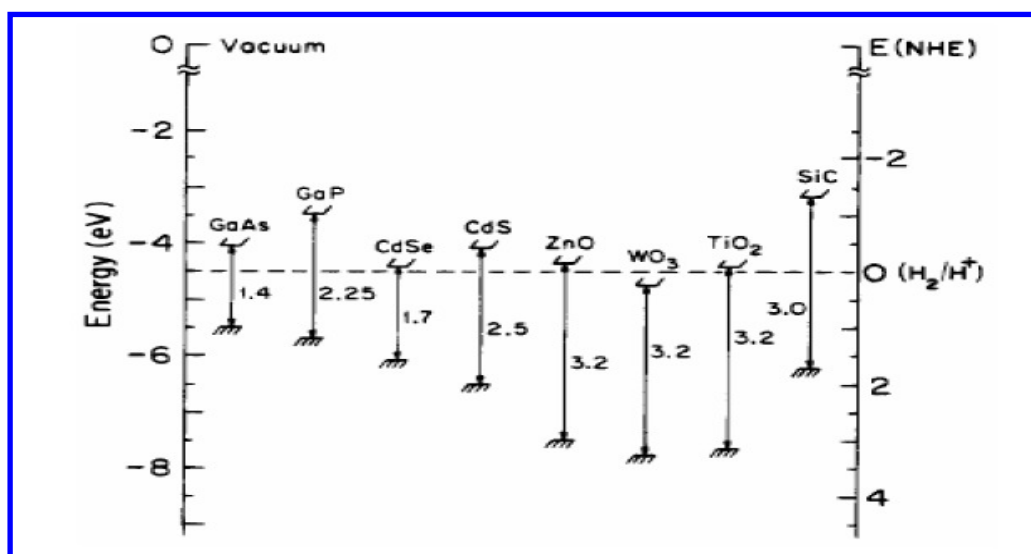
Figure 1.16 The band edge positions of various semiconductors (electrolyte solution pH=1) [46] [52].

The internal energy scale is given on the left for comparison to the vacuum level and on the right for comparison to normal hydrogen electrode (NHE). The positions are derived from the flat band potentials in a contact solution of aqueous electrolyte at pH = 1. The pH of the electrolyte solution influences the band edge positions of the various

semiconductors compared to the redox potentials for the adsorbate. Contact between a semiconductor and another phase (i.e. liquid, gas, or metal) generally involves a redistribution of electric charges and the formation of a double layer. The transfer of mobile charge carriers between the semiconductor and the contact phase, or the trapping of charge carriers at surface states at the interface, produces a space charge layer. For semiconductor-gas phase interactions, an n-type semiconductor such as TiO_2 can have surface states available for electron trapping. The surface region will become negatively charged [46][52].

TiO_2 is a ubiquitous opaque white pigment and widely used in various applications such as paper, plastics, pharmaceutical tablets, self-cleaning window glass, air and water purification systems, and pollutants degradation [46][52]. Titanium oxide has high photocatalytic and photovoltaic activity. It is very stable in aqueous solution (anticorrosive for photocorrosion and chemical corrosion). In addition, it is inexpensive and its preparation methods are simple and green, low cost and environmentally benign. Therefore, it is strong candidate semiconductor for water-splitting under solar energy. However, the band gap of anatase phase TiO_2 is about 3.2 eV (UV light response only) and the band edge positions are not appropriate with redox potential energy level of water-splitting reaction. The applications of TiO_2 are related to their properties which are related to the atomic structure. TiO_2 crystallizes have three different structures: rutile, anatase and brookite (Table 1.1, Figure 1.17, Figure 1.18) [46][52][53].

Table 1.1 TiO$_2$ crystal structure [46] [52] [53]

	Rutile[a]	Anatase[a]	Brookite[b]
Crystal structure	tetragonal	tetragonal	orthorhombic
Lattice constants (Å)	$a=4.5936$	$a=3.784$	$a=9.184$
	$c=2.9587$	$c=9.515$	$b=5.447$
			$c=5.145$
Space group	$P4_2/mnm$	$I4_1/amd$	$Pbca$
Molecule/cell	2	4	8
Volume/molecule (Å^3)	31.2160	34.061	32.172
Density (g/cm^3)	4.13	3.79	3.99
Ti—O bond length (Å)	1.949(4)	1.937(4)	1.87~2.04
	1.980(2)	1.965(2)	
O—Ti—O bond angle	81.2°	77.7°	77.0°~105°
	90.0°	92.6°	
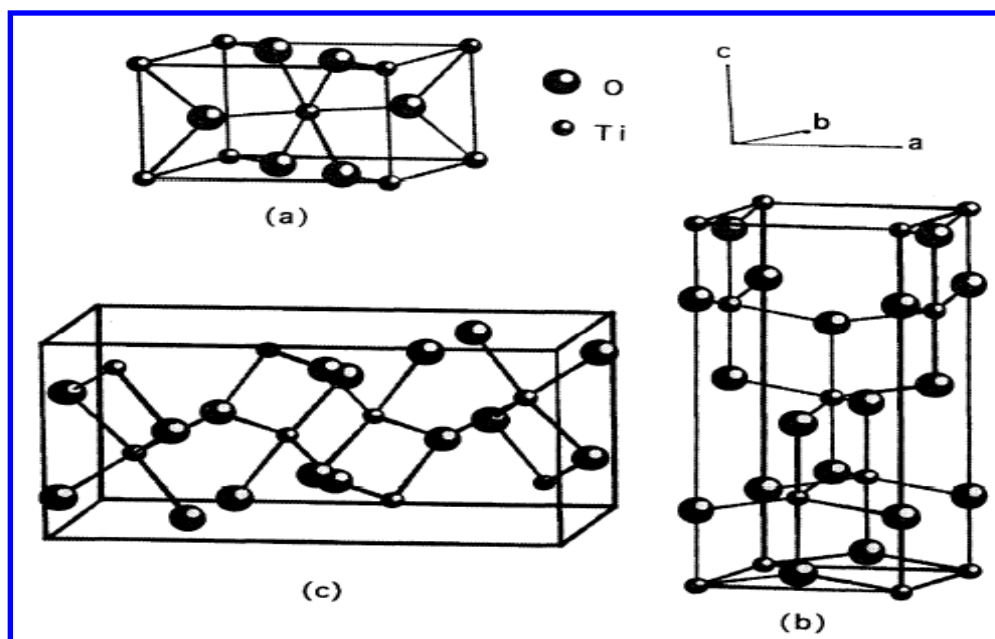
Figure 1.17 TiO$_2$ crystal structure (a) Rutile (b) Anatase (c) Brookite [46] [52] [53].
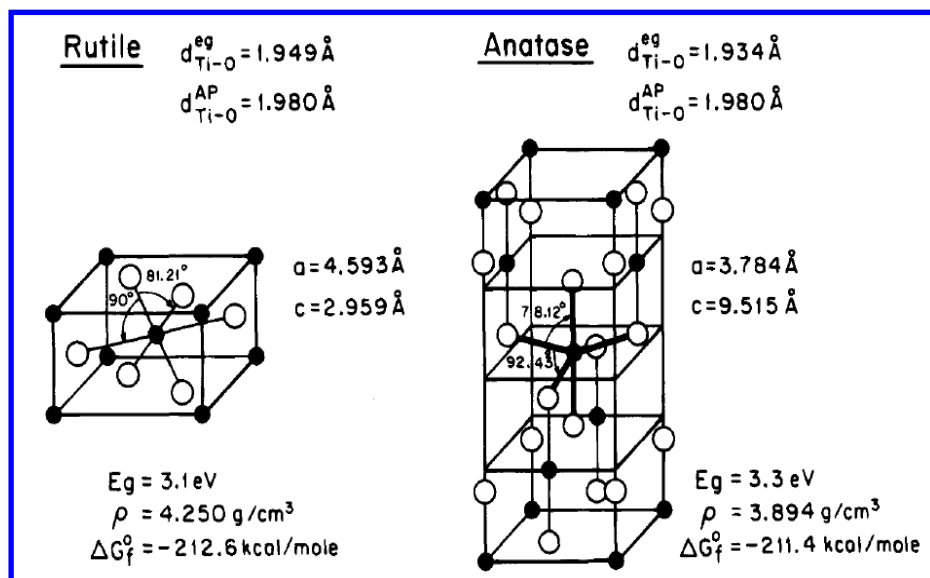
Figure 1.18 Anatase TiO_2 is the most active photocatalytically crystal structure [54].

The photocatalytic activity of TiO_2 related to the electrical properties. The band gap energy of rutile is 3.0 eV and for anatase phase is 3.2 eV. The electrons mobility and diffusivity of the rutile is much lower than that in anatase phase. Since the flat-band potential of rutile is faintly more positive than that of the standard H_2 electrode, and the flat-band potential of anatase is more negative to it, the reduction of water molecules to hydrogen by photoexcited conduction band electrons takes place spontaneously on anatase polymorphs than on rutile. On the other hand, O_2 evolution occurs at similar rates on anatase and rutile since the potential of the photogenerated holes is above the potential of oxygen evolution. These two characteristics make anatase the only crystalline titania phase where photo dissociation of water molecules can take place without an external applied voltage. In addition, the enhanced photo activity of anatase over rutile is attributed to the larger band gap of the former (3.2 eV versus 3.0 eV) which

helps in increasing the surface redox potentials and prolonging the electron/hole lifetime. Charge carrier trapping would suppress recombination and increase the lifetime of the separated electron and hole. Surface and bulk defects naturally occur during the synthesis and they may help suppress the recombination by trapping charge carriers. Primary process and characteristic time of TiO_2 photocatalysis in an aqueous system is listed in (Table 1.2) [46] [52] The modification of TiO_2 during the preparation methods and techniques highly affect the size and shape of photocatalyst, these modifications could alter the energetic of the water splitting reaction by favoring an efficient charge transfer and minimizing the electron/hole recombination process. Figure 1.19 shows the dopants used in the TiO_2 nanomaterials [46] [52]. The main objective is to fine tune the band gap response of TiO_2 to higher wave length radiations in order to tailor its response towards the visible light region of the solar spectrum (Figure 1.20) [46] [52].

Figure 1.19 The dopants used in the TiO_2 nanomaterials in the periodic table [46] [52].

Figure 1.20 The absorption region of TiO$_2$ with solar spectrum [46] [52].

In conclusion, TiO$_2$ is strong candidate for water-splitting under solar energy and will be used through the experiments in this dissertation due to the following reasons [53] (1) high stability and resistance to corrosion (2) high photocatalytic and photovoltaic properties (3) high activity in both light and water environment (4) the properties can be widely altered by varying the lattice defect chemistry and the related electronic structure through alteration of the oxygen nonstoichiometry. (5) Environmentally friendly, abundant, and low cost [53] [55].

Table 1.2 Primary process and characteristic time of TiO$_2$ photocatalysis in an aqueous system [46] [52].

Primary Process	Characteristic time (second)
Charge-carrier generation $TiO_2 \xrightarrow{hv} h_{VB}^+ + e_{CB}^-$	10^{-15} (very fast)
OH$^{\bullet+}$ formation at the TiO$_2$ surface $h_{VB}^+ + > Ti^{IV}OH \rightarrow \{> Ti^{IV}OH^{\bullet}\}^+$	10^{-9} (fast)
Electron trapping $e_{CB}^- + > Ti^{IV}OH \leftrightarrow \{> Ti^{III}OH\}$ $e_{CB}^- + > Ti^{IV} \leftrightarrow > Ti^{III}$	10^{-10} (shallow trap; dynamic equilibrium) 10^{-8} (deep trap; irreversible)
Charge-carrier recombination $e_{CB}^- + \{> Ti^{IV}OH^{\bullet}\}^+ \rightarrow > Ti^{IV}OH$ $h_{VB}^+ + \{> Ti^{III}OH\} \rightarrow > Ti^{IV}OH$	10^{-7} (slow) 10^{-9} (fast)
Interfacial charge transfer $\{> Ti^{IV}OH^{\bullet}\}^+ + Red \rightarrow > Ti^{IV}OH + Red^{\bullet+}$ $e_t^- + O_x \rightarrow > Ti^{IV}OH + O_x^{\bullet-}$	10^{-7} (slow) 10^{-3} (very slow)

NANOTECHNOLOGY

The first time the idea of nanotechnology was introduced was in 1959, when Richard Feynman, a physicist at California Institute of Technology, gave a talk called "There's Plenty of Room at the Bottom." Though he never explicitly mentioned "nanotechnology," Feynman suggested that it will eventually be possible to precisely manipulate atoms and molecules. Ultimately, we can arrange the atoms the way we

want; the very atoms, all the way down [56]. The impact of nanotechnology on our life can be as great as the invention of the steam engines, electricity, and even the information and telecommunication technologies. Nanomaterials and nanodevices hold great potential to help in solving or at least minimizing the most problems we faced today starting from diseases and ending with energy and environment challenges, not to mention the electronics and other consumer products that we use every day. Nanotechnology is to study and manipulate the properties of materials at a scale of less than 100 nanometers (1 nm $=1\times10^{-9}$ m). At this scale, the materials can be fabricated and tailored to achieve significantly unique and better properties than materials on a larger scale. Nanotechnology is a discipline that growing very fast because of recent tremendous advances in characterization tools such as scanning probe microscopy (SPM) and atomic force microscopy (AFM). These techniques enable to gain insight and to have better understanding of how to manipulate materials at atomic-scale to achieve the desired effects. This ability to manipulate materials on the nano scale allows enhancing the materials properties. For thermal properties, it can be designed to conduct substantially than bulk material and increase the thermal stability. For chemical properties, it has large surface area to volume ratio and large contribution of surface atoms. For mechanical properties, it has great resistance and strength with light weight. For electronic and optical properties, it can be defect free-electrons move and quantum confinement. For electrical properties, it improves the electrical conductivity. The three categories of nanotechnology are (1) nanomaterials and quantum structure (2) nanodevices (3) Simulation and modeling at *Nano*-scale. The applications are diverse in

many fields such as energy, water, medical, and electronics. Nanotechnology is all about properties of materials at the *Nano*-scale and then transferring those properties to the *Macro*-scale. Specifically, the application of nanotechnology "nanomaterials and quantum structures" toward renewable, clean, and sustainable energy production technologies like hydrogen production from seawater and solar energy hold a great potential to be a future energy carriers. The state-of-art nanomaterials with portable and unique properties can be prepared as multifunctional materials to achieve the desired effects required in the specific application. Cost-effective nanomaterials with environmentally clean manufacture also can be designed, prepared and applied.

At *Nano*-scale, the materials properties are highly depend on their size, shape, structure, crystal structure, and internal & external compositions. The change in semiconductor properties is not because of the length scale, it is due to the further confinement of the electronic motion to a length scale comparable or smaller than the length scale characterizing the electronic motion in bulk semiconducting material (called the electron Bohr radius) [46] [52]. If the size is (< 10 nm) with different composition, the properties of the materials are changed by the quantum size confinement or effects. In this case, it will be same or less than the Bohr exciton radius, the natural length scale of the electron-hole pair of the bulk material. Also the surface atoms play a more important role at nano-scale size. The surface atoms usually have fewer adjacent coordinate atoms and unsaturated sites or more dangling bonds. Thus these atoms are chemically more active compared to the bulk atoms, which renders them to be more accessible for chemical modification [46] [52]. It is possible to design efficient and cost-effective

photocatalysts using the quantum confinement and surface atoms effects to harness visible light wavelength and have more than electron-hole pairs for single photons. Photocatalyst is accelerating or speeding up a chemical reaction induced by the presence of material that is chemically unchanged at the end of the reaction by lower the activation energy of the reaction, provide alternate reaction pathways to get the products and increase the rate of reactions and lower the rate-limiting free energy (Figure 1.21 & Figure 1.22).
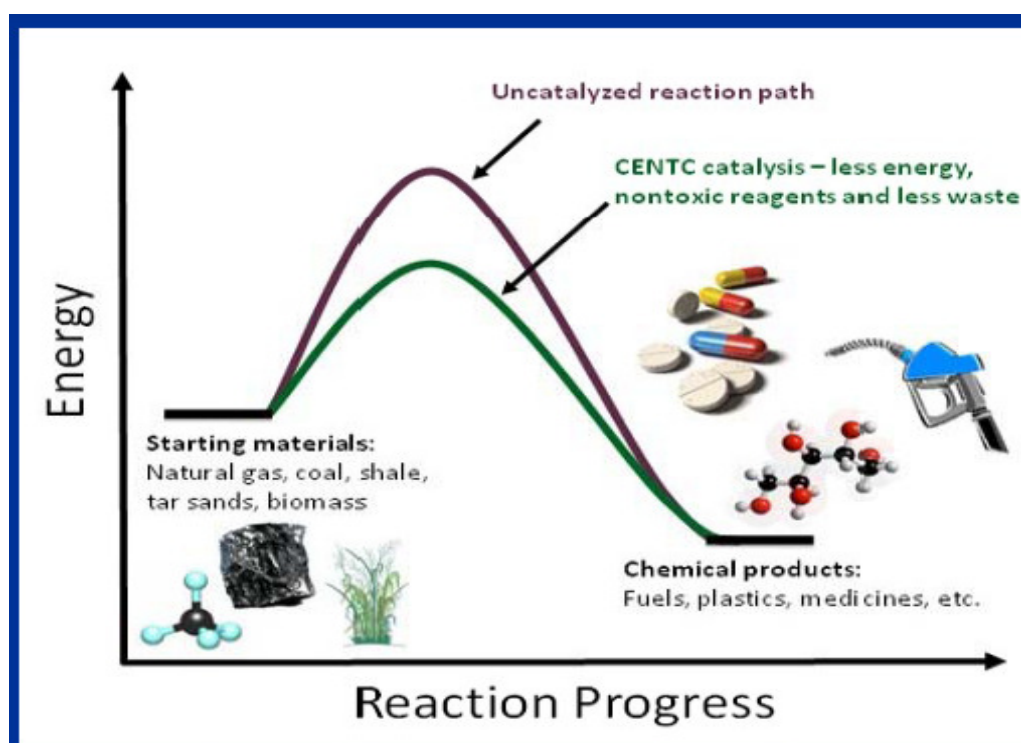
Figure 1.21 Photocatalyst accelerate the chemical reaction by providing alternate reaction pathways [57]
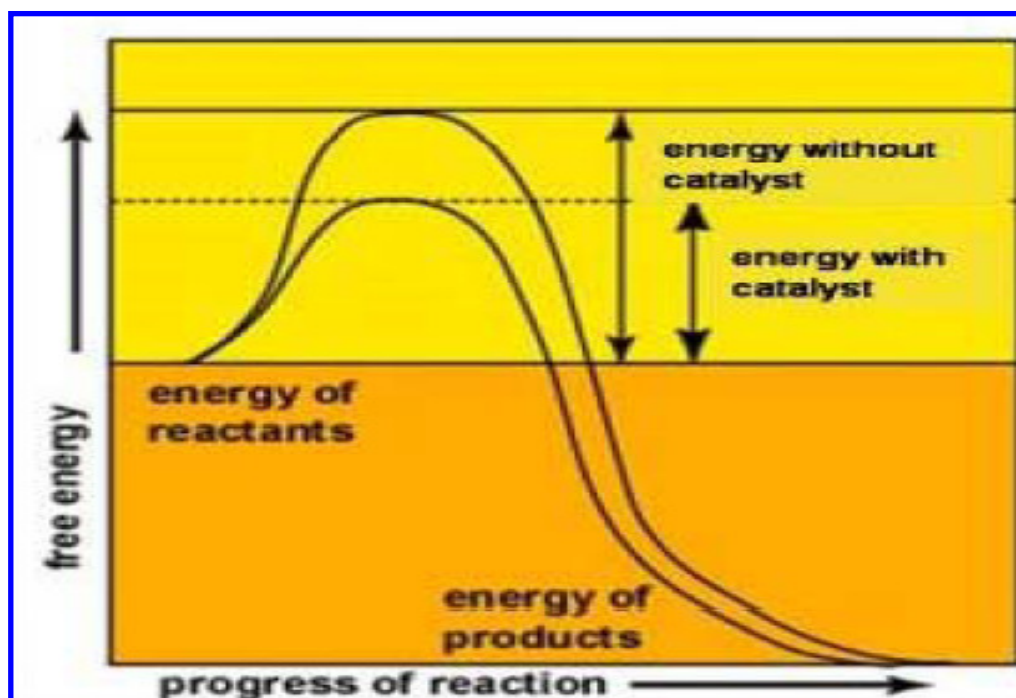
Figure 1.22 Photocatalyst materials accelerate the chemical reaction by lowering the activation energy and remain unchanged chemically [57]

There are two synthesis or fabrication approaches to prepare nanostructure materials: **(1) Bottom-up** where materials and devices are built from molecular component which assemble themselves chemically (layer by layer self-assembly) by principles of molecular recognition. **(2) Top-down** where nanostructure material and devices are fabricated or constructed using larger objects without atomic level control. The synthesis or preparation methods used to make nanoparticles are the key to govern and manipulate the size and other parameters that impact on the nanoparticles properties. The preparation methods are chemical, physical and physicochemical methods. The chemical methods are deposition-precipitation, ion-exchange, impregnation, successive reduction, calcinations, surface capping, microemulsions, photochemistry, chemical vapor deposition, electrochemical reduction …etc. The physical and physicochemical

methods are sonochemistry, microwave irradiation, pulsed laser ablation, supercritical fluids, and plasma. After synthesis, it can confirm that the desired properties were achieved by using several characterizations. The ability to precise control up to atomic-level by ordered and arranges the atoms and crystal lattice will lead to explore portable and unique properties to these materials and make them stable, efficient, cheaper, cleaner, stronger, lighter and durable for desired applications. For instant, the tremendous properties of carbon nanotubes make them promising materials in solar cells, electronics, batteries and other applications (Figure 1.23). Gold is chemically stable material, however, recently it shows high catalytic activity when the gold size in less than 5 nm and also the common yellow color of gold changed to red color due to the size effect. Figure 1.24 shows the size of many objects in *Nano*-scale.
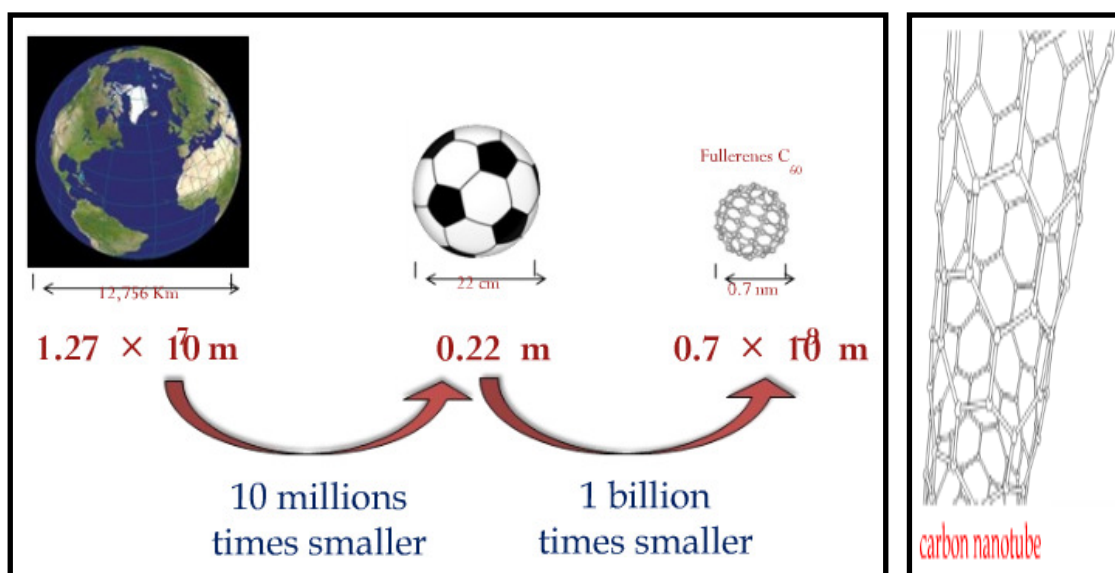
Figure 1.23 Shows how small the *Nano*-scale and the carbon nanotube [57].
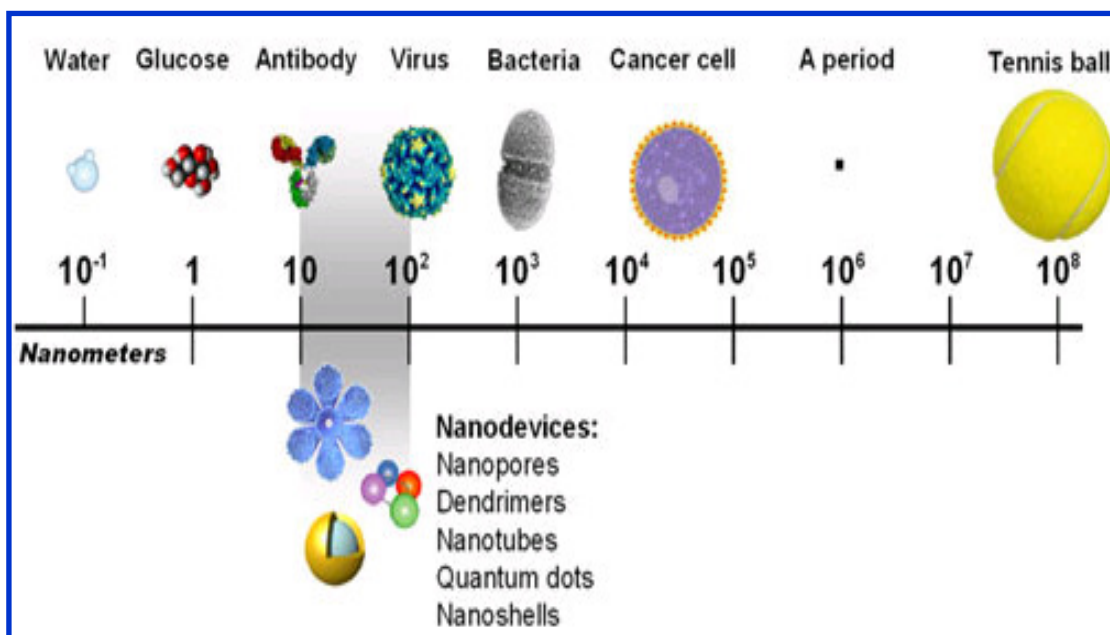
Figure 1.24   The size of many objects in *Nano*-scale [58].

The surface of materials can also be modified by treatment, adsorption of a surfactant and hydrophilic and hydrophobic in order to reduce the surface and interface tension, to promote the assembly. (e.g. to serve as a nanoelectrical wire in DNA molecule), to functionalized for specific application and to passivation and stabilization of nanoparticles. Understanding the nucleation and growth rate of nanoparticles are vital to have better control at atomic-level and tailor the size-properties design of the material Control the atoms nucleation and growth rate during synthesis is the key to manipulate the properties of nanomaterials (Figure 1.25).
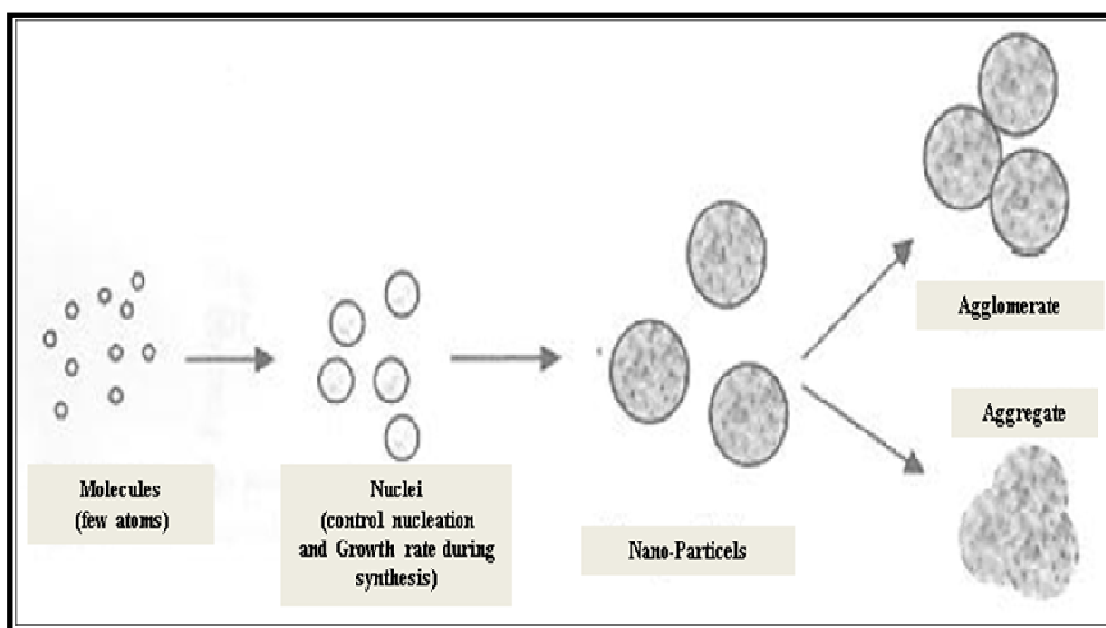
Figure 1.25 Atoms nucleation and growth rate during synthesis [57].

SOLAR ENERGY

The amount of energy hitting the earth in one hour is about 4.3×10^{20} J, which is more than the amount of energy consumed on the planet in one year (about 4.1×10^{20} J). The global energy consumption is 13×10^{12} watt or 13 terawatts (TW), where, on average, 120,000 TW of solar energy strikes the earth. On other words, at sun power intensity of 1000 W/m^2 [12], just 0.16% of land area on earth with 10% efficient solar cells would supply 20 TW of power globally [59]. The sunlight is almost shinning everywhere providing clean, abundant and free source of energy to entire world. As a carbon-neutrally and environmentally benign, the sunlight could be the permanent solution for the energy and environment challenges we faced today if the technologies to harness the solar energy are well developed in cost-effective techniques and materials. The sun is the

source of all other energy sources such as fossil fuels, wind, geothermal and wave energy that existed on the earth. The solar energy can be converted into electricity, chemical fuels and thermal systems [59]. In 2001, only 0.1% of world's electricity derived from solar energy and solar fuel derived from biomass is less than 1.5% of world's energy [59]. For solar electricity, the common photovoltaic solar cells are used to converted solar energy into electricity. Harnessing the full spectrum of wavelengths in solar radiation using cost-effective nanostructures materials considered the main target for the next generation of solar cells (Figure 1.26). Several technologies like single-crystal solar cell, thin film, organic semiconductor, and quantum dot and dye sensitization are used to increase the efficiency of solar energy conversion to electricity as well as reduce the cost of technology to be competing with the cost of electricity generated by fossil fuels or nuclear energy [59]
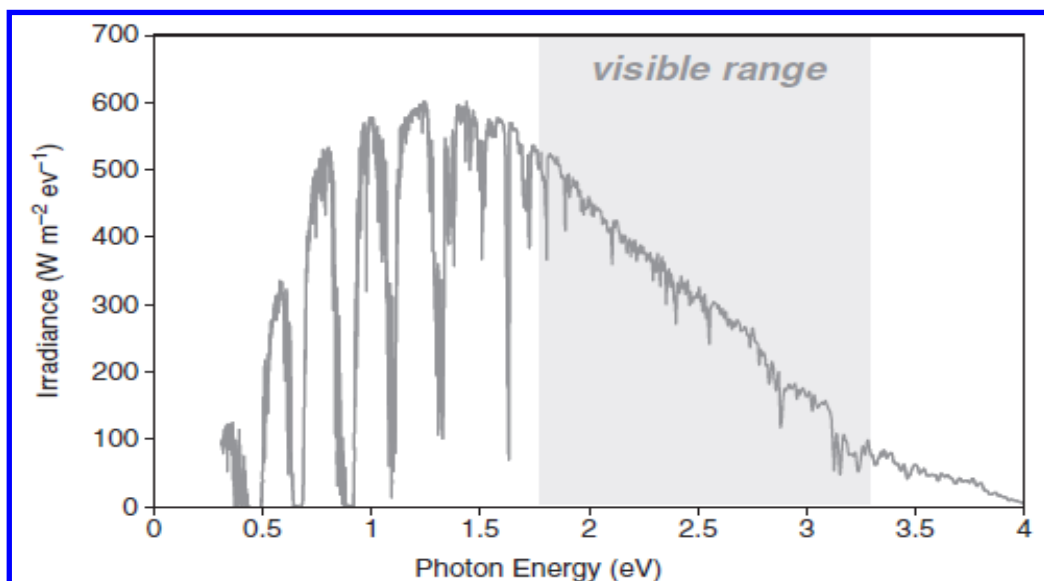
Figure 1.26 The AM 1.5 solar spectrum as function of photon energy [10].

For the solar thermal systems, the focused and concentrated sunlight in thermal reactors and towers can be stored and converted into chemical and mechanical energy (Figure 1.27). In conversion systems from solar to thermal energy, concentrated sunlight produces high temperatures to drive heat-engines for generating mechanical work, electrical energy, or chemical products [10] Water-splitting to generate hydrogen can be achieved by thermolysis at very low pressure and very high temperature (reached to 2500K) [5]. However, by solar-thermochemical cycles such as sulfur iodine and copper chlorine can be achieved with reaction temperature up to 1200K [10].
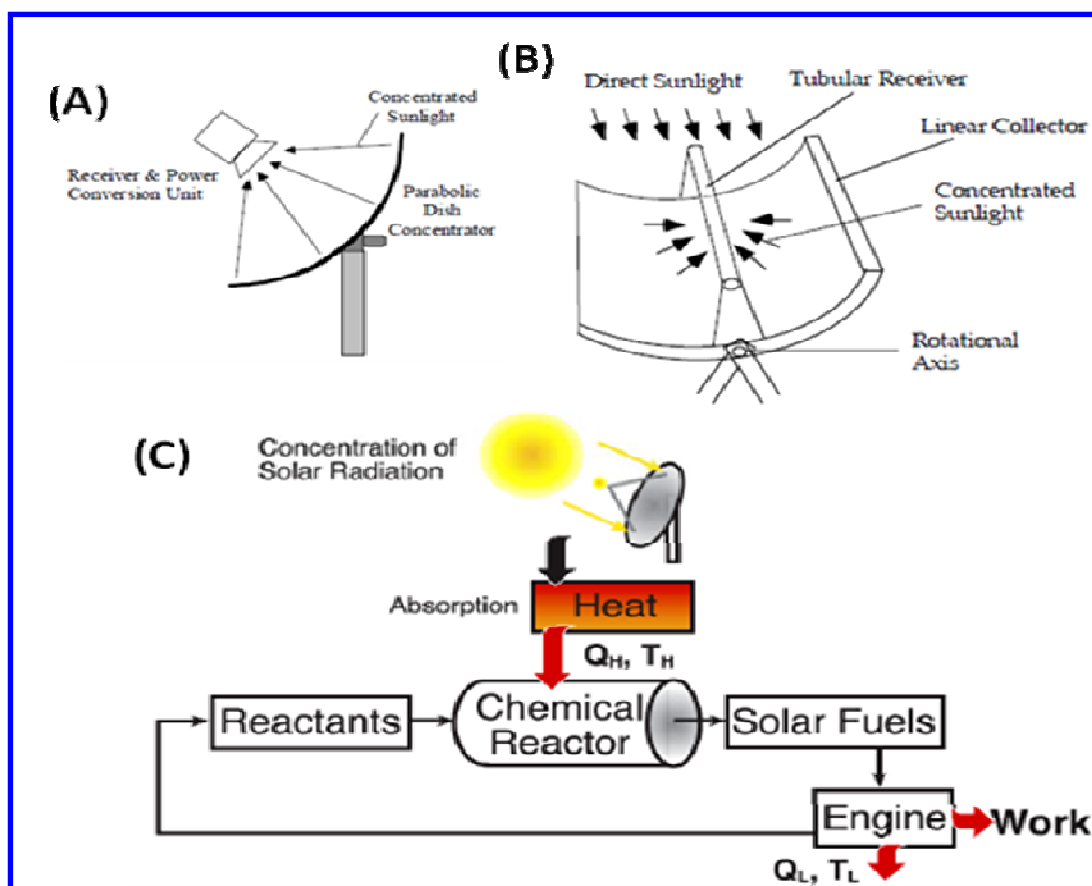
Figure 1.27 Thermal solar energy systems (A) parabolic dish (B) line focus (C) solar-driven thermochemical cycle [59].

Therefore, a high temperature thermal conversion system with robust and cost-effective methods must be developed to enhance hydrogen production from water splitting.

Solar-hydrogen Fuel Production

In natural photosynthesis in the plant, the plant harness, store and convert the sunlight into chemical energy (Figure 1.28). The storage of solar energy by conversion into chemical fuels is very important approach due to the day-night and sunny-cloudy cycles of solar radiation. A cost-effective technology is required to store the sunlight into chemical fuels just by mimicking the natural photosynthesis. The artificial photosynthesis or solar-hydrogen production by water-splitting is a very promising technology to store the solar energy into hydrogen fuel. The key is to develop nanostructures architectures of new materials based on organic/inorganic hybrid materials to enhance the solar to hydrogen conversion efficiency with low cost materials and approaches [59].
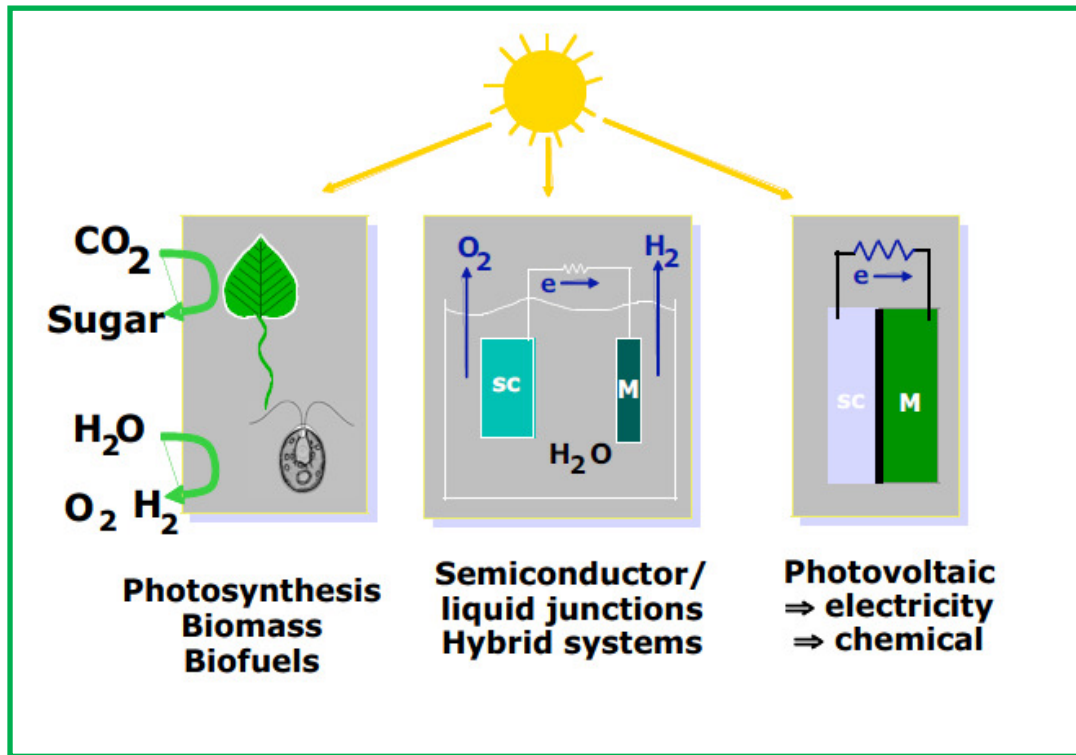
Figure 1.28 Learning from nature (plant photosynthesis) how to harness solar energy for sustainable production of energy [60].

OVERVIEW OF THE DISSERTATION

The goal of this dissertation is to search for structure-properties relationship of various platforms of TiO_2 nanocomposites semiconductor with quantum dots sensitization or other solar energy capture techniques to enhance hydrogen production from the photoelectrochemical water-splitting (PWS). The design, synthesis, characterization and application of these TiO_2 nanostructured photocatalysts are based on simple, low cost, precise control, and green synthesis methods, in the mean time maintain high efficiency and high stability.

The time course of hydrogen production (under natural sunlight and light source in the laboratory) was used to calculate photo hydrogen production rate and monitor it stability over long time. The improvement in energy harvest was evaluated by calculating the energy efficiency (%).

Towards achieving the ultimate goal, three objectives are proposed here, each with several tasks to accomplish. Tasks in each objective will be conducted by design, synthesis, characterizations, and application of TiO_2 nanocomposites to measure hydrogen production rate from water splitting reactions under light illumination. The research objectives are (1) Low cost metals as photocathode for solar water-splitting and the role of asdditives (2) Electrospinning nanofiber-network as effective photocatalyst support. (3) Band gap engineering through Quantum dots sensitization, dye sensitization and nitrogen-doping to harvest visible solar energy. The tasks are (1) Investigate the effect of semiconductor configurations such as a nanosphere (0D), a nanorod (1D), and a nanotube (1D) on overall process performance. The factors that affect the semiconductor

band gap are number of electrons at valence level, orbital hybridization, and crystal lattice configuration. (2) Investigate the effect of inexpensive nanocatalysts on redox reactions and hydrogen production. Nitrogen-doping at illumination of TiO_2 will change the structure and locations in crystal lattice. Therefore, the quantum confinement will change. The change on quantum confinement will tune the band gap structure of the semiconductor. (3) Investigate the effect of various concentration of NaCl (wt %) in water/methanol solution to know the possibility of splitting seawater to produce hydrogen. Methanol added to limit the oxygen separation. (4) Identify the effect of adding dye sensitizer for visible solar energy absorption under UV light and sunlight (5) Assess the effect of the quantum dots sensitization on the overall hydrogen production. (6) Calculate the solar to hydrogen conversion efficiency (energy efficiency %). The experimental results are expected to provide better understanding of process mechanism which helps to gain insight for useful process modeling and simulation and to improve the materials design.

Simple, cheap, and green physical and chemical synthesis methods (Sol-gel method, autoclave, microwave, electrospinning, porous anodic alumina templates membrane [61] and wet impregnation) were used based on rational design of photocatalyst to achieve the desired properties and multifunctional nanomaterials. High through-put screening process of nano-scale photocatalysts to evaluate the water photocatalytic reduction reaction for hydrogen generation was established. A single-photo reaction cell was used in order to measure the hydrogen gas only.

Therefore, methanol was mixed with water to stop the oxygen evolution and produce carbon dioxide. Methanol is strong electron donor and act as oxidation agent. The photocatalysts will be tested under UV light (100 W/m^2) and/or natural sunlight (240 W/m^2) college station, Texas. The results must guide to better understanding about structure-properties relationship, surface/ interface chemistry between solid/solid (grain boundaries) and solid/liquid (semiconductor and electrolyte). Figure 1.29 summarizes the goals, objectives and tasks of this research.

Objective 1: Low cost metals as photocathode for solar water-splitting. There are two tasks must be conducted to fulfill the first objective: **Task 1:** to evaluate low cost metals as water photo reduction catalysts under sunlight. **Task 2:** to investigate photo-hydrogen production rate dependence on TiO_2 crystal structures.

Objective 2: Electrospinning nanofiber-network as effective photocatalyst support. There are two tasks must be conducted to fulfill the second objective: **Task 1:** to investigate the effect of one-pot synthesis of Ag/TiO_2 nanofiber on performance under UV light with water and methanol (as electron donor). **Task 2:** to study the impact of PVP (polymer component) nanofiber-network support of Cu/TiO_2 nanopowders by avoiding the aggregation process of the photocatalyst.

Objective 3: Band gap engineering through Quantum dots sensitization and nitrogen-doping to harvest visible solar energy. The research tasks for objective 3 are: **Task 1:** Band gap and defect engineering by Nitrogen-doping: Synthesis of $Cu/TiO_{2-x}.N_x$ and to be tested under UV light and directly under sunlight by narrowing TiO_2 band

gap. **Task 2:** Synthesis of QDots-TiO$_{2-x}$.N$_x$.Ag film: to harvest visible solar energy by using QD'S as composite semiconductor with lower band gap than TiO$_2$.

The main goals, objectives and related tasks for this research are included in the following chapters; **Chapter I:** Introduction, **Chapter II:** Nanocomposites thin-films using Ag /TiO$_2$, **Chapter III:** Role of electron donor/accepter on electron transportation between electrode/electrolyte interfaces, **Chapter IV:** Band gap and defect engineering by nitrogen doping to harness visible light of solar energy, **Chapter V:** Quantum dots sensitization, **Chapter VI:** TiO$_2$ nanostructures-properties relationship and the Impact on solar to hydrogen conversion efficiency, **Chapter VII:** Nanofibers as effective supporter for TiO$_2$ nanocomposites photocatalyst system including quantum dots and dye sensitization, **Chapter VIII:** Comparison of results, and **Chapter IX:** Conclusions.
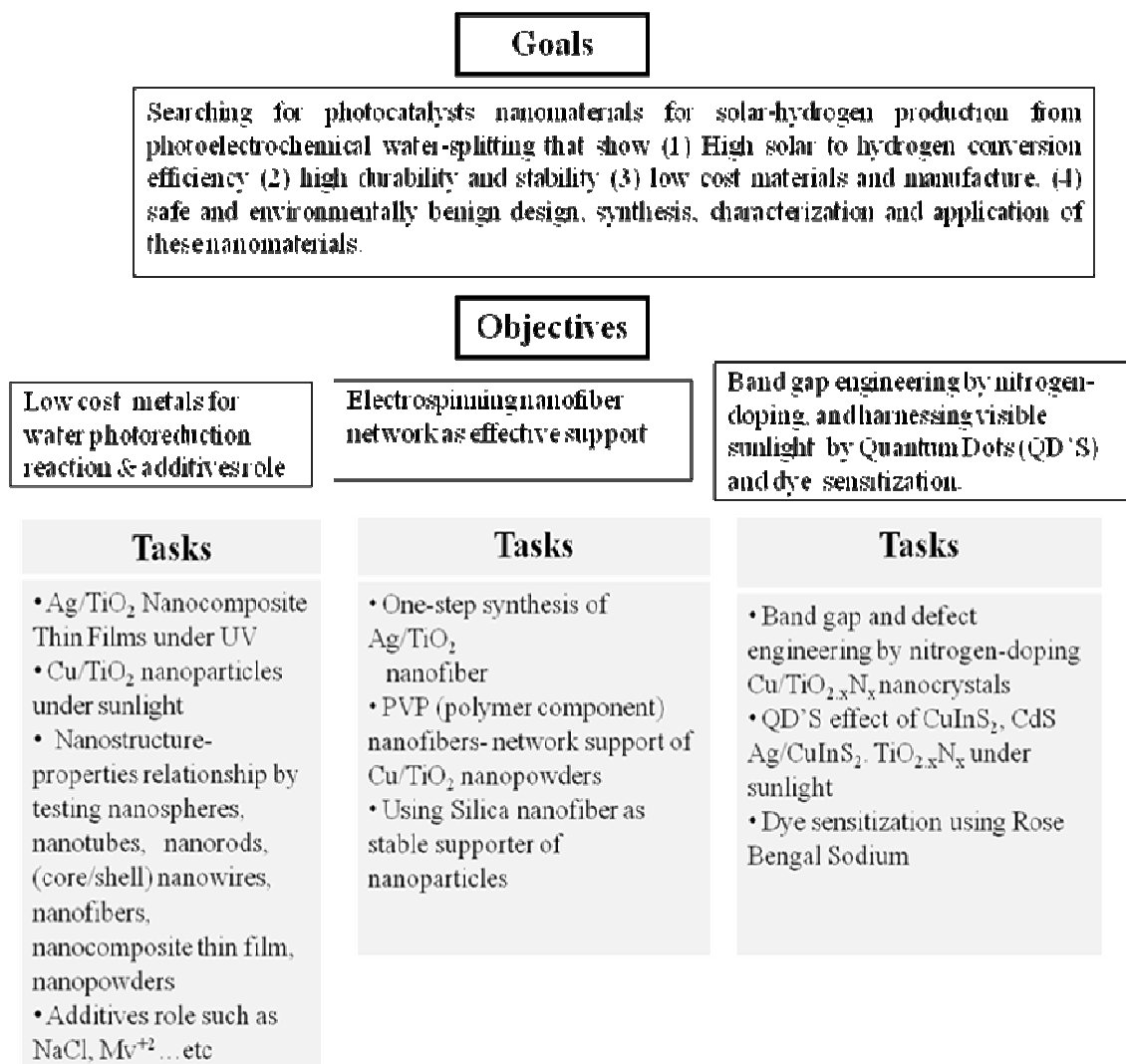
Figure 1.29 Schematic diagram summaries the road-map of this dissertation.

CHAPTER II

NANOCOMPOSITE THIN FILMS USING Ag/TiO$_2$

OVERVIEW

Though less frequently studied for solar-hydrogen production, films are more convenient to use than powders and can be easily recycled. Anatase TiO$_2$ films decorated with Ag nanoparticles are synthesized by a rapid, simple, and inexpensive method. They are used to cleave water to produce H$_2$ under UV light in the presence of methanol as a hole scavenger. A simple and sensitive method is established here to monitor the time course of hydrogen production for ultralow amounts of TiO$_2$. The average hydrogen production rate of Ag/TiO$_2$ anatase films is 147.9±35.5 μmol/h/g. Without silver, it decreases dramatically to 4.65±0.39 μmol/h/g for anatase TiO$_2$ films and to 0.46±0.66 μmol/h/g for amorphous TiO$_2$ films fabricated at room temperature. Our method can be used as a high through-put screening process in search of high efficiency heterogeneous photocatalysts for solar-hydrogen production from water-splitting.

INTRODUCTION

Energy production and environmental challenges are paramount issues in the 21st century[7]. Limited fossil fuel resources and strict environmental regulations motivate the search for sustainable, efficient and environmentally friendly energy sources [62] . Hydrogen has great potential as a future energy carrier. It is the most abundant element on the earth. In fact, H$_2$ molecules have a higher energy content per weight than coal and

gasoline [41]. Moreover, hydrogen can be used in fuel cells to generate electricity, or directly as a transportation fuel [63].

Hydrogen can be generated from hydrocarbons and water resources; however it does not exist in nature in its rich energy state. Currently, most hydrogen is produced from methane-steam reforming [64], which consumes energy and produces greenhouse gas emissions, mainly, carbon dioxide [63]. In contrast, a photoelectrochemical water-splitting process is a zero emission process and uses free solar energy [40,55,65]. Extensive studies have been searching for the best material candidate for this process since it was discovered by Fujishama and Honda in 1972 [66]. The main criteria for these materials are low-cost, environmentally friendly, high efficiency and stability. TiO_2 is a strong candidate due to its high stability in aqueous solutions and high photovoltaic and photocatalytic activity [67,45].

Nanotechnology, which manipulates materials at the nano or atomic scale, has a great potential for design and synthesis of multifunctional materials with desired and unique properties. It also can reduce the cost of materials manufacture. The purpose of this work is to pursue the possibility of using anatase Ag/TiO_2 nanocomposite films to generate hydrogen by water splitting and improving their quantum efficiency. To split water using photocatalytic materials and solar energy, there are three main obstacles need to be overcome: (1) narrowing of the band gap to harness visible light [11], (2) increasing the efficiency of charge separation, and (3) reducing the recombination reaction of O_2 and H_2 to form water [12]. Previous studies have focused heavily on these issues to find a strong candidate that matches all the criteria. The properties, size,

geometry and compositions of materials are the keys to modify the material activity to improve hydrogen production [45]. Many tested semiconductors are either unstable in aqueous solution such as CdS, or possess too large a band gap such as SnO_2 [49].

Effect of Noble Metal Loading on Charge Separation

Different semiconductor geometries have been extensively used in the harvesting of solar energy [68-70]. Nano-films are widely used to design photovoltaic solar cells [71]. However, to the best of our knowledge, only limited studies discussed nano-film TiO_2 for hydrogen production from the photoelectrochemical splitting of water. For example, Kitano, M., et al. in 2005 [72] reported that Pt-loaded visible light responsive TiO_2 thin films fabricated by the radio-frequency magnetron sputtering deposition (RF-MS) method decomposed water in the presence of methanol or silver nitrate solution under visible light irradiation.

The immobilization of the photocatalyst in the form of a thin film overcomes the drawbacks encountered with powder suspensions: (1) the difficulty of separating inactive catalysts, (2) the difficulty of applying them to continuous flow systems, and (3) the intendancy of the particle catalysts to aggregate. Novel methods to increase efficiency will enhance the appeal of photocatalyst thin films for applications [73].

In a photoelectrochemical process, the probability that separated charges will recombine highly depends on water solution additives and the metal loading of the semiconductor. After separation, electrons in the conduction band can be trapped by metal on the semiconductor's surface due to the difference in Fermi energies and work function. For water and methanol solutions, protons are generated via oxidation of water

or methanol by holes. Then protons are reduced at the metal catalyst surface by electrons

to produce hydrogen molecules. The following reactions occur during the process [74] :

$h\upsilon \rightarrow e^- + hole^+$,

$4hole+ + 2H_2O \rightarrow O_2 \uparrow + 4H^+$,

$2H^+ + 2e^- \rightarrow H_2 \uparrow$.

The overall reaction is

$4h\upsilon + 2H_2O \rightarrow O_2 \uparrow + 2H_2 \uparrow$.

(A)

$$TiO_2 + h\nu \rightarrow TiO_2(e^-, h^+)$$

$$2H_2O + 2e^- \rightarrow H_2 + 2OH^-$$

$$H_2O + 2h^+ \rightarrow \frac{1}{2}O_2 + 2H^+$$

(B)

$$e^-(TiO_2) \rightarrow e^-(Pt)$$

$$e^-(Pt) + H^+_{(aq)} \rightarrow H_{ads}$$

$$H_{(ads)} + H_{(ads)} \rightarrow H_2$$

(C)

$$h^+(TiO_2) + OH^- \rightarrow TiO_2 + OH$$

$$OH \rightarrow O^-_{(aq)} + H^+_{(aq)}$$

$$h^+(TiO_2) + O^-_{(aq)} \rightarrow TiO_2 + O^\bullet_{(ads)}$$

$$O^\bullet_{(ads)} + O^\bullet_{(ads)} \rightarrow O_2$$
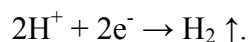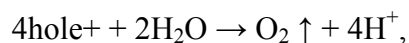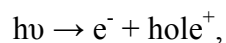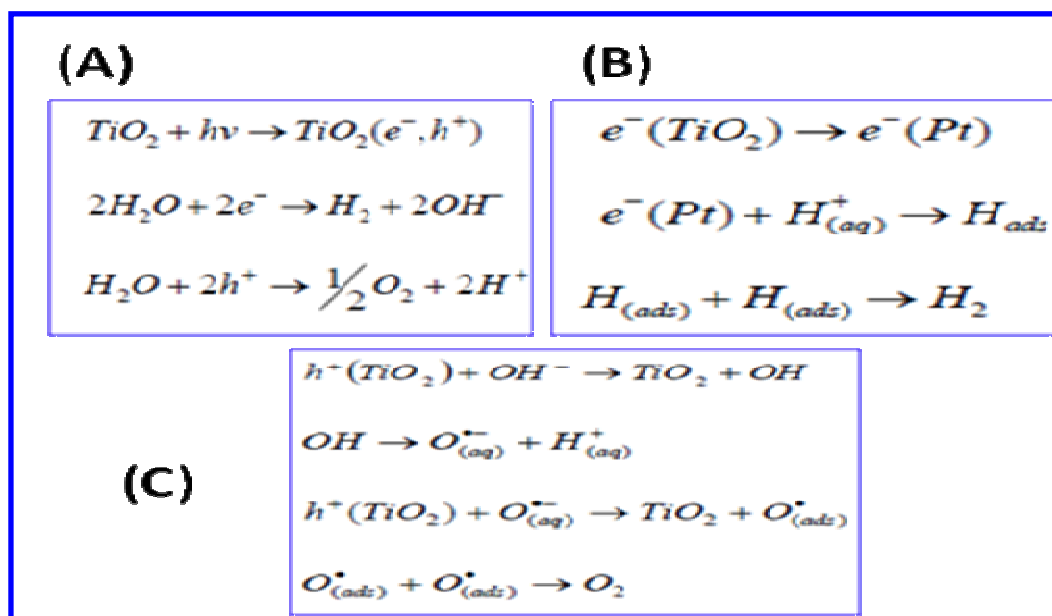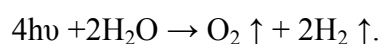
Figure 2.1 Water-splitting reaction mechanism details (A) photogenerated charges at TiO$_2$ surface (B) electrons captured by metal (cathod) (C) In presence of electron donor (methanol), hydroxyl radicals captured the holes not water at TiO$_2$ (anode) [53] .

For water-splitting, the energy of the absorbed photon must be at least 1.23 eV

[$E_i = \Delta G^o$(water) /2NA with ΔG^o(water) =237.141 kJ/ mol and NA = Avogadro's

number = 6.022×10^{23}/ mol] [74]. Methanol was added to water as strong oxidation agent (electron donor) in order to stop the oxygen gas that evolved when the water species adsorbed at photoanode (TiO_2 surface) get oxidized (Figure 2.1). Therefore, methanol is used here to efficiently separate the hole-charges, which leads to the reduction of hole-electron pair recombination process. This enables testing the activity of nanomaterials photocatalyst for water photoreduction reaction in a single photo-electrode system (photoreduction column) in simple, safe, flexible, accurate and inexpensive experimental set-up. However, in practical application, methanol will be replaced by photooxidation co-catalyst (e.g. nanocrystalline Fe_2O_3 (Eg=2.3 eV)) which enable to use a two-column photo-electrodes (H-type photoelectrochemical cell or tandem cell system). In addition to its role as a hole scavenger, methanol may contribute to the generation of hydrogen via decomposition which enhances the overall hydrogen production rate. These side reactions also lead to the evolution of some carbon dioxide. The following reactions have been reported for methanol decomposition [74]:

$MeOH \leftrightarrow H_2CO + H_2 \uparrow$,

$H_2CO + H_2O \leftrightarrow H_2CO_2 + H_2 \uparrow$,

$H_2CO_2 \leftrightarrow CO_2 \uparrow + H_2 \uparrow$.
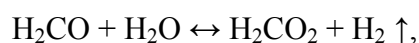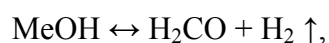
However, in this work we do not measure the CO_2 which may be evolved. An equal volume mixture of water and methanol solution is used based on previous studies [74].

The optimum band gap for solar hydrogen production from water-splitting is between 1.5- 2.0 eV to maximize the utilization of solar energy by harvesting the available visible light spectrum to split the water, in addition to overcome the thermodynamic losses [74].

The photons energy must match or be larger than the band gap energy of the semiconductor to be absorbed and excite the electrons. It is important to engineer the band gap of semiconductors to harness longer wavelength photons.

To increase the hydrogen production from the photoelectrochemical water-splitting process, materials with appropriate properties (chemical, electronic, thermal, and optical, etc.) need to be tailored, fabricated, characterized and evaluated. Platinum is widely used as effective metal and with TiO_2 as photocathode catalyst for water reduction reaction; however it is an unpractical option because it is expensive (Figure 2.2).

Herein, an attempt is conducted to use low cost and abundant metals such as Ag and Cu for hydrogen production as photocathode catalyst and study their activity. The impact work function, size, and composition of cheaper metal on reactivity were also investigated. Metal-semiconductor junction is enhanced through metal deposition on TiO_2 surface by photo-electron reduction technique.
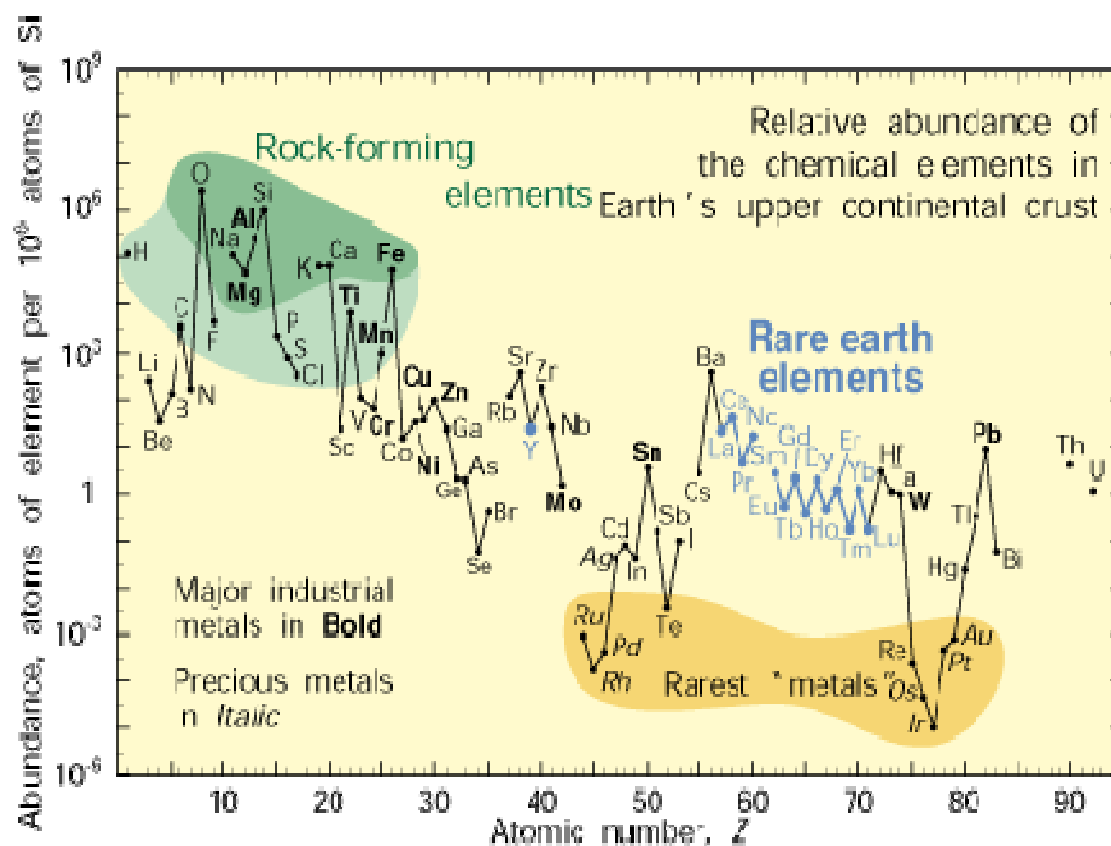
Figure 2.2 Shows that platinum is one of the rare earth elements, where Ag and Cu are preferable to use in industries [75].

Effect of TiO$_2$ Crystal Structure

We present here Ag/TiO$_2$ anatase nanocomposite films that are synthesized and evaluated as photocatalysts for hydrogen production. The fabrication method of Ag/TiO$_2$ films reported by Liao and Cremer [76,77] for biosensor applications [78] is modified to synthesize the anatase Ag/TiO$_2$ nanocomposite films. Silver nanoparticles are used here

to effectively separate electron and hole pairs produced in the photoelectrochemical reactions. Prior to the silver deposition, the TiO_2 thin-films were heated for 5 hours at 500°C to form the anatase crystal structure of TiO_2. In order to investigate the effect of crystal structure (atoms are well-ordered or arranged to form crystal lattice geometry), another sample of amorphous Ag/TiO_2 was prepared at room temperature without annealing step and were tested under same reaction condition and water solution. In addition, pure TiO_2 thin film with anatase phase and amorphous phase were prepared by the same above procedure without silver loading. We demonstrated herein a sensitive screening method for production of hydrogen from an ultralow amount of photocatalyst.

Effect of Intermediate Organic Layer: Ag/Linker/TiO_2 for "Schottky Junction"

A potential drop in the potential within the interface layer of the solid, formed as a result of concentration gradients, surface states, and adsorption states, is termed a Schottky barrier. The Schottky barrier plays an important role in preventing recombination of the charge formed as a result of photo-ionization. It can be formed as a result of the following [30] structural deformations within the near-surface layer due to an excess of surface energy; segregation-induced chemical potential gradients of aliovalent ions across the surface layer imposed during processing and chemical potential gradients of aliovalent ions across the surface layer imposed as a result of surface processing [30]. When the metal with a higher work function is in contact with a semiconductor with a lower work function, electron migration from the semiconductor to the metal occurs until the two Fermi levels are aligned and forms a space charge layer [30]. The Schottky barrier produced at the metal-semiconductor interface can serve as an efficient electron

trap preventing electron-hole recombination. The formation of a Schottky barrier in a semiconductor-metal system is shown in Figure 2.3 [46][52].
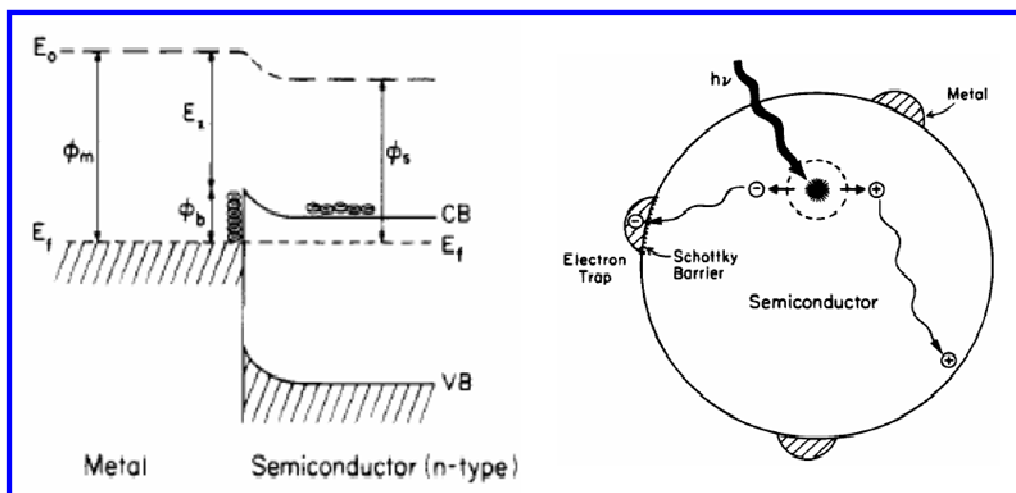
Figure 2.3 Schottky barrier in a semiconductor-metal system [46][52].

Effect of Synthesis Method: Chemical Vapor Deposition (CVD) OF Ag/TiO$_2$ Thin Film

To investigate the effect of synthesis method on Ag/TiO$_2$ activity and hydrogen production performance, Ag/TiO$_2$ thin film prepared by chemical vapor deposition method at room conditions. The smooth film was grown by hydrolysis of titanium (IV) isopropoxide by OH groups and water vapor. The difference in synthesis method of TiO$_2$ film between chemical vapor deposition and drop coating might lead to difference in film properties and consequently their performance and activity on hydrogen production rate [77].

DESIGN AND SYNTHESIS

Materials and Synthesis of Ag/ TiO$_2$ Nanocomposite Films

As noted above, Ag/TiO$_2$ films were synthesized by following the procedure developed by Liao and Cremer [76,77] with an modification to form anatase TiO$_2$. The precursor solution for TiO$_2$ consisted of 1 g of titanium (IV) isopropoxide (Sigma-Aldrich), 0.15 g of HCl (Fisher Scientific), and 8.0 g of isopropyl alcohol (Sigma-Aldrich). Polished Pyrex 7740 wafers (25.4 mm2, 0.5 mm thick) were purchased from Precision Glass and Optics (Santa Ana, CA). The Pyrex wafers were cleaned in piranha solution for 45 min (1:3 ratio of 30% H$_2$O$_2$ and H$_2$SO$_4$), and rinsed extensively with purified water (18.2 MΩ/cm2, NANO pure Ultrapure Water System, Barnstead, Dubuque, IA), dried with nitrogen, and heated at 500°C for 5 hours. The precursor solution was prepared by first adding titanium (IV) isopropoxide followed by the acid. A TiO$_2$ film was made by depositing approximately 150 µL of the solution onto the Pyrex wafer dropwise. After waiting for 5-10 minutes for the precursor to dry, the sample was heated to 500°C for 5 hours to form the anatase crystal structure of TiO$_2$, which is known to be more photocatalytically active and more thermally stable than the rutile and brookite crystal structures of TiO$_2$ [79]. Silver nitrate (Sigma-Aldrich) is used for the reduction of silver from a 0.1 M aqueous silver nitrate solution; it is performed with a standard 420 W Hg Arc lamp (Newport, Model 97435-1000-1, Oriel Instruments, CA, USA) as the UV light source. The aqueous silver nitrate solution was dropped inside a polydimethylsiloxane (PDMS) well. The light illuminated the TiO$_2$ through the Pyrex side of the sample. The Pyrex sample is transparent in the near UV range, which is the critical wavelength region

for reducing silver ions from solution. Figure 2.4 illustrates the fabrication procedures. The sample of amorphous Ag/TiO$_2$ prepared at room temperature by the same procedure but without annealing step and tested under same reaction condition and water solution. The sample of pure TiO$_2$ thin film with anatase phase was prepared by the same above procedure with annealing step at 500˚C for 5 hours and without silver loading. The sample of pure TiO$_2$ thin film amorphous phase was synthesized by the same above procedure but at room temperature and also without silver loading.
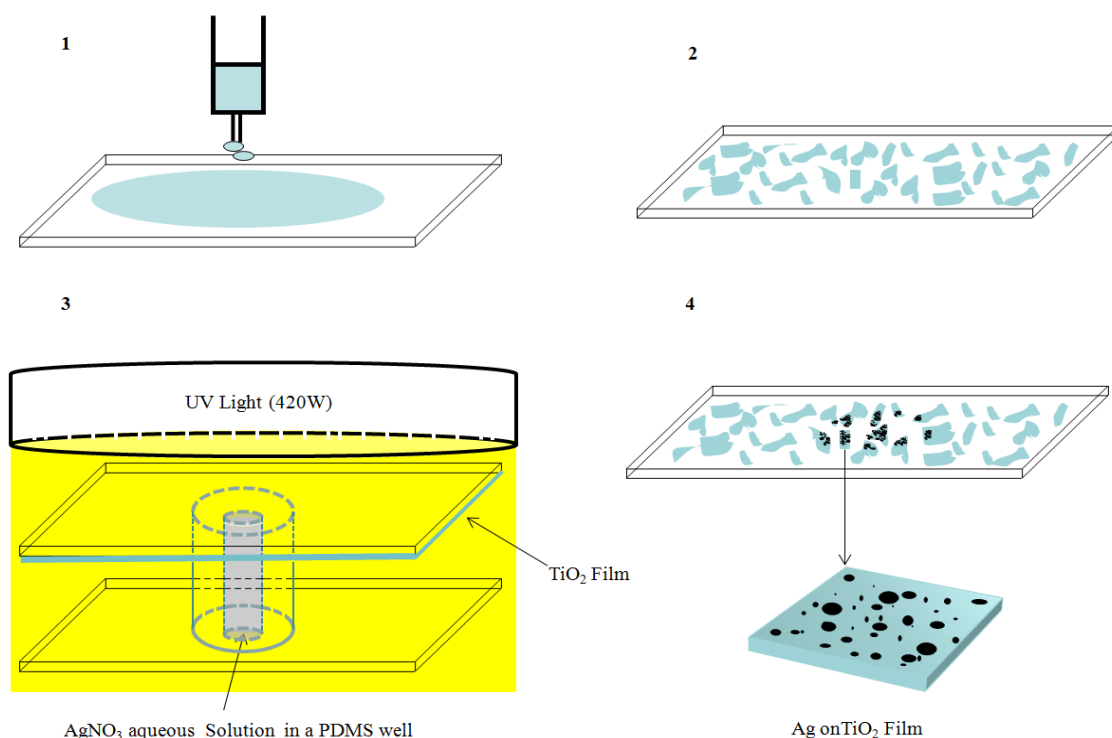
Figure 2.4 Schematic diagram for the fabrication procedure of Ag/TiO$_2$ nanocomposite films. (1) A TiO$_2$ precursor is dropped onto a 2.5 cm × 2.5 cm planar Pyrex substrate. (2) The thin layer is dried and heated to 500°C for 5 hours to form islands of anatase TiO2 films. (3) A AgNO$_3$ aqueous solution is dropped into a PDMS well, and silver is reduced by a photoelectron using UV radiation (420 W and Ag deposition time is 5 minutes). (4) The Ag/TiO$_2$ thin film is washed with water and ethanol and dried with nitrogen.

Materials   and   Synthesis   of   Intermediate   Linker   Layer   Ag/   4-Mercaptobenziocacid/TiO$_2$

The substrate preparation steps and preparation of the anatase TiO$_2$ thin films (annealed at 500˚C for 5 hours) as mentioned above (drop deposition). However, for silver and organic intermediate layer (linker) deposition, dip coating technique was used. 4-Mercaptobenziocacid (Sigma-Aldrich) as thin organic linker layer coated the TiO$_2$ films then followed by decoration of silver nanoparticles with size about 50 nm (Sigma-Aldrich). Toluene used as the media for better coating chemistry to avoid self-assembly and aggregation (nanoparticles stabilization). Briefly, two 20 ml vials were filled with toluene. The anatase TiO$_2$ films deposited on substrate were immersed inside both vials. In one vial, added small amount of 4-Mercaptobenziocacid and silver nanopowders was added. In the other vial, the silver nanopowders were added directly. Then both vials put under sonication at 48˚C and room pressure for 30 minutes for dip coating. The hydrophobic nature of the organic linker leads to link Ag and TiO$_2$ on both sides. After sonication, both vials were kept under room conditions for 24 hours. The films were removed and dried with nitrogen.
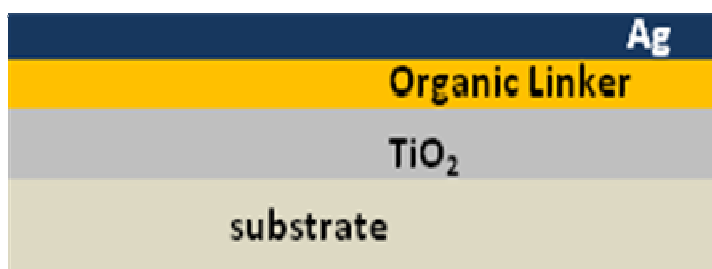
Figure 2.5 Ag/4-Mercaptobenziocacid/ TiO$_2$ thin film deposited on substrate.
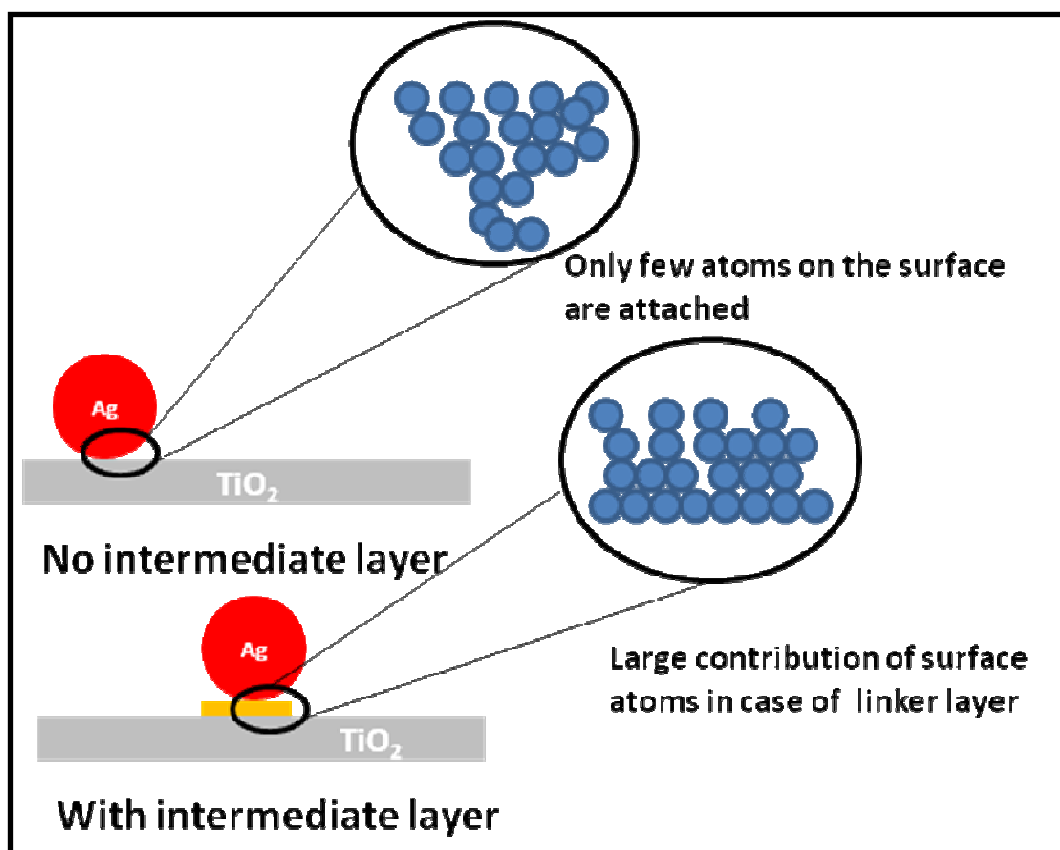
Figure 2.6 The linker layer (organic) between metal and semiconductor enhance the electrons transportation by attached more surface atoms than the case where no layer used.

The large contribution of surface atoms in case of intermediate layer is expected to enhance the activity of nanocomposites thin film (Figures 2.5 and 2.6).

Materials and Synthesis of Ag/TiO$_2$ by Chemical Vapor Deposition (CVD) Method

TiO$_2$ thin films were prepared at room temperature and pressure by chemical vapor deposition. First, the substrate (Pyrex wafers) cleaned as mentioned above. A Petri dish was used as the reaction chamber. The Pyrex substrates sticks carefully in one side (cover) of Petri dish and fill the dish with titanium (IV) isopropoxide and closed it. The substrate exposed to the titanium (IV) isopropoxide vapor at room temperature for 2

hours (Figure 2.7). Then, the substrate rinsed with purified water and acetone to stop the surface reaction and annealed at 500 °C for 5 hours to form anatase phase of TiO_2. The silver ions adsorbed at TiO_2 surface by photoelectrons reduction from aqueous $AgNO_3$ solution using UV illumination (420 W for 5 minutes illumination) as mentioned above [77].
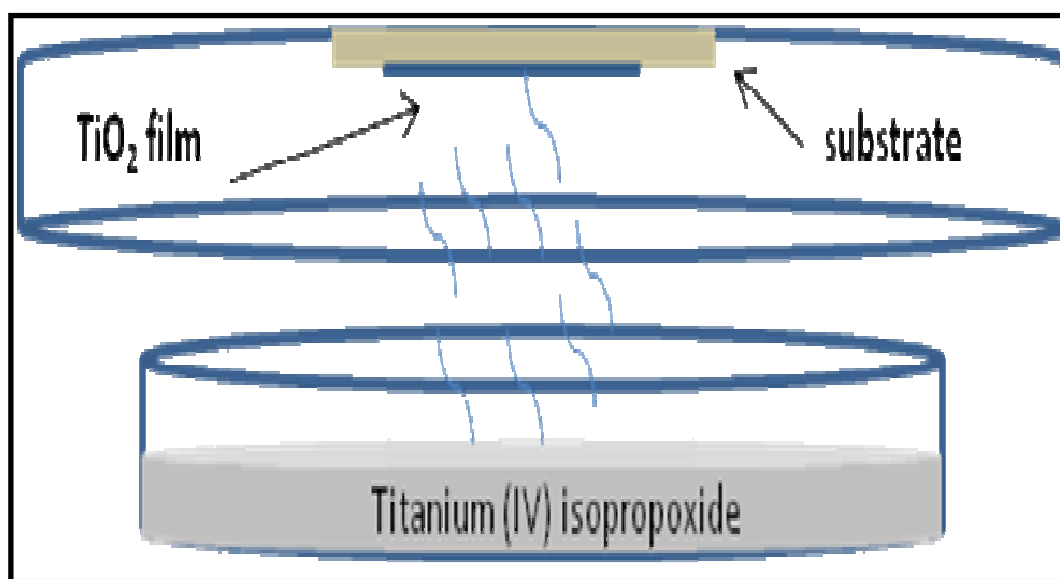
Figure 2.7 Chemical vapor deposition of TiO_2 thin film.

CHARACTERIZATION

Nanocomposite Films

After synthesis, the Ag/TiO_2 nanocomposite films were characterized using Scanning Electron Microscopy (SEM) (Figure 2.8). The SEM images were taken using JEOL

JSM-6400. The Surface element analysis was obtained using Energy dispersive X-ray spectroscopy (EDS) as shown in Table 2.1.

The EDS results were obtained using JEOL JSM-6400. The peak positions and chemical compositions were obtained using X-ray photoelectron spectrometer (XPS) as shown in Figure 2.9 and Table 2.2. The XPS results were obtained using a Kratos Axis Ultra Imaging X-ray photoelectron spectrometer. Figure 2.10 (a, b, c, d) showed the X-ray diffraction (XRD) patterns of the Ag/TiO$_2$ film and the TiO$_2$ film with and without annealing. The powder X-ray diffraction data was collected using a Bruker D8 Advance powder diffractometer (CuKα; λ = 1.5418 Å) fitted with LynxEye detector.

Figure 2.11 and Figure 2.12 showed the UV-visible spectra of anatase TiO$_2$ film and TiO$_2$ powders, respectively. The UV-vis-NIR spectrophotometer was measured using a Hitachi U4100 with an integrating sphere. Figure 2.13 shows optical microscopic image of Ag/TiO$_2$ prepared by Chemical vapor deposition (CVD) of TiO$_2$.
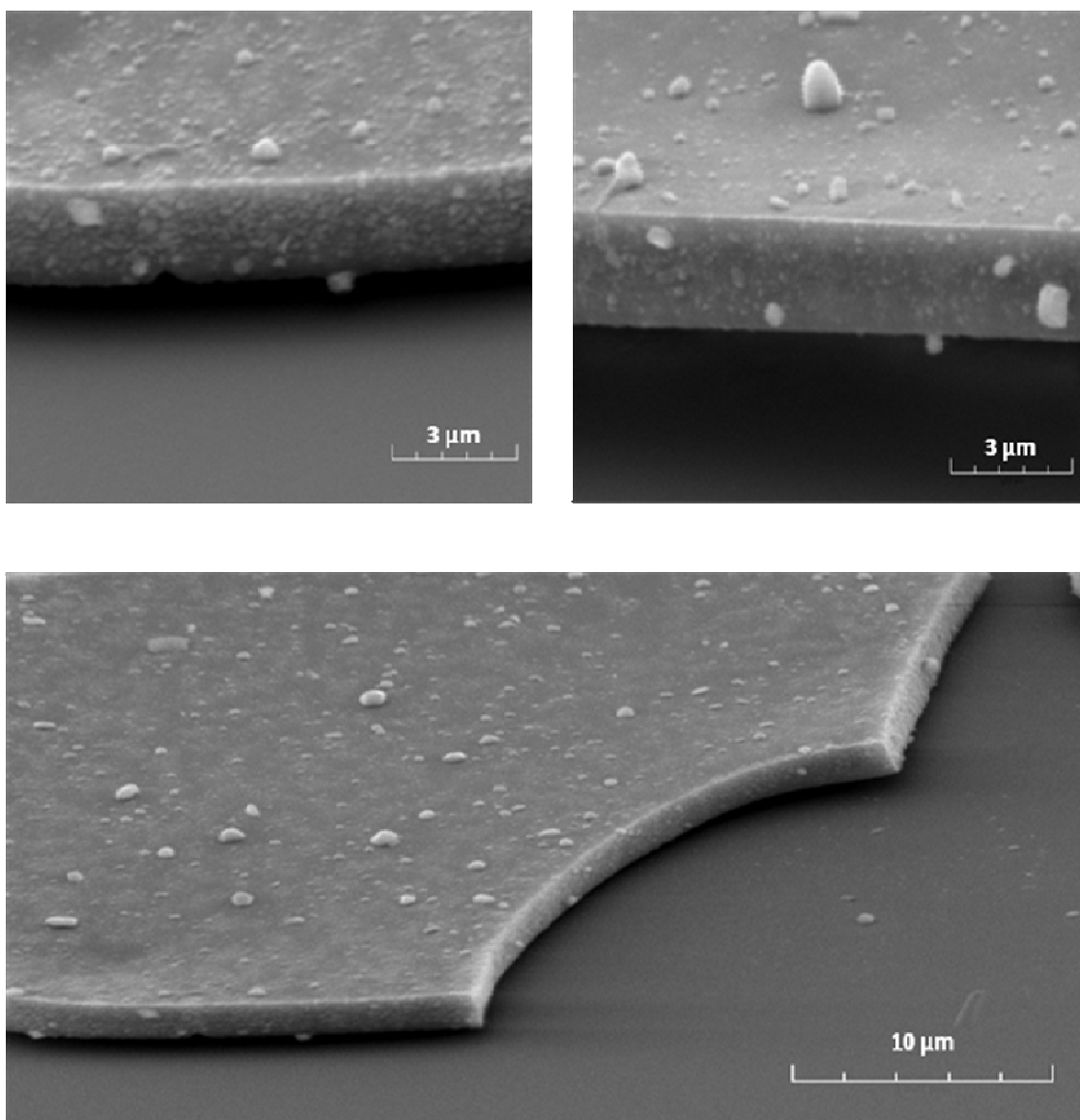
Figure 2.8 SEM micrographs of Ag/TiO$_2$ nanocomposite films. The averaged film thickness is about 2.0 ± 0.2 μm. The size of the Ag nanoparticles deposited on the TiO$_2$ films is not uniform. The averaged size of Ag nanoparticles is around 200 ± 50 nm.

Table 2.1 Surface element analysis using EDS.

Glass Surface		Particle surface		Surface of TiO$_2$ film	
Element	Wt%	Element	Wt%	Element	Wt%
Al	5.36	Ti	38.64	Ti	83.01
Si	92.79	Pd	0.00	Pd	0.50
K	1.86	Ag	57.59	Ag	12.96
		Au	3.77	Au	3.54
Total	100	Total	100	Total	100
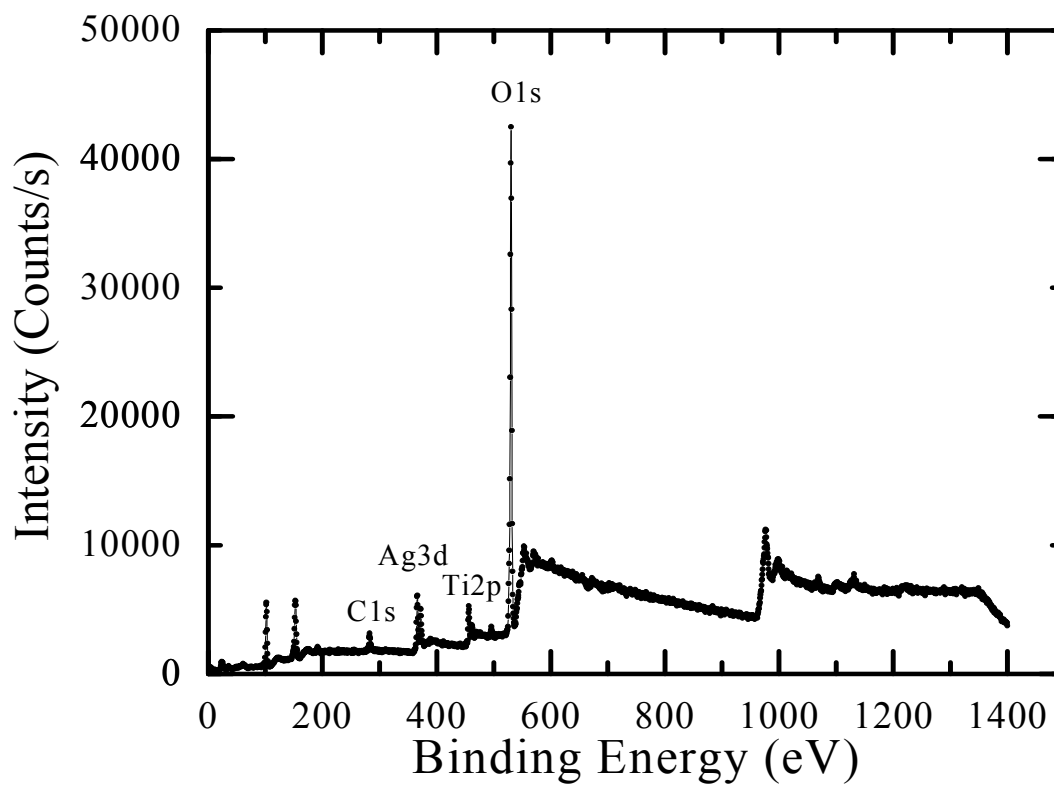
Figure 2.9 XPS of a Ag/TiO$_2$ nanocomposite film shows intensity versus binding energy for all components.

Table 2.2 The peaks, atomic concentration and mass concentration from XPS analysis.

Peak	Position BE (e V)	FWHM (e V)	Raw Area (CPS)	RSF	Atomic mass	Atomic Conc. %	Mass Conc. %
O1s	530.55	1.542	22002.8	0.78	15.999	94.62	79.76
Ti2p	456.55	1.181	1873.8	2.001	47.878	3.26	8.23
Ag3d	366.25	1.282	3484.2	5.987	107.878	2.11	12.01
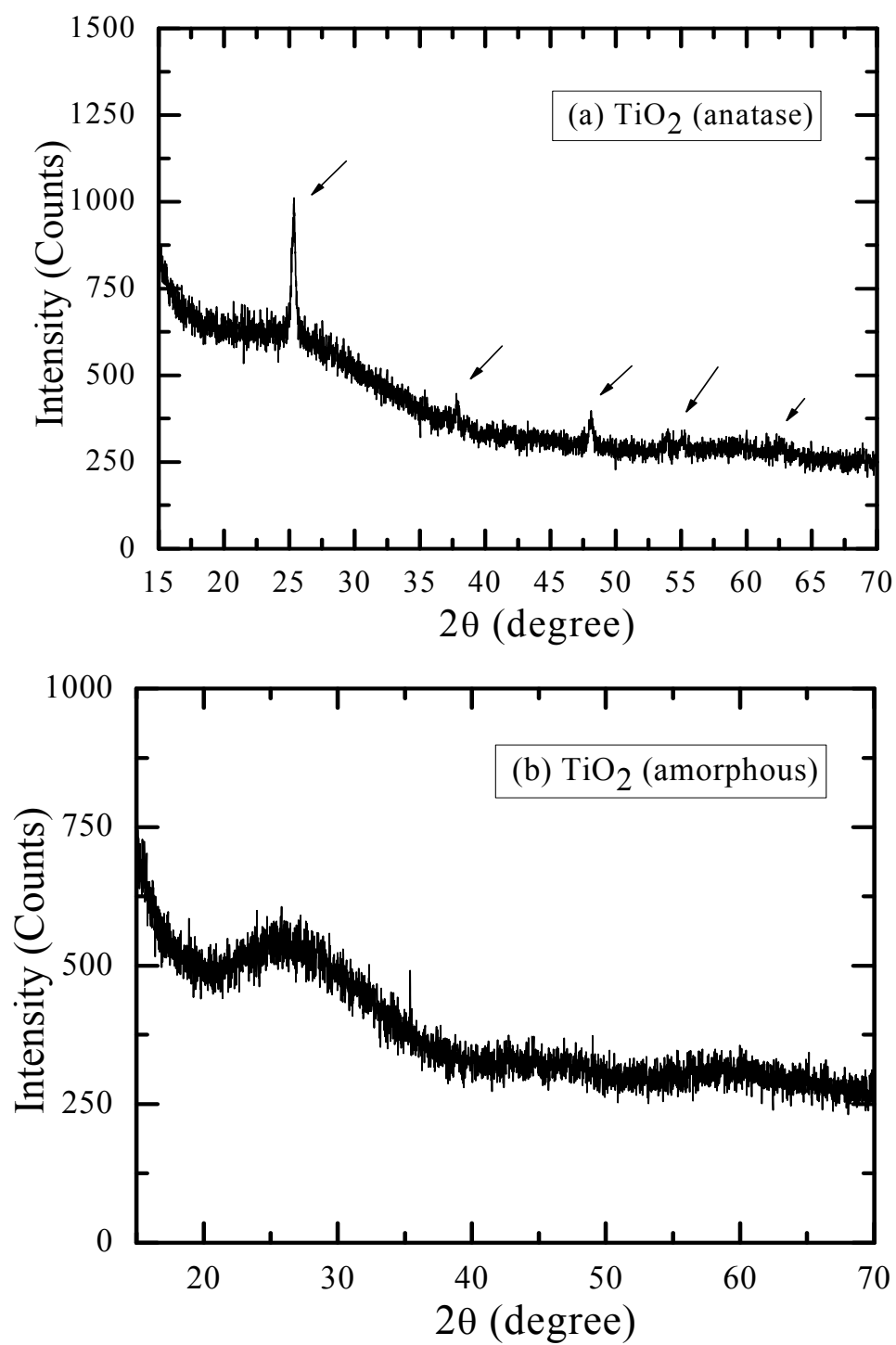
Figure 2.10 XRD patterns of (a) TiO_2 (anatase), (b) TiO_2 (amorphous).
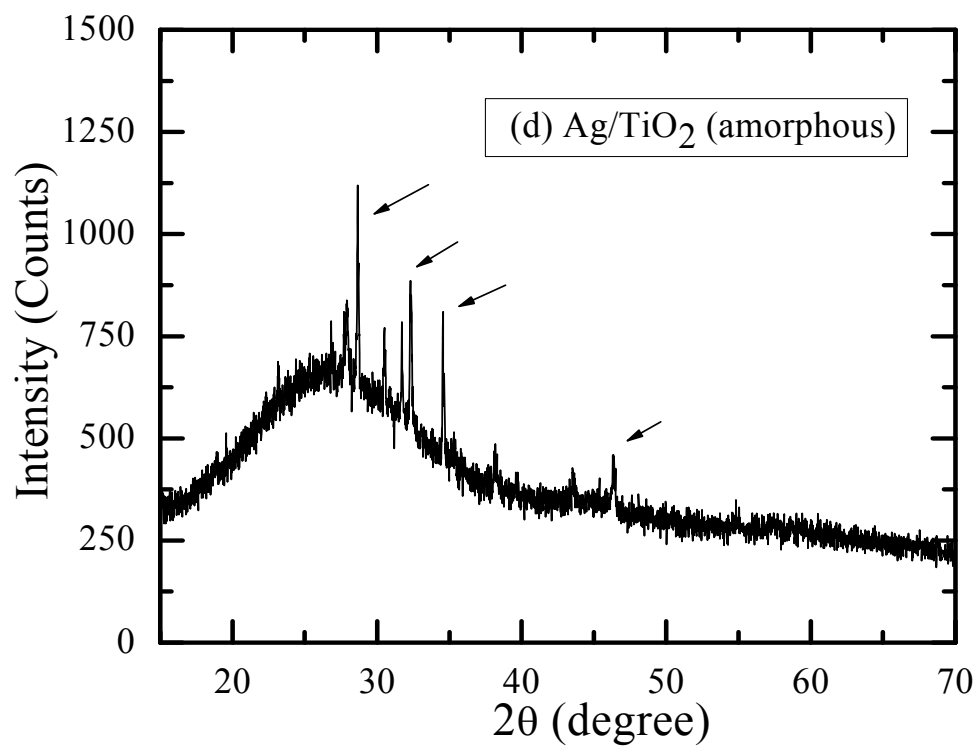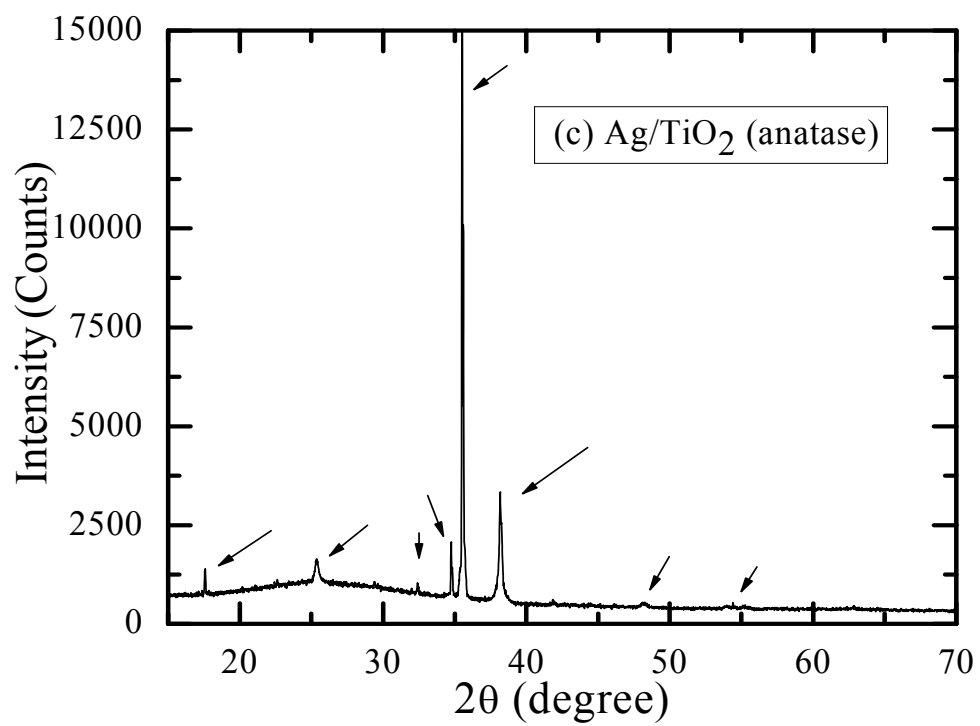
Figure 2.10 continued (c) Ag/TiO$_2$ (anatase), (d) Ag/TiO$_2$ (amorphous).
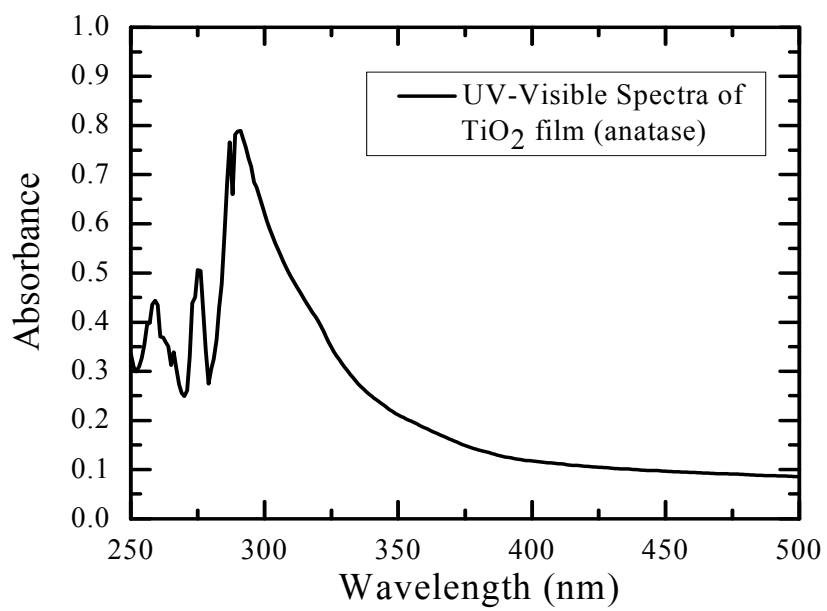
Figure 2.11 UV-visible spectra of anatase TiO_2 film (after annealing at 500°C for 5 hours).
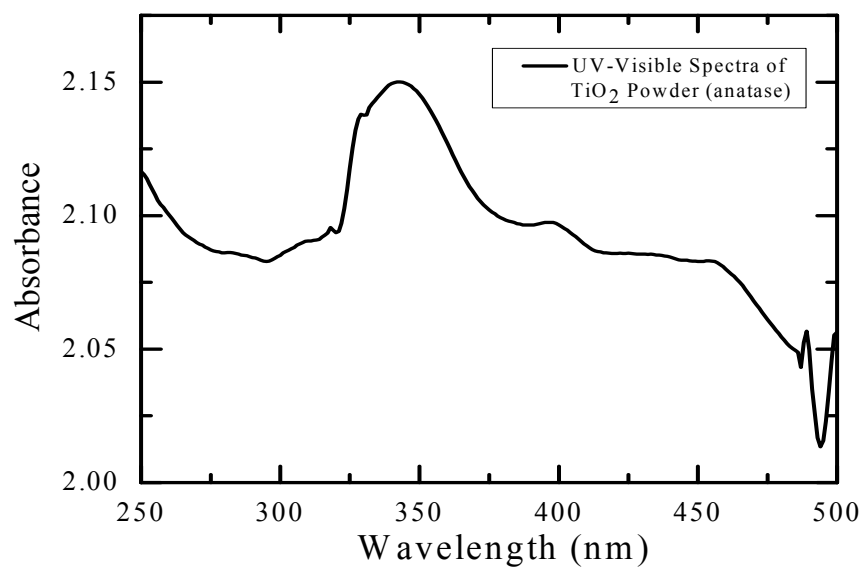
Figure 2.12 UV-visible spectra of anatase TiO_2 powder (after annealing at 500°C for 5 hours).
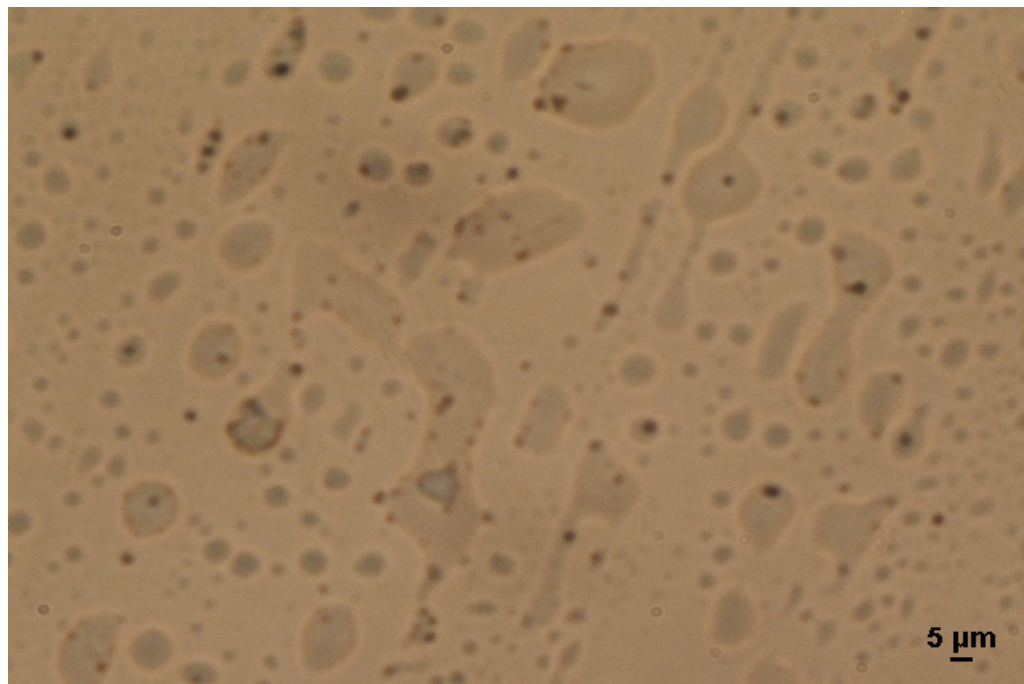
Figure 2.13 Optical microscopic image of Ag/TiO$_2$ prepared by chemical vapor deposition (CVD) of TiO$_2$, Ag embedded by photoelectron reduction of AgNO$_3$ using UV illumination at 420W for 5 minutes.

HIGH THROUGHPUT SCREENING PROCESS OF H$_2$ PRODUCTION MEASUREMENT

The experiments were carried out in a Pyrex flask (250 ml, transparent in the near UV range). A 10 ml 1:1 volume mixture of water and methanol was added. The photocatalyst (Ag/TiO$_2$ thin-film sample) was inserted into the flask carefully, and immersed just under the water/methanol solution surface. The 250 ml Pyrex flask was well sealed by a silicon septum. Prior to the reaction, the solution was purged with

nitrogen (from 30 to 60 minutes) to remove air from the flask as well as the air and oxygen species dissolved in the solution. Hydrogen was detected before the reaction (usually it less than 3.00 ± 0.25 µmol) and all data are reported with this background subtracted. UV light (Long Wave Ultraviolet lamp, Model B-100AP, UVP, CA, USA) illuminated the reaction cell. The straight distance between the UV source and the photocatalyst sample was 16 ± 1.0 cm (Figure 2.14); vertical and horizontal measurements were carried out using a smart UV intensity meter and it was found that the maximum power intensity possible hitting the photocatalyst sample was 10 m W/cm^2. The reaction cell and the lamp were fully covered with alumina foil to avoid light leakage for safety considerations. Hydrogen generated in the head space of the flask was measured using a 50 µL aliquot by gas chromatography (GC) using a 6890 N gas chromatograph (Agilent Technologies, Glastonbury, CT) equipped with a 80–100 mesh Porapak Q column (Suppelco, Bellefonte, PA) and a thermal conductivity detector. The injector temperature was 100°C and detector temperature was 200°C. The pressure of nitrogen as carrier gas was 15 psi and the flow rate was 21 ml/min. The temperature of the column was 70°C. The retention time for hydrogen was 0.4 minutes and the sensitivity was about 0.1 µmol for the above conditions. Retention times were determined by comparisons to neat standards as well as by co-elution with standards [80,81]. The experimental data is reported in appendix (A), under the following information:

Experiment	Run No.
Ag/TiO$_2$ anatase under UV light	4,21,22
Ag/TiO$_2$ amorphous under UV light	54
TiO2 anatase under UV light	9
TiO$_2$ amorphous under UV light	10, 15
Ag/4-Mercaptobenziocacid/TiO$_2$ amorphous under UV light	36,37,38
Ag/TiO$_2$ anatase under UV light by (CVD)	47
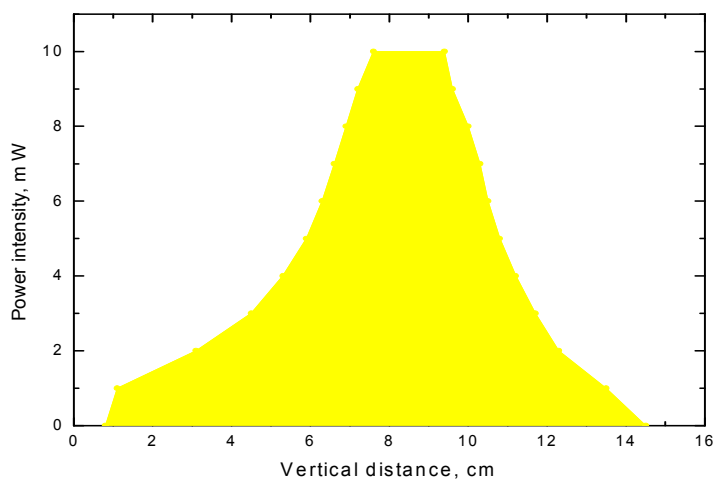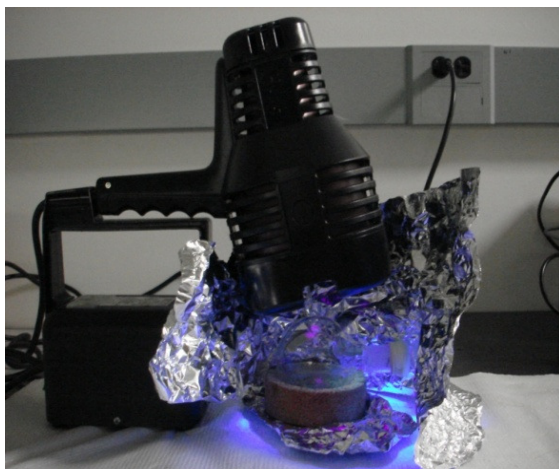
Figure 2.14 Shows how to conduct the experiments under UV light (left), gas chromatography for hydrogen detection (right), light power intensity versus sample distance (cm) (plot).

ENERGY EFFICIENCY % CALCULATION

The weight of photocatalyst found by two approaches; 1) measured the weight using high sensitive balance. 2) Calculated using the following equation:

$m = \rho \times V = \rho \times A \times L$

m= weight (g), ρ = density (g/cm^3), V = volume (ml), A = area (cm^2), L = thickness (cm)

Solar to hydrogen conversion efficiency (energy efficiency %) can be calculated using the following equation [82] :

$$\% \; \varepsilon_\circ = \frac{\Delta G^\circ \times R_{H_2}}{A \times P_t} \times 100$$

$\varepsilon_\circ$ = energy efficiency, ΔG° = Gibbs free energy = 237.2 KJ/mole, R_{H_2} = hydrogen production rate (mole/hour), P_t = Power intensity (W/m^2), for UV light = 100 (W/m^2), for sunlight = 240 (W/m^2), [Texas, college station, Latitude: 30.6277778, Longitude: -96.3341667, 30° 37' 40" N / 96° 20' 3" W]. A= the effective area (cm^2). It is important to mention that only a small portion of light that exposed to the photocatalyst will be absorbed and utilized for electron-hole pair excitation, and the rest are transmitted without absorption as heat loss. The transmission of light during the reaction should be measured. Therefore, the equation used to calculate energy efficiency % as follows:

$$\% \; \varepsilon_\circ = \frac{\Delta G^\circ \times R_{H_2}}{3600 \times A \times 100 \; (1-x)} \times 100 \qquad \text{for UV light}$$

$$\% \; \varepsilon_\circ = \frac{\Delta G^\circ \times R_{H_2}}{3600 \times A \times 240 \; (1-x)} \times 100 \qquad \text{for sunlight}$$

$$R_{H_2} = mol / h \; , \; \Delta G^\circ = 237200 \quad J / mol$$

Where "3600" is the hour to seconds conversion factor, x = the portion of light transmitted without absorption, A= effective area exposed to light, m^2, 100 & 240 is the power intensity for UV and sunlight respectively, in W/m^2 or J/sec.m^2. In addition, the reported energy efficiency % is for hydrogen production from water-splitting reaction, which account for 30% of total hydrogen produced based on reaction stoichiometry ratio. It is also assumed here that the hydrogen production rate will not be affected, if methanol replaced by any co-catalyst, in case of using two separated columns for hydrogen and oxygen evolution. If needed for calculation, quantum efficiency (QE %) can be calculated using this equation [83]:

$$\% \ QE \ = \ \frac{number \ of \ reacted \ electrons}{number \ of \ incident \ photons} \times 100$$

$$= \ \frac{number \ of \ evolved \ H_2 \ molecules \ \times 2}{number \ of \ incident \ photons} \times 100$$

The thermodynamic limit of solar to hydrogen conversion efficiency is estimated, as shown in Figure 2.15.
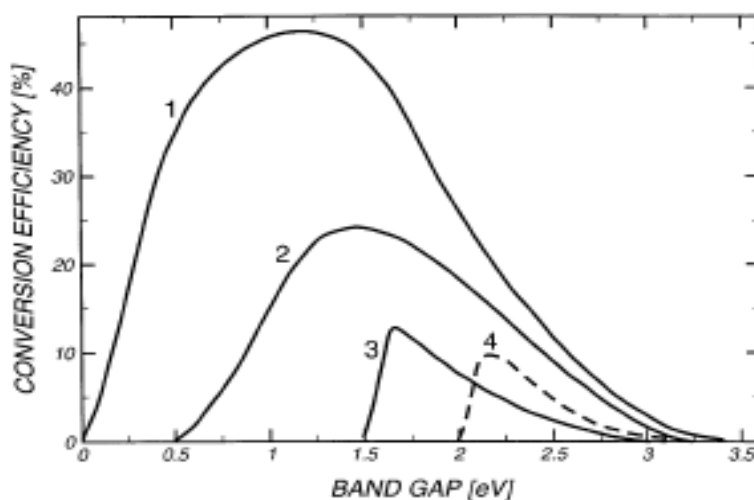
Figure 2.15 (a) Shows the conversion efficiency % corresponding to band gap [eV] [30].
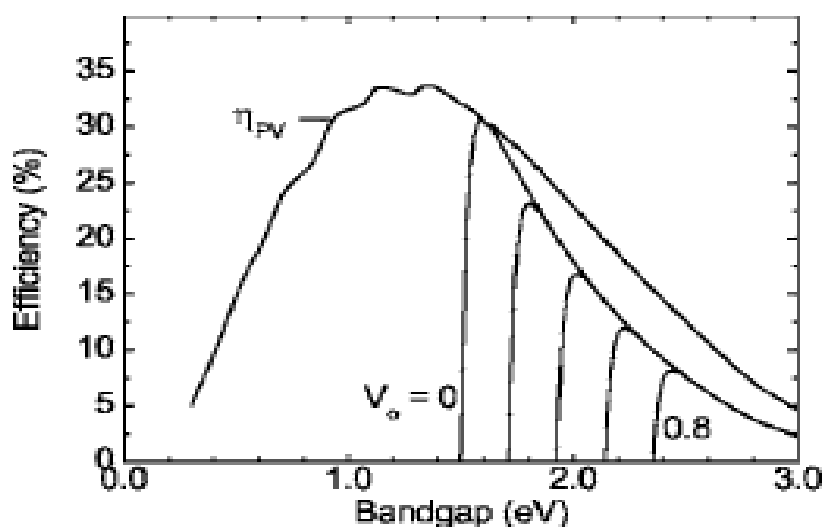
Figure 2.15 continued (b) Shows the maximum energy efficiency can be reached for solar to hydrogen conversion efficiency is around 30% [31].

SAMPLE OF CALCULATION

For Table 2.4; Ag/TiO$_2$ nanocomposites thin film tested under UV light and equal volume water/methanol solution for hydrogen production from water-splitting reaction:

Hydrogen production rate $= 0.085 \times 10^{-6}$ mol/h

Effective area estimated to be 1 cm^2 = 0.0001 m^2

@ x = 0 (assume all UV light absorbed by the photocatalyst and no light transmitted)

Energy Efficiency $\% = \dfrac{237200 \times 0.085 \times 10^{-6}}{0.0001 \times 3600 \times 100} \times 100 = 0.056\%$

Hydrogen produced from Water $-$ splitting reaction $= 30\%$ of the total hydrogen production measured

Energy Efficiency % of Water $-$ Splitting $= 0.3 \times 0.056 = 0.016\%$

@ x = 0.7 (assume that only 30% of UV light absorbed by the photocatalyst and the light transmitted is 70%)

$$\text{Energy Efficiency } \% = \frac{237200 \times 0.085 \times 10^{-6}}{0.0001 \times 3600 \times (100 \times (1-0.7))} \times 100 = 0.186\%$$

Hydrogen produced from Water $-$ splitting reaction $= 30\%$ of the total hydrogen production measured

Energy Efficiency $\%$ of Water $-$ Splitting $= 0.3 \times 0.186 = 0.056\%$

RESULTS AND DISCUSSION OF APPLICATION FOR H_2 PRODUCTION

The SEM micrographs revealed that the averaged film thickness was about 2.0 ± 0.2 μm and the silver nanoparticles were 200 ± 50 nm. The SEM images showed that the TiO_2 layer broke down to islands during annealing to 500°C. The images also showed that the size of silver nanoparticles deposited on TiO_2 films were not uniform by the photodeposition technique used here. The XPS presented the surface element analysis including the atomic concentration and mass concentration. The peaks are consistent with literature data for the binding energy of O1s, Ti2p and Ag3d [84]. The EDS results presented in Table 2.1 showed the weight percentage of glass surface, particle surface, and the surface of TiO_2 film. The Au and Pd were deposited on the film surface in order to do the SEM analysis.

To confirm how the anatase Ag/TiO_2 film has a substantial impact on film reactivity and also to compared the amorphous TiO_2 with anatase crystal structure TiO_2, X-ray diffraction (XRD) patterns characterization shown in Figure 2.10 (a, b, c, d) revealed the crystal structure of anatase TiO_2. The XRD patterns of amorphous TiO_2 showed no crystallites existed. For anatase Ag/TiO_2, it showed the diffraction peaks of

crystallites silver, anatase TiO_2 nanocrystals and crystals of some impurities due to the silver present on the surface of TiO_2. For amorphous Ag/TiO_2, it showed the diffraction peaks of crystallites silver and crystal peaks from some impurities due to the silver present on the surface of TiO_2 as well, which may react with other elements on the air such as oxygen. To demonstrate the band gap of anatase TiO_2 film, UV-visible spectra presented in Figure 2.11 showed that the absorbance wavelength of anatase TiO_2 film in the range of 290-320 nm. Figure 2.12 showed that the absorbance wavelength of anatase TiO_2 powder in the range of 340-360 nm. The higher absorbance wavelength of anatase TiO_2 means lower in band gap according to Planck–Einstein equation ($E=hc/\lambda$).

Ag/TiO$_2$ Anatase

Figure 2.16 and Tables 2.4 and 2.5 shows the hydrogen evolution for one of the three runs conducted using the Ag/TiO_2 films. The averaged hydrogen production rate was found to be 147.9 ± 35.5 µmol/h/g. The standard deviation for the three experiments was used to report the error. These variations might be attributed to films deactivation by air oxidation when exposed to the atmosphere during sample storage, or due to weight estimation errors. The Ag/TiO_2 nanocomposite films showed a high stability for the hydrogen production rate which exceeded one month. The fabrication of Ag/TiO_2 nanocomposite films [76,77] has been modified to form the anatase crystal structure of TiO_2 since it is known that this structure is more photocatalytically active. Previously, Jeon, et al. [85] tested Cu/TiO_2 powdered photocatalysts, 20 g, under 36 W/m^2 UV, revealed a hydrogen production of 648.52 µmol/h. For comparison, the data will be scaled to a light power of 100 W/m^2 and a unit sample weight of 1 g, which gives 90.07 µmol/h/g.

Clearly, the hydrogen production rate from their powdered Cu/TiO_2 is less than the hydrogen production rate of the Ag/TiO_2 nanocomposite film presented in this work. This may be attributed to the tendency of the powder to aggregate, which reduces the surface area exposed to the electrolyte solution and the overall reactivity. Also the metal-TiO_2 contact should be different due to the preparation procedures. The small difference in the work function of Ag and Cu may also influence the electron transport from the TiO_2 conduction band to the metal surface. It is possible that the size of the metal particles could create defects in the crystal structure and change the electronic confinement in TiO_2. Beside higher activity, our film can be easily recycled. Table 2.3 illustrated the comparison of results between this work and Jeon, et al. [85] to investigate the effect of TiO_2 geometry, metal, and TiO_2 crystal structure on hydrogen production rate.

TiO_2 Anatase and TiO_2 Amorphous

As a control, the performance of the anatase TiO_2 thin film was probed without silver deposition. As shown in Figure 2.17 and Tables 2.6 and 2.7, the hydrogen production rate for an anatase pure TiO_2 nanocomposite film without Ag is about 4.65 ± 0.39 μmol/h/g, which represents an enormous reduction in the hydrogen production rate. To investigate possible crystal structure effects, amorphous pure TiO_2 thin film was synthesized without the annealing step (at 500°C for 5 hours). This film exhibited a hydrogen production rate of 0.46 ± 0.66 μmol/h/g. It is clear that the anatase crystal structure (produced at 500°C for 5 hours) of the TiO_2 thin film has a substantial impact on the film's activity. This can be attributed to changes in the electronic structure,

electron confinement, and electron excitation between the crystalline and non-crystalline materials. Therefore, the Ag/TiO$_2$ nanocomposite film structure can be thought to facilitate the transportation of electrons from TiO$_2$ to the Ag surface which in turn enhances the hydrogen production rate.

Table 2.3 Comparison of the hydrogen production rate from water/methanol decomposition under UV light, scaling to 100 W/m^2 power intensity and 1 g photocatalyst weight.

No.	Photo-catalyst	H$_2$ production (μmol/h/g)	Solution Ratio (1:1, v/v)	Nano-structure	Reference	Parameters affect reactivity
1	Cu/TiO$_2$ (500ºC)	90.07	Water/ Methanol	Powder	[85]	Geometry
2	Ag/TiO$_2$ (anatase)	147.9±35.5	Water/ Methanol	Thin Film	This work	Metal
3	TiO$_2$ (anatase)	4.65±0.39	Water/ Methanol	Thin Film	This work	Crystal Structure
4	TiO$_2$ (amorphous)	0.46±0.66	Water/ Methanol	Thin Film	This work	-

Note: Between 1 & 2, the metal particle size and amount are also different.

Table 2.4 Results and conditions of anatase Ag/TiO$_2$ nanocomposites thin films

H$_2$ production (μmol/h)	H$_2$ production (μmol/h/g)	Effective Area, m^2	Energy Efficiency % @ x=0	Energy Efficiency % @ x=0.7
0.085 ± 0.02	147.9 ± 35.5	0.0001	0.016	0.056

Additives type and weight (g)	Photo catalyst type and weight (g)	Nano-structure and geometry	Photocatalyst Size, composition, Crystal structure	Water/ Methanol solution (1:1) Volume basis	Light Intensity If UV, (100 W/m^2) If Sunlight, ≈ (240 W/m^2)
-	Ag/TiO$_2$ (0.00058)	Nano - composites Thin film	Ag, < 200± 50 nm), TiO$_2$ (<3 μm, anatase)	10 ml (5 ml each)	UV
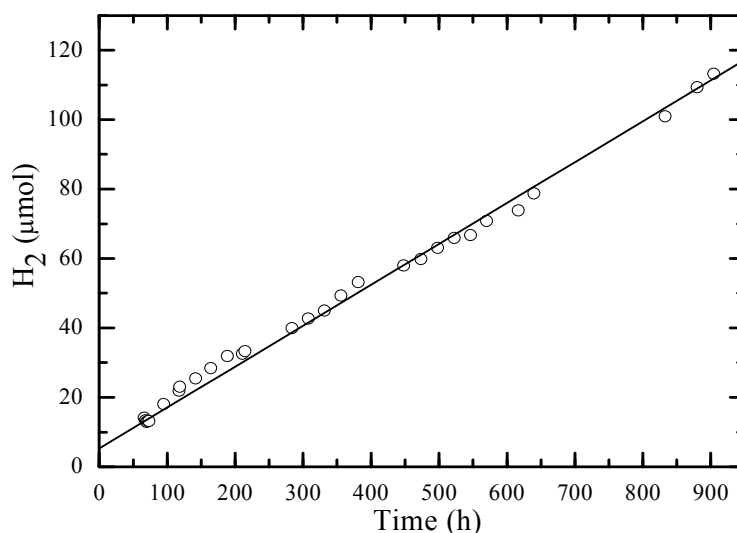
Figure 2.16 (a) Time course of hydrogen production using anatase Ag/TiO$_2$ nanocomposite films. The slope gives the production rate of this run as 188.7 ± 0.39 μmol/h/g. The weight of photocatalyst used in this run was estimated to be 0.58 mg. The stability of the hydrogen production rate using Ag/TiO$_2$ nanocomposite films exceeded one month in experimental duration.
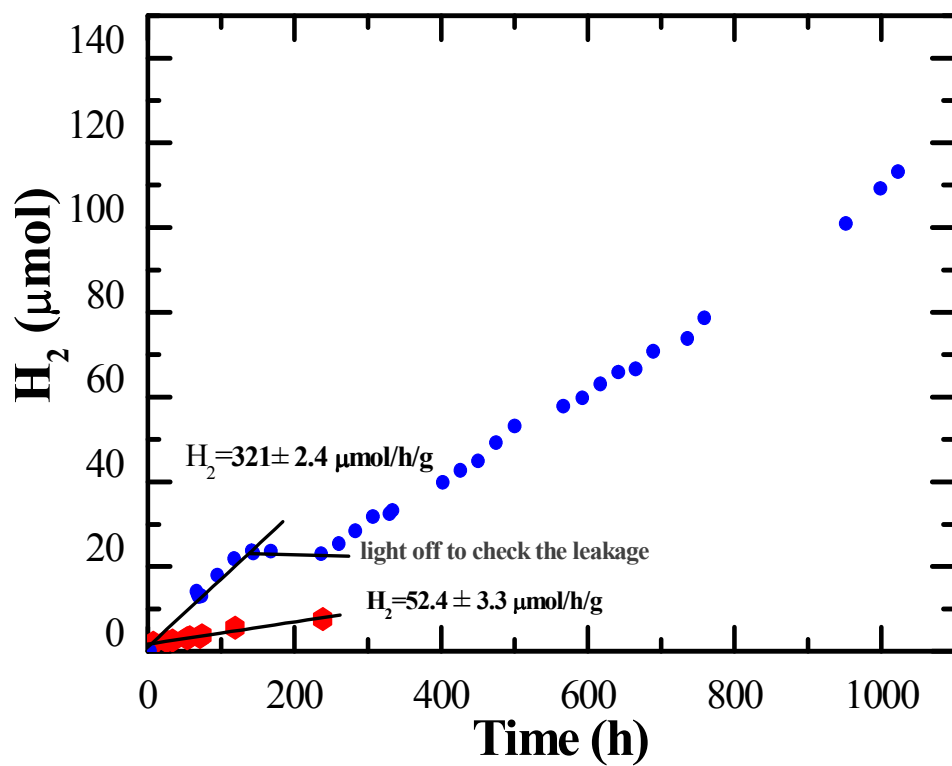
Figure 2.16 continued (b) the results of three experiments conducted to evaluate the performance of Ag/TiO$_2$ nanocomposites thin film.

Table 2.5 Shows the normalization of the results of three runs conducted to evaluate the performance of Ag/TiO$_2$ nanocomposites thin film.

Run No.	H$_2$*	Error*	area, cm^2	effective area, cm^2	Normalized H$_2$*	Normalized Error*	Standard Deviation, H$_2$	Standard Deviation, error
1	76.57	3.536	6.25	0.4375	131.263	6.062	279.284	11.169
2	123.888	1.7	6.25	0.75	123.888	1.704	580.167	1.03
3	188.773	0.33	6.25	0.75	188.773	0.393	1664.51	5.413
					147.975	2.72	1261.9	8.806
							35.524	2.967

* µmol/h/g

Notes:
1. The fitting of experimental data for hydrogen production rate is based on linear equation fitting.
2. Area of substrate is 2.5 cm by 2.5 cm, effective area is the area estimated to be fully covered of Ag on the surface of TiO$_2$.
3. Normalized H$_2$ and error is based on area of 0.75 cm^2.
4. Standard Deviation calculated as:

$$\sigma = \sqrt{\frac{1}{N}\sum_{i=1}^{N}\left(x_i - \mu\right)^2}$$

where the mean or average (μ) calculated as:

$$\mu = \frac{\sum_{i=1}^{N} x_i}{N}$$

Table 2.6 Results and conditions of anatase TiO$_2$ thin films

H$_2$ production (μmol/h)	H$_2$ production (μmol/h/g)	Effective Area, m^2	Energy Efficiency % @ x=0	Energy Efficiency % @ x=0.7
0.002 ± 0.00019	4.65 ± 0.39	0.0001	0.00039	0.0013

Additives type and weight (g)	Photo catalyst type and weight (g)	Nano-structure and geometry	Photocatalyst Size , composition, Crystal structure	Water/ Methanol solution (1:1) Volume basis	Light Intensity If UV, (100 W/m^2) If Sunlight , ≈ (240 W/m^2)
-	TiO$_2$ (0.0005)	Thin film	TiO$_2$ (<3 μm, anatase)	10 ml (5 ml each)	UV

Table 2.7 Results and conditions of amorphous TiO$_2$ thin films

H$_2$ production (μmol/h)	H$_2$ production (μmol/h/g)	Effective Area, m^2	Energy Efficiency % @ x=0	Energy Efficiency % @ x=0.7
0.00023 ± 0.00033	0.46 ± 0.66	0.0001	0.000045	0.00015

Additives type and weight (g)	Photo catalyst type and weight (g)	Nano-structure and geometry	Photocatalyst Size , composition, Crystal structure	Water/ Methanol solution (1:1) Volume basis	Light Intensity If UV, (100 W/m^2) If Sunlight , ≈ (240 W/m^2)
-	TiO$_2$ (0.0005)	Thin film	TiO$_2$ (<3 μm, amorphous)	10 ml (5 ml each)	UV
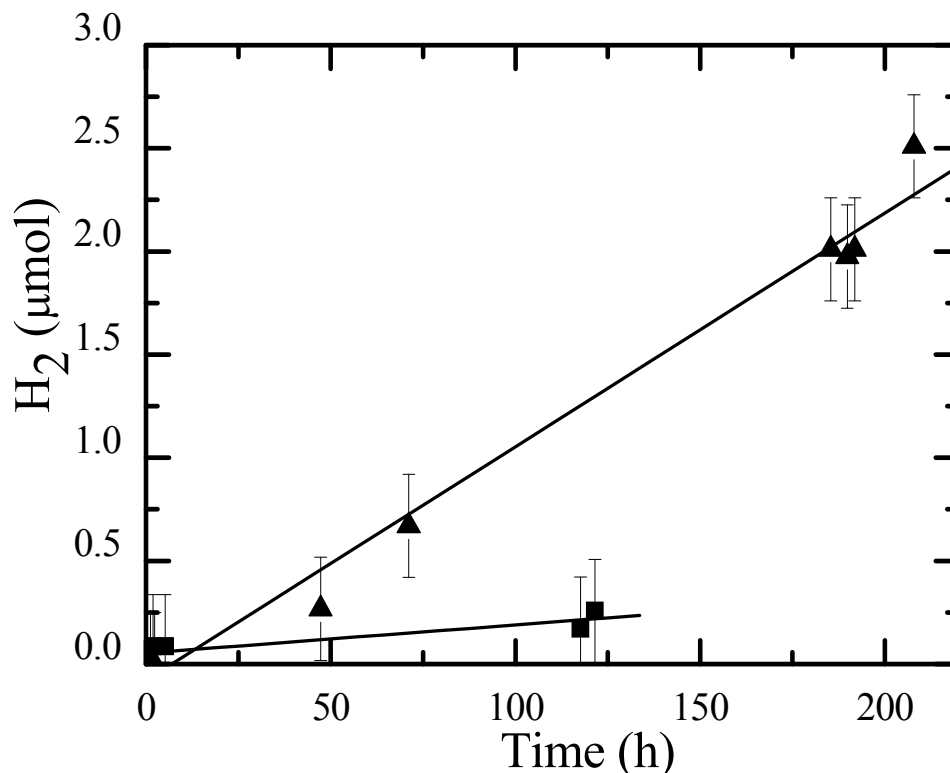
Figure 2.17 The time course of hydrogen production from TiO$_2$ films without silver deposition. The hydrogen evolution was extremely low, 0.46±0.66 μmol/h/g, for the non annealed (room temperature, amorphous TiO$_2$) sample (squares), while the annealed (at 500°C for 5 hours, anatase crystal structure TiO$_2$) sample (triangles) showed a slight improved hydrogen production rate of 4.65±0.39 μmol/h/g.

Ag/TiO$_2$ Amorphous

For the Ag/TiO$_2$ amorphous experiments (non annealed, room temperature), Figure 2.18 and Table 2.8 exhibited the hydrogen evolution as 29.7 ±1.18 μmol/h/g. The robust metal-semiconductor interface surface leads to high electron transport and therefore, high energy efficiency. However, the lower hydrogen production rate of amorphous Ag/TiO$_2$ than the anatase sample due to the crystallinity effect on quantum confinement and electrons ability to move with slight tune to band gap structure (direct and indirect band gap configuration).

Table 2.8 Results and conditions of amorphous Ag/TiO$_2$ nanocomposites thin films.

H$_2$ production (μmol/h)	H$_2$ production (μmol/h/g)	Effective Area, m^2	Energy Efficiency % @ x=0	Energy Efficiency % @ x=0.7
1.48 ± 0.059	29.7 ± 1.18	0.0001	0.29	0.975

Additives type and weight (g)	Photo catalyst type and weight (g)	Nano-structure and geometry	Photocatalyst Size, composition, Crystal structure	Water/ Methanol solution (1:1) Volume basis	Light Intensity If UV, (100 W/m^2) If Sunlight, ≈ (240 W/m^2)
-	Ag/TiO$_2$ (0.05)	Nano-composites Thin film	Ag, < 200± 50 nm), TiO$_2$ (<3 μm, amorphous)	10 ml (5 ml each)	UV
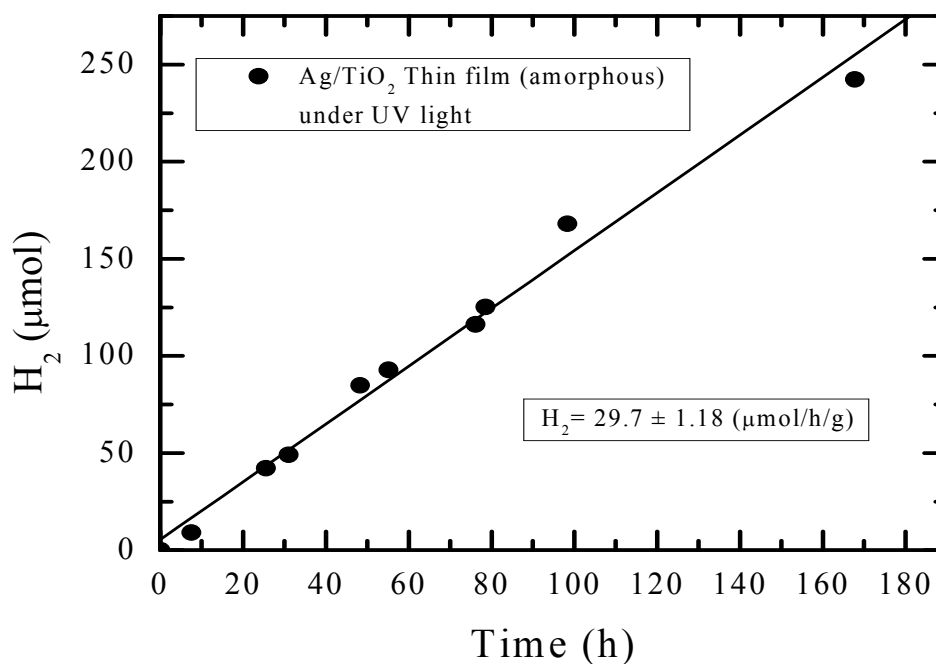
Figure 2.18 The time course of hydrogen production from Ag/TiO$_2$ films without annealing. The hydrogen evolution as 29.7 ± 1.18 μmol/h/g, for the non annealed (room temperature, amorphous TiO$_2$) sample. The robust metal-semiconductor interface surface leads to high electron transport and therefore, high energy efficiency.

Ag/4-Mercaptobenziocacid/TiO$_2$

For the Intermediate organic linker layer (4-mercaptobenzoic acid) experiments, the photoexcited electrons transfer from conduction band of the TiO$_2$ into metal surface because metal has low work function than TiO$_2$ (as low as in work function is better for electron transport). Also, due to difference in Fermi level of energies between metal and semiconductor. The electrons transfer will be inhibited if equilibrium state of Fermi level of energies of metal with semiconductor occurred. The linker is used here to connect or attach all atoms of both metal and TiO$_2$ surfaces link them like a wire for better electron transportation and to enhance the electron trap process and electrons transportation and mobility from conduction band of TiO$_2$ to the metal surface, the interface layer between Ag and TiO$_2$ must be highly connected. The organic layer used is 4-Mercaptobenzioc acid as intermediate linker was deposited between silver and TiO$_2$ to function as bridge of electrons flow and to overcome the Schottky barrier. Figure 2.19 and Tables 2.9 and 2.10 showed that the time course of hydrogen production from Ag/Linker/TiO$_2$ films as 87.08 ± 22.9 μmol/h/g and for non-linker films (Ag/TiO$_2$) as 141.62 ± 27.8 μmol/h/g. This is attributed to the following reasons:(1) In case of Ag/TiO$_2$ thin films, silver deposited using electron photodeposition by UV- light, where in case of Ag/Linker/TiO$_2$ silver deposited using dip coating technique. This leads to difference in silver amount loaded and different contact levels between metal and TiO$_2$.(2) large contribution of surface atoms due to the organic linker case which enhance the electrons mobility from TiO$_2$ to metal surface and leads to facilitate the electrons transportation and metal-trapped. (3) Slight difference in TiO$_2$ thickness between both samples and experiments

conditions control may to leads to this difference in performance. As result, more reduction reactions to generate hydrogen molecules.

Table 2.9 Results and conditions of anatase Ag/Linker/TiO$_2$ thin films.

H$_2$ production (μmol/h)	H$_2$ production (μmol/h/g)	Effective Area, m^2	Energy Efficiency % @ x=0	Energy Efficiency % @ x=0.7
0.043 ± 0.011	87.08 ± 22.9	0.0001	0.008	0.028

Organic linker layer and weight (g)	Photo catalyst type and weight (g)	Nano-structure and geometry	Photocatalyst Size, composition, Crystal structure	Water/ Methanol solution (1:1) Volume basis	Light Intensity If UV, (100 W/m^2) If Sunlight, ≈ (240 W/m^2)
Intermediate (4-MercaptoBenzoicAcid)(<0.0005)	Ag/TiO$_2$ (0.0005)	Nano - composites Thin film	(Ag ≈ 50 nm), TiO$_2$ (<3 μm, anatase)	10 ml (5 ml each)	UV

Table 2.10 Results and conditions of anatase Ag/TiO$_2$ thin films (no linker).

H$_2$ production (μmol/h)	H$_2$ production (μmol/h/g)	Effective Area, m^2	Energy Efficiency % @ x=0	Energy Efficiency % @ x=0.7
0.07 ± 0.01	141.62 ± 27.8	0.0001	0.013	0.046

Organic linker layer and weight (g)	Photocatalyst type and weight (g)	Nano-structure and geometry	Photocatalyst Size, composition, Crystal structure	Water/ Methanol solution (1:1) Volume basis	Light Intensity If UV, (100 W/m^2) If Sunlight, ≈ (240 W/m^2)
-	Ag/TiO$_2$ (0.0005)	Nano - composites Thin film	(Ag ≈ 50 nm), TiO$_2$ (<3 μm, anatase)	10 ml (5 ml each)	UV

Figure 2.19 The effect of organic linker material as intermediate linker layer between Ag and TiO$_2$ thin film on substrate is shown here. The time course of hydrogen production from Ag/Linker/TiO$_2$ films showed hydrogen production as 87.08 ± 22.9 µmol/h/g (using linear fit data of run 37). For non-linker films (Ag/TiO$_2$) prepared by same method, as 141.62 ± 27.8 µmol/h/g (using linear fit data of run 36 after adding run 38 data to last point of run 36 data). The weight for intermediate all samples sample is estimated to be 5 mg.

Ag/TiO$_2$ Anatase Prepared by CVD

For Ag/TiO$_2$ film prepared by chemical vapor deposition, the hydrogen production rate was 6.37 ± 4.5 µmol/h/g (Figure 2.20) and Table 2.11. The synthesis method is very important to govern the properties of thin film by manipulate the film size and thickness. The difference in preparation method between chemical vapor deposition and drop deposition method may lead to slight difference in film performance. Silver ions were reduced by photoelectron from aqueous AgNO$_3$ solution but with UV light at 420 W for 5 minutes illumination. The silver reduction time on film prepared by chemical vapor

deposition is longer than the time used for drop deposition films. This also may leads to difference in silver nanoparticles size and weight loaded.

Table 2.11 Results and conditions of anatase Ag/TiO$_2$ thin films synthesized by CVD.

H$_2$ production (μmol/h)	H$_2$ production (μmol/h/g)	Effective Area, m^2	Energy Efficiency % @ x-0	Energy Efficiency % @ x-0.7
0.031 ± 0.02	6.37 ± 4.5	0.0001	0.006	0.02

Synthesis method	Photo catalyst type and weight (g)	Nano-structure and geometry	Photocatalyst Size , composition, Crystal structure	Water/ Methanol solution (1:1) Volume basis	Light Intensity If UV, (100 W/m^2) If Sunlight , ≈ (240 W/m^2)
Chemical Vapor Deposition (CVD), Ag loaded by photoelectron Deposition	Ag/TiO$_2$ (0.005)	Nano - composites Thin film	Ag , < 200± 50 nm), TiO$_2$ (<200 nm, anatase)	10 ml (5 ml each)	UV
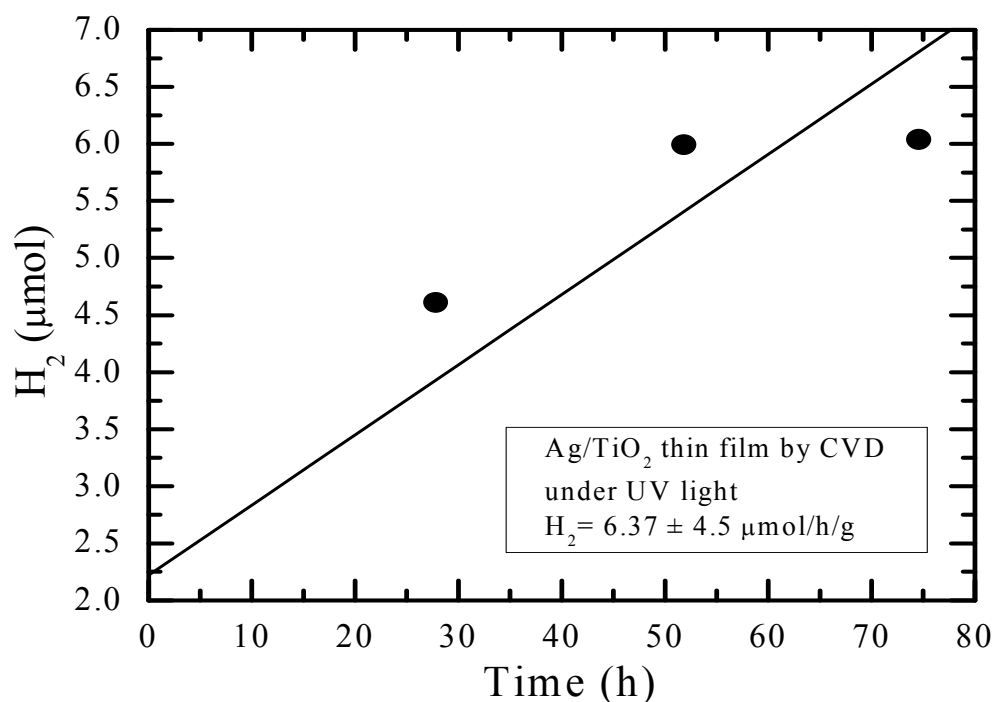
Figure 2.20 Hydrogen production rate from anatase Ag/TiO$_2$ thin films synthesized by CVD.

Due to its simplicity, low cost and high sensitivity to monitor the time course and hydrogen production rate, our method can be implemented as a high through-put screening process to search for high efficiency ultrathin films or nanostructures for photocatalytic solar-hydrogen production via the splitting of water. The method may also be very helpful to investigate the influence of many parameters on hydrogen production rate such as new materials, nanocomposites, additives, water purity, light intensity inside the laboratory and outside under direct sunlight. It will contribute to a better understanding of material function and photoelectrochemical reaction mechanism.

CONCLUSIONS

The feasibility of generating hydrogen photoelectrochemically from water/methanol decomposition using Ag/TiO_2 nanocomposite films has been demonstrated. The overall activity of hydrogen production was 147.9±35.5 μmol/h/g. In addition, the Ag/TiO_2 nanocomposite films showed high stability for hydrogen production for more than one month. The time course of hydrogen production from $Ag/Linker/TiO_2$ films showed hydrogen production as 87.08 ± 22.9 μmol/h/g and for non-linker films as 141.62 ± 27.8 μmol/h/g. For the Ag/TiO_2 amorphous experiments, the hydrogen evolution was 29.7 ± 1.18 μmol/h/g. It is found that several parameters are highly induced the reactivity and energy conversions from photons to electrons and then to hydrogen production. These parameters are metal size and amount, crystal structure, TiO_2 synthesis method, geometry, intermediate layer. Thin-film photocatalysts have an advantage in that they can be regenerated or reuse unlike the powdered catalysts. Previous fabrication of Ag/TiO_2 nanocomposite film [76,77] was modified to form the anatase crystal structure of TiO_2. The modification was observed to enhance the photocatalytic properties of these materials.

Our test methodology of detecting hydrogen production from an ultralow amount of photocatalyst can be used as a high through-put screening process to search for high efficiency photocatalysts for hydrogen production by photoelectrochemical water-splitting using solar energy.

CHAPTER III

ROLE OF ELECTRON DONOR/ACCEPTER ON ELECTRON TRANSPORTATION BETWEEN ELECTRODE/ELECTROLYTE INTERFACES

OVERVIEW

In this chapter, the role of electron donor such as methanol and electron relay such as Mv^{+2} will be evaluated for hydrogen production. The pH value of the solution and the ionic strength has important function corresponding to the TiO_2 surface charge potential. Not to mention that the ultimate goal of this method is to eventually split seawater using solar energy and photocatalytic nanomaterials, different weight % of NaCl were varied to explore the effect of impurities (e.g. salts) on the mechanism of water splitting reaction in presence of electrode the electrolyte. The influence of carbonate in the solution ($NaHCO_3$) and Iodide anions "KI" tested for their role in suppressing recombination reaction of photoexcited electron-hole pair. Based on the results obtained and in term of additives to equal volume of water/methanol solution under UV light using same photocatalyst, it is found that the ranking based on highest hydrogen production as follows: $NaHCO_3$ > NaCl (3.5 wt %) > KI > Mv^{+2}. The main conclusion from these results is that the hole-scavengers or oxidation agent works well in term of suppress the hole-electron recombination reaction that electron trapping by electron accepter or electron mediator.

INTRODUCTION

In order to effectively split water to generate hydrogen, water oxidation and reduction reactions must be happened at metal and semiconductor surfaces with robust trapped of electrons and holes charge carriers. In two column experimental set up as H-type photoelectrochemical cell, the photoanode (semiconductor) and the photocathode (metal) must be designed to separate the oxygen and hydrogen gases evolution in highly safe and efficient design. Figure 3.1 showed the typical H-type photoelectrochemical cell for hydrogen production from water-splitting method.
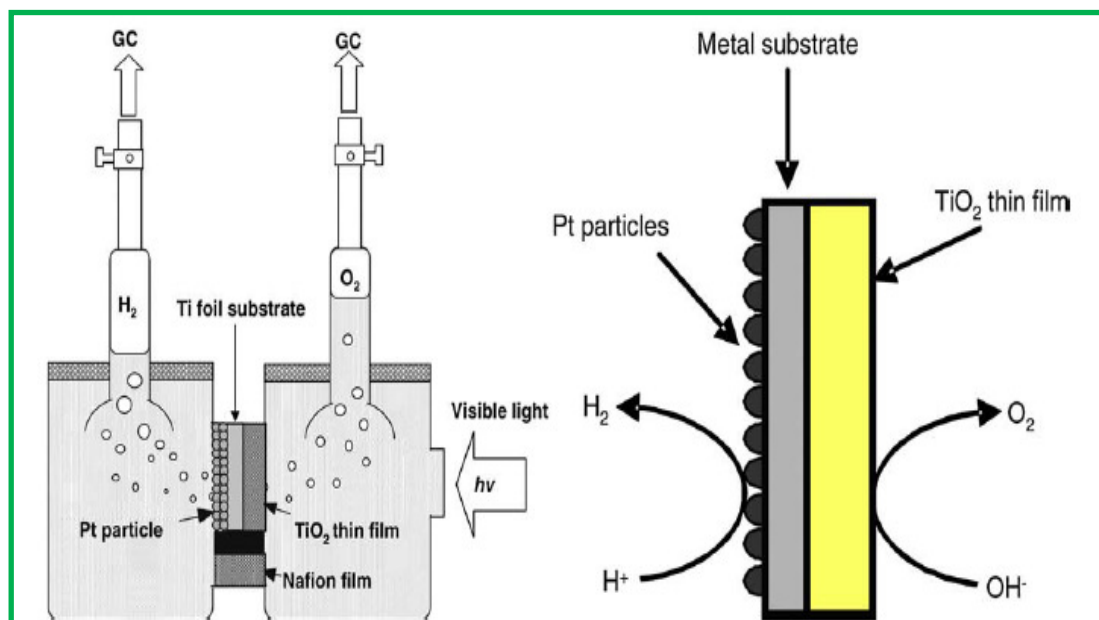
Figure 3.1 H-type photoelectrochemical water-splitting cell [86].

Water-splitting is a thermodynamically uphill reaction or endothermic process, a minimum potential of 1.23 e V versus Normal Hydrogen Electrode, NHE is required to complete the reaction. Upon light illumination, if the photon energy is matches or larger

than the band gap energy of the semiconductor (based on Planck relation), the photo-excite electrons are jumped from valence band to the unoccupied conduction band [39]. At the cathode (metal), electrons trapped due to lower work function and difference in Fermi level, reacted with protons to generate hydrogen molecules. At the anode (semiconductor), the holes reacted with water species adsorbed at the surface to generate oxygen molecules. As mentioned earlier in this dissertation, the criteria for strong candidate material to split water are stability in aqueous solution, extension in solar energy absorption to include visible light wavelength, and cost-effective materials [39]. More important, it must be highly efficient for charge separation and enhance the yield of conversion of electrons and holes into hydrogen and oxygen gases. The materials properties, mainly, the band gap and band edge position related to water reduction and oxidation reactions potentials are very crucial to split the water. The conduction band edge must be more negative than the hydrogen generation potential and the valence band edge must be more positive than oxygen generation potential [39].

Due to the uphill nature of water-splitting reaction, it is extremely difficult to split water using pure water. Therefore, an electron donors, also called hole scavengers or sacrificial reagents such as alcohols (methanol), added to the water solution. The sacrificial reagents are easily get oxidized by the photoexcited holes than water does which leads to extremely minimize the production of oxygen that generate from water oxidation reactions. This is contributing also to efficiently separate the charge carriers and suppress the electron-hole recombination reactions which enhance the quantum efficiency and overall energy efficiency. The evaluation of photocatalytic activities of

materials for water reduction or oxidation were examined in the presence of methanol or silver nitrate as a sacrificial reagent. The reactions using sacrificial reagents are not "overall" water splitting reactions but are often carried out as test reactions for overall water splitting. The decomposition of methanol leads to increase the hydrogen production yield. The stoichiometry (the quantitative relationships that exist among the reactants and products in chemical reactions) and reaction mechanism are as follows:

Water-splitting:
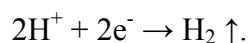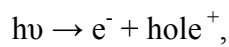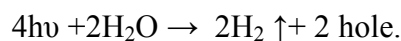
$h\upsilon \rightarrow e^- + hole^+$,

$2H^+ + 2e^- \rightarrow H_2 \uparrow$.

The overall reaction is

$4h\upsilon + 2H_2O \rightarrow 2H_2 \uparrow + 2\ hole$.

Methanol decomposition:

$2hole + MeOH \leftrightarrow H_2CO + H_2 \uparrow$,

$H_2CO + H_2O \leftrightarrow H_2CO_2 + H_2 \uparrow$,

$H_2CO_2 \leftrightarrow CO_2 \uparrow + H_2 \uparrow$.

The overall reaction is

$2hole + CH3OH + H_2O \leftrightarrow CO_2 + 3H_2 \uparrow$,

Water/Methanol:

$6\ h\upsilon \rightarrow 6e^- + 6hole^+$,

$6H^+ + 6e^- \rightarrow 3H_2 \uparrow$.

$6hole^+ + CH_3OH + H_2O \rightarrow 6H^+ + CO_2$.

The overall reaction is

$$6\ h\upsilon + CH_3OH + H_2O \rightarrow 3H_2 \uparrow + CO_2.$$
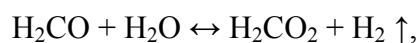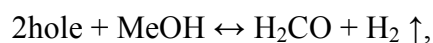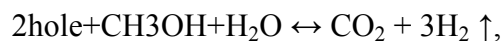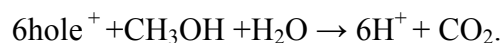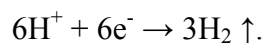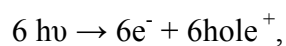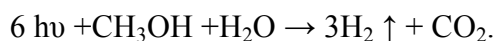
Based on above reactions mechanism, the hydrogen production from water-splitting is 30% and the remaining 70% is from methanol decomposition. The advantages of single-photoreaction cell: simple, low cost, flexible to test large numbers of nanomaterials, safe, and high throughput screening technique.

When the photocatalytic reaction is conducted in the presence of an electron donor such as methanol, photogenerated holes in the valence band irreversibly oxidize methanol instead of H_2O, thus facilitating water reduction by conduction band electrons if the bottom of the conduction band of the photocatalyst is located at a more negative potential than the water reduction potential.

In the presence of an electron acceptor such as silver cations, photogenerated electrons in the conduction band irreversibly reduce electron acceptors instead of H^+, thereby promoting water oxidation by valence band holes if the top of the valence band of the photocatalyst is positioned at a more positive level than the water oxidation potential. Figure 3.2 illustrate the effect of adding electron donor/acceptor to water on hydrogen production [13].
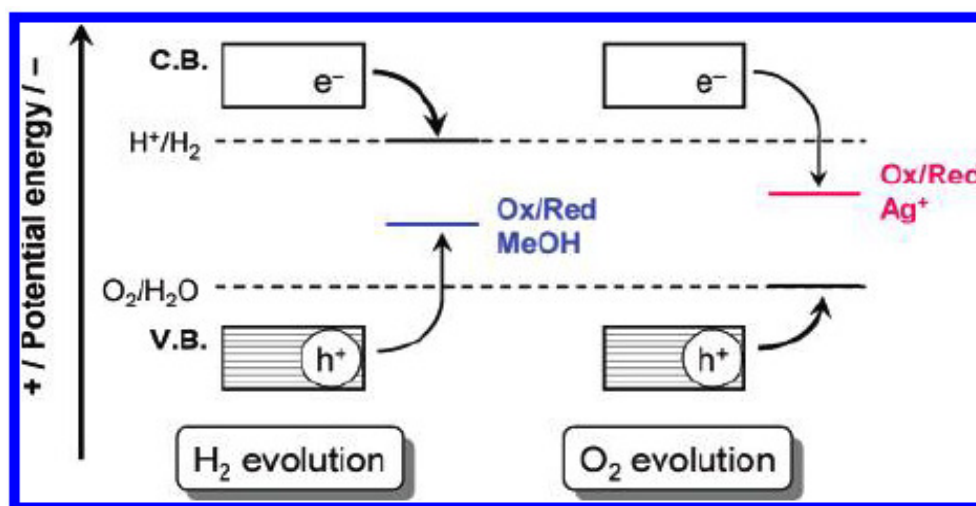
Figure 3.2 Illustrate the effect of adding electron donor / acceptor to water on hydrogen production [13].

Effect of Mv^{+2} as Electron Relay

Methyl viologen cation radical (MV^{+2}), electrogenerated from the colorless dictation (MV$^+$) at a standard redox potential is a strong reductant capable of reducing the proton to yield molecular hydrogen in neutral to acidic media [87]. Methyl viologen used as electron relay to electron mediation, transferring the electrons photogenerated from semiconductor surface to the metal surface to complete the water reduction reaction for hydrogen evolution. The change in concentration of MV^{+2} will change the photocatalytic hydrogen production, with increase in the concentration of MV^{+2} will increases the hydrogen production, however, increasing the concentration more would making the evolution of hydrogen thermodynamically less favorable. The heterogeneous reaction slows down by adsorption on the catalyst surface and blocking the reaction sites [88].

Influence of Adding NaHCO$_3$

In the presence of NaHCO$_3$ they act as oxidation agent, where carbonate species reacted with holes to form carbonate radicals, which is beneficial for photo-excited electron/hole separation. The peroxy carbonates were easily decomposed into O$_2$ and CO$_2$. The evolution of CO$_2$ and O$_2$ could promote desorption of O$_2$ from the photocatalyst surface and thus could minimize the formation of H$_2$O through the backward reaction of H$_2$ and O$_2$ [45].

Impact of Adding NaCl Aqueous Solution (Ionic Strength Effect)

The ultimate goal of this technology is to split seawater to generate hydrogen using solar energy. Seawater is rich of salts that affect the photocatalyst reactivity and the reaction mechanism of water-splitting. In order to study these effects, different weight (%) NaCl with respect to volume to water used (5 ml) were tested using Cu^{+2} and CuO/TiO$_2$ nanopowders as photocatalyst under UV light. Through these experiments, the effect of ionic strength of Na$^+$ and Cl$^-$ will be explored. If the solution pH value is higher than the point of zero charge of TiO$_2$, this means the TiO$_2$ surface potential is negatively charged (based on Nernst equation for surface charge potential). In this case, the sodium ions will be attracted to the TiO$_2$ surface to block some reaction sites and reduce the activity. If the pH value of the solution is less than the point of zero charge of TiO$_2$, the chloride ions will be attracted to the TiO$_2$ surface to block some reaction sites and reduce the activity. Therefore, controlling the pH value of the solution is important to control the TiO$_2$ surface potential charge which has great impact on the electrical conductivity between solid/liquid interfaces.

Therefore, pH play an important role on the photocatalytic reaction and generally attributed to the surface charge of titanium oxide. The point of zero charge (p.z.c) of calcined TiO_2 is 3.2; the catalyst's surface is positively charged at pH values lower than 3.2 and negatively charged at higher pH values. Electrostatic attraction or repulsion between the catalyst's surface and the reactant molecule is taking place, depending on the ionic form of the compound (anionic or cationic) and consequently enhances or inhibits, respectively, the photocatalytic reaction rate. The role of ionic strength on the photocatalytic of H_2 evolution was studied by changing the concentration of NaCl. At neutral pH, and at the point of zero charge of TiO_2, the reactants molecules are allowed to reach easily the catalyst's surface and achieve higher reaction rates [89].

Role of Proton Conductivity and Hole Scavengers

According to previous studies [89] it is found that the methanol is the most effective and strongest sacrificial reagents for hydrogen evolution activity. The photocatalytic hydrogen evolution is favorable in the neutral pH range. The hydrogen yield decreases with the increase of the carbon number of alcohol. This effect is mainly due to the decrease in the formation of formaldehyde for higher alcohols because it involves carbon-to-carbon bond breaking. The extent of carbon to carbon bond breaking decreases with the increase in chain elongation and complexity, as these factors contributes to enhancing the steric hindrance in the molecule.

Pure Water under UV Light and Sunlight

As mentioned earlier, it is difficult to split water into oxygen and hydrogen without adding electron donors such as alcohols due to uphill nature of the reaction. Because of the fast recombination reaction between photoexcited electron and holes from TiO_2 semiconductor, it is highly important to mix pure water with methanol in specific ratio to enhance hydrogen production. Continuous adding of alcohols (e.g. methanol) is also important to achieve successful separation of electrons-holes charges as a strong oxidation agent of the hole charges [45]. To estimate the amount of methanol that required to be added to water and to estimate the hydrogen production from only water-splitting reaction (methanol decomposition contribute to overall hydrogen production), it is very useful to conduct experiments using pure water only and tested the metal-TiO_2 photocatalyst under UV light and under natural sunlight. The metal-TiO_2 photocatalyst is speeding up the rate of reaction without being consumed on it, so it will generate the electron-hole pairs upon excite with light intensity. However, the activity and quantum efficiency (total electrons and holes generated and converted to oxygen and hydrogen) are highly dependent on surface and interface properties and the additives to water solution.

Iodide Anions KI under UV Light

Addition of iodide was also found to be advantageous for hydrogen production [43] . Iodide anion (I^-) in a suspension can be adsorbed preferentially onto metal surface, forming an iodine layer. The iodine layer can thus suppress backward reaction of H_2 and O_2 to form H_2O. Accordingly, the production of hydrogen and oxygen was enhanced

very significantly. However, adding too much carbonate salt or iodide anion beyond optimum level could reduce the beneficial effects, since these species adsorbed onto the catalyst surface could decrease light harvesting [45].

Seawater under UV Light and Sunlight

As ultimate goal of this technology, sea water splitting under sunlight require a superb nanostructure materials with high efficiency and cost-effective. The compositions of sea water include the salts, metals and inorganic will contribute to further increase the complexity of water-splitting reaction mechanism. Fortunately, the salts may leads to reduce the pH value which is less than the point zero charge of TiO_2 and leads to increase the surface potential reactivity between surface-electrolyte interfaces. As result, this facilities the electrons transfer (electrical current) from semiconductor surface to water molecules. It is important to note that other contamination such as solid particles might highly influence on the water-splitting reaction. They block the active sites on the photocatalyst from exposing to light and reduce the possibility to generate electron-hole charge carriers.

DESIGN AND SYNTHESIS

Cu^{+2} and CuO/TiO_2 Nanopowders

In typical procedure described by [85] [74] TiO_2 and 10 mol % of Cu/TiO_2 photocatalysts were prepared using the conventional sol-gel method, as shown in Figure 3.3. For the sol mixture, Titanium (IV) isopropoxide, TTIP (Sigma Aldrich), and Cu $(NO_3)_2.2.5H_2O$ (Sigma Aldrich) were used as the titanium and copper precursors, respectively, and

ethanol (Sigma Aldrich) was used as the solvent. To 500 ml of ethanol, were added 0.40 mol TTIP and 0.04 mol Cu $(NO_3)_2.2.5H_2O$ to 10 mol % of Cu. Then, 1.60 mol of distilled water was added to the mixture for hydrolysis. The TTIP and Cu $(NO_3)_2.2.5H_2O$ were hydrolyzed via the OH group during evaporation at 80ºC for 24 hours. The resulting dark-gray precipitate was dried at 100ºC for 24 hours.

Finally, TiO_2 and Cu/TiO_2 samples having anatase phase of crystal structure were obtained after annealing for 5 hours at 500ºC (ramping temperature is 2˚C/minutes). CuO and Cu_2O copper oxides also may be formed because the sample annealed at air atmosphere and not reduced by hydrogen gas. Based on previous study reported by [74] [85] CuO is form if Cu metal loading reached 10 mol %.

Therefore, the actual sample prepared is Cu^{+2} and CuO/TiO_2. The concentration of copper amount loaded changing the degree of copper oxides that may form on TiO_2 surface. The size of Cu^{+2} and CuO/TiO_2 nanoparticles is less than ≈ 100 nm, but it is ground mechanically to form nanopowders structure and to reduce the size to be less than ≈ 50 nm. Copper nanoparticles decorated the TiO_2 surface is less than ≈ 20 nm.

(8) Annealing at 500°C for 5 h (2°C/min), collect anatase Cu-TiO powder

(7) Evaporation at 80°C for 1 day, drying at 100°C for 1 day, collect amorphous Cu-TiO powder

(5) 1.6 mol of DI water   (6) Stirring 12 h

(4) Stirring 1 h

(2) 0.4 mol of TTIP   (3) 0.04 mol of Cu.(NO) .2.5H O

(1) 50 ml ethanol in 100 ml beaker
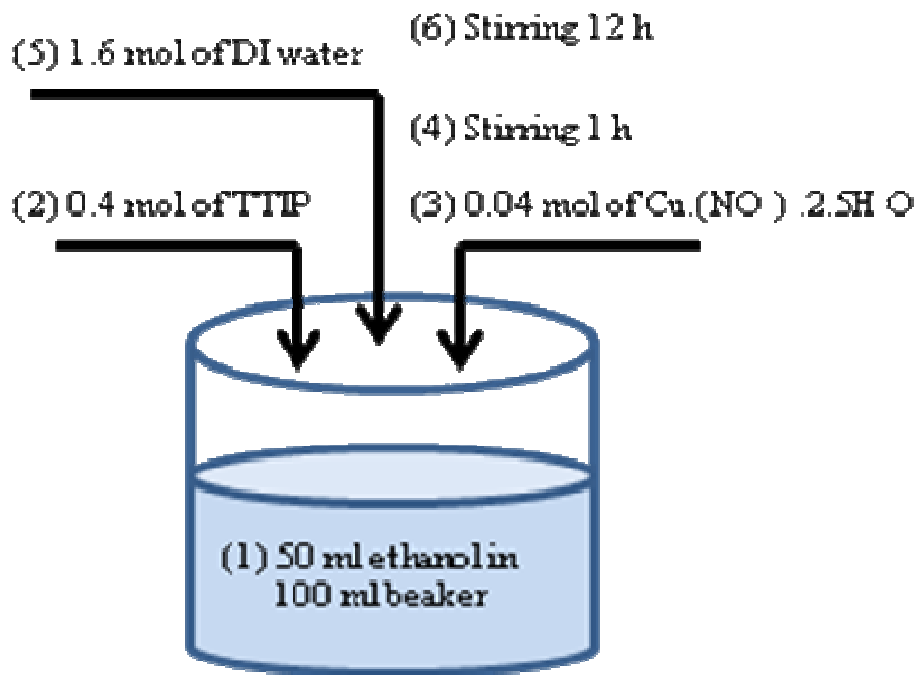
Figure 3.3 The preparation procedure of Cu^{+2} and CuO/TiO_2 nanoparticles using conventional sol-gel technique [85][74].

CHARACTERIZATION

After synthesis, the Cu^{+2} and CuO/TiO_2 nanopowders were characterized using Scanning

Electron Microscopy (SEM) (Figure 3.4). The SEM images were taken using JEOL

JSM-6400. The Surface element analysis was obtained using Energy dispersive X-ray

spectroscopy (EDS) as shown in Table 3.1. The EDS results were obtained using JEOL

JSM-6400. Image by digital camera is also taken for the sample. Digital image of the

sample before annealing is shown in Figure 3.5.
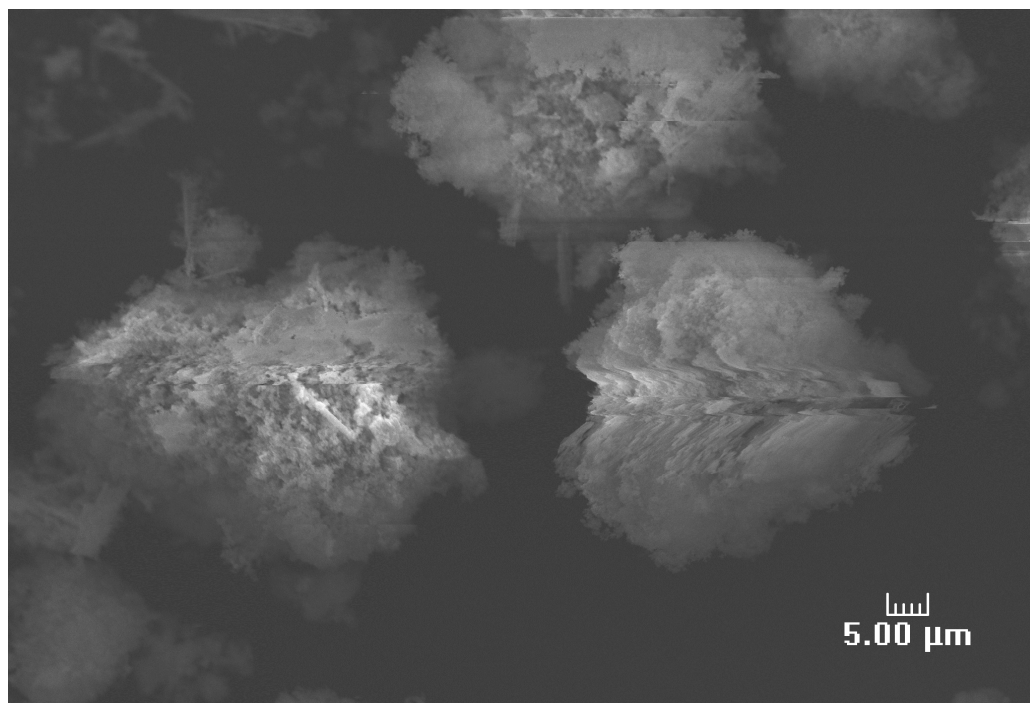
Figure 3.4 SEM image of Cu $^{+2}$ and CuO/TiO$_2$ nanopowders after annealing..

Figure 3.5 Digital image of Cu $^{+2}$ and CuO/TiO$_2$ nanoparticles before annealing..

Table 3.1 Surface element analysis of Cu $^{+2}$ and CuO/TiO$_2$ nanopowders using EDS.

Element	keV	KRatio	Wt%	At%	At Prop	ChiSquared
Ti	4.510	0.7049	66.96	67.64	0.0	33.01
Cu	8.046	0.2816	28.82	21.95	0.0	1.42
Ru	2.558	0.0080	0.92	0.44	0.0	1.43
O	0.523	0.0055	3.30	9.97	0.0	
Total		**1.0000**	**100.00**	**100.00**	**0.0**	**1.79**

Element	Gross (cps)	Z Corr	A Corr	F Corr
Ti	54.5	0.987	1.017	0.994
Cu	5.5	1.050	1.024	1.000
Ru	2.9	1.182	1.045	0.982
O	0.4	0.817	7.684	1.000
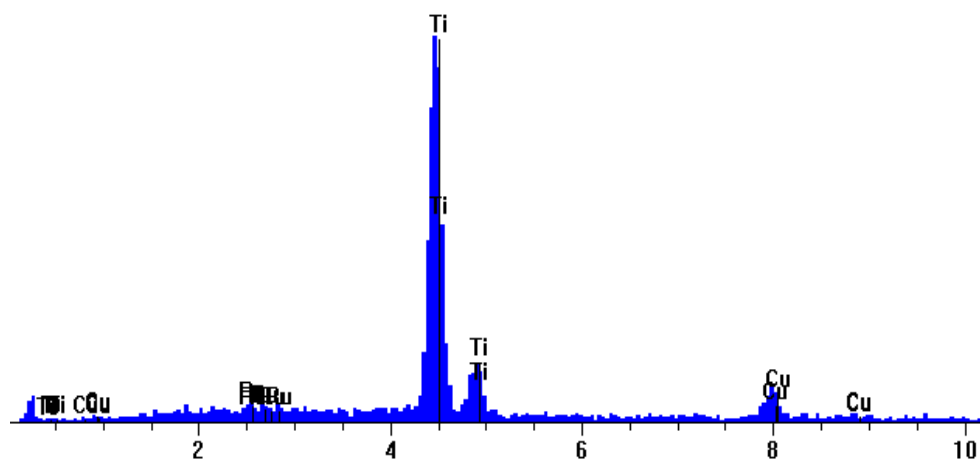
HIGH THROUGHPUT SCREENING PROCESS OF H$_2$ PRODUCTION MEASUREMENT

The procedure of hydrogen measurement was carried out as described in Chapter II. The experimental data is reported in appendix (B), under the following information:

Experiment	Run No.
NaHCO$_3$ under UV light	39
NaCl aqueous solution under UV light	
0.3%	33
0.7%	28
1.5%	31
2.5%	32
2.75%	34
3.5%	26
5.0%	35
7.0%	29
Iodide anions KI under UV light	40
Mv $^{+2}$ as electron relay under UV light	41
Pure water under UV light	27
Pure water under Sunlight	5, 12
Seawater under UV light	6
Seawater under Sunlight	11

Experiment	Run No.
Pure water only under UV light	30 (D)
Pure water only under Sunlight	42
(water + 0.175 g (3.5% wt of NaCl) only under UV light	52
Seawater only under UV light	*
Seawater only under sunlight	*
Methanol only under UV light	30 (C)
Methanol only under Sunlight	*

* Note: The runs are not conducted because the results obtained from runs 30 (D), 42, 52, 30 (C) show that there is no need to do it. Methanol, pure water, and seawater are not expected to generate hydrogen when they are used individually under either UV light or sunlight in the presence of same photocatalyst and same reaction conditions. Hydrogen can be only generated from the mixture of water/methanol or seawater/methanol solutions due to the nature of experimental set-up used here (single photoelectrochemical cell), which has no oxidation co-catalyst that used to stop oxygen production.

RESULTS AND DISCUSSION OF APPLICATION FOR H_2 PRODUCTION

The SEM micrographs revealed that the averaged size of individual Cu^{+2} and CuO/TiO_2 nanopowders is less than 100 nm. It also showed that the morphology of Cu^{+2} and CuO/TiO_2 nanopowders after annealing to 500°C appears as larger particles formed by aggregation process. The size of copper nanoparticles deposited on TiO_2 surface was not uniform. The EDS results presented in Table 3.1 showed the chemical analysis of the Cu^{+2} and CuO/TiO_2 nanopowders surface. The sample was coated with Ru element (by vapor coating) for better electron conductivity and better imaging.

H_2 Production of $NaHCO_3$ under UV

The main purpose of investigating adding $NaHCO_3$ to water/methanol solution is that it acts as oxidation agent, where carbonate species reacted with holes to form carbonate radicals, which is beneficial for photo-excited electron/hole separation. The results exhibited that the hydrogen production as 43.5 ± 2.0 µmol/h/g (Figure 3.6) and Table 3.2. The production is quit high if it compare with KI and MV^{+2} additives as will shown later in this section. This is means that hole-scavengers or electron donor additives as $NaHCO_3$ works better to reduce the recombination reaction of electron-hole pair. Trapping holes by get oxidized the strong oxidation agent is faster process and more efficient that trapping electrons on the metal surface or by electron accepter (relay).The elucidation of this phenomena can be explained by that the high energy of electron upon excitation need to be suppress with robust trapping step.

Table 3.2 Results and conditions of NaHCO$_3$ under UV.

H$_2$ production (µmol/h)	H$_2$ production (µmol/h/g)	Effective Area, m^2	Energy Efficiency % @ x=0	Energy Efficiency % @ x=0.7
2.17 ± 0.1	43.5 ± 2.0	0.00008	0.529	1.76

Additives type and weight (g)	Photo catalyst type and weight (g)	Nano-structure and geometry	Photocatalyst Size, composition, Crystal structure	Water/ Methanol solution (1:1) Volume basis	Light Intensity If UV, (100 W/m²) If Sunlight, ≈ (240 W/m²)
NaHCO$_3$ (0.0144)	Cu^{+2} & CuO/TiO$_2$ (0.05)	Nano-powders, Nano-composites	Cu (10 mol %, <50 nm), TiO$_2$ (<500nm, anatase)	10 ml (5 ml each)	UV
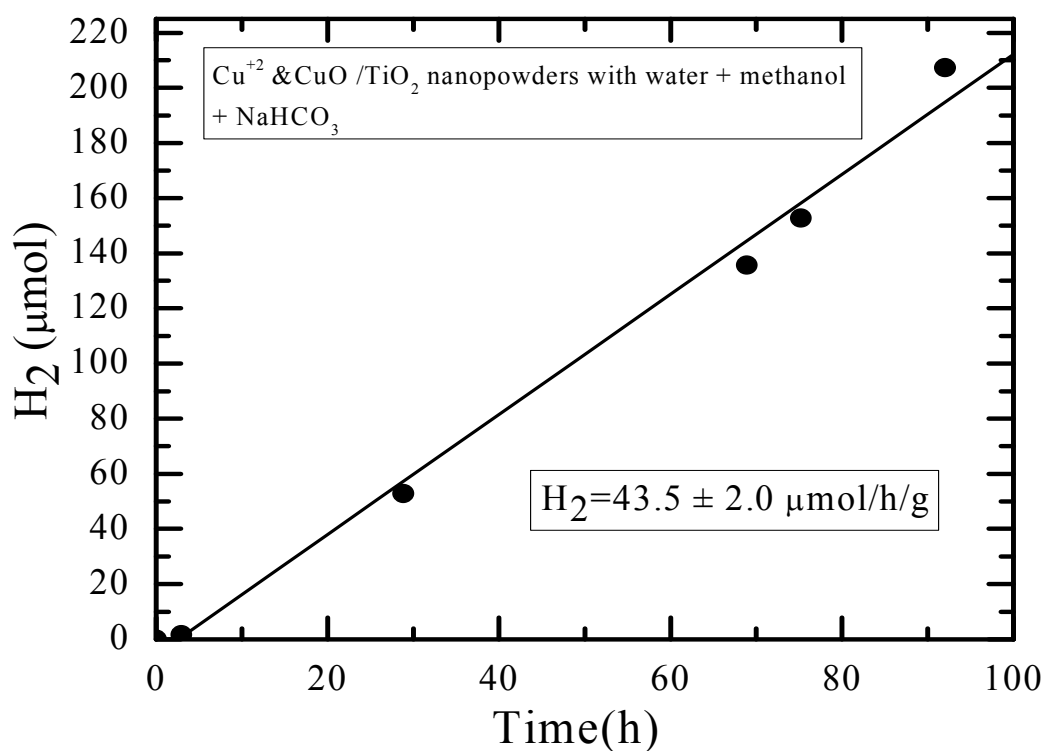
Figure 3.6 Hydrogen production rate after adding NaHCO$_3$.

H$_2$ Production of NaCl Aqueous Solution under UV (Ionic Strength Effect)

It is very important to study the effect of NaCl concentration on the performance of photocatalyst for hydrogen production because the ultimate goal of this technology is to split abundant and free seawater which is salty water. As main salt exist in seawater, NaCl weight % were varied and evaluated under same reaction conditions as mentioned in above procedures. It found that adding NaCl with 3.5% by weight to water under UV light is exhibited the highest hydrogen production rate among other values (Figures 3.7 and 3.8) and Table 3.3, (3.5% salt in water is the average value for world seas and oceans). Also there is no proportional relationship between NaCl weight % and hydrogen production rate, this is lead to conclude that NaCl has no effect on electrolyte pH value as expected (NaCl is neutral)   and no enhancement is expected for proton conductivity. However, the methanol aqueous solution is basic solution (pH > 7) and according to "Nernst equation", the surface potential charge: E ≈ 0.06 [*p*.z.c – pH] where *p*.z.c is point of zero charge, (for TiO$_2$ = 6, TiO$_2$ (calcined) = 3.2) and pH of solvent. If pH > *p*.z.c, surface is negatively charged and if pH < *p*.z.c, surface is positively charged. Therefore and based on catalyst and aqueous solution conditions, the surface potential of TiO$_2$ is negatively charged. By controlling the pH value of the solution, it can be controlling the surface potential charge, the electrical potential of solid surface, and also the aggregation process of nanoparticles. The impact of NaCl ionic strength on hydrogen production rate for the water/methanol mixture in the presence of Cu^{+2} and CuO/TiO$_2$ is in three ways. (1) Adsorption of Na$^+$ and Cl$^-$ ions. (2) Dissociation of surface charged species. (3) Physical adsorption of charged species.

Table 3.3 Results and conditions of adding different concentration of NaCl

NaCl Wt (g) /(Wt %)	H_2 production (μmol/h)	H_2 production (μmol/h/g)	Effective Area, m^2	Energy Efficiency % @ x=0	Energy Efficiency % @ x=0.7
(0.015)/(0.3)	5.22 ± 0.0016	26.1 ± 0.008	0.00008	1.27	4.24
(0.035)/(0.7)	6.27 ± 0.0019	31.35 ± 0.0095	0.00008	1.53	5.1
(0.075)/(1.5)	6.47 ± 0.001	32.38 ± 0.007	0.00008	1.57	5.26
(0.125)/(2.5)	4.89 ± 0.0015	24.48 ± 0.007	0.00008	1.19	3.97
(0.137)/(2.75)	5.069 ± 0.0014	25.3 ± 0.007	0.00008	1.23	4.12
(0.175)/(3.5)	12.66 ± 0.001	63.3 ± 0.0069	0.00008	3.089	10.29
(0.25)/(5)	5.61 ± 0.0018	28.06 ± 0.009	0.00008	1.36	4.56
(0.35)/(7)	11.91±0.001	59.56 ± 0.009	0.00008	2.9	9.68

Additives type	Photo catalyst type and weight (g)	Nano-structure and geometry	Photocatalyst Size, composition, Crystal structure	Water/ Methanol solution (1:1) Volume basis	Light Intensity If UV, (100 W/m^2) If Sunlight, ≈ (240 W/m^2)
NaCl (FW=58.44)	Cu^{+2} & CuO/TiO$_2$ (0.2)	Nano- powders, Nano-composites	Cu (10 mol %, <50 nm), TiO$_2$ (<500nm, anatase)	10 ml (5 ml each)	UV
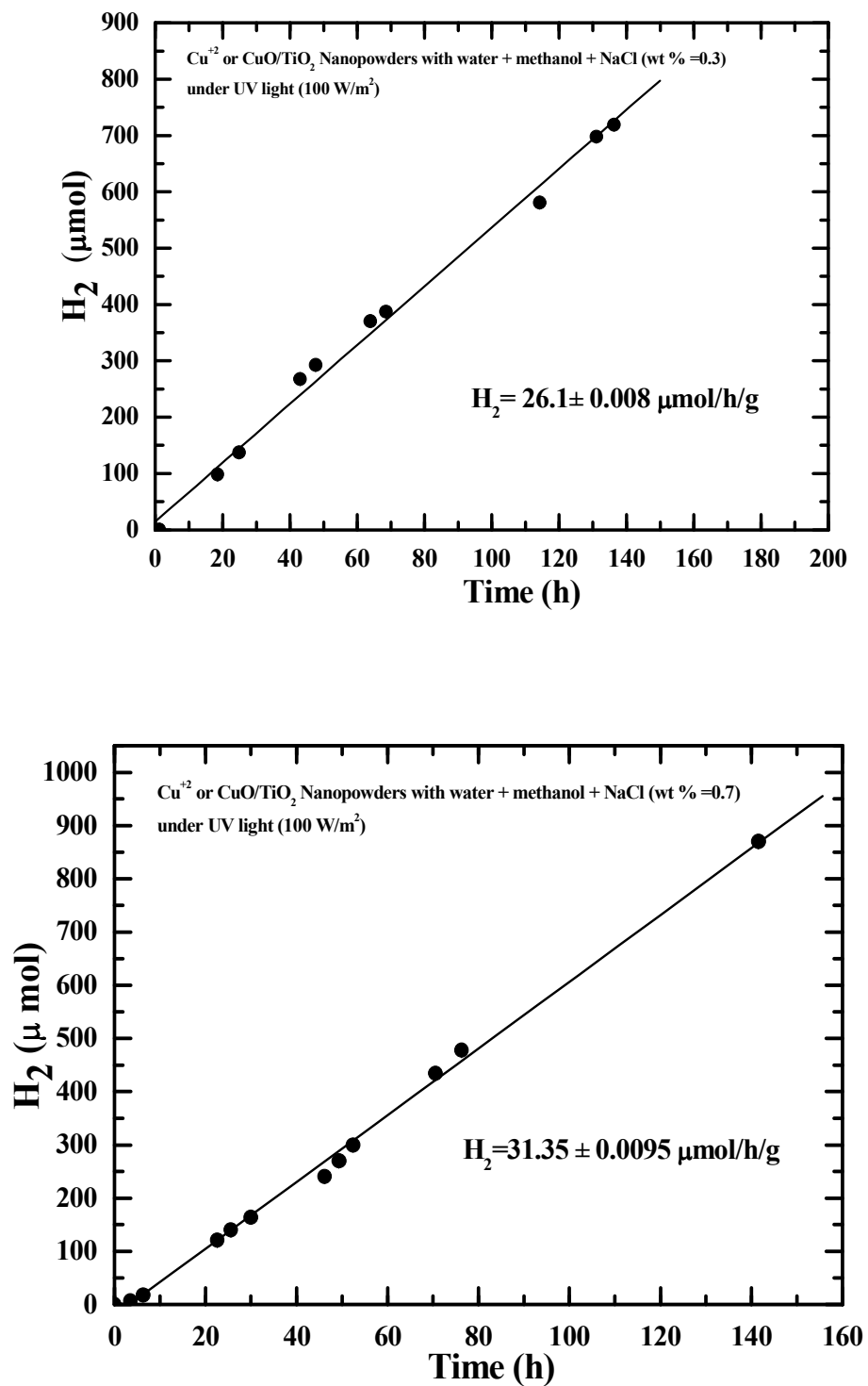
Figure 3.7 Hydrogen production rate after adding different NaCl (wt %) [0.3, 0.7, 1.5, 2.5, 2.75, 3.5, 5, 7], respectively.
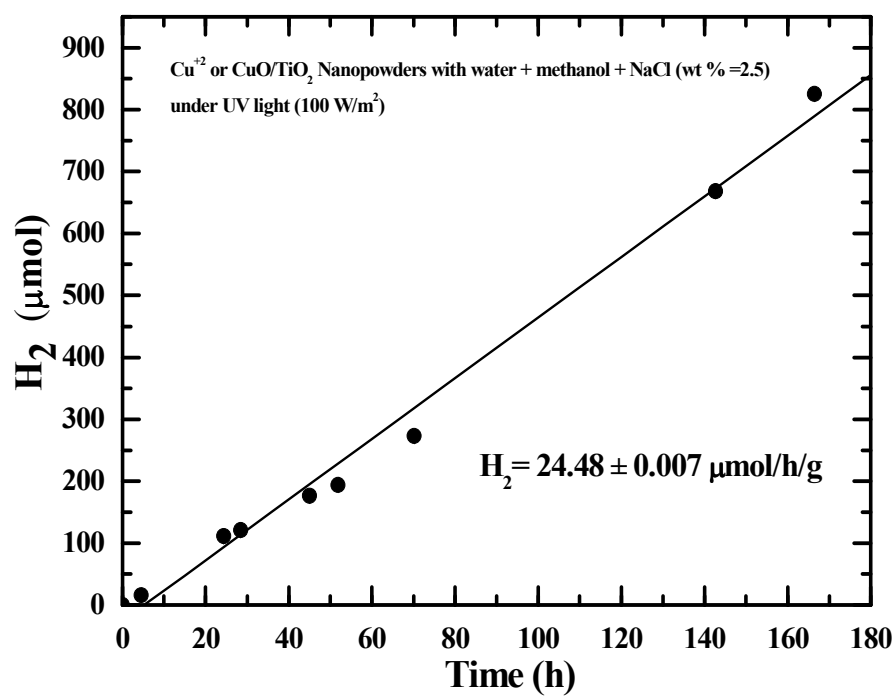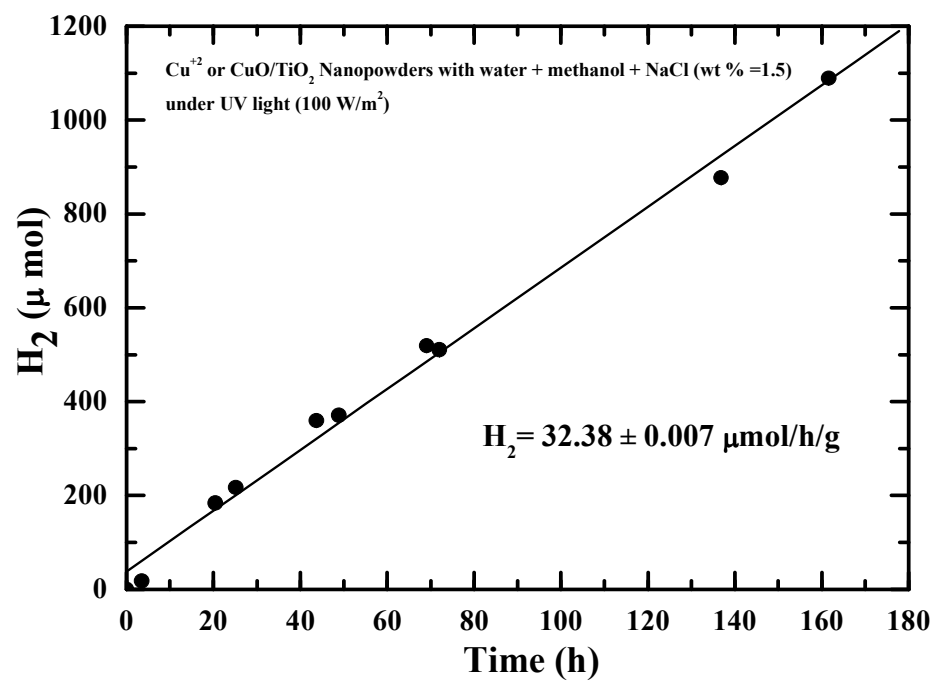
Figure 3.7 continued.
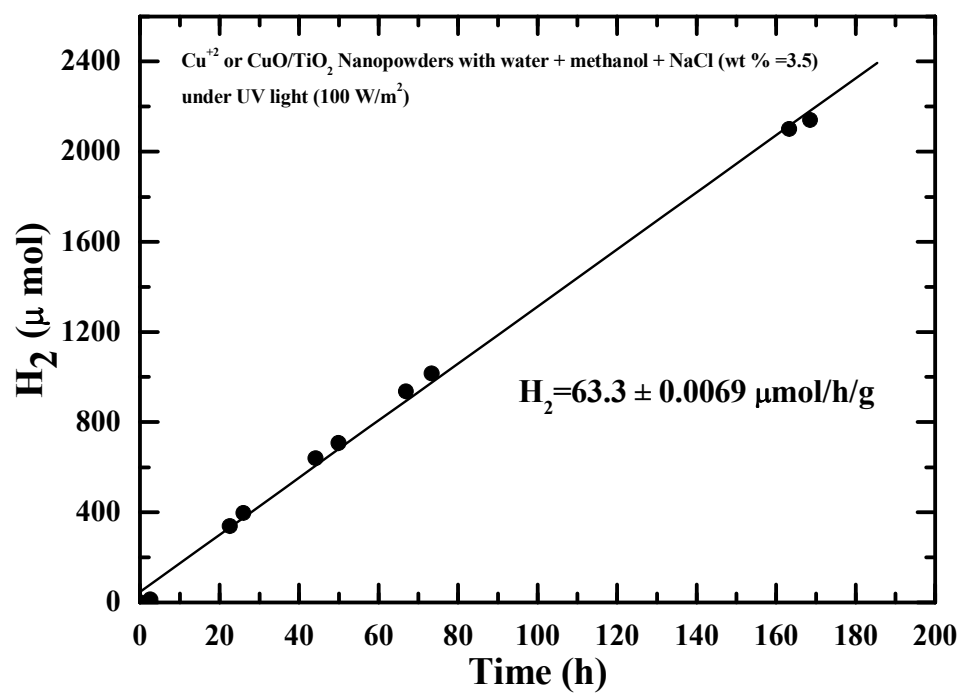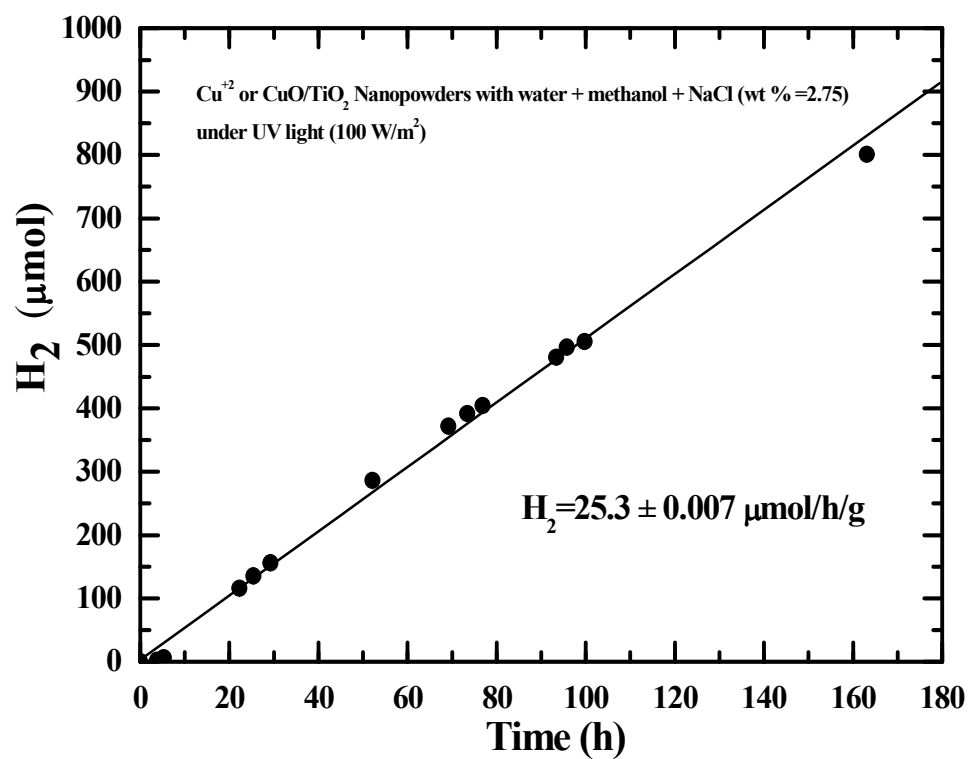
Figure 3.7 continued.
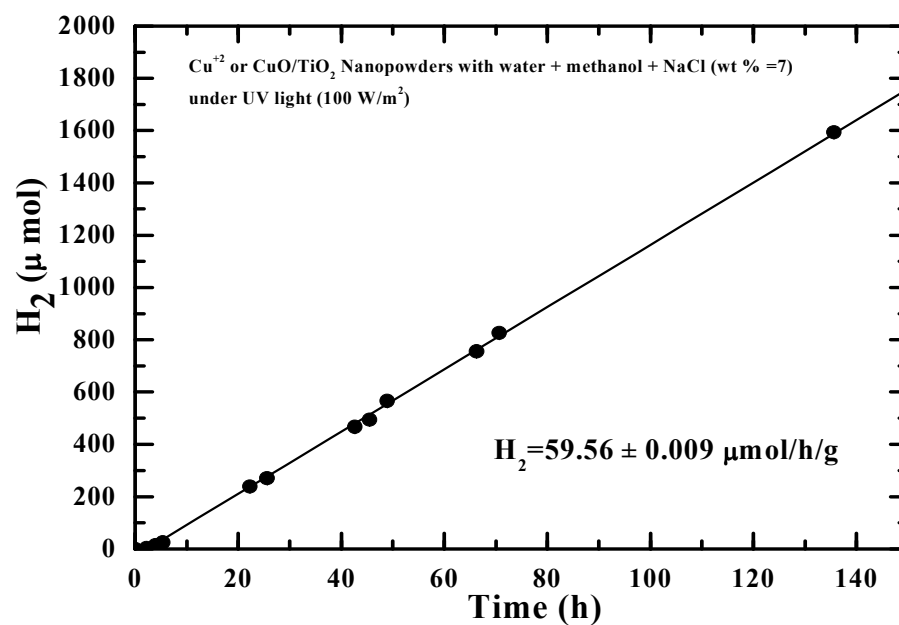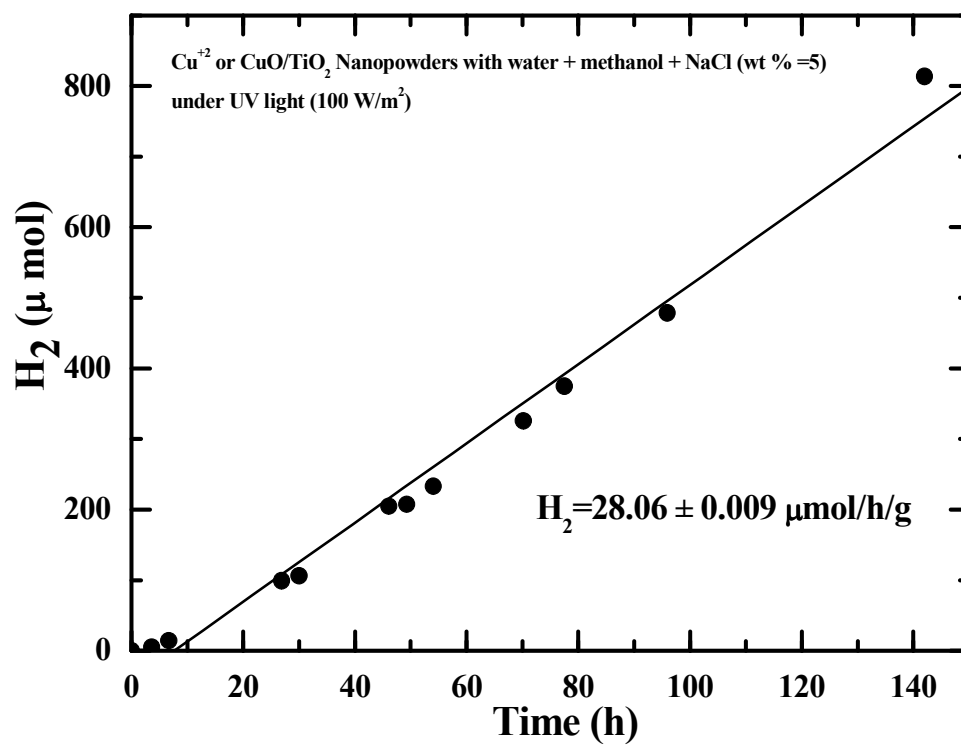
Figure 3.7 continued.
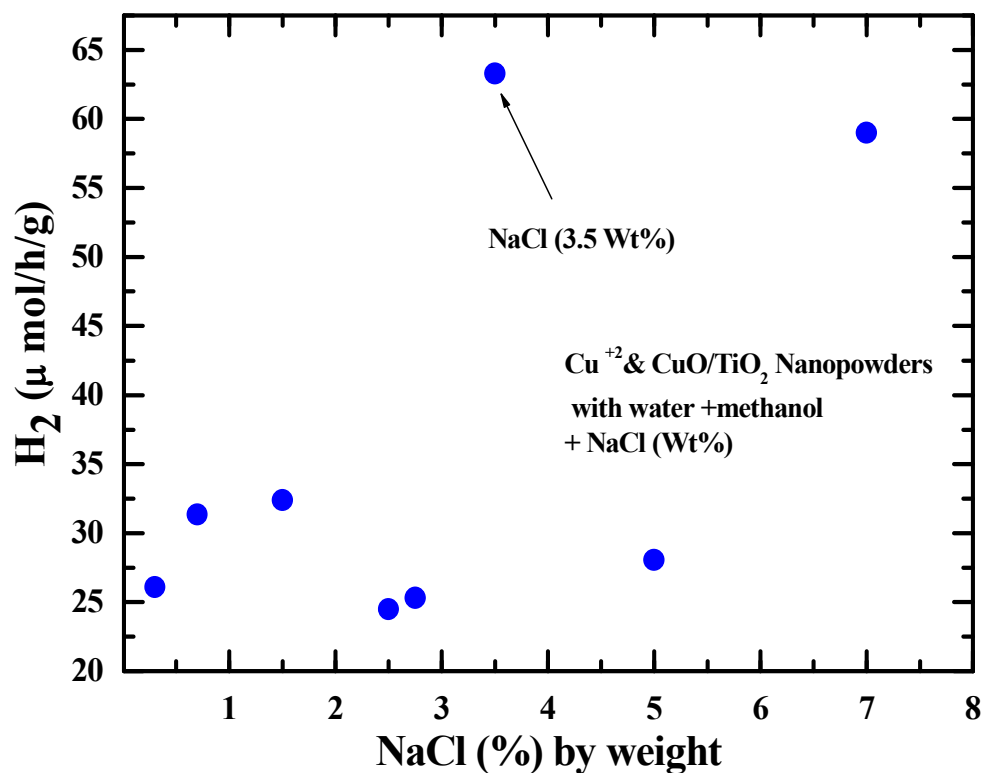
Figure 3.8 Hydrogen production corresponding to various NaCl (wt %).

H₂ Production of Iodide Anions KI under UV

Usually iodide anions as KI is added to electrolyte solution in order to suppress the backward reaction of hydrogen and oxygen produced into water molecular. In this experiment, oxygen was prevented from production by adding methanol as oxidation agent. But KI can be adsorbed preferentially onto metal surface, forming an iodine layer. The iodine layer can enhance the electron trap on the metal surface which reduces the recombination reaction of electron-hole reaction. In this case, the quantum efficiency will increase and lead to increase the energy efficiency. The result show that the

hydrogen production rate as 25.2 ± 2.8 μmol/h/g (Figure 3.9) and Table 3.4 which is higher than the result when adding Mv^{+2} as electron relay 16.38 ± 1.00 μmol/h/g as described in the next section. It implies that the iodine layer that formed on the metal surface is attached to photocatalyst nanocomposite and has direct impact than the suspended Mv^{+2} molecular. It facilitates the electron transfer on solid/solid and solid/liquid interfaces and enhances the properties by increase the electrical conductivity at interfaces sites.

Table 3.4 Results and conditions of using KI.

H_2 production (μmol/h)	H_2 production (μmol/h/g)	Effective Area, m^2	Energy Efficiency % @ x=0	Energy Efficiency % @ x=0.7
1.26 ± 0.14	25.2 ± 2.8	0.00008	0.307	1.02

Additives type and weight (g)	Photo catalyst type and weight (g)	Nano-structure and geometry	Photocatalyst Size , composition, Crystal structure	Water/ Methanol solution (1:1) Volume basis	Light Intensity If UV, (100 W/m²) If Sunlight , ≈(240 W/m²)
KI (0.0166)	Cu^{+2} & CuO/TiO$_2$ (0.05)	Nano- powders, Nano- composites	Cu (10 mol %, <50 nm), TiO$_2$ (<500nm, anatase)	10 ml (5 ml each)	UV
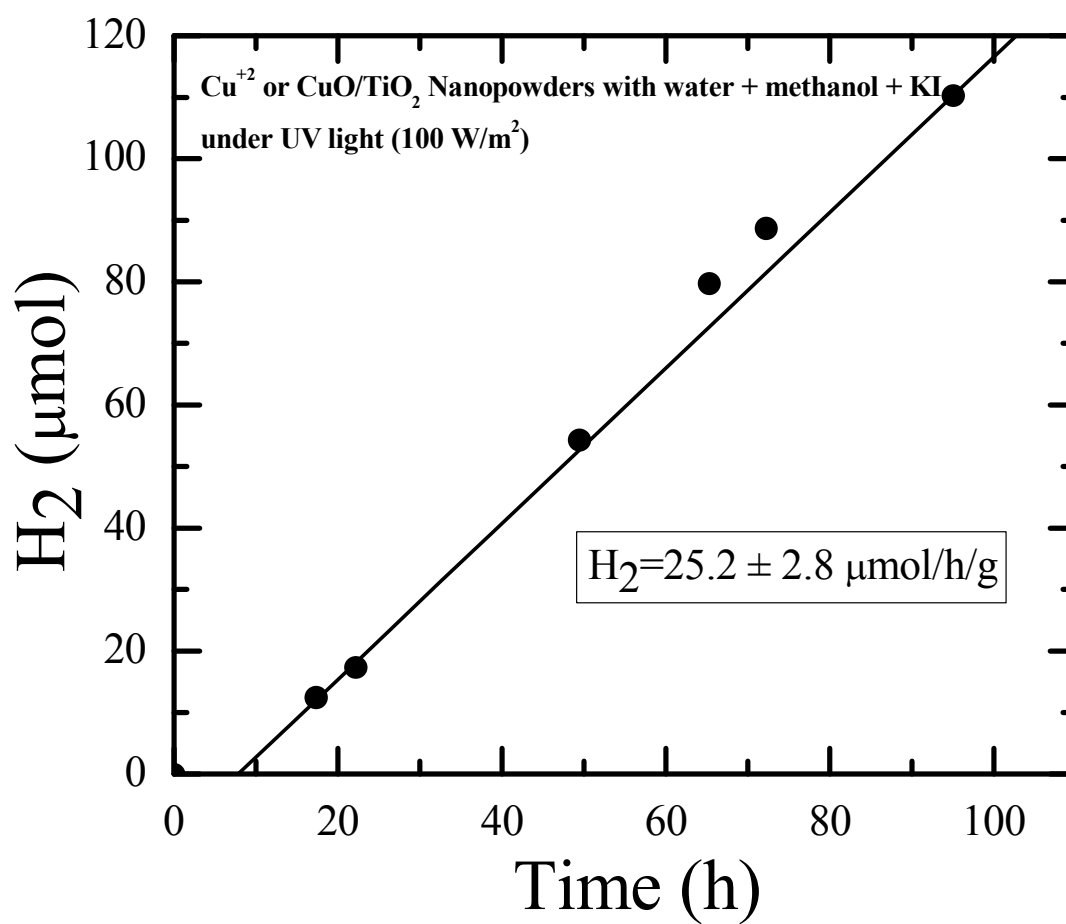
Figure 3.9 Hydrogen production rate after using KI in water/methanol solution.

H$_2$ Production of MV $^{+2}$ as Electron Relay under UV

Adding Mv^{+2} to water/methanol solution has positive impact by enhance the electrons transportation from TiO$_2$ surface to Cu surface which reduce the recombination reaction between electron-hole photogenerated. However, it could also have negative impact by adsorption on catalyst surface and block the site for light harvesting. This is will reduce the light absorption and quantum efficiency. The optimum concentration of Mv^{+2} should be used to avoid the negative impact and increase the chance for positive impact. By conducting several experiments of different Mv^{+2} concentrations, it can find the optimum value. Therefore, the concentration used in this work is based on literature review, the optimum value is 2.5e^{-5} mol/dm^{-3} of Mv^{+2} as electron relay [87] [45]. The hydrogen production rate was 16.38 ± 1.00 μmol/h/g (Figure 3.10) and Table 3.5. The result indicate that Mv^{+2} could not increase the hydrogen production because the electron relay added (Mv^{+2}) effect is not as fast as recombination reaction of electron-hole photogenerated. Also, the (Mv^{+2}) molecules diffusion through interface between the TiO$_2$ surface and Cu surface is not efficient enough due to the nature of Sol-gel synthesis method.

Table 3.5 Results and conditions of using Mv^{+2}.

H$_2$ production (μmol/h)	H$_2$ production (μmol/h/g)	Effective Area, m^2	Energy Efficiency % @ x=0	Energy Efficiency % @ x=0.7
0.508 ± 0.031	16.38 ± 1.00	0.00008	0.123	0.413

Additives type and weight (g)	Photo catalyst type and weight (g)	Nano-structure and geometry	Photocatalyst Size, composition, Crystal structure	Water/ Methanol solution (1:1) Volume basis	Light Intensity If UV, (100 W/m²) If Sunlight, ≈ (240 W/m²)
Mv^{+2} (0.027) Methyl viologen dichloride hydrate (FW=257.16)	Cu^{+2} & CuO/TiO$_2$ (0.031)	Nano-powders, Nano-composites	Cu (10 mol %, <50 nm), TiO$_2$ (<500nm, anatase)	10 ml (5 ml each)	UV
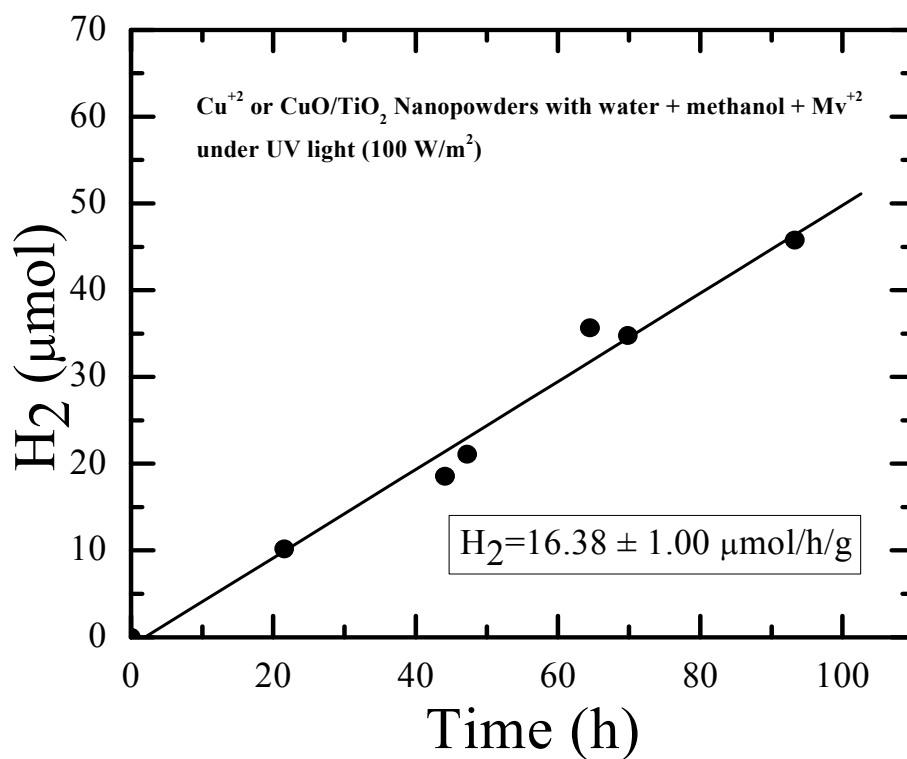
Figure 3.10 Hydrogen production rate of using Mv^{+2} in the water/methanol solution.

H₂ Production of Pure Water under UV and Sunlight

The performance of Cu^{+2} and CuO/TiO_2 photocatalyst to generate hydrogen from pure water/methanol solution was evaluated under both UV light $=100$ W/m^2, and sunlight $=240$ W/m^2. The hydrogen production rate of pure water/methanol solution under UV light was higher than the hydrogen production rate under sunlight (Figures 3.11, 3.12, and 3.13) (Tables 3.6, 3.7, and 3.8). This is attributed to the photocatalyst sensitivity and response to shorter wavelength photons (UV-region) better than response to longer wavelength photons (visible-region) due to large bang gap energy.

Table 3.6 Results and conditions of nanopowders Cu^{+2} and CuO/TiO_2 under UV light.

H₂ production (μmol/h)	H₂ production (μmol/h/g)	Effective Area, m²	Energy Efficiency % @ x=0	Energy Efficiency % @ x=0.7
12.57 ± 0.0022	62.8 ± 0.01	0.00008	3.06	10.22

Additives type and weight (g)	Photo catalyst type and weight (g)	Nano-structure and geometry	Photocatalyst Size, composition, Crystal structure	Water/ Methanol solution (1:1) Volume basis	Light Intensity If UV, (100 W/m²) If Sunlight, = (240 W/m²)
-	Cu⁺² & CuO/TiO₂ (0.2)	Nano-powders, Nano-composites	Cu (10 mol %, <50 nm), TiO₂ (<500nm, anatase)	10 ml (5 ml each)	UV

Figure 3.11 Hydrogen production rate of nanopowders Cu^{+2} and CuO/TiO_2 under UV light.
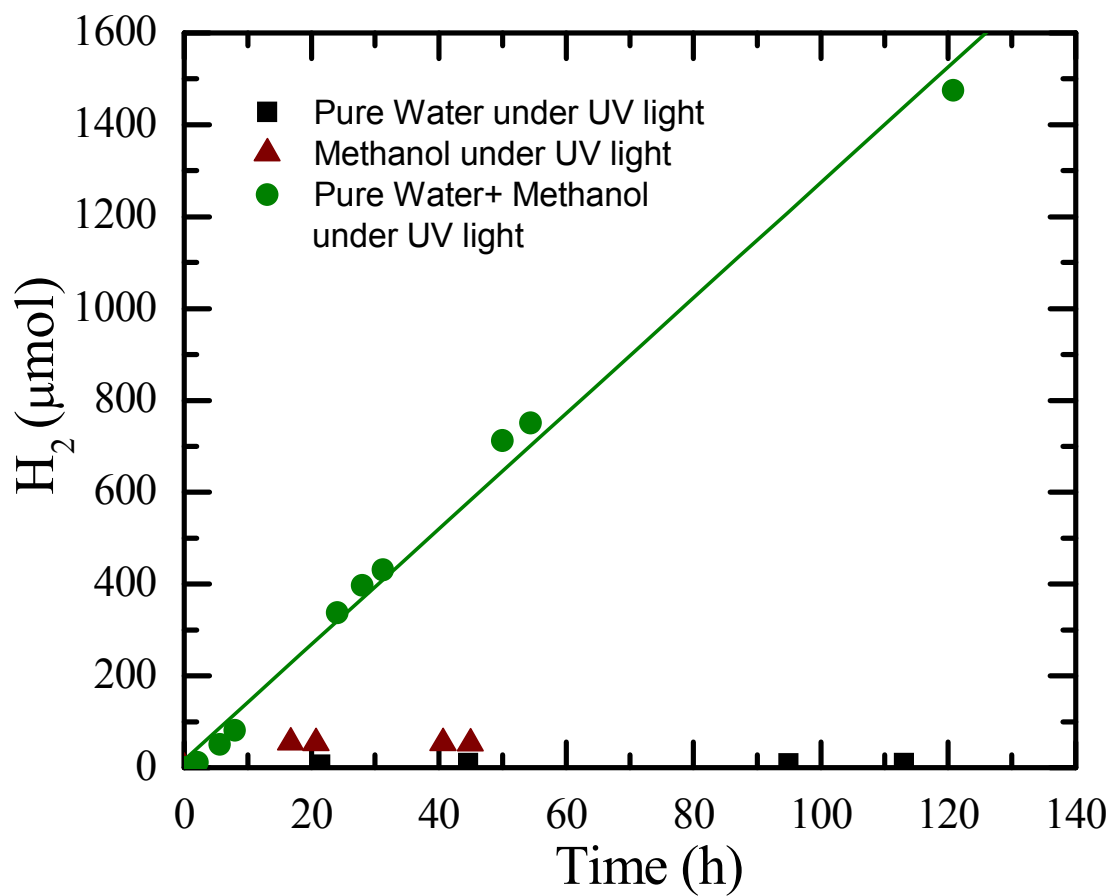
Figure 3.12 the effect of adding methanol on hydrogen production using Cu^{+2} and CuO/TiO_2 nanopowders under UV light.

Table 3.7 Results and conditions of nanopowders Cu^{+2} and CuO/TiO_2 under sunlight.

H_2 production (μmol/h)	H_2 production (μmol/h/g)	Effective Area, m^2	Energy Efficiency % @ x=0	Energy Efficiency % @ x=0.7
5.1 ± 0.12	24.88 ± 0.58	0.00008	0.51	1.72

Additives type and weight (g)	Photo catalyst type and weight (g)	Nano-structure and geometry	Photocatalyst Size , composition, Crystal structure	Water/ Methanol solution (1:1) Volume basis	Light Intensity If UV, (100 W/m²) If Sunlight , ≈ (240 W/m²)
-	Cu^{+2} & CuO/TiO_2 (0.205)	Nanopowders, Nanocomposites	Cu (10 mol %, <50 nm), TiO_2 (<500nm, anatase)	10 ml (5 ml each)	Sunlight (Texas, College Station, Latitude: 30.6277778 Longitude: -96.3341667)

Table 3.8 Results and conditions of nanopowders TiO_2 under sunlight.

H_2 production (μmol/h)	H_2 production (μmol/h/g)	Effective Area, m^2	Energy Efficiency % @ x=0	Energy Efficiency % @ x=0.7
0.097 ± 0.004	0.489 ± 0.024	0.00008	0.0098	0.03

Additives type and weight (g)	Photo catalyst type and weight (g)	Nano-structure and geometry	Photocatalyst Size , composition, Crystal structure	Water/ Methanol solution (1:1) Volume basis	Light Intensity If UV, (100 W/m²) If Sunlight , ≈ (240 W/m²)
-	TiO_2 (0.2)	Nanopowders	TiO_2 (<500nm, anatase)	10 ml (5 ml each)	Sunlight (Texas, College Station, Latitude: 30.6277778 Longitude: -96.3341667)
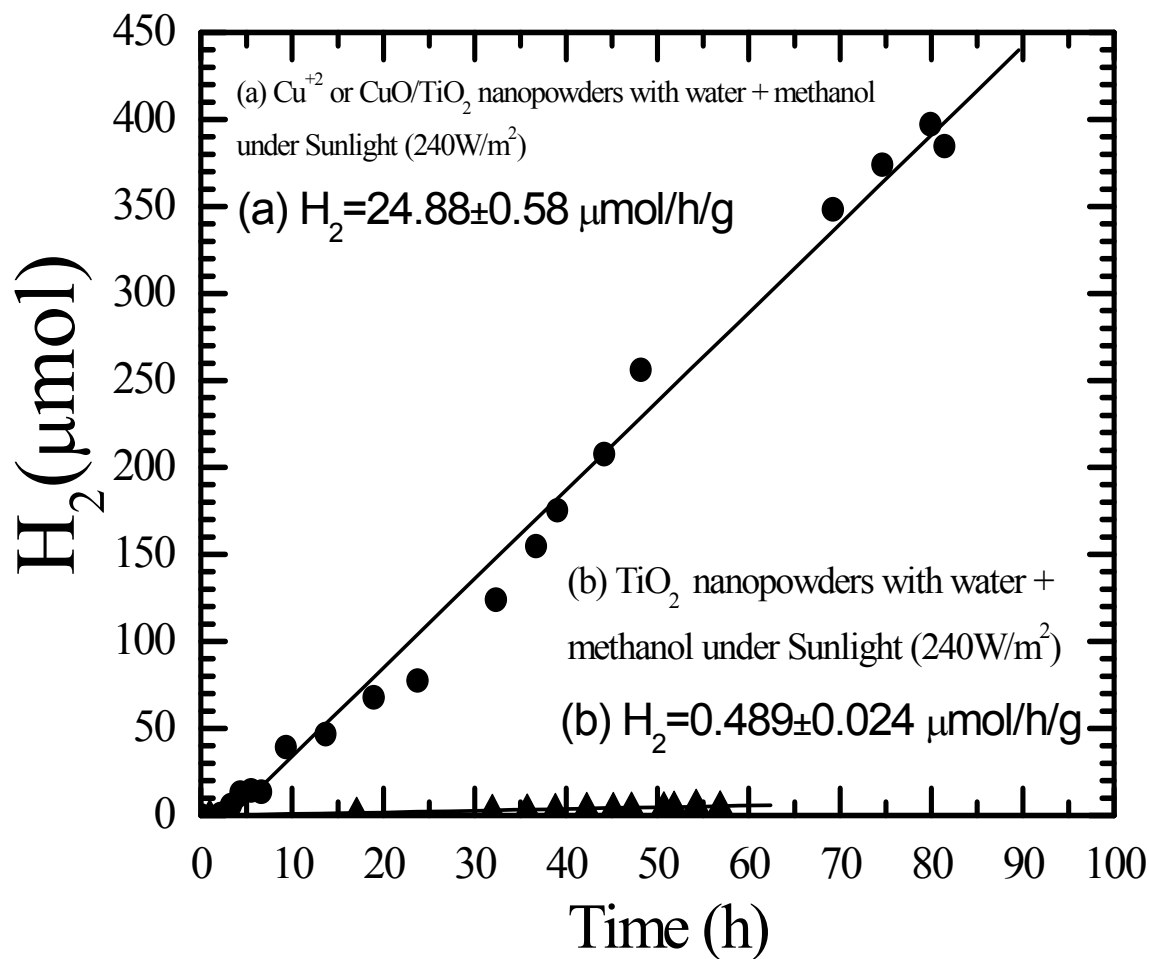
Figure 3.13 (a) Hydrogen production using nanopowders Cu^{+2} and CuO/TiO_2 under sunlight (circle). (b) Hydrogen production using nanopowders TiO_2 under sunlight (triangle)

H$_2$ Production of Seawater under UV and Sunlight

The seawater sample provided from Gulf of Mexico, (Galveston, Texas). The composition and salt concentration of this seawater is close to Atlantic Ocean. The performance of Cu^{+2} and CuO/TiO$_2$ photocatalyst to generate hydrogen from sea water/methanol solution was evaluated under both UV light =100 W/m^2, and sunlight = 240 W/m^2.

The hydrogen production rate of seawater/methanol solution under UV light was higher than the hydrogen production rate under sunlight (Figures 3.14 and 3.15) (Tables 3.9 and 3.10). This is attributed to the photocatalyst sensitivity and response to shorter wavelength photons (UV-region) better than response to longer wavelength photons (visible-region) due to large bang gap energy.

In addition, the higher activity of photocatalyst for pure water/methanol solution than for seawater/methanol solution in term of reactivity with methanol and generate hydrogen under both UV and sunlight is probably due to effect of pH value difference. The change in pH leads to change the surface charge potential and in results leads to change in electron transportation in solid/liquid (electrode-electrolyte interface). Some impurities are existed in seawater that might block the reactive site of TiO$_2$.

Table 3.9 Results and conditions of nanopowders Cu^{+2} and CuO/TiO_2 under UV light with seawater/methanol.

H_2 production (μmol/h)	H_2 production (μmol/h/g)	Effective Area, m^2	Energy Efficiency % @ x–0	Energy Efficiency % @ x–0.7
3.33 ± 0.13	16.65 ± 0.67	0.00008	0.81	2.7

Additives type and weight (g)	Photo catalyst type and weight (g)	Nano-structure and geometry	Photocatalyst Size, composition, Crystal structure	SeaWater/ Methanol solution (1:1) Volume basis	Light Intensity If UV, (100 W/m²) If Sunlight, ≈ (240 W/m²)
-	Cu^{+2} & CuO/TiO_2 (0.2)	Nanopowders, Nanocomposites	Cu (10 mol %, <50 nm), TiO_2 (<500nm, anatase)	10 ml (5 ml each) (Sea Water from Texas, Galveston; Gulf of Mexico)	UV

Figure 3.14 Hydrogen production using nanopowders Cu^{+2} and CuO/TiO_2 under UV light using seawater/methanol.

Table 3.10 Results and conditions of nanopowders Cu^{+2} and CuO/TiO_2 under sunlight with seawater/methanol.

H_2 production (μmol/h)	H_2 production (μmol/h/g)	Effective Area, m^2	Energy Efficiency % @ x=0	Energy Efficiency % @ x=0.7
0.54 ± 0.13	5.4 ± 1.3	0.00008	0.054	0.18

Additives type and weight (g)	Photo catalyst type and weight (g)	Nano-structure and geometry	Photocatalyst Size, composition, Crystal structure	Sea Water/ Methanol solution (1:1) Volume basis	Light Intensity If UV, (100 W/m²) If Sunlight, ≈ (240 W/m²)
-	Cu^{+2} & CuO/TiO_2 (0.1)	Nanopowders, Nanocomposites	Cu (10 mol %, <50 nm), TiO_2 (<500nm, anatase)	10 ml (5 ml each) (Sea Water from Texas, Galveston, Gulf of Mexico)	Sunlight (Texas, College Station, Latitude: 30.6277778 Longitude: -96.3341667)
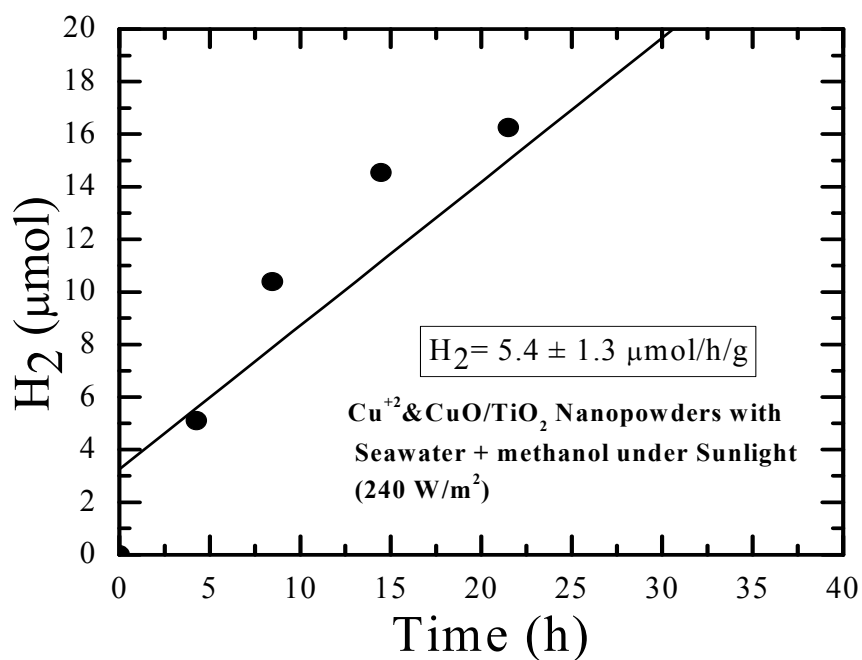
Figure 3.15 Hydrogen production using nanopowders Cu^{+2} and CuO/TiO_2 under sunlight using seawater/methanol.

CONCLUSIONS

In term of additives to equal volume of water/methanol solution under UV light using same photocatalyst (Cu^{+2} and CuO/TiO_2), the ranking based on highest hydrogen production is as follows: $NaHCO_3$ > NaCl (3.5 wt %) > KI > Mv^{+2}. The main conclusion from these results is that the hole-scavengers or oxidation agent works well in term of suppress the hole-electron recombination reaction that electron trapping by electron accepter or electron mediator. However, pure water/methanol solution under same reaction conditions without additives generate more hydrogen than the case of additives under UV light. The results indicate that the additives, in addition to their positive role to enhance hydrogen production, may also block the surface area available for reaction due to the nature of nanostructure photocatalyst. Under sunlight, pure water/methanol solution generates less hydrogen than under UV light due to low efficiency to harvest visible light from sunlight and more responses to shorter wavelength (UV-region). The hydrogen production rate of seawater/methanol solution is lower than the hydrogen production rate of pure water/methanol solution under same reaction conditions for both UV light and sunlight.

CHAPTER IV

BAND GAP AND DEFECT ENGINEERING BY NITROGEN

DOPING TO HARNESS VISIBLE LIGHT OF SOLAR ENERGY

OVERVIEW

To maximize the utilization of solar energy, the TiO_2 band gap must be reengineered to harness the longer wavelength of visible-light region that contribute to 50% of solar spectrum radiation [10]. Currently, TiO_2 is UV light sensitive and response to only about 4% of solar energy [10]. Several approaches have been reported to fine tuned the band gap and also shift the band edge positions. Nitrogen doping is known as effective approach to do the band gap engineering by introduced into crystal lattice of TiO_2 and replaced the Ti atoms with N atoms. Triethylamine (Et3N) is used to introduce nitrogen into TiO_2 nanoparticles by chemical bath deposition method. Copper metal nanoparticles also loaded into surface of TiO_2 using wet impregnation method.

A photocatalyst of $Cu/TiO_{2-x}.N_x$ showed remarkable improve to harness visible light and harvest longer wavelength. The photocatalyst is tested under sunlight for water/methanol solution and exhibited high hydrogen production rate (16.0 ± 1.8 μmol/h/g) than a photocatalyst tested under same UV light (0.81 ± 0.27 μmol/h/g). It implies that portions of visible light was absorbed and contributed to generate electron-hole pairs to do the redox reactions of water-splitting and methanol decomposition as well.

INTRODUCTION

Bearing in mind the fact that a solar cell generates electricity only during daytime, a new challenge emerges: for large-scale use, energy storage solutions are required. A practical way to overcome this problem is using sunlight to split water into hydrogen and oxygen by means of a photoelectrochemical (PEC) cell [90] This process is extremely attractive for several reasons. Firstly, this type of solar energy conversion alleviates the energy storage problem since hydrogen can be stored much more easily than electricity or even heat. Secondly, hydrogen produced from solar radiation is valuable as a potential fuel and energy carrier since it is non-polluting, renewable, inexhaustible and very flexible with respect to further conversion to other forms of energy, such as hydrocarbons. However, these devices achieve very low conversion efficiencies since most of the semiconductors used for this application have a large energy band gap [90]. Furthermore, the band edge potentials of many semiconductors are not suitable for oxygen and hydrogen evolution. In fact, for efficient water cleavage, the conduction band of the n-type semiconductor needs to be positioned at a more negative potential than the reduction potential of water, while the valence band needs to be positioned at a more positive potential than the oxidation reaction. No material was found up to date that can simultaneously and efficiently oxidize and reduce water without any external assistance. Tandem cell of two devices with semiconductors of different band gaps can be used.

Spectral region	Wavelength [nm]	Energy [eV]	Contribution to total spectrum [%]
near-UV	315–400	3.93–3.09	2.9
blue	400–510	3.09–2.42	14.6
green/yellow	510–610	2.42–2.03	16.0
red	610–700	2.03–1.77	13.8
near-IR	700–920	1.77–1.34	23.5
infrared	920–>1400	1.34–<0.88	29.4

Figure 4.1 Energy distribution in the solar spectrum (AM 1.5) [91].

For single photoelectrochemical cell, TiO_2 band gap should be with reengineer to harness visible light spectrum of sunlight (Figures 4.1 and 4.2) [92].
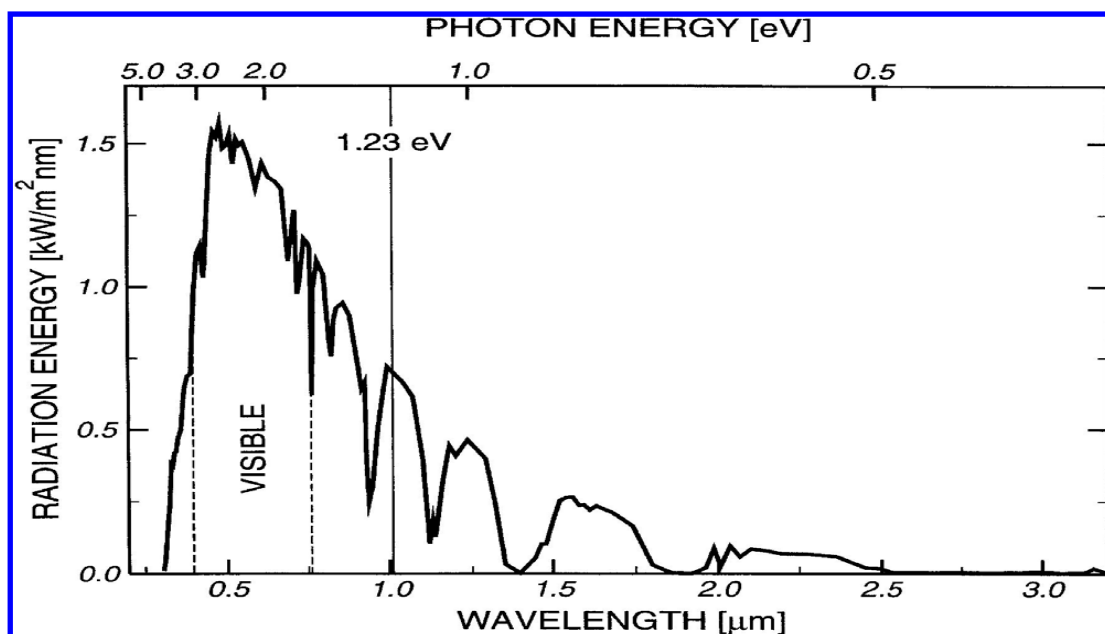
Figure 4.2 The optimum band gap required to harvest visible light and split water is 1.23 eV [30].

Band Gap and Defect Engineering with Redox Positions

The TiO_2 can be oxidized or reduced within a single phase leading to the formation or removal of point defects in the crystal lattice, such as: (1) Oxygen Vacancies: oxygen ion is missing from its lattice site. (2) Metal Vacancies: metal ion is missing from its lattice site. (3) Metal Interstitials: metal ion is located in an interstitial site. (4) Electrons: the $Ti3^+$ ions in their lattice sites. (5) Electron Holes: the O^- ions in their lattice sites [92]. Ionization of ionic defects leads to the formation of electronic defects (electrons and electron holes), which are responsible for the charge transport. It was shown that defect disorder is closely related to reactivity, photoreactivity, and the related charge transfer. It will be shown that the photocatalytic properties of nonstoichiometric compounds, such as TiO_2, are dependent on defect disorder in much greater extent than the commonly studied properties, such as crystal structure and surface area [92].
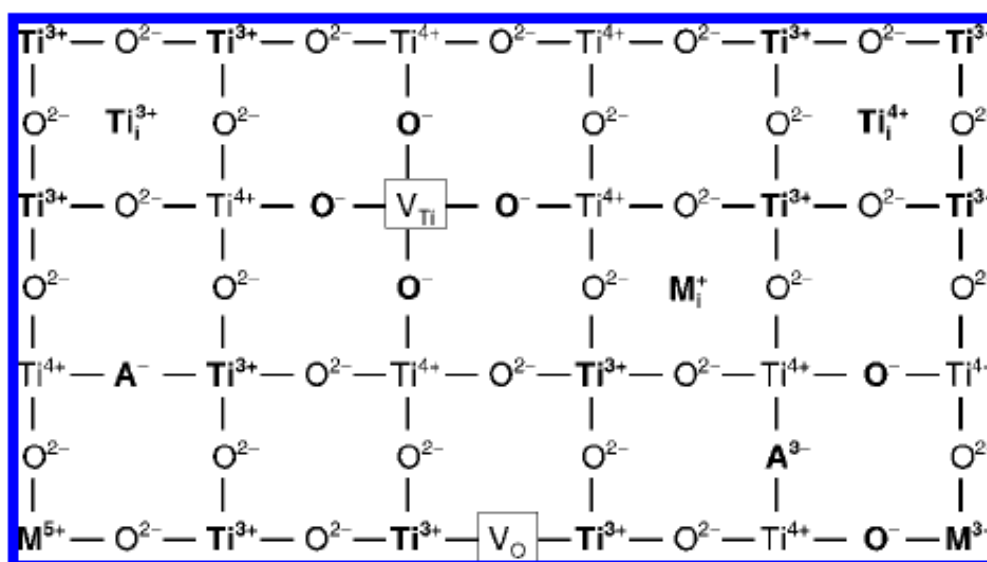
Figure 4.3 Schematic represent the defected lattice of TiO_2 [92].

TiO_2 may exhibit both n-type and p-type properties. Its defect disorder and defect-related properties are closely related to oxygen activity in the TiO_2 lattice (Figure 4.3). Titanium vacancies have a strong effect on properties of titanium dioxide. These defects form surface active sites for water splitting. Recent studies have shown that nanosize TiO_2 exhibits much larger concentrations of these defects than that in the bulk phase. Defect disorder diagrams may be used for the processing of TiO_2 with controlled properties that are desired for specific performance. The concept of defect engineering is based on the imposition of desired properties by controlled combination of the concentrations of lattice species, which are a function of the following variables: (1) Temperature (2) Oxygen activity (3) Concentration of aliovalent ions. The reactivity and photoreactivity of TiO_2-based oxide semiconductors and related photocatalytic properties are determined by defect disorder. The development of high performance photocatalysts for water splitting and water purification requires that both collective and local factors are taken into account. The latter factor is determined by defect disorder of the outermost surface layer.

For comparison purpose, the introduction of nitrogen in crystal lattice of ZnO will result in an intermediate energy level in the band gap, and reduce the absorption energy. Nitrogen doping in n-type ZnO film have shown a significant red shift in light absorption wavelength. In addition, the typical electron mobility in ZnO is 10-100 folds higher than TiO_2 leading to reduced electrical resistance and enhanced electron transfer efficiency. However, TiO_2 still is promising because of high stability, high efficiency and low cost [93].

Metal Ion and Anion Doping Effect on Surface

A small amount of doping with different metal ions converts inactive chemical compounds to be photocatalytically active for water splitting although some dopant effect on the photocatalytic performance has been limited. The photocatalytic activity for overall water splitting is not known yet for the transition-metal and typical-metal oxides, rare-earth-metal oxides As for metal nitrides, GaN is inactive, but doping with a small amount of divalent metal ions change it to have remarkably high activity [10]. It is also found that metal ions doping could expand the photo-response of TiO_2 into visible spectrum by incorporate into TiO_2 lattice and the impurity energy levels in the band gap of TiO_2 are formed. For photocatalytic reactions, carrier transferring is as important as carrier trapping. Only if the trapped electron and hole are transferred to the surface, photocatalytic reactions can occur. Therefore, metal ions should be doped near the surface of TiO_2 particles for a better charge transferring. In case of deep doping, metal ions likely behave as recombination centers, since electron/hole transferring to the interface is more difficult. Metal ion-implantation was recently reported to be an effective method to modify semiconductor electronic structures to improve visible light response when TiO_2 is bombarded with high energy transitional metal ions (accelerated by high voltage), these high-energy ions are injected into the lattice and interact with TiO_2 [45].

The reported effects of doping with aliovalent ions include both cations and anions. For cations, in most cases doping aims at the incorporation into the TiO_2 lattice of cations with a valency larger or lower than that of $Ti4^+$ leading to the formation of

donors, such as Nb and Ta, and acceptors, such as Cr and Fe, respectively. For anions, incorporation of TiO_2 lattice by nitrogen. The reported TiO_2 doping procedures with nitrogen include sputtering, annealing (in N-containing gas phase), sol-gel technique, and implantation [92]. The latter process leads to the destruction of the lattice and, therefore, subsequent annealing is required. The effect of this kind of doping on properties depends on the surface coverage, the size of particles, and the nature of the interface formed between these particles and the TiO_2 grain.

For the effect of doping, the incorporation of aliovalent ions into the TiO_2 lattice results in the formation of donor- and acceptor type levels. The energy levels of several transition-metal ions in TiO_2 are shown in (Figure 4.4). For the effect on band gap, doping results in changes of electronic structure, leading to the formation of donor and acceptor levels as is shown in (Figure 4.4) [92].

For the effect of impurities, the properties of different TiO_2 specimens may be compared only when the effect of impurities may be ignored (or is comparable). The selection of doping conditions (temperature and time) should be based on the knowledge of the diffusion data. The procedure of doping is well-defined when leading to the formation of a solid solution, which is equilibrated in the gas phase of controlled oxygen activity [92]. When doping aims at the imposition of concentration gradients, the doping process leads to reproducible effects only when the applied doping procedure is reproducible. Doping frequently leads to the formation of precipitates of other phases. Their properties may differ entirely from a solid solution. Therefore, correct assessment of the effect of doping requires that their presence, if any, is identified [92].
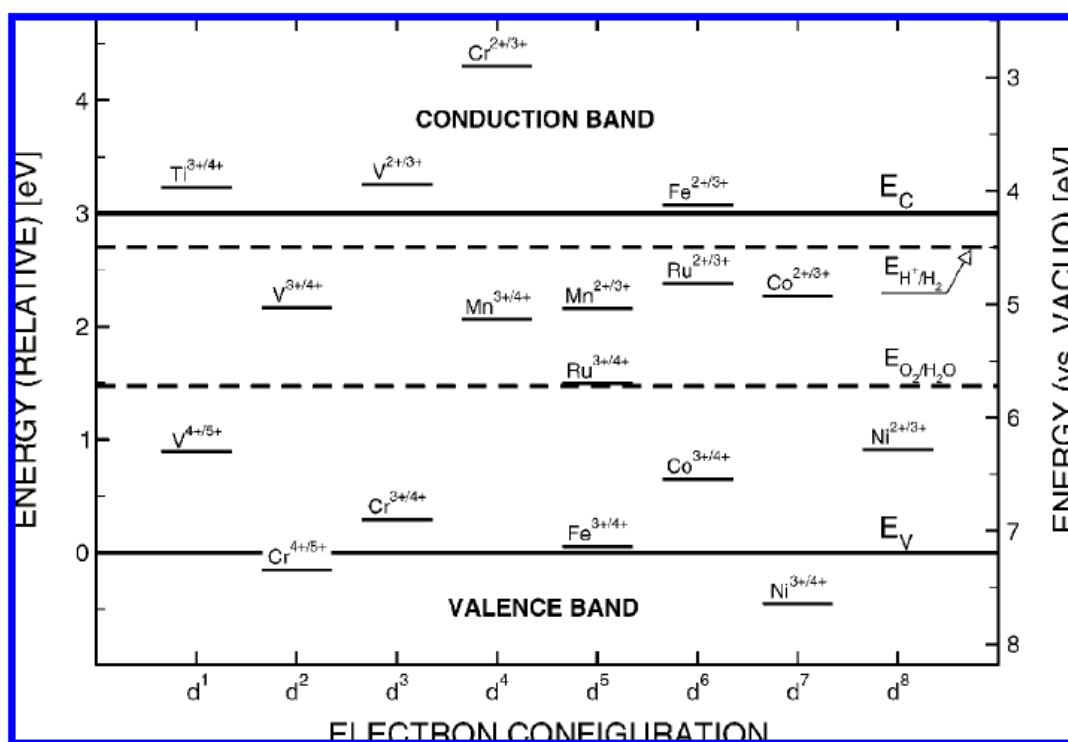
Figure 4.4 Electronic structure of TiO$_2$ showing energy levels of different ions [92].

It is essential that the standards are well-defined in terms of their solid-state chemistry related properties, which have an impact on photocatalytic properties, such as: (1) Structure (2) Microstructure (surface area, grain size, density, porosity) (3) Processing conditions: (a) Temperature and time of annealing (b) Oxygen activity of the gas phase during the annealing (c) Conditions of cooling (4) Composition (a) Nonstoichiometry (b) Impurity level (c) Dopant level and its distribution (5) Defect-related properties, such as electrical conductivity (6) Surface properties (7) Photocatalytic activity in selected reactions [92].

For Nitrogen doping, it is found that introducing nitrogen in the titanium crystal lattice will lead to overlap the orbitals of O_2p and N_3d. The electronic confinement changes narrowing the band gap of TiO_2. Several technique used for nitrogen incorporation, in this study, simple and fast method used for nitrogen doping of TiO_2 film using triethylamine dip coating method. On other hand, the photocathode or metal doping using photo-electron reduction is used to embed silver on photoanode surface. Anatase TiO_2 film prepared based on previous procedure mentioned earlier in first objective. To investigate the effect of nitrogen doping on the absorption properties of TiO_2, the samples prepared should be characterized to test the morphology, size, structure, chemical compositions, and crystal structure, then, tested for hydrogen production from water/methanol solution under UV light and sunlight.

DESIGN AND SYNTHESIS

The typical synthesis method is reported by [46] [52] and it is used here. The Synthesis of $Cu/TiO_{2-x}.N_x$ nanoparticles and image of solutions prepared are exhibited on (Figure 4.5). The result will significantly confirm that such a combination of two or three strategy of photocatalyst synthesis could be efficiently works to split water under solar energy. In contrast, without nitrogen doping, the TiO_2 still active to absorb and convert UV spectrum of sunlight to electrical and then to chemical energy and the QD'S play the key role of visible spectrum absorption. From comparing the results of hydrogen production rate for both photocatalysts, one can investigate functions of each composite in solar energy harvesting and catalyze the water-splitting reactions. For electron

transportation, the probability of electron-hole separation may change in both of them due to change in the overall quantum efficiency.

TiO$_2$ Nanocolloides and Nanoparticles

A 5 ml aliquot of TTIP (Sigma Aldrich), dissolved in isopropyl alcohol (0.5:9.5 volume ratio), was added dropwise (1 ml/min) to 90 ml of distilled water at pH= 2 (adjusted with HNO$_3$). A clear TiO$_2$ nanocolloid solution is generated after continuous stirring of this mixture for 12 hours [46][52]. Extended exposure of the colloid solutions to air at room temperature or heating to 50 °C produces an agglomeration of the TiO$_2$ nanoparticles and results in the formation of a gel that can range from transparent to virtually opaque as the function of an increasing nanoparticle size distribution [46][52].

TiO$_{2-x}$.N$_x$ Nanocolloids Suspensions

Both an initial nanoparticle colloidal solution and a partially agglomerated gel (solution) have been nitriding the TiO$_2$ nanocolloid to TiO$_{2-x}$.N$_x$. This experiment has been done by involving the direct exposure of the nanocolloid to an alkylammonium salt. 5 ml was placed of the TiO$_2$ nanocolloid solution or (0.5 g) of the TiO$_2$ nanoparticles into a 25 ml beaker. As the colloidal solution is mixed with a Teflon-coated magnetic stirrer, an excess of Triethylamine (Fluka) is added, bringing the total solution volume to 15 ml. The agglomerated gel is also can be treated directly with the amine, creating a less viscous solution that is thoroughly stirred. Reaction to form a nitrided TiO$_{2-x}$.N$_x$ nanocolloid suspension is seen to take place in seconds coincidental with heat release [46][52].

Cu/TiO$_{2-x}$N$_x$ Nanocrystals

The TiO$_{2-x}$.N$_x$ nanocolloid solution, after direct treatment with triethylamine (Et3N) forms a yellowish, partially opaque mixture. Upon evaporation of the Et3N, with continued stirring of the solution. Then the solution was centrifuged to separate organic layer from inorganic layer and followed by vacuum-drying at 62 Torr for several hours, the dried, treated, mixture forms deep yellow crystallites [94]. The copper is loaded into TiO$_{2-x}$.N$_x$ nanocolloid using conventional wet impregnation by using 0.1 M of Cu (NO$_3$)$_2$.2.5H$_2$O aqueous solution (water volume is 5 ml, Cu loading is 3% by weight). After mixing TiO$_{2-x}$.N$_X$ solution with copper precursor by stirring, the sample heated at 80°C for 12 hours. Finally, the sample is annealed at 500°C for 5 hours to form the anatase crystal phase of Cu/TiO$_{2-x}$.N$_X$ nanocrystals [94] [74] [85].
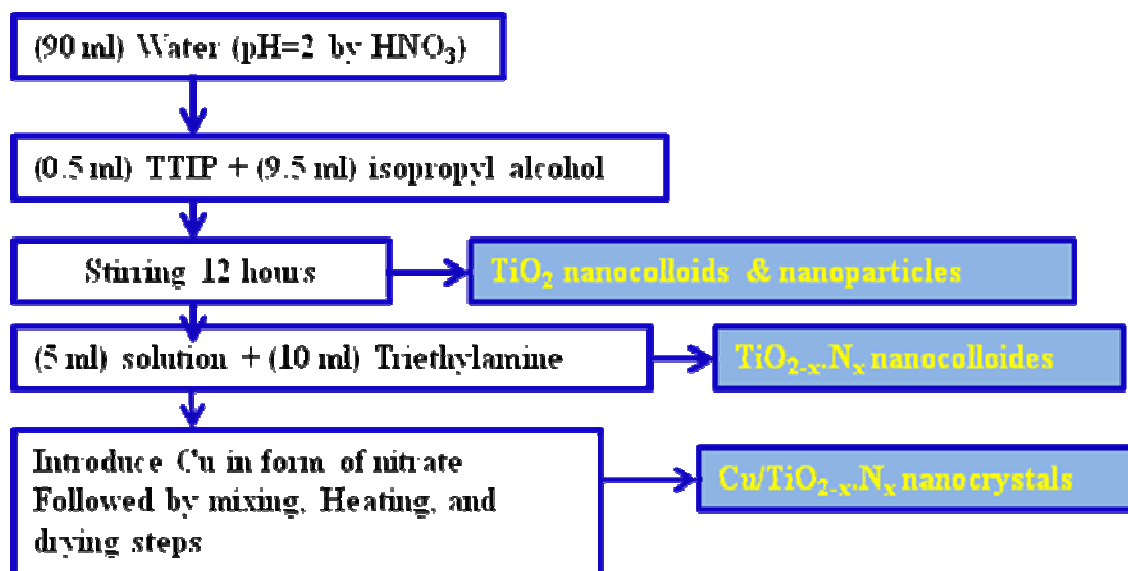
Figure 4.5 Synthesis method of Cu/TiO$_{2-x}$.N$_x$.nanoparticles expected to exhibits a high hydrogen production under sunlight by changing the electron confinement in TiO$_2$ lattice crystal structure which enhances the absorption and optical properties of TiO$_2$ [94].

CHARACTERIZATION

After synthesis, the TiO_2, $TiO_{2-x}.N_x$, $Cu/TiO_{2-x}.N_x$ nanocrystals were characterized using Scanning Electron Microscopy (SEM) (Figure 4.6). The SEM images were taken using JEOL JSM-6400. The Surface element analysis was obtained using Energy dispersive X-ray spectroscopy (EDS) as shown in Table 4.1. The EDS results were obtained using JEOL JSM-6400. Figure 4.7 showed the UV-visible spectra of $Cu/TiO_{2-x}.N_x$ nanocrystals measured by UV-vis-NIR spectrophotometer. In addition, images were taken using digital camera for the solutions prepared of TiO_2 nanocolloids, and after nitrogen-doping, and after copper loading (Figure 4.8).
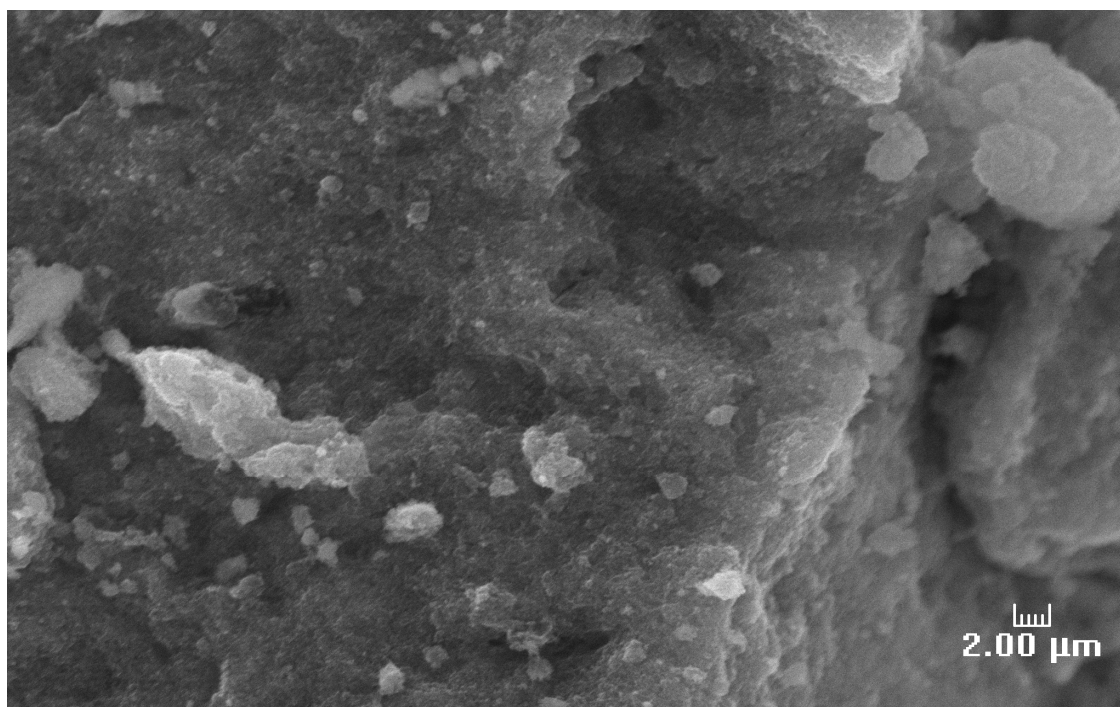
Figure 4.6 SEM image of $Cu/TiO_{2-x}.N_x$ nanocrystals.

Table 4.1 Surface element analysis of $Cu/TiO_{2-x}.N_x$ nanocrystals using EDS.

Element	keV	KRatio	Wt%	At%	At Prop	ChiSquared
Ti	4.510	0.0525	5.02	6.57	0.0	16.07
Cu	8.046	0.9199	91.23	90.02	0.0	1.89
Ru	2.558	0.0262	3.44	2.13	0.0	4.18
O	0.523	0.0010	0.21	0.83	0.0	7.08
N	0.392	0.0004	0.10	0.44	0.0	
Total		**1.0000**	**100.00**	**100.00**	**0.0**	**2.13**

Element	Gross (cps)	Z Corr	A Corr	F Corr
Ti	21.6	0.939	1.054	0.978
Cu	67.7	1.001	1.003	1.000
Ru	11.1	1.122	1.183	0.999
O	0.5	0.774	2.695	0.997
N	0.5	0.760	3.476	0.999
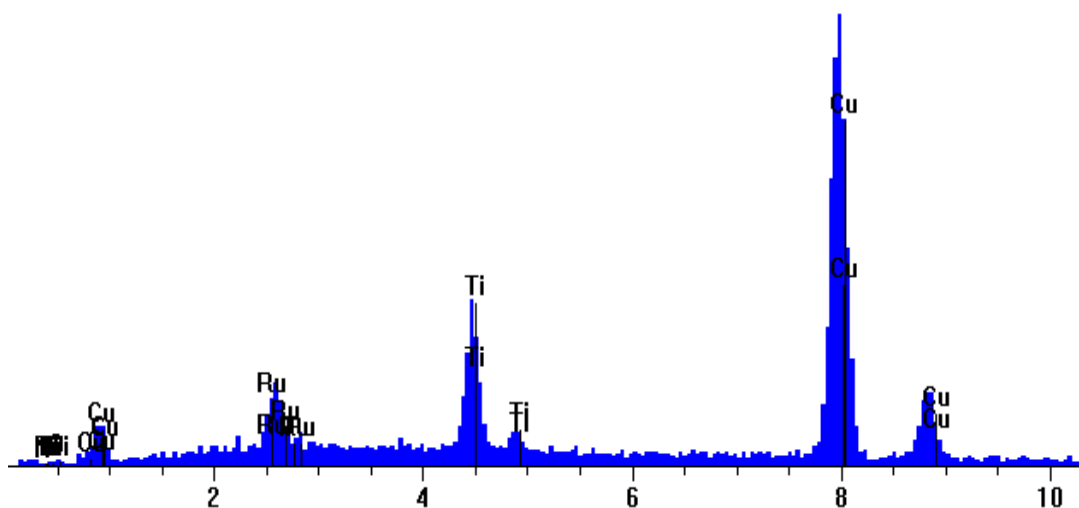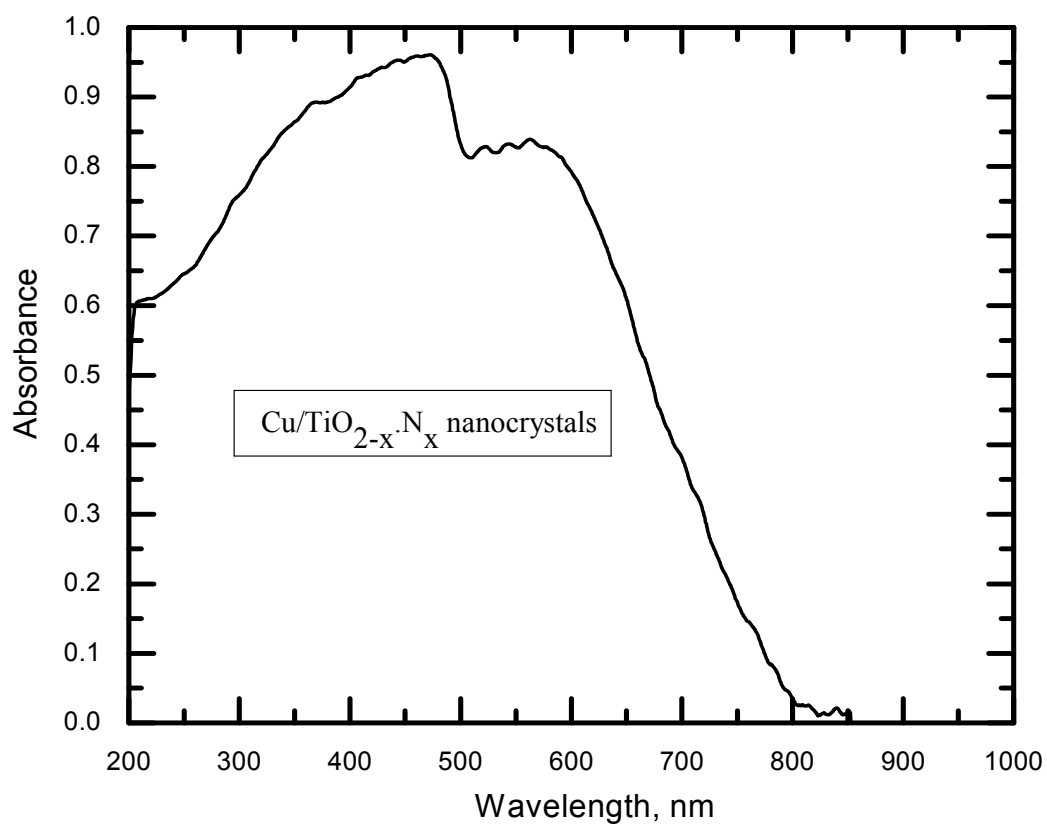
Figure 4.7 The UV-visible spectra of $Cu/TiO_{2-x}.N_x$ show that the absorption and optical properties enhanced to harvest the longer wavelength (visible light region).
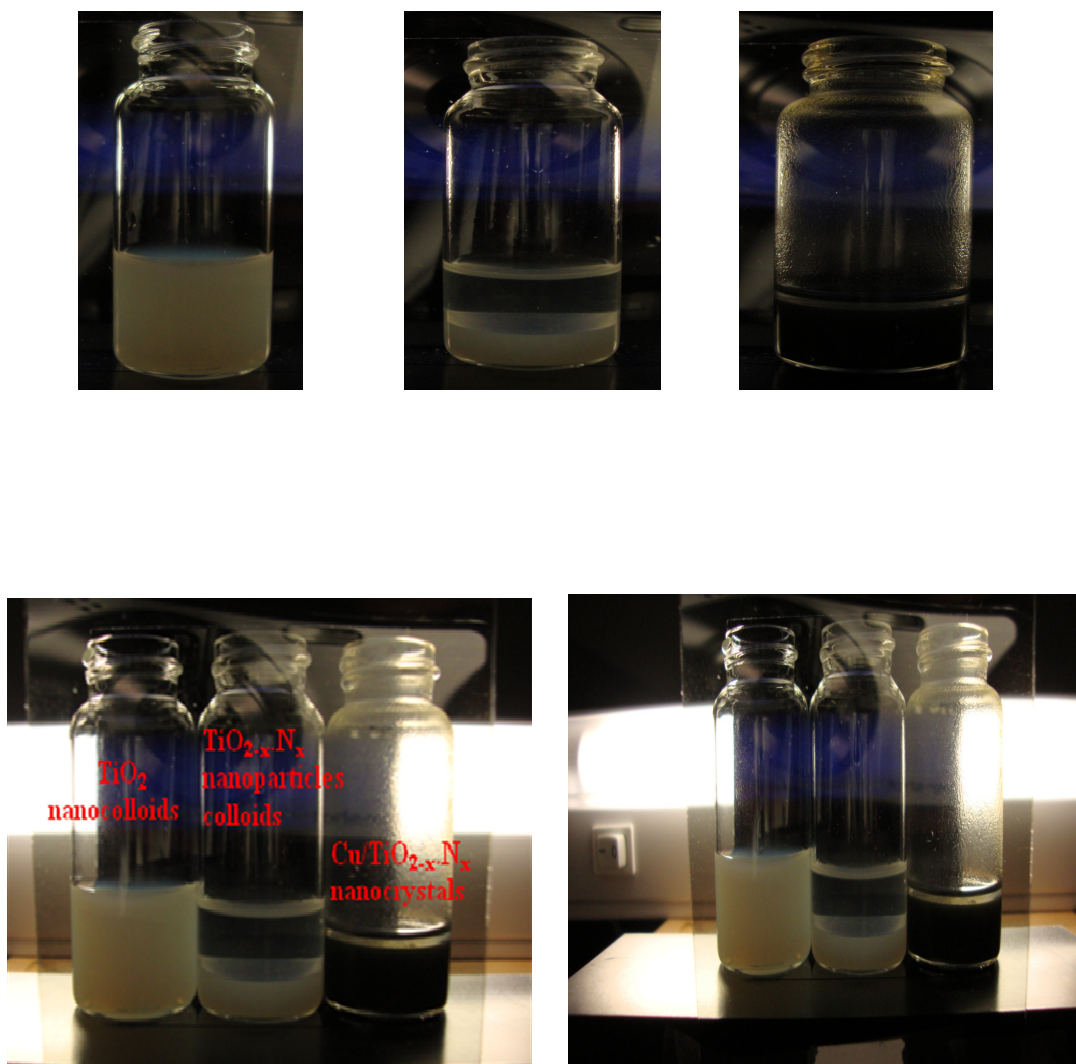
Figure 4.8 The digital images show the solutions of the TiO_2 nanocolloids, $TiO_{2-x}.N_x$ nanoparticles, and $Cu.TiO_{2-x}.N_x$ nanocrystals.

HIGH THROUGHPUT SCREENING PROCESS OF H_2 PRODUCTION MEASUREMENT

The procedure of hydrogen measurement was carried out as described in Chapter II. The experimental data is reported in appendix (C), under the following information:

Experiment	Run No.
Cu/TiO$_{2-x}$.N$_x$ nanocrystals suspensions under Sunlight	48
Cu/TiO$_{2-x}$.N$_x$ nanocrystals on substrate (as film) under Sunlight	49
Cu/TiO$_{2-x}$.N$_x$ nanocrystals on substrate (as film) under UV light	50

RESULTS AND DISCUSSION OF APPLICATION FOR H_2 PRODUCTION

The SEM micrographs revealed that the averaged Cu/TiO$_{2-x}$.N$_x$ nanocrystals size was about 100 ± 20 nm and the copper nanoparticles were 20 ± 5 nm. The SEM images showed that the morphology of Cu nanoparticles deposited on the surface of TiO$_2$ and fairly distribution were found due to the wet impregnation method used. The EDS results presented in Table 4.1 showed the chemical compositions. The sample was coated with Ru element (by vapor coating) for better electron conductivity and better imaging. To demonstrate the band gap of anatase TiO$_2$ film, UV-visible spectra presented in Figure 4.7 showed that the absorbance wavelength of anatase Cu/TiO$_{2-x}$.N$_x$ film in the range of 400-600 nm.

H$_2$ Production of Cu/TiO$_{2-x}$.N$_x$ Suspensions under Direct Sunlight

After synthesis, the change in color of TiO$_2$ nanocolloids upon nitrogen incorporation demonstrated the effect on their optical response in visible wavelength range. The hydrogen production rate from equal volume of water/methanol solution in presence of suspensions nanocrystals of Cu/TiO$_{2-x}$.N$_x$ under sunlight as high as 20.8 ± 11.1 μmol/h/g (Figure 4.9 and Table 4.2). This results indicate that enhancement in hydrogen production is attributed to extend in light absorption and promote in optical properties of TiO$_2$ due to nitrogen doping. However, the overall activity might not be as efficient as previous results reported here because the synthesis method used is different which govern the other chemical and photocatalytic properties of nanostructures TiO$_2$. In this technique, the TiO$_2$ is formed by adjusting pH value.

H$_2$ Production of Cu/TiO$_{2-x}$.N$_x$ as Film under Direct Sunlight

For this experiment, the nanocrystals of Cu/TiO$_{2-x}$.N$_x$ were deposited using drop by drop coating on glass substrate to form a film shape. The purpose is to study the effect of suspension colloids and film activity in term of light absorption and photo reactivity. The hydrogen production rate from equal volume of water/methanol solution in the presence of a film structure of nanocrystals Cu/TiO$_{2-x}$.N$_x$ under sunlight as high as 16.0 ± 1.8 μmol/h/g (Figure 4.10 and Table 4.3). It implies that a suspension photocatalyst has higher activity that a film structure under same reaction conditions. The suspension provide large surface area to volume ratio for photo reactivity and the water species can adsorbed into full coverage surface area of nano-photo-catalyst.

H$_2$ Production of Cu/TiO$_{2-x}$.N$_x$ as Film under UV Light

To study a different light wavelength and power intensity, the Cu/TiO$_{2-X}$.N$_X$ nanocrystal as film tested under UV light (100 W/m^2). The hydrogen production rate from equal volume of water/methanol solution in the presence of a film structure of nanocrystals Cu/TiO$_{2-x}$.N$_x$ under UV light was 0.81±0.27 μmol/h/g (Figure 4.11 and Table 4.4). This result shows significantly low production and unexpected result. For more than 60 hours of time course of experiment, the extremely low production may attribute to extremely low quantum efficiency due to very fast electron-hole recombination reaction that make occurs if UV light (λ<400nm) is illuminated to TiO$_2$ surface that lead to have extremely low hydrogen production. The shorter wavelength of UV light than that of the visible light means more photon energy. In case of sunlight illumination, this explanation is not preferable because the full spectrum of solar radiation with different wavelength range.

Table 4.2 Results and conditions of Cu/TiO$_{2-x}$.N$_x$ nanocolloids suspensions under sunlight

H$_2$ production (μmol/h)	H$_2$ production (μmol/h/g)	Effective Area, m^2	Energy Efficiency % @ x=0	Energy Efficiency % @ x=0.7
0.062 ± 0.03	20.8 ± 11.1	0.000064	0.00797	0.0265

Additives type and weight (g)	Photo catalyst type and weight (g)	Nano-structure and geometry	Photocatalyst Size, composition, Crystal structure	Water/ Methanol solution (1:1) Volume basis	Light Intensity If UV, (100 W/m^2) If Sunlight, ≈ (240 W/m^2)
-	Cu /TiO$_{2-x}$.N$_x$ (0.003)	Nanocolloids (suspensions)	Cu (<20 nm), TiO$_2$ (<100 nm, anatase nanocrystal)	10 ml (5 ml each)	Sunlight (Texas, College Station)
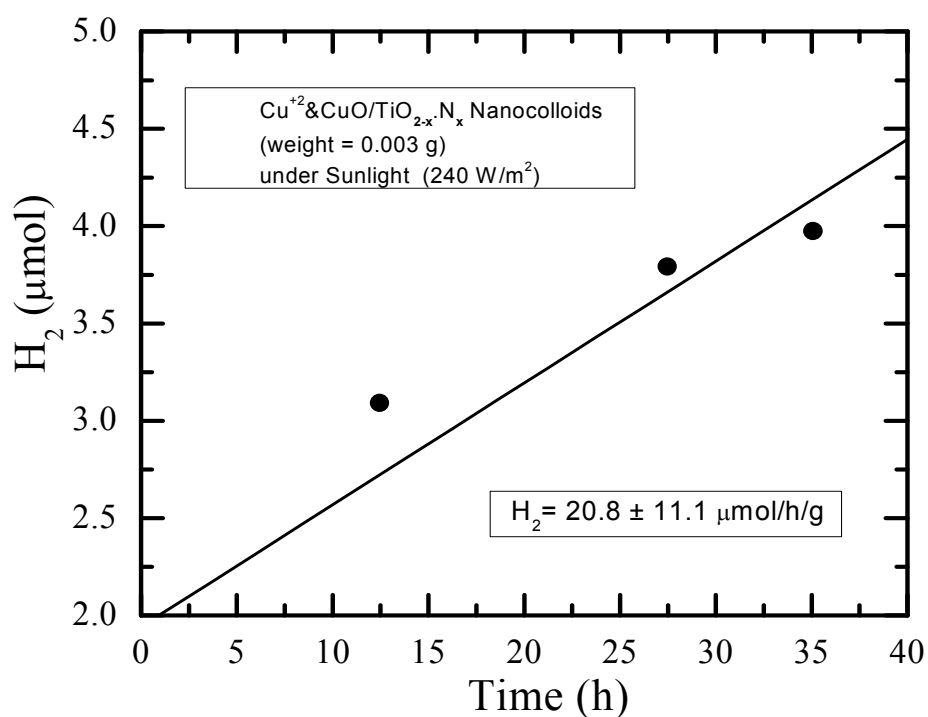
Figure 4.9 Hydrogen production rate of Cu/TiO$_{2-x}$.N$_x$ nanocolloids suspensions under sunlight.

Table 4.3 Results and conditions of Cu/TiO$_{2-x}$.N$_x$ nanocolloids as film under sunlight.

H$_2$ production (µmol/h)	H$_2$ production (µmol/h/g)	Effective Area, m^2	Energy Efficiency % @ x=0	Energy Efficiency % @ x=0.7
0.064 ± 0.007	16.0 ± 1.8	0.000064	0.0082	0.027

Additives type and weight (g)	Photo catalyst type and weight (g)	Nano-structure and geometry	Photocatalyst Size, composition, Crystal structure	Water/ Methanol solution (1:1) Volume basis	Light Intensity If UV, (100 W/m^2) If Sunlight, ≈ (240 W/m^2)
-	Cu /TiO$_{2-x}$.N$_x$ (0.004)	Nanocolloids on substrate (as Film)	Cu (<20 nm), TiO$_2$ (<100 nm, anatase nanocrystal)	10 ml (5 ml each)	Sunlight (Texas, College Station)

Figure 4.10 Hydrogen production rate of Cu/TiO$_{2-x}$.N$_x$ nanocolloids as film under sunlight.

Table 4.4 Results and conditions of Cu/TiO$_{2-x}$.N$_x$ nanocolloids as film under VU light.

H$_2$ production (µmol/h)	H$_2$ production (µmol/h/g)	Effective Area, m^2	Energy Efficiency % @ x=0	Energy Efficiency % @ x=0.7
0.003 ± 0.001	0.81 ± 0.27	0.000064	0.0009	0.003

Additives type and weight (g)	Photo catalyst type and weight (g)	Nano-structure and geometry	Photocatalyst Size, composition, Crystal structure	Water/ Methanol solution (1:1) Volume basis	Light Intensity If UV, (100 W/m^2) If Sunlight, ≈ (240 W/m^2)
-	Cu /TiO$_{2-x}$.N$_x$ (0.004)	Nanocolloids on substrate (as Film)	Cu (<20 nm), TiO$_2$ (<100 nm, anatase nanocrystal)	10 ml (5 ml each)	UV

Figure 4.11 Hydrogen production rate of Cu/TiO$_{2-x}$.N$_x$ nanocolloids as film under UV light.

CONCLUSIONS

The size effect (nano-scale) photocatalyst and their relation with optical properties also can be realized from the results. The colloidal TiO$_2$ (size<20nm) doped with nitrogen and decorated with Cu nanoparticles exhibited high response to visible light wavelength. The change in color of the nanocrystals upon nitrogen incorporation demonstrates a profound effect on their optical response in the visible wavelength range   A

photocatalyst of $Cu/TiO_{2-x}.N_x$ showed remarkable improve to harness visible light and harvest longer wavelength. The nanocrystals of $Cu/TiO_{2-x}N_x$ were deposited on substrate (as film-structure) and tested under sunlight for water/methanol solution and exhibited high hydrogen production rate (16.0 ± 1.8 μmol/h/g) than a like-sample tested under UV light (0.81 ± 0.27 μmol/h/g). It implies that photocatalyst is response to a portion of visible light, absorbed it, and contributed to generate electron-hole pairs to do the redox reactions of water-splitting and methanol decomposition for hydrogen production. In addition, the hydrogen production rate of nanocolloids suspensions of the same photocatalyst system tested under sunlight was (20.8 ± 11.1 μmol/h/g).

The results indicated suspensions photocatalyst has better performance than a film-structure and exhibited higher hydrogen production. This is attributed to the large surface area to volume ratio of suspensions nanocolloids that enhance the light absorption and also provide large area for water species to adsorb into TiO_2 surface. The synthesis method used to prepare TiO_2 nanocolloids and nitrogen doping is simple and carried out at room temperature. Generally, the low hydrogen production rate from $Cu/TiO_{2-x}.N_x$ nanocrystals compared to previous results reported in this dissertation may be due to the nature of synthesis method. The nitrate treatment of $TiO_{2-x}.N_x$ to loaded Cu metal, lead to preserve the structure distribution of $TiO_{2-x}.N_x$ and reduce the nitrogen uptake then reduce the photocatalytic activity [94].

CHAPTER V

QUANTUM DOTS SENSITIZATION

OVERVIEW

Three techniques have been presented in this section in order to enhance the harvesting of semiconductor system of photocatalyst to visible spectrum of sunlight. Photons energy harvested used for hydrogen production from water-splitting in presence of methanol as electron donor. TiO_2 film was sensitized by quantum dots ($CuInS_2$), dye (Rose Bengal sodium), and nanocomposite semiconductor ($CuInS_2/CdS$) in addition to metal nanoparticles (Ag). $CuInS_2$ has 1.5 eV band gap which is the optimum band gap required to absorb visible light and as same time provide the minimum energy required to split water into hydrogen and oxygen (not produced due to presence of methanol as strong oxidation agent). The weight of samples varied to plot the trend of photocatalyst weight verses the energy efficiency %. The highest hydrogen production rate observed was 57.1±9.2 μmol/h/g and energy efficiency was 0.023%. CdS as simply prepared quantum dots has band gap of 2.25-2.5 eV, contribute to harvest solar photons has longer wavelength (λ≈550nm) which cannot be absorbed by TiO_2 due to large band gap. CdS also promote the electron transportation from conduction band of TiO_2 surface and contribute to reduce the protons into hydrogen molecules.

INTRODUCTION

The aim of most effort toward maximize the benefit form solar energy is to shift the materials properties, mainly, electronic and optical, to harness the visible-region

radiation (largest portion of solar power radiation). The design and synthesis of these materials is based on narrowing the band gap to photon wavelength where the intensity of sunlight is very high. The photon energy (longer wavelength has low energy and vice versa) should match or exceeds band gap energy of the materials used to harvest the sunlight is a main criteria of this process. Therefore, a new strategy by using nanocomposites semiconductors that have different band gap energy level and band edge positions would enhance the absorption of full spectrum of sunlight. The photoexcited electron-hole pairs transferred from conduction and valence bands are highly depend on the position of band edge. The selection of appropriate materials based on these conditions to achieve the desired effect and be applicable for hydrogen production from water-splitting under sunlight. Quantum dots materials are very promising to play this role due to their size-dependent band gap properties and their electron confinement.

What Are Quantum Dots? Why They Are Important?

The difference between a semiconductor and an insulator material is that the semiconductor has a small band gap between the valence band and conduction band. An exciton pair is the photo generated electron-hole pair upon excitation. An exciton Bohr radius is the distance in an electron-hole pair. Quantum dots are a semiconductor so small that the size of the crystal is on the same order as the size of the exciton Bohr radius.

Quantum dots are also called artificial atoms because they are closely related to atoms than the bulk materials due to their discrete, quantized energy levels. The band gap depends on the relation between the size of the crystal and exciton bohr radius. The

Band gap and energy levels increases if the size of quantum dots decreases. This means smaller quantum dots, larger band gap, higher energy and higher absorption of shorter wavelength of radiation and blue shift. The large quantum dots have red shift absorption (Figure 5.1). The size-dependent properties make the applications of quantum dots as state-of-art in solar energy harnessing especially, the aim to absorb the full spectrum of solar radiation. In other definition, quantum dots (QD'S) are semiconductor materials with 3D electron confinement. The size of quantum dots is typically about 2-10 nm (50 to 1000 atoms). The extremely small size of QD'S induced the electronic structure such as band gap and band edge positions. Therefore, the relation of size with emission wavelength extends their uses in medical and energy application. Titanium dioxide is a well known semiconductor for its high photocatalytic activity, photovoltaic, and high stability in aqueous solution [34].
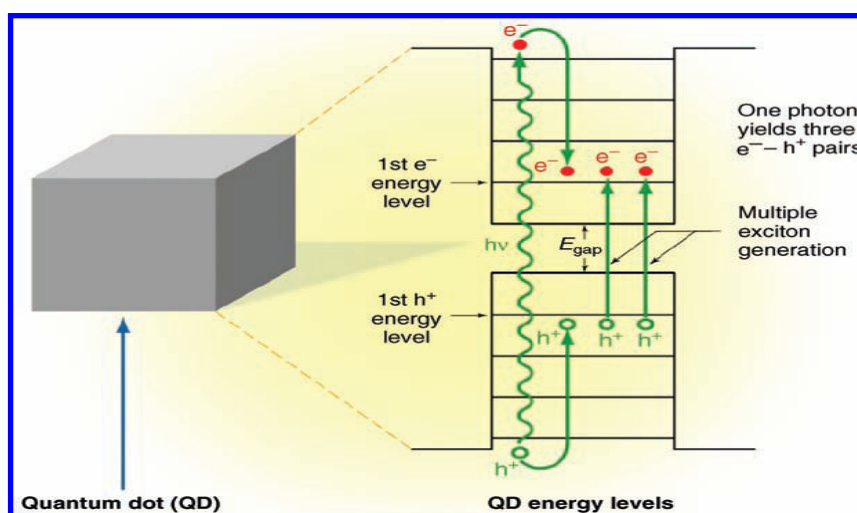
Figure 5.1 Schematic representation of the multiple exciton generation process observed in quantum dots. A single absorbed photon whose energy is at least three times the energy difference between the first energy levels for electrons and holes can create three excitons [10][59].

However, it has an UV responsive band gap energy (Eg=3.2 eV for anatase crystal structure). This band gap is not effective and too big to harvest visible solar spectrum. Quantum dots can be utilized to harvest solar visible light. Also, the band gap energy of TiO_2 can be modified to be responsive to visible solar spectrum by several approaches, such as noble metals loading, ions doping, dye and composite semiconductors sensitization [45]. The changes in electron confinement are achieved by defect and band gap engineering. Within this study, QD'S has two advantages to use; first enable to absorb the visible spectrum, second is the control of light absorption by controlling the particle size and the band gap engineering.

Nanoscience and nanotechnology has a great potential to develop novel functional nanomaterials for renewable energy production. Active metal oxide nanostructures make it possible to harness visible light by using quantum confinement effects for photovoltaics solar energy and photocatalysis [10]. One of the major limiting steps to the development of materials for solar photoconversion with high efficiency is the 1:1 ratio between the absorption of photons and the creation of electron hole pairs in the materials. A process called impact ionization, allows the creation of more than one electron hole pair per absorbed photon. Although, such a process is not efficient for bulk semiconductors (due to the high photon energy threshold), it becomes very attractive and very efficient when dealing with nanoscale semiconductors, where the threshold photon energy to generate multiple electron hole pairs could occur in the visible or near-infrared (IR) spectral region [10].

Semiconductors sensitized with quantum-dot is vital for this challenge because it has slow rate of electron relaxation. The formation of discrete energy levels allows photons of lower energy (visible to IR range) to be efficiently absorbed, thus contributing to enhancing the efficiency of the systems [10]. The concept of an intermediate band seems to be the most appropriate as far as metal-oxide semiconductors are concerned to develop visible-light-active materials for efficient photoconversion [10].

A new approach using smart materials design and quantum-confinement effects along with simple and cost-effective fabrication of advanced metal-oxide materials for direct solar-to hydrogen generation by photocatalytic oxidation and reduction of water-splitting under visible-light conditions. Quantum Confinement tuning band gap and band-edge positions, as well as the overall band structure of semiconductors are of crucial importance in photovoltaic and photocatalytic cells and even more drastically for direct water-splitting applications (optimum energy required is 1.23 eV) [10]. Herein, CIS-nanoparticles or $CuInS_2$ (QD'S) used for water-splitting reaction due to their appropriate band gap (1.5 eV). At this photon energy level, both the visible light harvesting and the water splitting reaction are achieved. Therefore, a photocatalyst system of $Ag/CuInS_2/TiO_{2-x}.N_x$ as film will be prepared and tested for hydrogen production under sunlight from water/methanol solution.

Co-Qd's Sensitization onto TiO_2 Film

A quantum dot is a granule of a semiconductor material of size on the nanometer scale. These nanocrystallites behave essentially as a three-dimensional potential well for electrons. Quantum dots have already been used successfully to improve the

performance of devices such as lasers, light-emitting diodes, and photodetectors. Comparing between CdS and CuInS$_2$, CdS has a higher conduction band edge with respect to that of TiO$_2$ which is advantageous to the injection of excited electrons from CdS (Figure 5.2 and Figure 5.3).
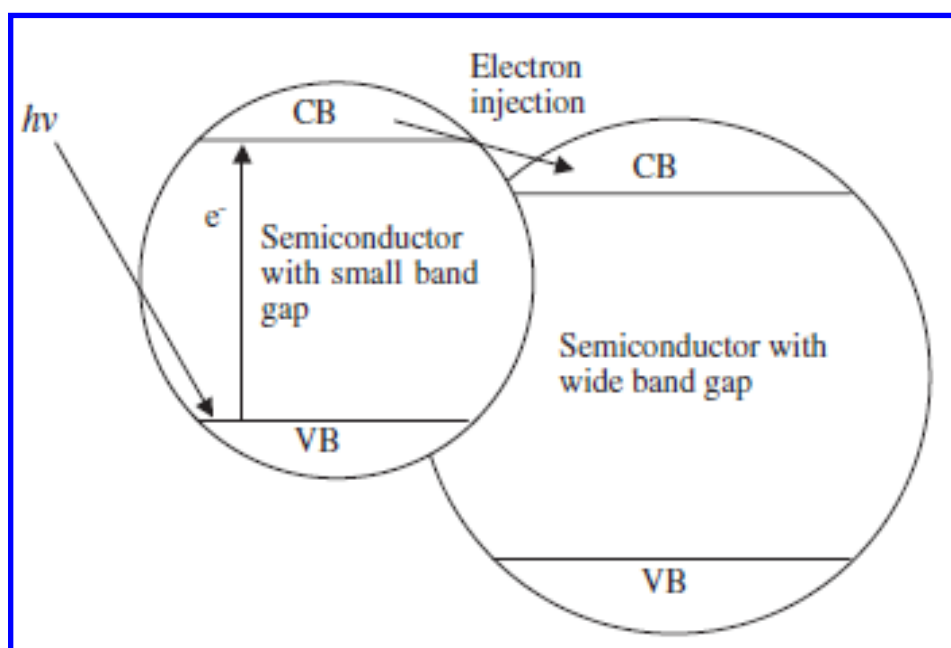
Figure 5.2 In composite semiconductors, the electron injection from small band gap to wide band gap [45].

However, the band gap of CdS (2.25 eV-2.5 eV in bulk) limits its absorption range below the wavelength of approximately 550 nm. On the contrary, although CuInS$_2$ has a wider absorption range (below ca.730 nm), the electron injection efficiency is less than CdS because its conduction band edge is located below that of TiO$_2$. To take both

advantages of the twomaterials, CdS and CuInS$_2$ were used as co-sensitizers of aTiO$_2$ film. The two materials were sequentially assembled onto a TiO$_2$ film, forming co-sensitized photocatalyst.
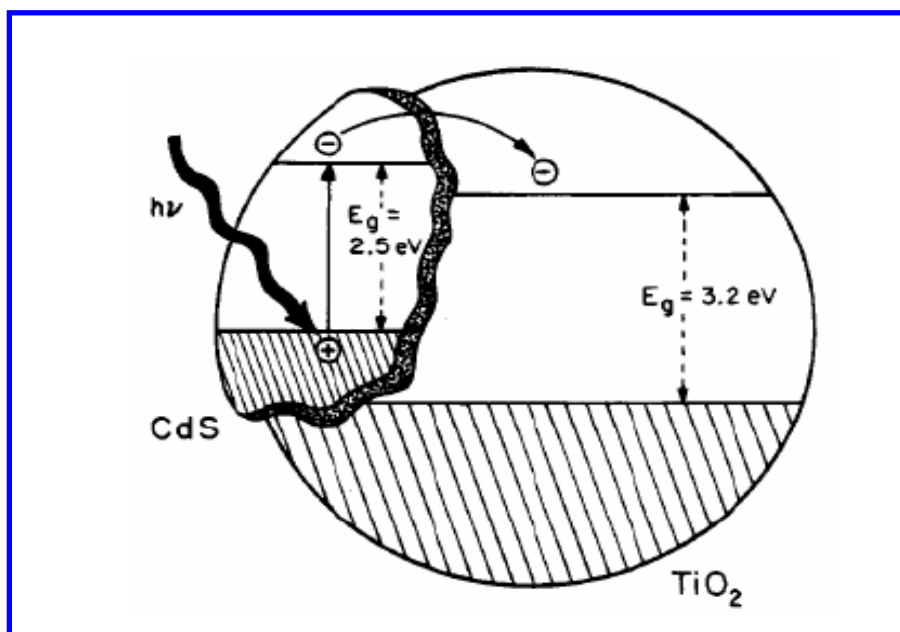
Figure 5.3 Photoexcitation in composite semiconductor photocatalyst [46] [52].

DESIGN AND SYNTHESIS

Ag/CuInS$_2$/TiO$_{2-x}$.N$_x$ as Film on Substrate

All chemicals were obtained from Sigma-Aldrich and used without further purification. Reactions were carried out in a CEM Discover ® S class Microwave reactor. In a typical experimental procedure, CuInS$_2$ can be prepared in good yield from a mixture of

CuCl$_2$·2H$_2$O (0.33 mmol), InCl$_3$ (0.3 mmol), Na$_2$S (0.2 mmol), and thioglycolic acid (50 mmol) in water under microwave irradiation. CuCl$_2$·2H$_2$O, InCl$_3$, and Na$_2$S were each dissolved in 5 ml of distilled deionized H$_2$O. In a 35 ml thick walled microwave vial, thioglycolic acid was dissolved in 10 ml of distilled deionized H$_2$O under vigorous stirring. To the solution was added the aqueous solutions of InCl$_3$, CuCl$_2$·2H$_2$O, and Na$_2$S allowing for complete mixing between additions. The vial was capped and the reaction was irradiated in the microwave with 100W with constant stirring to a temperature of 120°C at a ramp rate of 24°C/min and held for 20 seconds. After cooling to room temperature the reaction was centrifuged for 10 minutes at a rate of 8500 rpm, the water was decanted off and centrifuged again for 30 min at a rate of 8500 rpm. The water was decanted off, and the product was washed with methanol and dried at 70°C for 2 hours to obtain 10 mg of CuInS$_2$ of less than 100 nm in size. The film of TiO$_2$ is prepared as described in Chapter II, nitrogen also doped as mentioned earlier using triethylamine (Chapter IV). Prior to silver deposition using photoelectron deposition, the CuInS$_2$ nanoparticles (≈ 65nm) deposited on the surface of the film by spray deposition using atomization technique. The nanoparticles mixed with ethanol and sprayed, followed by drying and heating at 400°C for 30 minutes. Table 5.1, Figure 5.4, and Figure 5.5 give information about synthesis method and show the image of CuInS$_2$ nanoparticles.
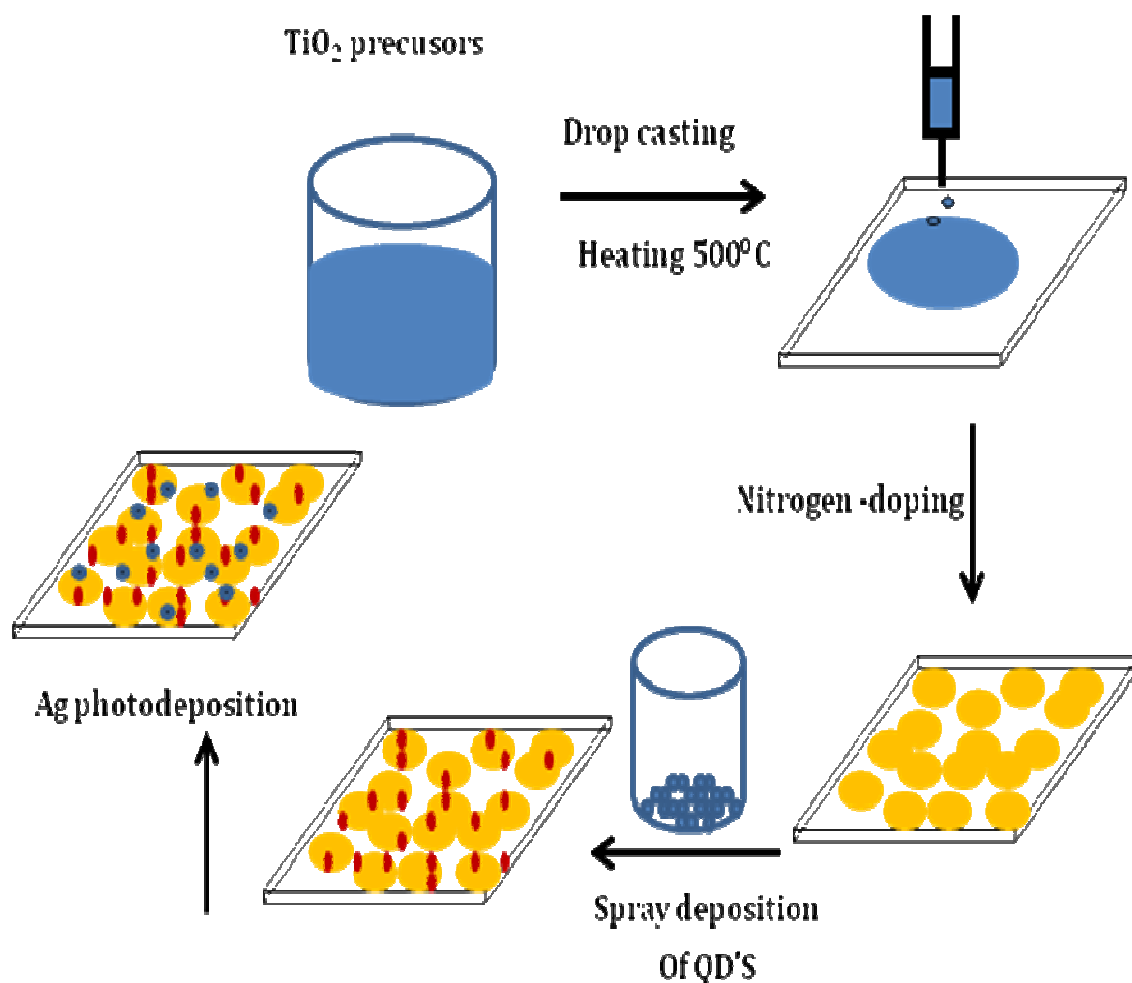
Figure 5.4 Synthesis of Ag/CuInS$_2$/TiO$_{2-x}$.N$_x$ nanoparticles using simple and low cost preparation procedure.

The results of Ag/CuInS$_2$/TiO$_{2-x}$.N$_x$ system exhibit a high hydrogen production under sunlight due to effect of quantum dots to harvest visible spectrum, and N-doping to enhance the absorption properties of TiO$_2$. The junction or interaction between QD'S or CIS-nanoparticels and TiO$_2$ from one side, and metal on TiO$_2$ on other side, is very important for the materials properties utilization and to do their functions. Therefore, the

synthesis method is highly crucial to control and effectively the deposition of QD'S and metal. Several deposition methods such as spray deposition, dip coating, chemical vapor deposition, spin coating, and drop by drop deposition can be used based on effect desired. Herein, we are used drop by drop deposition technique to control the deposition as well as the weight.

Table 5.1. The table provides the chemicals weight and the microwave reaction time and temperature.

Scale	$CuCl_2 \cdot 2H_2O$	$InCl_3$	Na_2S	MAA	H_2O	Time	Temp	Power
1X	0.019 g	0.025 g	0.016 g	0.035 ml	5 ml	1:40	120 °C	40 W
3X	0.054 g	0.056g	0.04g	5 ml	25 ml	4:20	120 °C	100 W
3X	0.054 g	0.056g	0.04g	5 ml	50 ml	4:20	120 °C	100 W
5X	0.107 g	0.117g	0.08 g	2 ml	25 ml	4:20	120 °C	100 W
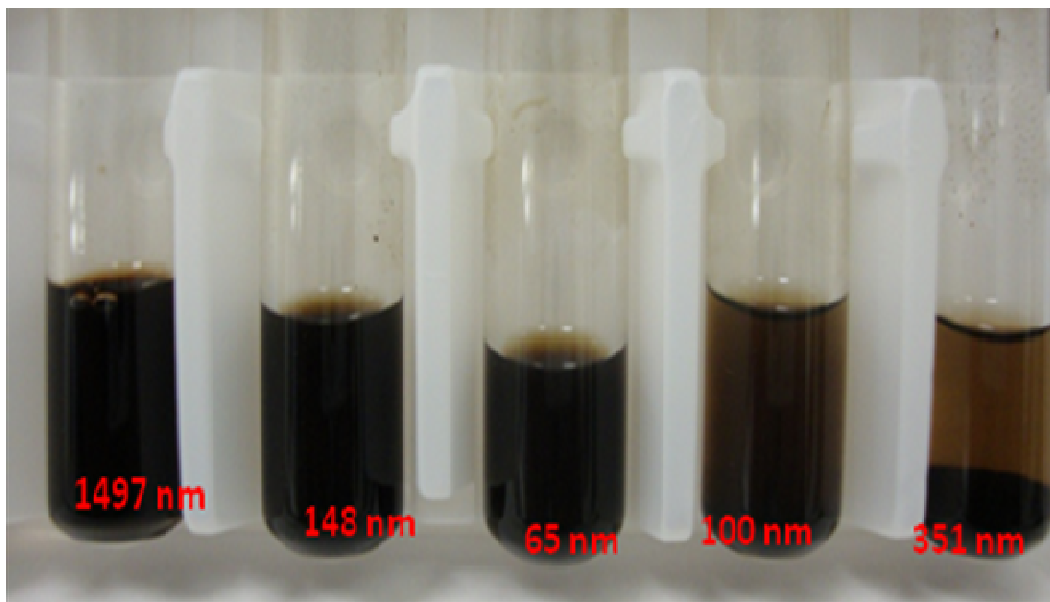
Figure 5.5 Digital image of the CuInS$_2$ nanoparticles or CuInS$_2$ "QD'S".

Ag/CuInS$_2$/CdS/TiO$_{2-x}$.N$_x$ as Film on Substrate

Co-sensitized of quantum dots on nanocrystalline TiO$_2$ film and photocatalyst was prepared as follows: the procedure to make CuInS$_2$ quantum dots is described elsewhere by [95] and it summaries here. Cupric chloride dihydrate (Sigma-Aldrich), indium chloride (Sigma-Aldrich), and sodium sulphide (Sigma-Aldrich), are the three precursors used to synthesize CuInS$_2$. Deionized water was used as solvent. Mercapto-acetic acid (MAA) is used as surfactant. The choice of solvent to carry out nanoparticle synthesis is critical. Water is a well known solvent with a very high dielectric constant making it quite suitable for microwave heating. Proposed process should allow recycling of used water solvent. A water soluble surfactant should be used to avoid agglomeration and obtain size distribution with fairly uniform diameters. Ideally, the surfactant should be easily

stripped away during the solar cell fabrication steps. These surfactants should then be weakly bonded to the nanoparticle. For this purpose, we have used (MAA), although other surfactants may also work. Copper and indium precursors are first mixed thoroughly with MAA to provide high dilution. Sodium sulphide (Na_2S) is then added to the previous solution. Cu:In:S atomic ratio of the starting materials is set to 1.1:1:2 to synthesize $CuInS_2$ nanoparticles. Atomic/molecular ratio of In:MAA is set to about 1:50 [95]. The solution is then introduced inside the microwave and heated to about 90°C for 30 minutes using controlled ramping for a total duration of 2 minutes. Resulting solution is allowed to cool down. Centrifugation is also used to clean product reaction and then check the size of these particles using dynamic light scattering (DLS technique). The synthesis of TiO_2 film, nitrogen doping, silver deposition is exactly same as mentioned in the previous section [95].

However, CdS nanoparticles were assembled and deposited prior to $CuInS_2$ nanoparticles deposition. In order to extend the absorption of sunlight power, quantum dots of CdS with a 2.25-2.5 eV band gap and act as nanocomposite semiconductor with TiO_2. It will contribute to harvest some portion of visible light and it work as bridge to transfer electrons from $CuInS_2$ nanoparticles surface to TiO_2 surface due to difference in band gap and band edge positions between these three semiconductors (Figure 5.6).

(a)

(b)
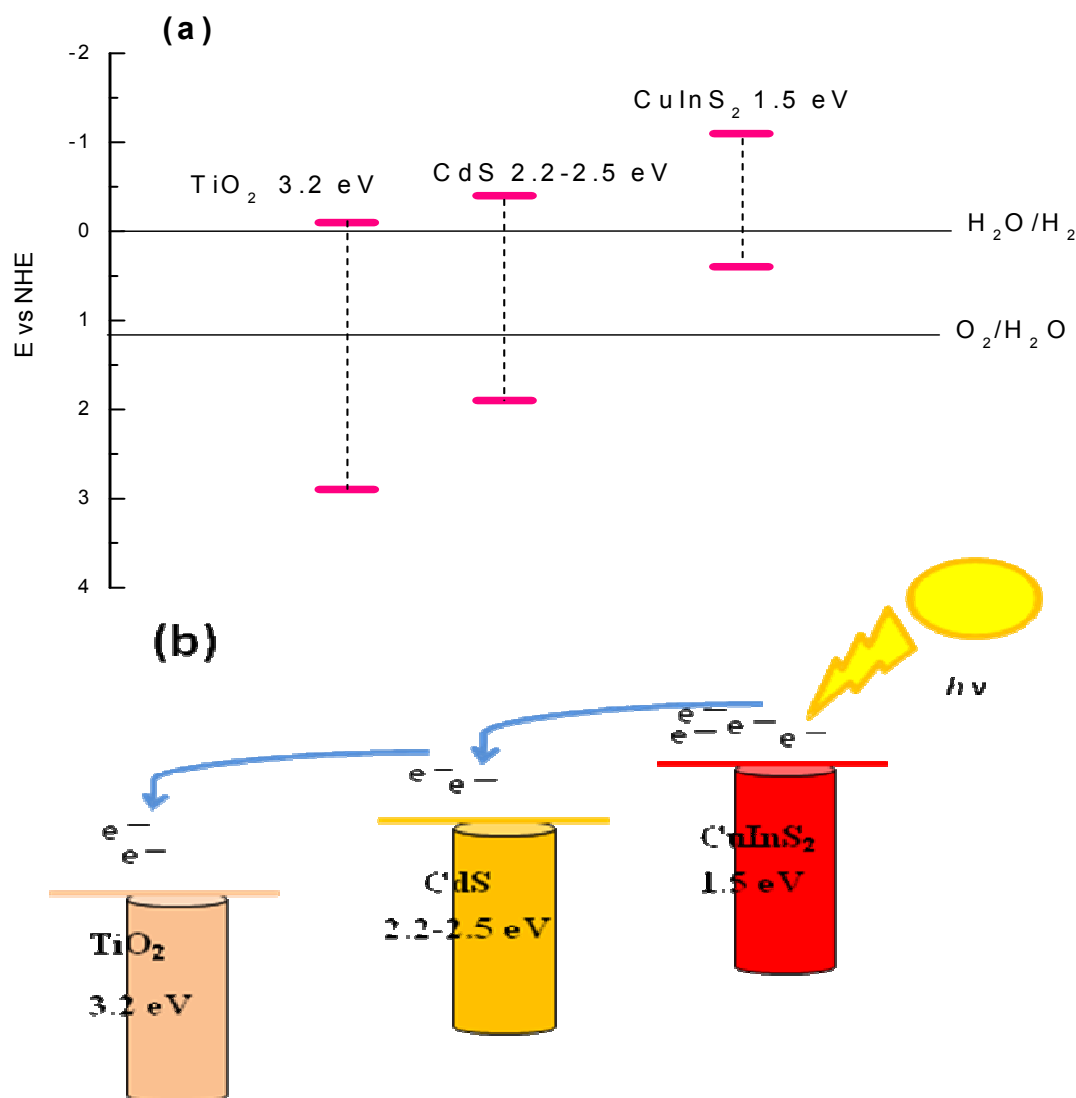
Figure 5.6 Diagrams of (a & b) show the potential band positions of composites semiconductors and quantum dots in E vs. NHE. The band edge positions for photoexcited electrons and holes in CdS/CuInS$_2$ co-sensitized electrode. Band gap energy levels of TiO$_2$, CdS in the bulk phase [96] which is band gap properties required for harvesting solar visible light and water-splitting reaction.

In typical procedure to prepare CdS reported by G.A. Martines Gatnon [97], CdSO$_4$.2.5H$_2$O was dissolved in 1 L of deionized water to a concentration of 2 mM. This solution was placed in a 2 L reaction vessel. Under stirring (200 rpm) 18 mmol of 1-thioglycerol were added and the mixture was stirred for an additional five minutes.

Ammonium sulfide (30 mmol) was rapidly added under ambient conditions to form cadmium sulfide nanoparticles. This method yields dispersions that are stable even during months [97].

The procedure is described by [96] and it summaries here. Chemical bath deposition (CBD) is used to assemble CdS onto a TiO_2 film prior to deposit $CuInS_2$ by spray deposition as described in above section. For CdS nanoparticles, the CBD method was used to resembles nanoparticels of CdS. A TiO_2 film was dipped into a 0.5 M Cd $(NO_3)_2$ ethanol solution for 5 min, rinsed with ethanol, and then dipped for another 5 min into a 0.5 M Na_2S methanol solution and rinsed again with methanol. The two-step dipping procedure is termed of one CBD cycle, and the incorporated amount of CdS can be increased by repeating the assembly cycles [96]. After synthesis of CdS, it is deposited before the $CuInS_2$ nanoparticles on TiO_2 surface (Figure 5.7).
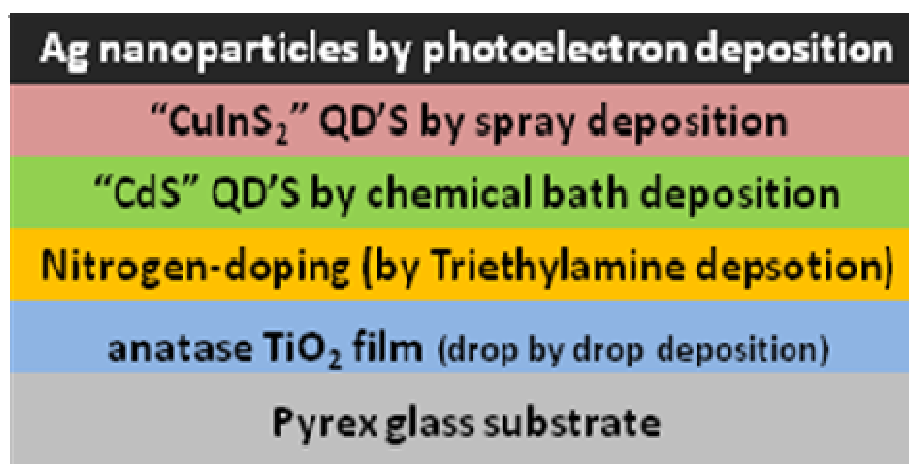
Figure 5.7 Diagram shows the arrangement of $Ag/CuInS_2/CdS/TiO_{2-x}.N_x$ as film on glass substrate.

CHARACTERIZATION

The $Ag/CuInS_2/TiO_{2-x}.N_x$ & $Ag/CuInS_2/CdS/TiO_{2-x}.N_x$ films photocatalys system that include quantum dots were charecterized using Scanning Electron Microscopy (SEM) (Figure 5.8). The SEM images were taken using JEOL JSM-6400. The Surface element analysis was obtained using Energy dispersive X-ray spectroscopy (EDS) as shown in Table 5.2. The EDS results were also obtained using JEOL JSM-6400. Figure 5.9 showed the UV-visible spectra using UV-vis-NIR spectrophotometer. Figure 5.10 digital image shows the sample of two films with and without nitrogen-doping. Figure 5.11 exhibit optical microscopic image of $CuInS_2/TiO_2$ film. Figure 5.12 show optical microscopic image of CdS nanoparticles. Figure 5.13 Dynamic light scattering results show narrow size distribution of $CuInS_2$ nanoparticles (uniform size of nanoparticles can be prepared in short time using microwave reactor).
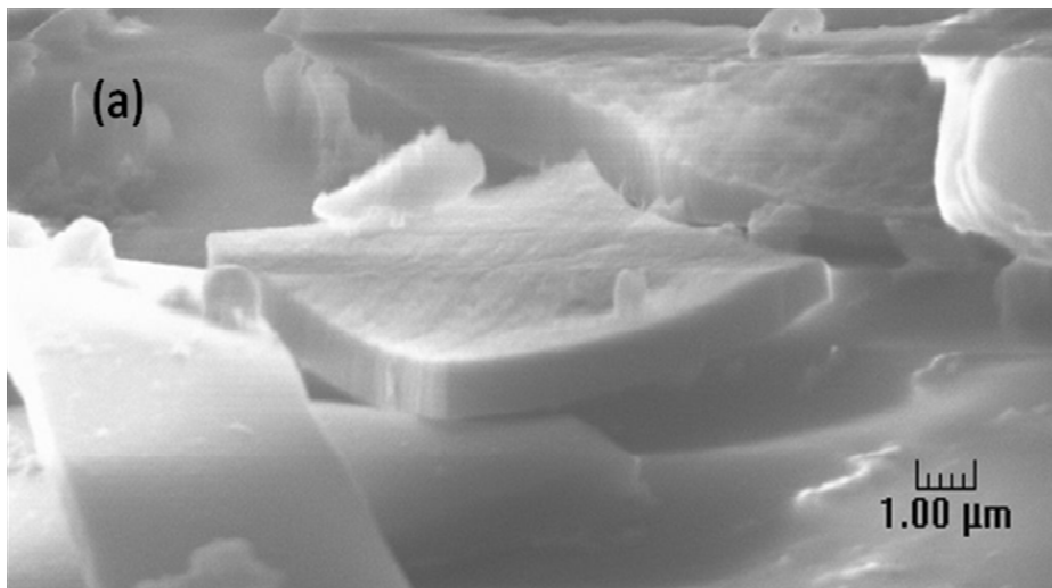
Figure 5.8 (a) SEM image of $Ag/CuInS_2/TiO_{2-x}.N_x$ nanocomposites thin film.

Figure 5.8 continued (b) SEM image of Ag/CuInS$_2$/CdS/TiO$_{2-x}$.N$_x$ nanocomposites thin film.
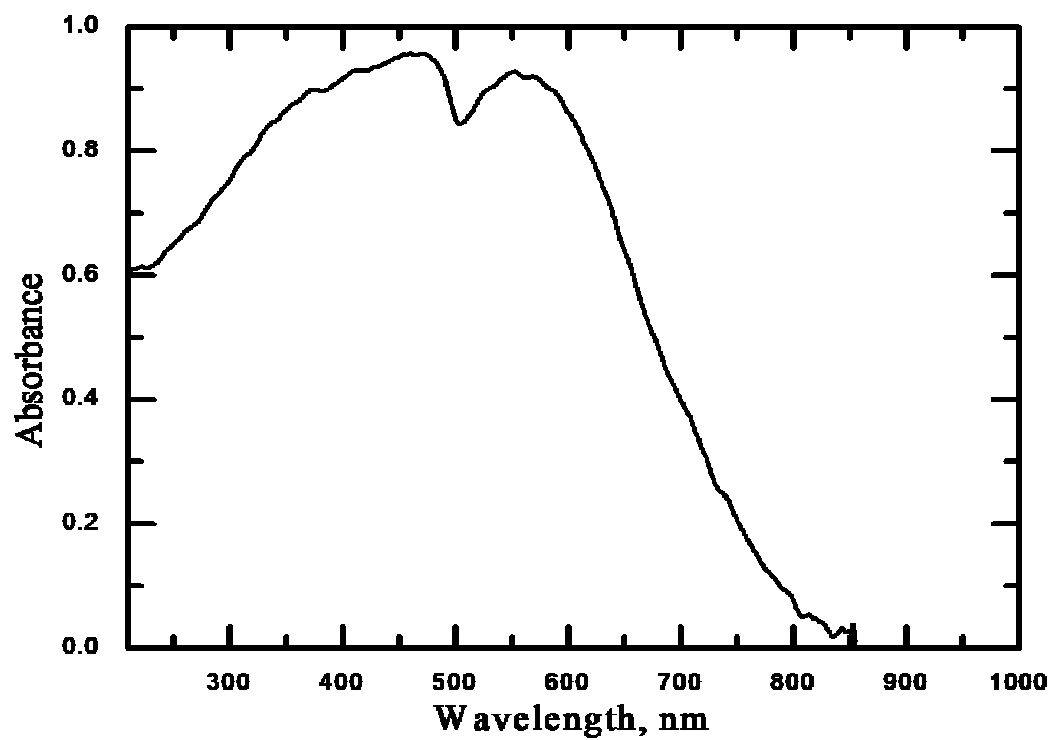
Figure 5.9 UV-visible spectra of CuInS$_2$ nanoparticles synthesized by microwave reactor.

Table 5.2 Surface element analysis using EDS (a) Ag/CuInS$_2$/TiO$_{2-x}$.N$_x$ nanocopmposites thin

Element	keV	KRatio	Wt%	At%	At Prop	ChiSquared
Ti	4.510	0.0346	3.26	3.93	0.0	1.92
Ag	2.984	0.0878	9.32	4.99	0.0	4.12
S	2.307	0.0810	8.25	14.87	0.0	0.69
In	3.286	0.3300	34.19	17.21	0.0	6.93
Cu	8.046	0.3418	29.91	27.20	0.0	0.94
Ru	2.558	0.0000	0.00	0.00	0.0	3.55
O	0.523	0.0015	0.51	1.86	0.0	5.00
Si	1.740	0.1232	14.55	29.94	0.0	23.69
N	0.392	0.0000	0.00	0.00	0.0	5.28
Total		**1.0000**	**100.00**	**100.00**	**0.0**	**9.36**

Element	Gross (cps)	Z Corr	A Corr	F Corr
Ti	41.3	0.922	1.176	0.996
Ag	82.5	1.122	1.087	0.999
S	103.5	0.859	1.375	0.989
In	166.6	1.136	1.048	0.999
Cu	57.0	0.984	1.021	1.000
Ru	37.1	1.101	1.183	0.985
O	4.6	0.760	5.106	0.999
Si	223.7	0.836	1.631	0.994
N	3.5	0.746	3.761	1.000
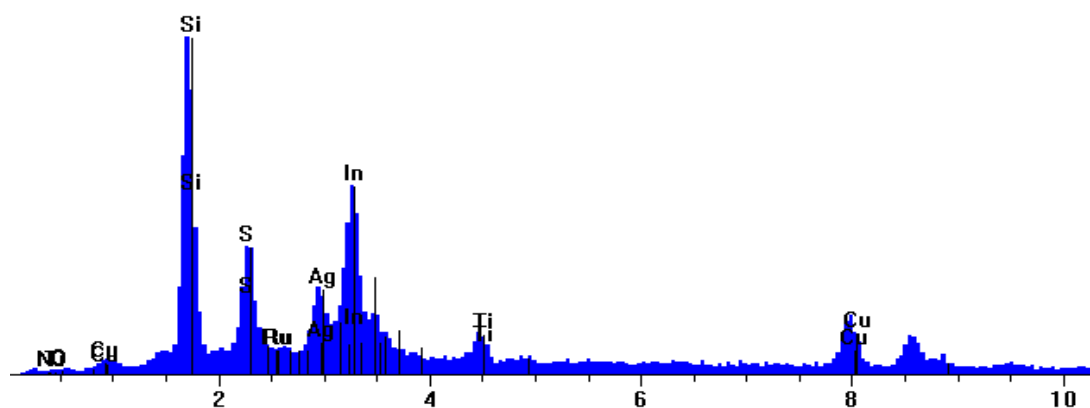
Table 5.2 continued. (b) Ag/CuInS$_2$/CdS/TiO$_{2-x}$.N$_x$ nanocopmposites thin film.

Element	keV	KRatio	Wt%	At%	At Prop	ChiSquared
Ti	4.510	0.0519	4.99	6.79	0.0	1.39
Ag	2.984	0.0234	2.49	1.51	0.0	45.82
S	2.307	0.0995	9.77	19.87	0.0	3.05
In	3.286	0.2101	21.88	12.43	0.0	5.93
Cd	3.133	0.2436	25.63	14.87	0.0	26.04
Cu	8.046	0.2859	25.26	25.93	0.0	1.40
Ru	2.558	0.0257	2.82	1.82	0.0	5.17
O	0.523	0.0003	0.09	0.38	0.0	6.58
Si	1.740	0.0596	7.07	16.41	0.0	4.05
N	0.392	0.0000	0.00	0.00	0.0	7.42
Total		**1.0000**	**100.00**	**100.00**	**0.0**	**4.83**

Element	Gross (cps)	Z Corr	A Corr	F Corr
Ti	25.1	0.902	1.194	0.997
Ag	47.2	1.097	1.085	0.999
S	58.9	0.840	1.325	0.985
In	104.4	1.110	1.050	0.998
Cd	91.8	1.104	1.066	0.998
Cu	25.5	0.963	1.024	1.000
Ru	25.2	1.076	1.157	0.982
O	2.9	0.742	5.647	1.000
Si	56.6	0.817	1.633	0.993
N	2.0	0.728	3.200	1.000
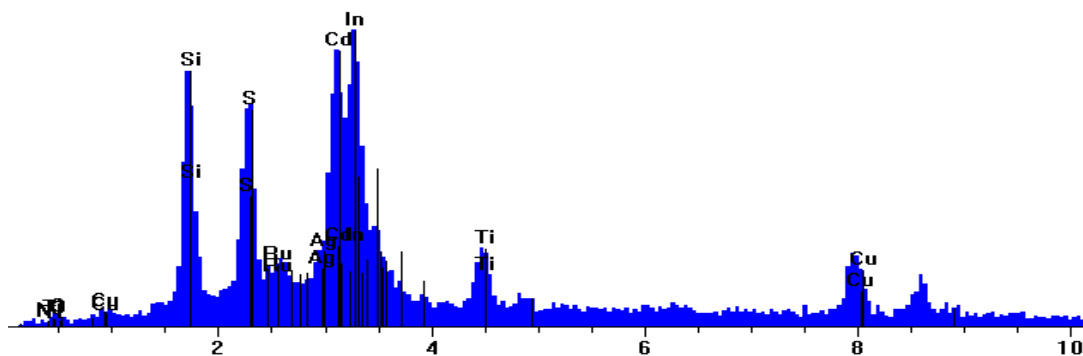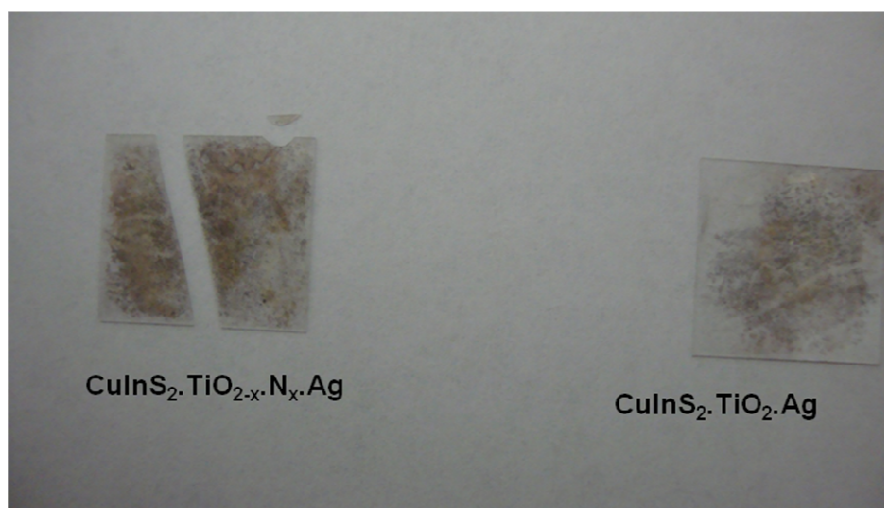
Figure 5.10 Digital image shows the sample of two films with and without nitrogen-doping..
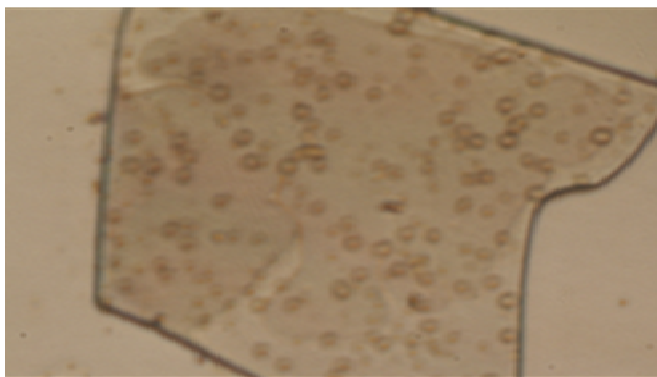
Figure 5.11 Optical microscopic image shows a sample of $CuInS_2/TiO_2$ film.
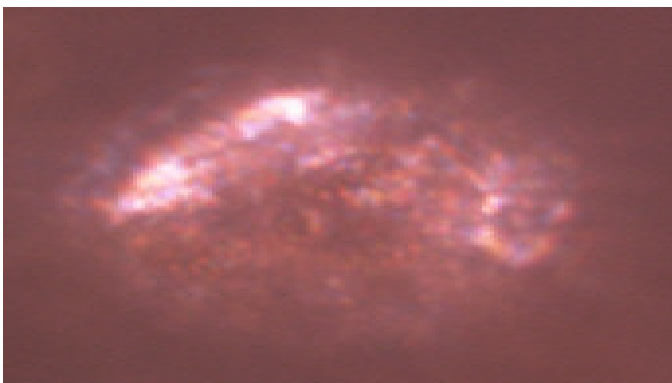
Figure 5.12 Optical microscopic image of CdS nanoparticles.

d	G(d)	C(d)	d	G(d)	C(d)	d	G(d)	C(d)
108.75	0	0	115.49	100	55	122.65	0	100
109.35	0	0	116.12	89	83	123.32	0	100
109.95	0	0	116.76	48	98	124.00	0	100
110.55	0	0	117.40	7	100	124.68	0	100
111.16	0	0	118.04	0	100	125.36	0	100
111.76	0	0	118.69	0	100	126.05	0	100
112.38	0	0	119.34	0	100	126.74	0	100
112.99	0	0	120.00	0	100	127.43	0	100
113.61	0	0	120.65	0	100	128.13	0	100
114.24	18	6	121.31	0	100	128.83	0	100
114.86	59	24	121.98	0	100	129.54	0	100
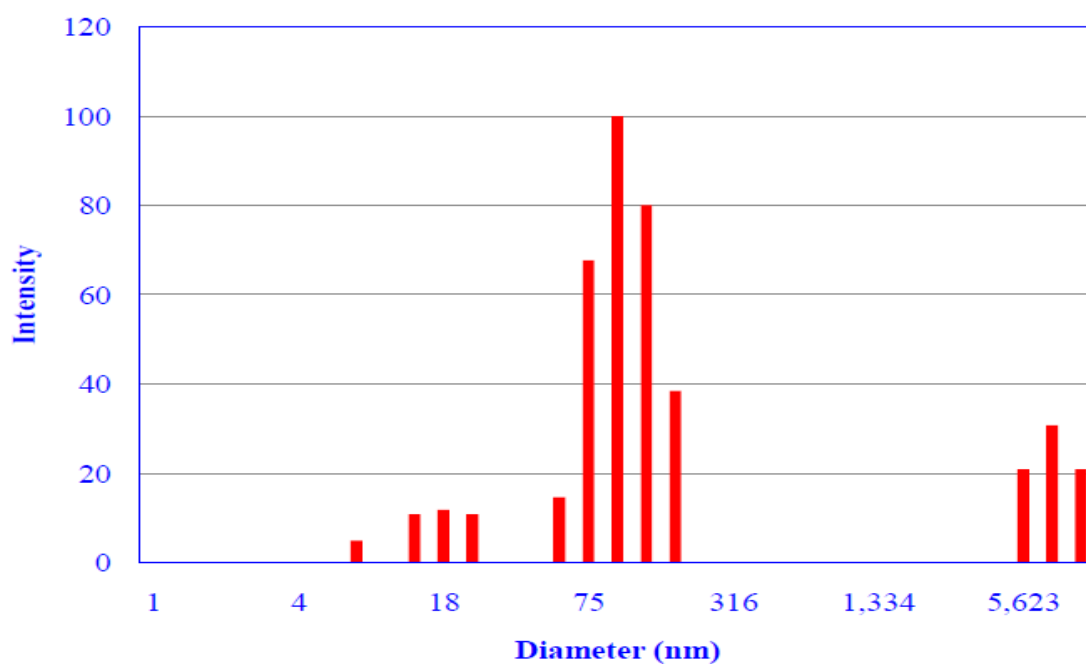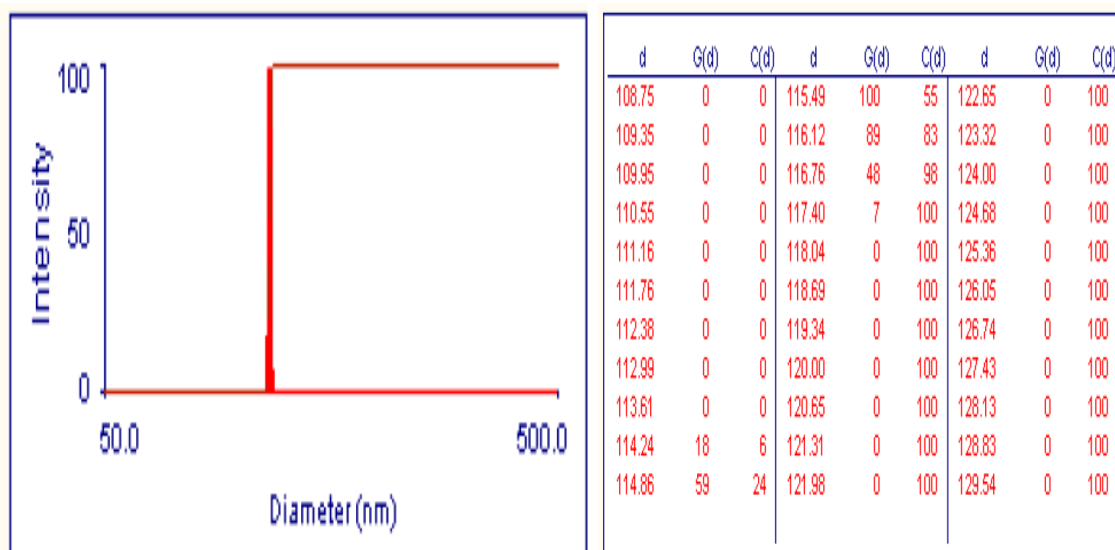
Figure 5.13 Dynamic light scattering (DLS) results show narrow size distribution of CuInS$_2$ nanoparticles (uniform size of nanoparticles can be prepared).

HIGH THROUGHPUT SCREENING PROCESS OF H_2 PRODUCTION MEASUREMENT

The procedure of hydrogen measurement was carried out as described in Chapter II. The experimental data is reported in appendix (D), under the following information:

Experiment	Run No.
Ag/CuInS$_2$/TiO$_{2-x}$.N$_x$ (film) under Sunlight	
0.0025 g	51
0.005 g	46
0.01 g	56
0.05 g	57
0.075 g	58
0.1 g	59
1 g	60
Ag/CuInS$_2$/CdS/TiO$_{2-x}$.N$_x$ (film, 0.01 g) under Sunlight	61

RESULTS AND DISCUSSION OF APPLICATION FOR H2 PRODUCTION

The Initial result of Ag/CuInS$_2$/TiO$_2$.N$_x$ was expected to be the highest hydrogen production rate in (μmol/h/g) under natural sunlight among all nanomaterials tested in this study. The reason behind this expectation is that the QD'S effectively enhance the capture of visible solar light which has the largest portion of solar energy. Also, the electron mobility from QD'S conduction band (CB) to TiO$_2$ (CB) is transferred with high efficiency due to the fact that the bottom of CB of QD'S is above the CB of TiO$_2$ (more negative potential energy) even with anticipated slightly shifting of band edge position of TiO$_2$ due to nitrogen doping incorporation. The SEM images revealed that the averaged film thickness was about 1.0 ± 0.2 μm and the silver nanoparticles were

200 ± 50 nm. The SEM images showed that the TiO_2 layer broke down to islands during annealing to 500°C. The images also showed that the size of silver nanoparticles deposited on TiO_2 films were not uniform by the photoelectron deposition technique used here. The EDS results showed the chemical analysis of nanocomposites thin films. Due to the minimum limit of EDS analysis that can be detected, nitrogen composition does not appear in the results because of a very thin layer of nitrogen deposited The sample was coated with Ru element (by vapor coating) for better electron conductivity and better imaging. DLS analysis showed that it is possible to prepare $CuInS_2$ nanoparticles with size less than 100 nm. UV-visible spectra showed that the absorbance wavelength of anatase TiO_2 film in the range of ≈ 550 nm.

H_2 Production of Ag/CuInS$_2$/TiO$_{2-x}$.N$_x$ as Film under Direct Sunlight

The experiments were carried out under same reaction condition and film structure of Ag/CuInS$_2$/TiO$_{2-x}$.N$_x$ with only varying the total weight of the film to know the effect of photocatalyst weight on overall energy effeceincy (%). Specifically, the weight of CuInS$_2$ nanoparticles are also varied but it is not estimated due to exteremly small size of these particles (≈ 65 nm). The highest hydrogen production rate of Ag/CuInS$_2$/TiO$_{2-x}$.N$_x$ film acheived was (57.1 ± 9.2 μmol/h/g) and energy efficiency is 0.023% when the film weight is equal to 0.005 g (Figures 5.14-5.20) and (Tables 5.3-5.9). The total weight of the film is the weight of all the deposited materials. For other results, surprisingly, when the weight of the film increased, the energy efficiency (%) deceased. This indicate that only the amount of TiO_2 layer, nitrogen layer, CuInS$_2$ layer, and silver dots well connected to each other are efficient to absorb light and converted to electrons and then

redox reactions occur to split water or decompose methanol in form of hydrogen molecular. The synthesis method used and the arrangement of the samples inside the reaction cell need to be improved in order to utilize maximum amount of weight used. By theory, more photocatalyst weight show produces more hydrogen. Based on the results, it is found that the preparation method is extremely important to attach all nanocomposites to each others. In addition, the arrangement of extra weight deposited on films on the substrates need to be fully exposed to light and not blocked or overlapped by other sample to enhance the light absorption.

H$_2$ Production of Ag/CuInS$_2$/CdS/TiO$_{2-x}$.N$_x$ as Film under Direct Sunlight

Co-nanocomposite of small and wide band gap semiconductors is used here to extend the absorption from full spectrum of solar radiation (visible-region). CdS nanoparticles with band gap energy between TiO$_2$ and CuInS$_2$ can absorb light with wavelength (λ>400 nm) and act as electron injector from conduction band to another. TiO$_2$ is a UV-response (λ<420 nm) with little improvement to longer wavelength due to nitrogen incorporation into its crystal lattice. CuInS$_2$ is active for absorbing longer wavelength (λ≈600-800 nm). The hydrogen production rate of Ag/CuInS$_2$/CdS/TiO$_{2-x}$.N$_x$ under same conditions and the weight used was 0.01 g as (21.6 ±1.6 μmol/h/g) (Figure 5.21 and Table 5.10) and energy efficiency is 0.017%. To investigate the effect of coating CdS nanoparticles, the run is compared with the same run that used from previous results, under same film structure and same weight just without the CdS deposition. It is found that hydrogen production rate as (3.9 ±0.4 μmol/h/g) and energy efficiency is 0.0032%.

Clearly, the deposition of CdS nanoparticles enhances the production because it contributed to more light absorption and energy conversion.

Table 5.3 Results and conditions of $Ag/CuInS_2/TiO_{2-x}.N_x$ as film under direct sunlight (0.005 g).

H_2 production (μmol/h)	H_2 production (μmol/h/g)	Effective Area, m^2	Energy Efficiency % @ x=0	Energy Efficiency % @ x=0.7
0.28 ± 0.04	57.1 ± 9.2	0.000121	0.019	0.063

Photocatalyst type and weight (g)	Nano-structure and geometry	Photocatalyst Size, composition, Crystal structure	Water/ Methanol solution (1:1) Volume basis	Light Intensity If UV, (100 W/m^2) If Sunlight, ≈ (240 W/m^2)
$Ag/CuInS_2/TiO_{2-x}.N_x$ (0.005 g)	QD'S on Nanocomposite thin film	Ag(<200 nm), TiO_2 (<3 μm, anatase) $CuInS_2$ (≈ 65 nm)	10 ml (5 ml each)	sunlight (Texas, College Station, Latitude: 30.6277778 Longitude: -96.3341667)
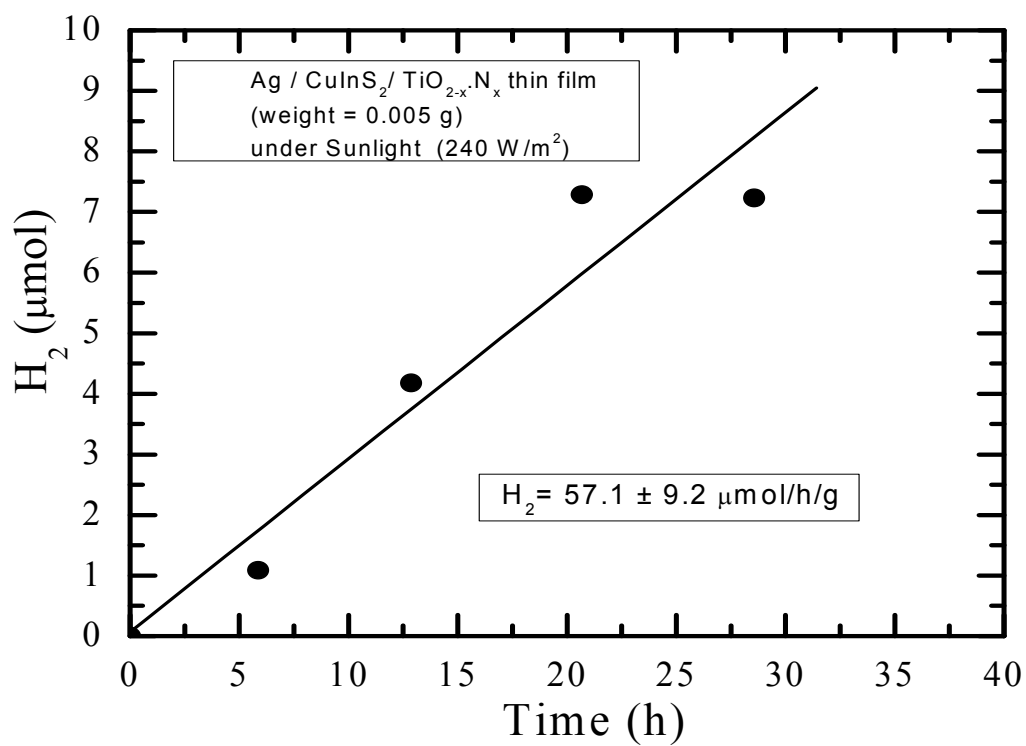
Figure 5.14 Hydrogen production rate of Ag/CuInS$_2$/TiO$_{2-x}$.N$_x$ as film under direct sunlight (0.005 g).

Table 5.4 Results and conditions of Ag/CuInS$_2$/TiO$_{2-x}$.N$_x$ as film under direct sunlight (0.0025 g).

H$_2$ production (µmol/h)	H$_2$ production (µmol/h/g)	Effective Area, m^2	Energy Efficiency % @ x=0	Energy Efficiency % @ x=0.7
0.076 ± 0.006	30.6 ± 2.6	0.000121	0.0051	0.017

Photocatalyst type and weight (g)	Nano-structure and geometry	Photocatalyst Size , composition, Crystal structure	Water/ Methanol solution (1:1) Volume basis	Light Intensity If UV, (100 W/m^2) If Sunlight , ≈ (240 W/m^2)
Ag/CuInS$_2$/TiO$_{2-x}$.N$_x$ (0.0025 g)	QD'S on Nanocomposite thin film	Ag(<200 nm), TiO$_2$ (<3 µm, anatase) CuInS$_2$ (≈ 65 nm)	10 ml (5 ml each)	sunlight (Texas, College Station, Latitude: 30.6277778 Longitude: -96.3341667)
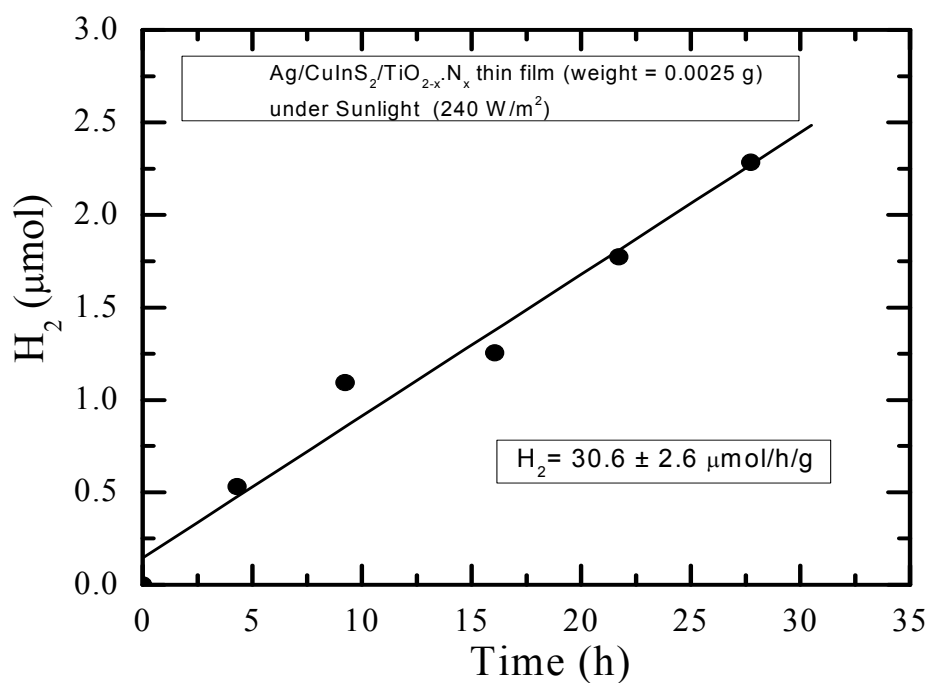
Figure 5.15 Hydrogen production rate of Ag/CuInS$_2$/TiO$_{2-x}$.N$_x$ as film under direct sunlight (0.0025 g).

Table 5.5 Results and conditions of Ag/CuInS$_2$/TiO$_{2-x}$.N$_x$ as film under direct sunlight (0.01 g).

H$_2$ production (µmol/h)	H$_2$ production (µmol/h/g)	Effective Area, m^2	Energy Efficiency % @ x=0	Energy Efficiency % @ x=0.7
0.039 ± 0.004	3.9 ± 0.4	0.000121	0.0026	0.0088

Photocatalyst type and weight (g)	Nano-structure and geometry	Photocatalyst Size, composition, Crystal structure	Water/ Methanol solution (1:1) Volume basis	Light Intensity If UV, (100 W/m^2) If Sunlight, ≈ (240 W/m^2)
Ag/CuInS$_2$/TiO$_{2-x}$.N$_x$ (0.01 g)	QD'S on Nanocomposite thin film	Ag(<200 nm), TiO$_2$ (<3 µm, anatase) CuInS$_2$ (≈ 65 nm)	10 ml (5 ml each)	sunlight (Texas, College Station, Latitude: 30.6277778 Longitude: -96.3341667)
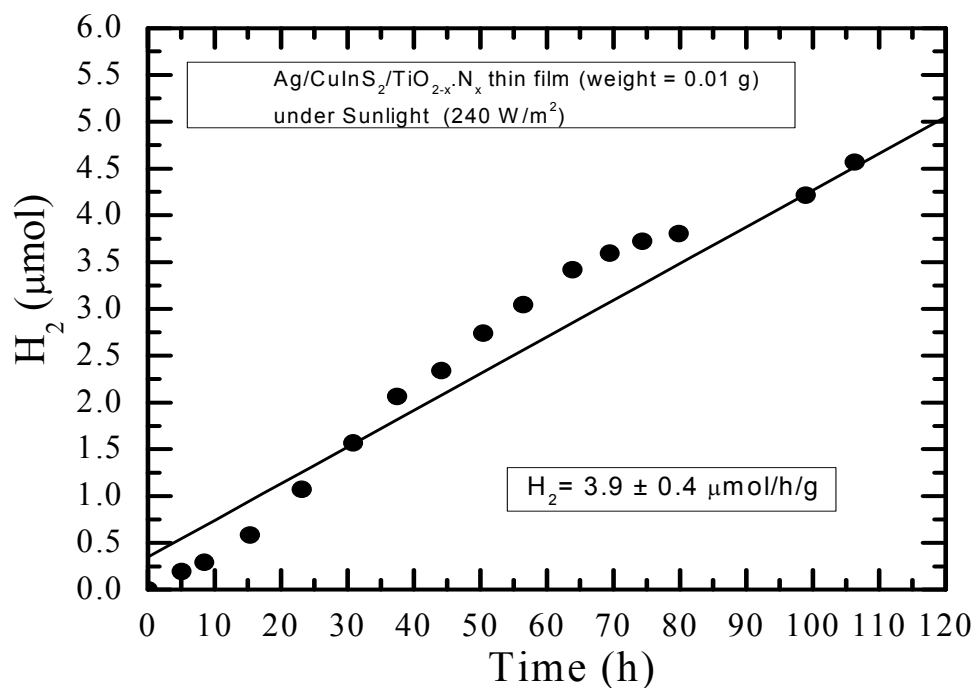
Figure 5.16 Hydrogen production rate of Ag/CuInS$_2$/TiO$_{2-x}$.N$_x$ as film under direct sunlight (0.01 g).

Table 5.6 Results and conditions of Ag/CuInS$_2$/TiO$_{2-x}$.N$_x$ as film under direct sunlight (0.05 g).

H$_2$ production (μmol/h)	H$_2$ production (μmol/h/g)	Effective Area, m^2	Energy Efficiency % @ x=0	Energy Efficiency % @ x=0.7
0.092 ± 0.01	1.8 ± 0.2	0.000121	0.0062	0.02

Photocatalyst type and weight (g)	Nano-structure and geometry	Photocatalyst Size, composition, Crystal structure	Water/ Methanol solution (1:1) Volume basis	Light Intensity If UV, (100 W/m²) If Sunlight, ≈ (240 W/m²)
Ag/CuInS$_2$/TiO$_{2-x}$.N$_x$ (0.05 g)	QD'S on Nanocomposite thin film	Ag(<200 nm), TiO$_2$ (<3 μm, anatase) CuInS$_2$ (≈ 65 nm)	10 ml (5 ml each)	sunlight (Texas, College Station, Latitude: 30.6277778 Longitude: -96.3341667)
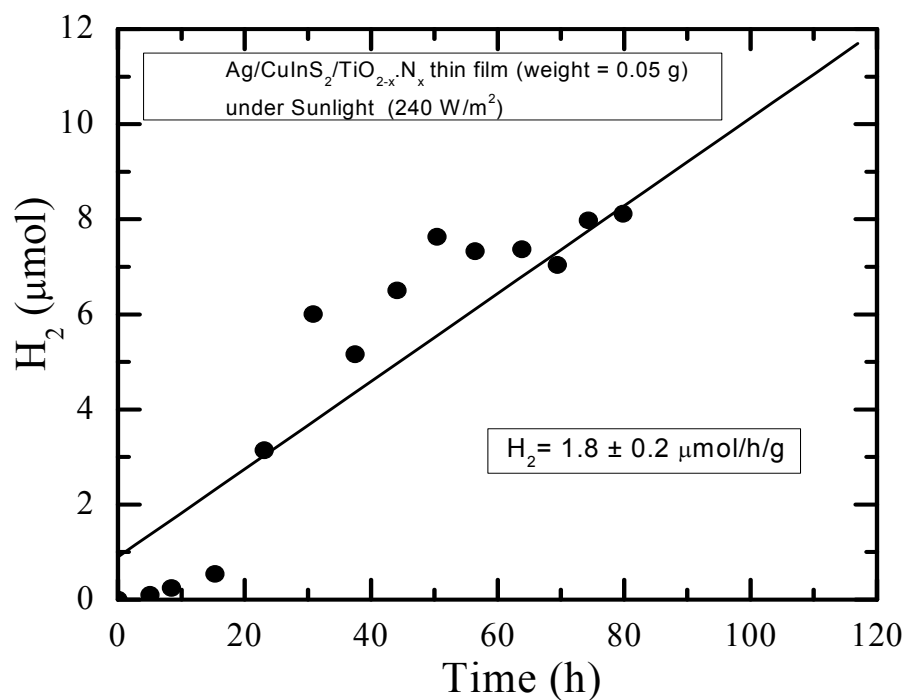
Figure 5.17 Hydrogen production rate of Ag/CuInS$_2$/TiO$_{2-x}$.N$_x$ as film under direct sunlight (0.05 g).

Table 5.7 Results and conditions of Ag/CuInS$_2$/TiO$_{2-x}$.N$_x$ as film under direct sunlight (0.075 g).

H$_2$ production (µmol/h)	H$_2$ production (µmol/h/g)	Effective Area, m^2	Energy Efficiency % @ x=0	Energy Efficiency % @ x=0.7
0.044 ± 0.003	0.59 ± 0.05	0.000121	0.00299	0.0099

Photocatalyst type and weight (g)	Nano-structure and geometry	Photocatalyst Size, composition, Crystal structure	Water/ Methanol solution (1:1) Volume basis	Light Intensity If UV, (100 W/m²) If Sunlight, ≈ (240 W/m²)
Ag/CuInS$_2$/TiO$_{2-x}$.N$_x$ (0.075 g)	QD'S on Nanocomposite thin film	Ag(<200 nm), TiO$_2$ (<3 µm, anatase) CuInS$_2$ (≈ 65 nm)	10 ml (5 ml each)	sunlight (Texas, College Station, Latitude: 30.6277778 Longitude: -96.3341667)
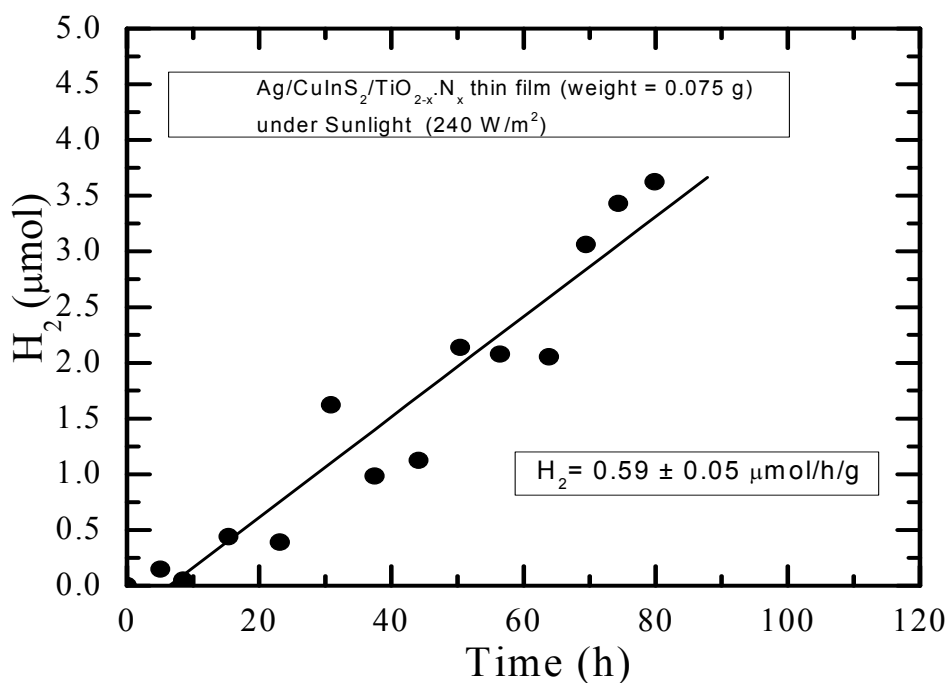
Figure 5.18 Hydrogen production rate of Ag/CuInS$_2$/TiO$_{2-x}$.N$_x$ as film under direct sunlight (0.075 g).

Table 5.8 Results and conditions of Ag/CuInS$_2$/TiO$_{2-x}$.N$_x$ as film under direct sunlight (0.1 g).

H$_2$ production (μmol/h)	H$_2$ production (μmol/h/g)	Effective Area, m^2	Energy Efficiency % @ x=0	Energy Efficiency % @ x=0.7
0.034 ± 0.001	0.34 ± 0.01	0.000121	0.0023	0.0077

Photocatalyst type and weight (g)	Nano-structure and geometry	Photocatalyst Size, composition, Crystal structure	Water/ Methanol solution (1:1) Volume basis	Light Intensity If UV, (100 W/m²) If Sunlight, ≈ (240 W/m²)
Ag/CuInS$_2$/TiO$_{2-x}$.N$_x$ (0.1 g)	QD'S on Nanocomposite thin film	Ag(<200 nm), TiO$_2$ (<3 μm, anatase) CuInS$_2$ (≈ 65 nm)	10 ml (5 ml each)	sunlight (Texas, College Station, Latitude: 30.6277778 Longitude: -96.3341667)
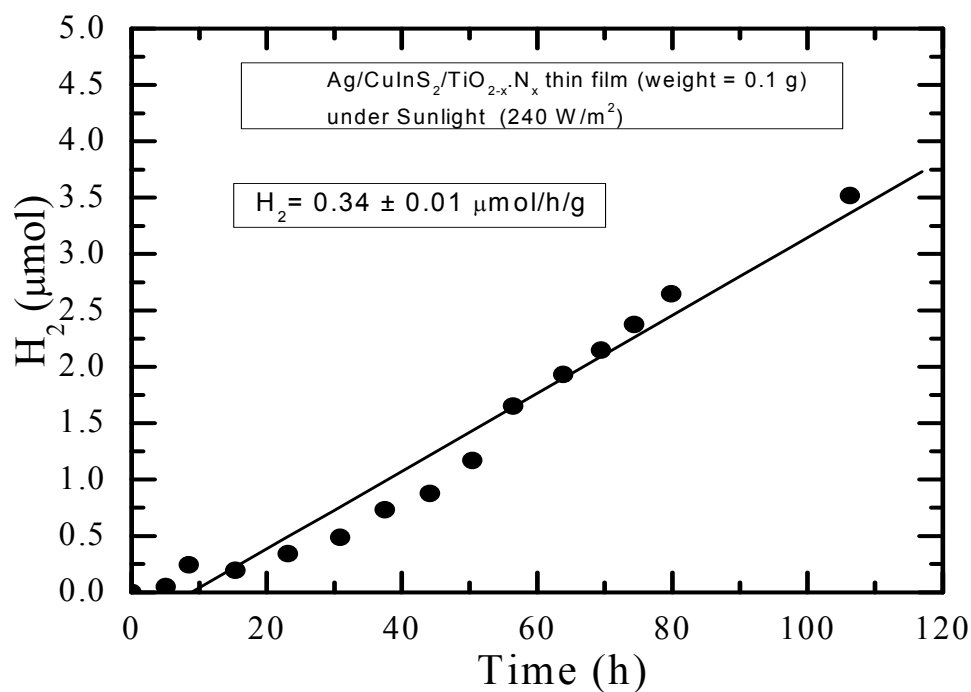
Figure 5.19 Hydrogen production rate of Ag/CuInS$_2$/TiO$_{2-x}$.N$_x$ as film under direct sunlight (0.1 g).

Table 5.9 Results and conditions of Ag/CuInS$_2$/TiO$_{2-x}$.N$_x$ as film under direct sunlight (1.0 g).

H$_2$ production (μmol/h)	H$_2$ production (μmol/h/g)	Effective Area, m^2	Energy Efficiency % @ x=0	Energy Efficiency % @ x=0.7
0.063 ± 0.005	0.06 ± 0.005	0.000121	0.00428	0.0142

Photocatalyst type and weight (g)	Nano-structure and geometry	Photocatalyst Size, composition, Crystal structure	Water/ Methanol solution (1:1) Volume basis	Light Intensity If UV, (100 W/m^2) If Sunlight, ≈ (240 W/m^2)
Ag/CuInS$_2$/TiO$_{2-x}$.N$_x$ (1.0 g)	QD'S on Nanocomposite thin film	Ag(<200 nm), TiO$_2$ (<3 μm, anatase) CuInS$_2$ (≈ 65 nm)	10 ml (5 ml each)	sunlight (Texas, College Station, Latitude: 30.6277778 Longitude: -96.3341667)
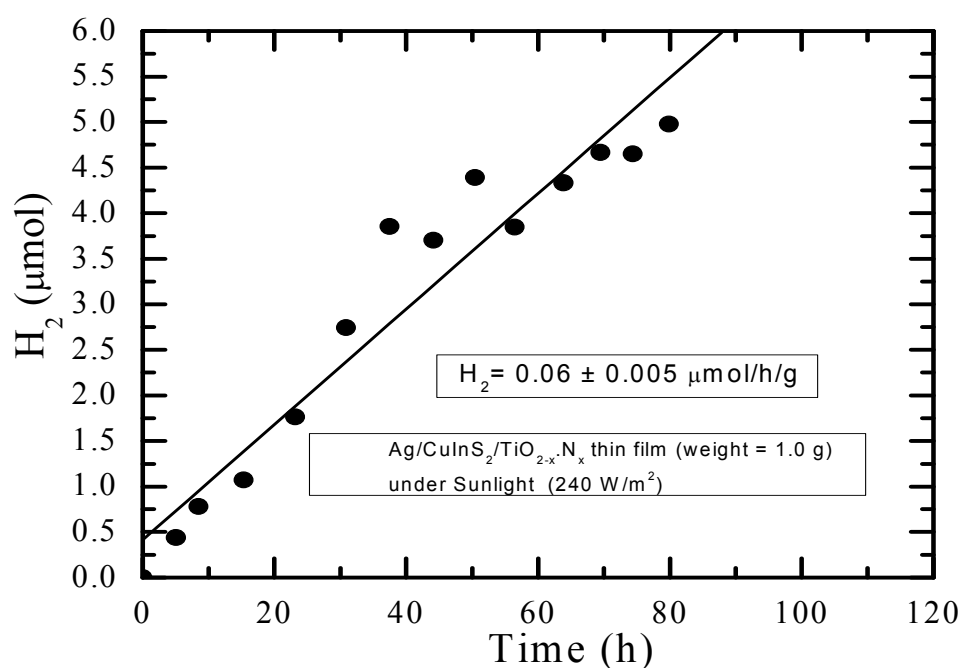
Figure 5.20 Hydrogen production rate of Ag/CuInS$_2$/TiO$_{2-x}$.N$_x$ as film under direct sunlight (1.0 g).

Table 5.10 Results and conditions of Ag/CuInS$_2$/CdS/TiO$_{2-x}$.N$_x$ as film under direct sunlight (0.01 g).

H$_2$ production (μmol/h)	H$_2$ production (μmol/h/g)	Effective Area, m^2	Energy Efficiency % @ x=0	Energy Efficiency % @ x=0.7
0.21 ± 0.01	21.6 ± 1.6	0.000121	0.014	0.047

Photocatalyst type and weight (g)	Nano-structure and geometry	Photocatalyst Size, composition, Crystal structure	Water/ Methanol solution (1:1) Volume basis	Light Intensity If UV, (100 W/m^2) If Sunlight, ≈ (240 W/m^2)
Ag/CuInS$_2$/ CdS /TiO$_{2-x}$.N$_x$ (0.01 g)	QD'S on Nanocomposite thin film	Ag(<200 nm), TiO$_2$ (<3 μm, anatase) CuInS$_2$ (≈ 65 nm) CdS (< 100 nm)	10 ml (5 ml each)	sunlight (Texas, College Station, Latitude: 30.6277778 Longitude: -96.3341667)
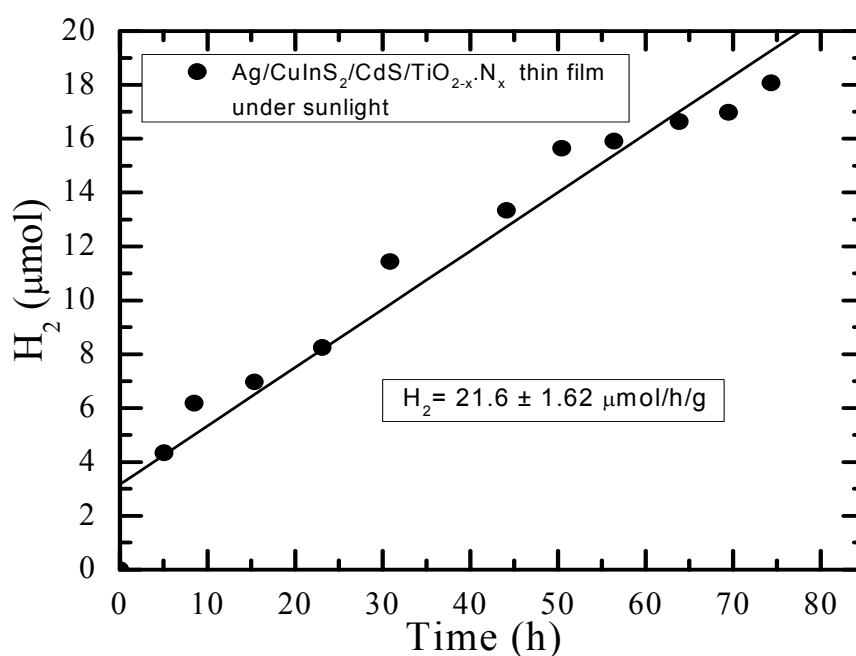
Figure 5.21 Hydrogen production rate of Ag/CuInS$_2$/CdS/TiO$_{2-x}$.N$_x$ as film under direct sunlight (0.01 g).

CONCLUSIONS

The performance of coating anatase TiO_2 film with different functional nanomaterials such as nitrogen-doping, nanoparticles $CuInS_2$ (65 nm), and Ag nanoparticles were evaluated. The evaluation is based on rate of hydrogen production and the energy efficiency (%). All runs are carried out under direct sunlight with same geological location, height, water/methanol solution, and reaction conditions except changing the weight of the film.

The idea is to know the trend of weight of film verses the energy efficiency % to know the maximum limit can be reached by this photocatalytic system to enhance hydrogen production from water-splitting under sunlight.

The initial experimental results and calculation of energy efficiency showed that energy efficiency can be improved, if one-gram of $Ag/CuInS_2/CdS/TiO_{2-x}.N_x$ film used to generate hydrogen from water/methanol equal volume soution under sunlight. Then, the experiments were designed based on this important result by varying the weight up to one-gram. The expectation of weight verses energy effeceincy (%) is linear trend.

However, it is found that the results show poor performance than the results reported in above chapters for diffrent photocatalys systems. The justification of this obseravtion summaried as follows: (1) under sunlight, the light intensity highely effected by weather and not constant as in case of using UV light in the labiratory. (2) The layer by layer deposition of each nanomaterials might has negative impact on overall performance.(3) the arrangment of film species (broken into small species) sometimes ovelapped to each other and share the same light wavelength and reduce the

total surface area exposed to light. (4) Grain boundaries and interfaces act as recombination center to charge carriers (electron-hole) and they reduce the quantum efficiency (photon-to-electron-conversion efficiency) (5) Interfaces between layers reduce the surface tension and also interface tension between electrode/electrolyte surfaces. (6) Clusters of nanoparticles accumulate to prevent the quantum effect on properties (prevent the generation of more than one electron-hole pair for a single incident photon).

The three major limiting processes in obtaining efficient photoconversion from metal-oxide electrodes are: (a) bulk recombination via band gap state; (b) electron loss in valence band; (c) surface recombination; (d) the excited electron can be lost to an electron scavenger in the electrolyte [5].

CHAPTER VI

TiO$_2$ NANOSTRUCTURES-PROPERTIES RELATIONSHIP AND THE IMPACT ON SOLAR TO HYDROGEN CONVERSION EFFICIENCY

OVERVIEW

The (0-D) dimensional nanostructure materials (nanosphere, nanopowders) was tested relatively with (1-D) dimensional nanostructure materials (nanotube, nanorod, core/shell nanowires), for hydrogen production from water-splitting under UV light to investigate the effect of size, structure-dependent properties and activity. 2-D nanostructure such as thin film already tested in Chapter II and (1-D) such as nanofiber will be presented in Chapter VII. Several fabrication methods to synthesis these nanostructures material are applied such as hydrothermal, sol-gel, chemical vapor deposition, elctrospinning...etc. The main preparations parameters need to be controlled are the area, temperature, pressure, ionic strength, aging time, pH value (acid or base), the water solution and nanomaterials. The performance of nanomaterials is highly depends on processing, structure-properties, relationship and their interaction with solid or liquid interfaces.

INTRODUCTION

Water is a polar molecule; it has two oppositely charged atoms. Within each water molecule, hydrogen binds with oxygen atoms through regular electron sharing. As a result, two hydrogen atoms have their positively charged proton core partly exposed. The negatively charged electrons from the oxygen atoms bind to the free protons. This

combination is a so-called hydrogen bond. It allows water to remain liquid instead of gaseous at higher temperatures than any other fluid; you need to heat it up to 100°C (at 1 atmosphere) before the hydrogen bonds dissolve (Figure 6.1) [98]. Direct water splitting requires extremely high temperature and an efficient and safe separation of an explosive mixture of hydrogen and oxygen. Thermochemical cycles are widely used to split water at significantly lower temperature. In contrast, photoelectrochemical water-splitting or artificial photosynthesis can overcome these obstacles by producing hydrogen and oxygen separately using sunlight (Figure 6.2).
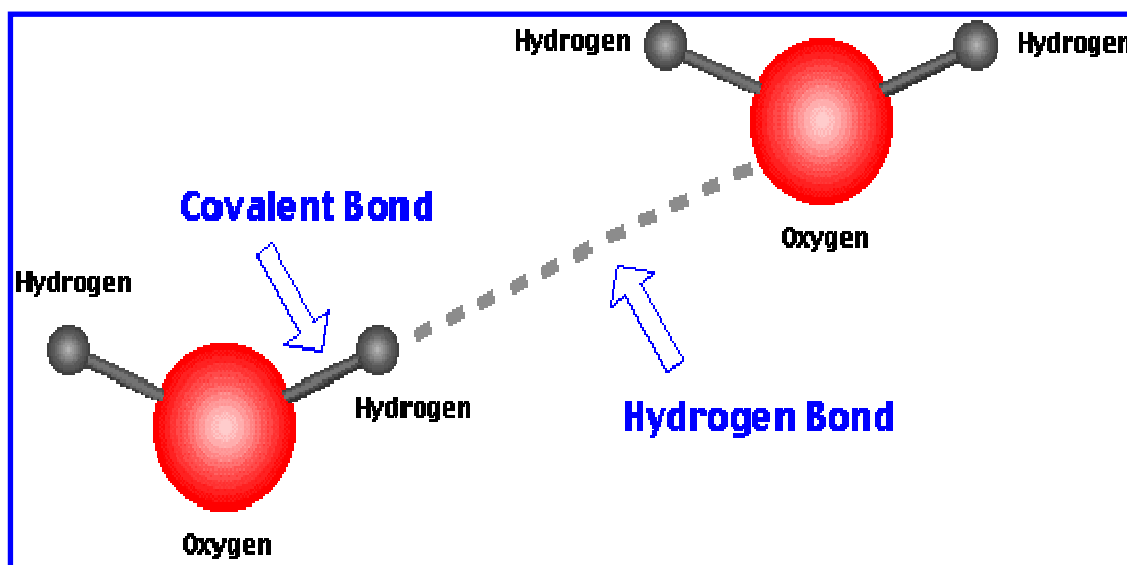
Figure 6.1 Shows the bonding energy between oxygen and hydrogen atoms to form water. Minimum energy required to split water is $E = [\Delta G°_{water}/2NA] = 1.23$ eV, $2H_2O + h\nu \rightarrow O_2 + 2H_2$ [98].

The application of one-dimensional nanostructure such as nanowires, nanorods, and nanotubes of TiO_2 nanocomposites for photoelectrochemical water-splitting provide great advantages to improve the performance due to their structure-properties

relationship [99]. The nature of one dimensional nanostructure suppresses the recombination of the charge carriers by removing the electrons as quickly as possible [100].
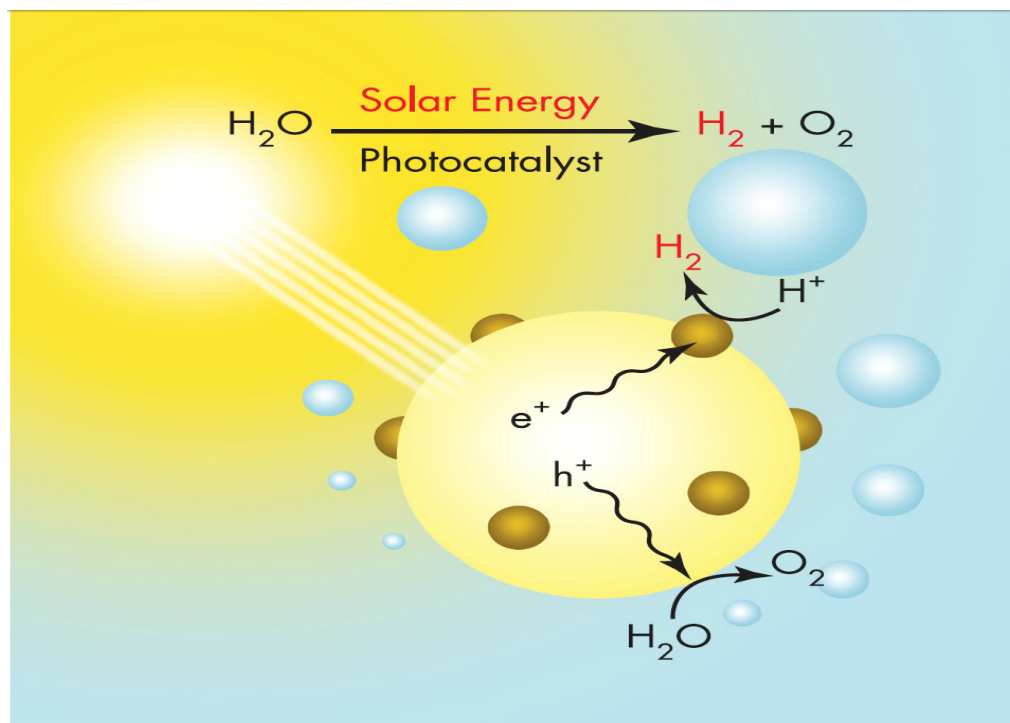
Figure 6.2 Diagram shows simple description of hydrogen production from water-splitting by solar energy [101].

Cu/TiO$_2$ Nanotube and Nanorod by PAATM

Recently, there is growing interest in nanostructured metal oxides photoelectrodes, including nanotubes and nanorods as they offer advantages over their bulk counterparts for photoelectrodes due to their large surface area, short lateral diffusion length and low reflectivity. Nevertheless, most of the metal oxides have large band gap energies, leading to limited light absorption in the visible region of interest, which imposes a fundamental

limitation on overall photon to hydrogen efficiency. One-dimensional nanostructures, such as nanowires, offer the added potential advantage of improved charge transport over zero-dimensional nanostructure, such as nanoparticles and nanosphere [93]. TiO_2 nanowire, nanorod, and nanotube were synthesized by porous anodic aluminum oxide template membrane (PAATM) which will be described in details in design and synthesis section.

Cu/TiO$_2$ Nanowire (Core/Shell) by PAAM & CBD

(Core/shell) nanowires as one-dimensional nanostrucuters were used in order to investigate the deposition of copper inside the TiO_2 nanotube. The surface area provided in Cu/TiO$_2$ (core/shell) nanowire suppose to be less than the surface area of Cu/TiO$_2$ nanotube, therefore, it is expected to have less hydrogen production rate. The Cu/TiO$_2$ (core/shell) nanowire can be prepared by making TiO_2 nanotube first as mentioned in the above paragraph. Then, the nanotubes filled with copper metal using chemical bath deposition method to deposited Cu inside the tube holes. Later, these samples will be tested for hydrogen production from water/methanol solution under UV light under same reaction conditions to study the relationship between nanostructure and their photocatalytic and optical properties.

Cu/TiO$_2$ Uniform Nanosphere

The morphology control of uniform size of TiO_2 is very difficult due to high reactivity of titanium precursors. It is important to control the structure and surface area because they govern the photocatalytic activity and properties of TiO_2 [102] Uniform nanosphere TiO_2 as 0-D nanostructure synthesized using hydrothermal procedures and autoclave reactor.

Cu/TiO$_2$ uniform nanosphere is evaluated for hydrogen production from water/methanol solution under UV light to study the effect of structure on overall activity and compared with 1-D nanostructure like nanotube and nanorod. TiO$_2$ and Cu/TiO$_2$ nanoparticels will also prepared as shown in Chapter III and tested under sunlight to investigate the performance of hydrogen production.

DESIGN AND SYNTHESIS

Porous anodic aluminum oxide template membrane (PAATM) is widely used to fabricate nanotubes, nanorods, and nanowires by sol-gel deposition of chemical precursor into their nanoporous providing simple and low cost fabrication technique [61] The membranes obtained from (Whatman Company). The pore diameter is ~200 nm and the thickness is ~60 μm.

Cu/TiO$_2$ Nanotubes and Nanorods

The fabrication procedure of TiO$_2$ nanotube and nanorod by PAATM was described by [61] and it used here as follows: 150 ml de-ionized water added to 0.74 gm TiF$_4$ (Sigma Aldrich), (should be store in vacuum or argon environment). The mixture Stirred for one hour with magnetic stirrer and closed with foil. Magnetic stirrer removed, then, heated the beaker up to 60°C (thermometer inserted in the beaker) while keeping the beaker closed. At 60°C, the membranes inserted in the mixture (should be hold carefully because it is fragile). If membranes kept inside the mixture for 60 minutes, thin wall TiO$_2$ nanotube will formed or if kept for 24 hours, TiO$_2$ nanorod will formed. After 10 minutes, membranes dried by tissue carefully. The membranes annealed at 225°C for 2

hours, then, it cold for overnight. Then, the two surfaces of membrane were polished using glue and polish paper. To remove the membrane, it dissolved with 0.5 M solution of water and NaOH (EMD company), stirred it for 1 hour and centrifuged many times to etch the ammonium oxide and separate the liquid phase from the solid phase (TiO_2 nanotube or nanorod). The samples washed with water two times and then dried in room conditions for 10 minutes.

Figure 6.3 shows the diagram of fabrication procedures of TiO_2 nanotube and nanorod using PAATM. The copper embedded on surface of TiO_2 nanotube and TiO_2 nanorod using common wet impregnation method that mentioned earlier in Chapter III in details. 15 ml ethanol and 0.032 g of Cu $(NO_3)_2.2.5H_2O$ mixed with 0.1 g of either TiO_2 nanotube or nanorod to have 10% mole of Cu deposition. Following by stirring for 2 hours and then heating overnight at 80°C, and drying overnight at 100°C. Finally, it annealed for 5 hours at 500°C to form anatase TiO_2 phase.
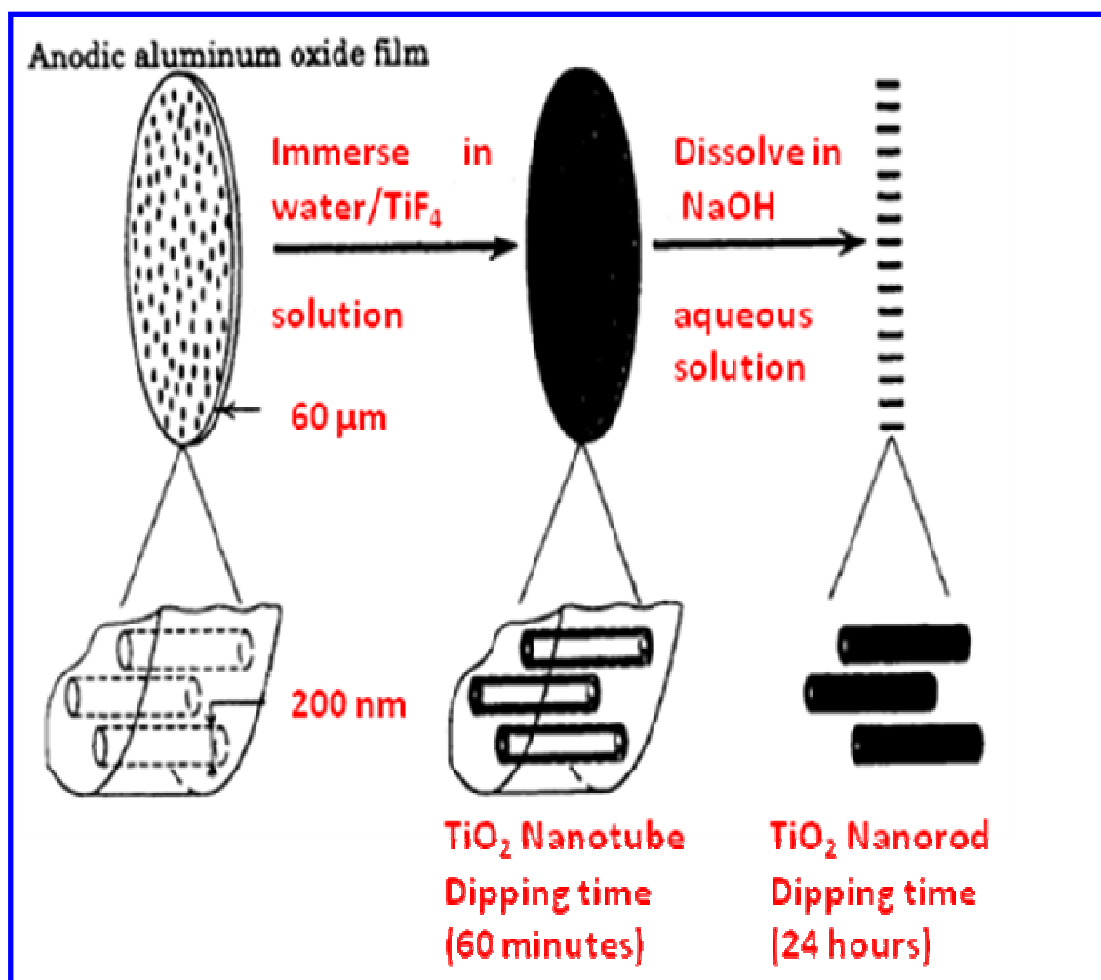
Figure 6.3. Schematic diagram shows the procedure to synthesized TiO$_2$ nanotube and nanorod using porous anodic aluminum oxide template membrane PAATM [103].

Cu/TiO$_2$ Nanowires (Core/Shell)

The fabrication procedures of Cu/TiO$_2$ (core/shell) nanowires (Figure 6.4) are simple and as follows; after fabrication of TiO$_2$ nanotube and before etching step, the membranes were closed from one-end side by glass substrate using high vacuum grease. The solution prepared to immerse the membranes is 10 ml ethanol, 0.07 g of TiO$_2$ (estimation) and 1.15 g of copper nitrate to have 85% mol of Cu deposition. Then, the

nanoporous of membranes were filled with copper precursor (Cu $(NO_3)_2.2.5H_2O$) by capillary force for 2 hours. The membranes were dried at 100°C for another 2 hours, washed with water, aceton. Separate the Cu/TiO_2 (core/shell) nanowires by etching using 0.5 M NaOH aqueous solution. After removing the alumimium oxide template, the Cu/TiO_2 (core/shell) nanowires annealed for 5 hours at 500°C to form anatase TiO_2 phase.
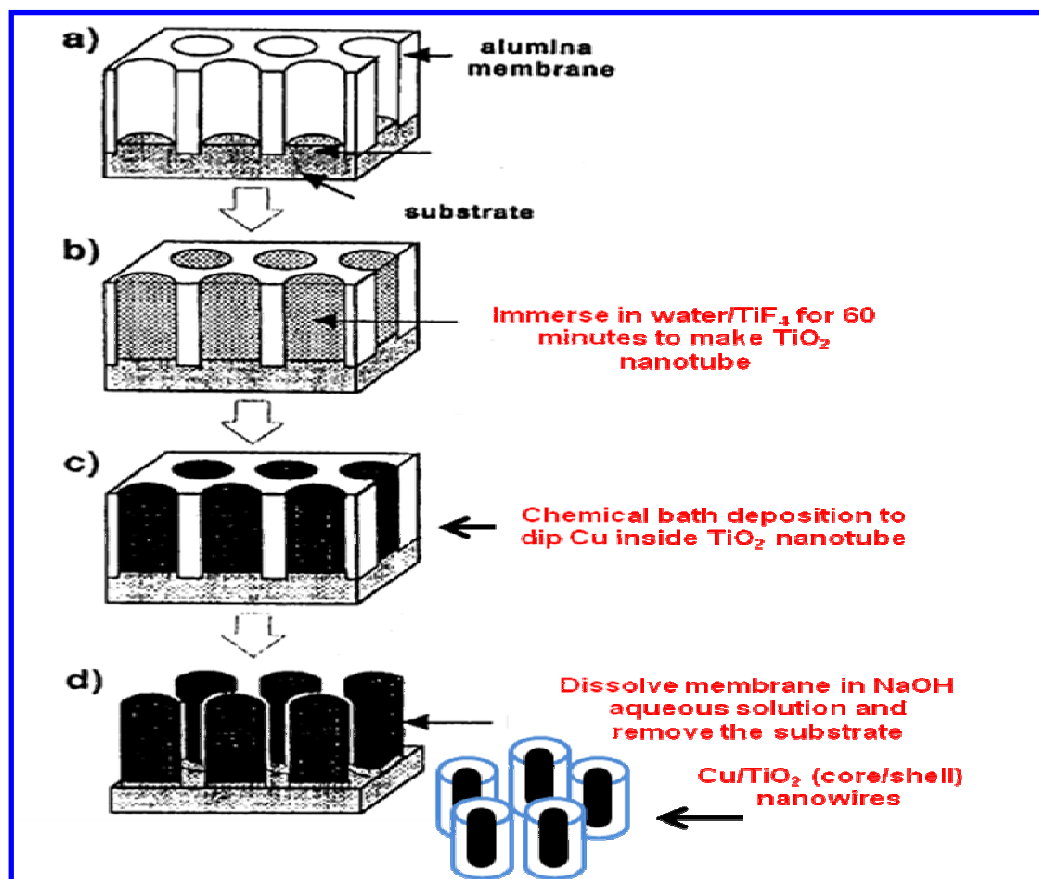
Figure 6.4 The diagram shows the procedure to fabricate Cu/TiO_2 (core/shell) nanowires [103].

Cu/TiO₂ Uniform Nanospheres

Typically, for the preparation of uniform nanosphere TiO_2, 2 mmol of titanium isopropoxide (TTIP, Sigma Aldrich) was dissolved in 20 ml of ethanol (Sigma Aldrich). 4 mmol of tetrabutylammonium hydroxide (TBAH, 40% aqueous solution, Sigma Aldrich) was then added slowly to this solution. The molar ratio in the resultant solution was 1.0 TTIP/2.0 TBAH/43.5 H_2O/170 ethanol. The mixture was stirred for 30 minutes to obtain a clear solution, and transferred to an autoclave (Figure 6.5).

The temperature of the autoclave was raised to 240°C at a rate of 5°C min^{-1}, and held at this temperature for 6 hours. The white precipitate obtained was washed several times with ethanol [104] The copper embedded on surface of TiO_2 uniform nanosphere using common wet impregnation method. 15 ml ethanol and 0.032 g of Cu $(NO_3)_2.2.5H_2O$ mixed with 0.1 g of either TiO_2 uniform nanosphere to have 10% mole of Cu deposition. Following by stirring for 2 hours and then heating overnight at 80°C, and drying overnight at 100°C. Finally, it annealed for 5 hours at 500°C to form anatase TiO_2 phase.

The molar ratio was
1.0 TTIP : 2.0 TBAH : 43.5 H_2O : 170 ethanol.

Stirring 30 min

transferred to
autoclave

240 °C
for 6h
(5 °C/min)

Cu deposition by wet
impregnation method

Annealing at 500°C
for 5h
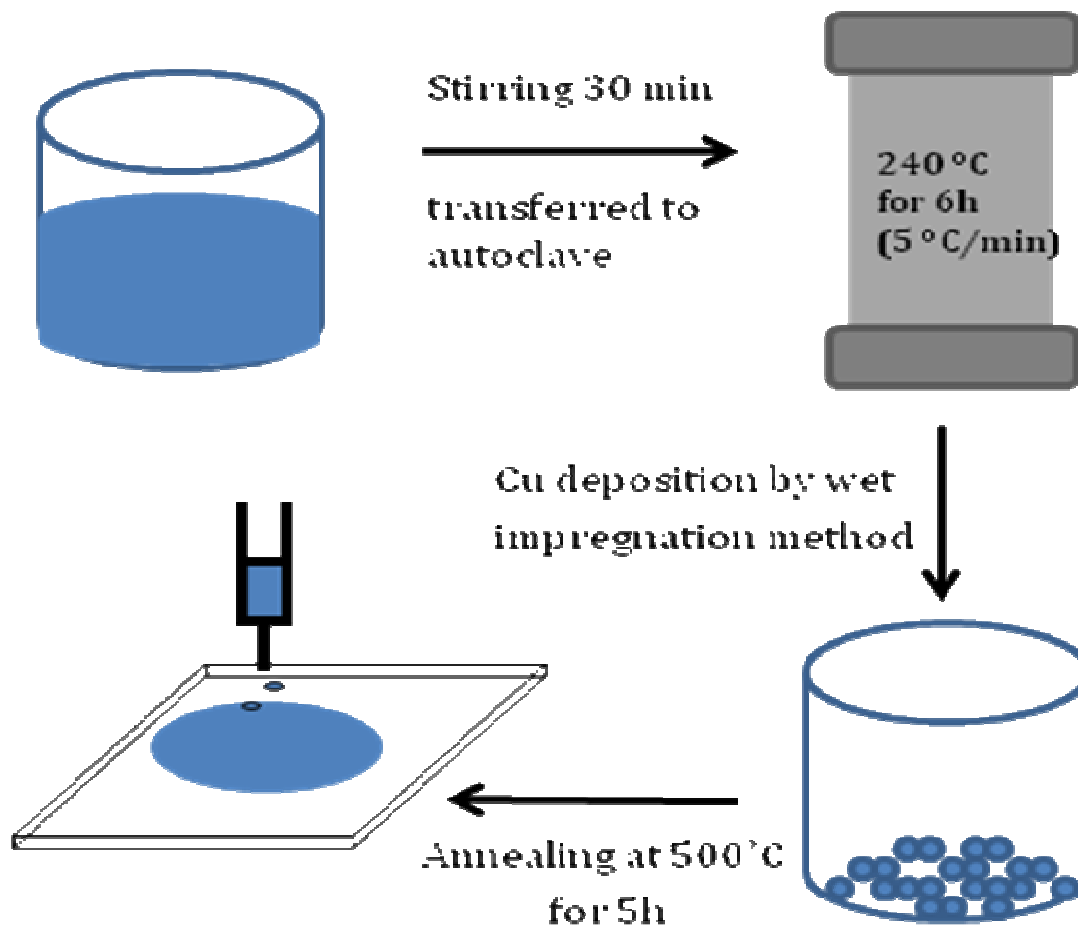
Figure 6.5 The synthesis of Cu^{+2} and CuO/TiO_2 uniform nanosphere [104].

Cu^{+2} and CuO/TiO_2 Nanoparticles and then Nanopowders

The synthesis procedure of TiO_2 nanoparticels and Cu^{+2} and CuO/TiO_2 nanoparticles and then nanopowders was described in details in Chapter III.

Adding Dye (Rose Bengal Sodium) in the Water/Methanol Solution in the Presence of Cu^{+2} and CuO/TiO_2 Nanoparticles

The dye used to sensitize TiO_2 film is Rose Bengal Sodium salt, the empirical formula is $C_{20}H_2C_{14}I_4Na_2O_5$ with dye content ~90 % (Figure 6.6) was obtained from (Sigma Aldrich). It is powder and solubility color is pink to red. This dye is selected to be used because it has strong light absorption with excellent photovoltaic, electrochemical, and catalytic properties as well as low cost. The dye will be added and mixed with water/methanol solution to study the effect of dye on overall performance in term of light absorption and focusing the light toward TiO_2 photoelectrode.
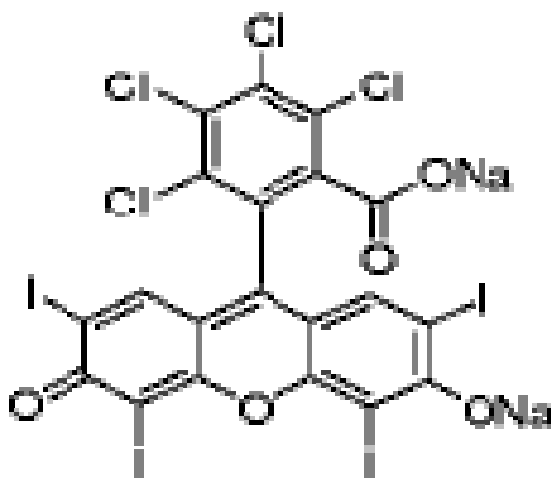
Figure 6.6 Rose Bengal Sodium dye chemical structure [105].

CHARACTERIZATION

The images of Cu^{+2} and CuO/TiO_2 nanostructures that include nanotube, nanorod, nanosphere, and (core/shell) nanowire were charecterized using Scanning Electron

Microscopy (SEM) (Figure 6.7). The SEM images were taken using JEOL JSM-6400. The Surface element analysis was obtained using Energy dispersive X-ray spectroscopy (EDS) as shown in Table 6.1. The EDS results were obtained using JEOL JSM-6400. Figure 6.8 Optical microscopic images of anatase Cu^{+2}/TiO_2 uniform nanosphere prepared by autoclave reactor. Figure 6.9 Digital image of Cu^{+2} and CuO/TiO_2 nanoparticles prepared by sol-gel method.
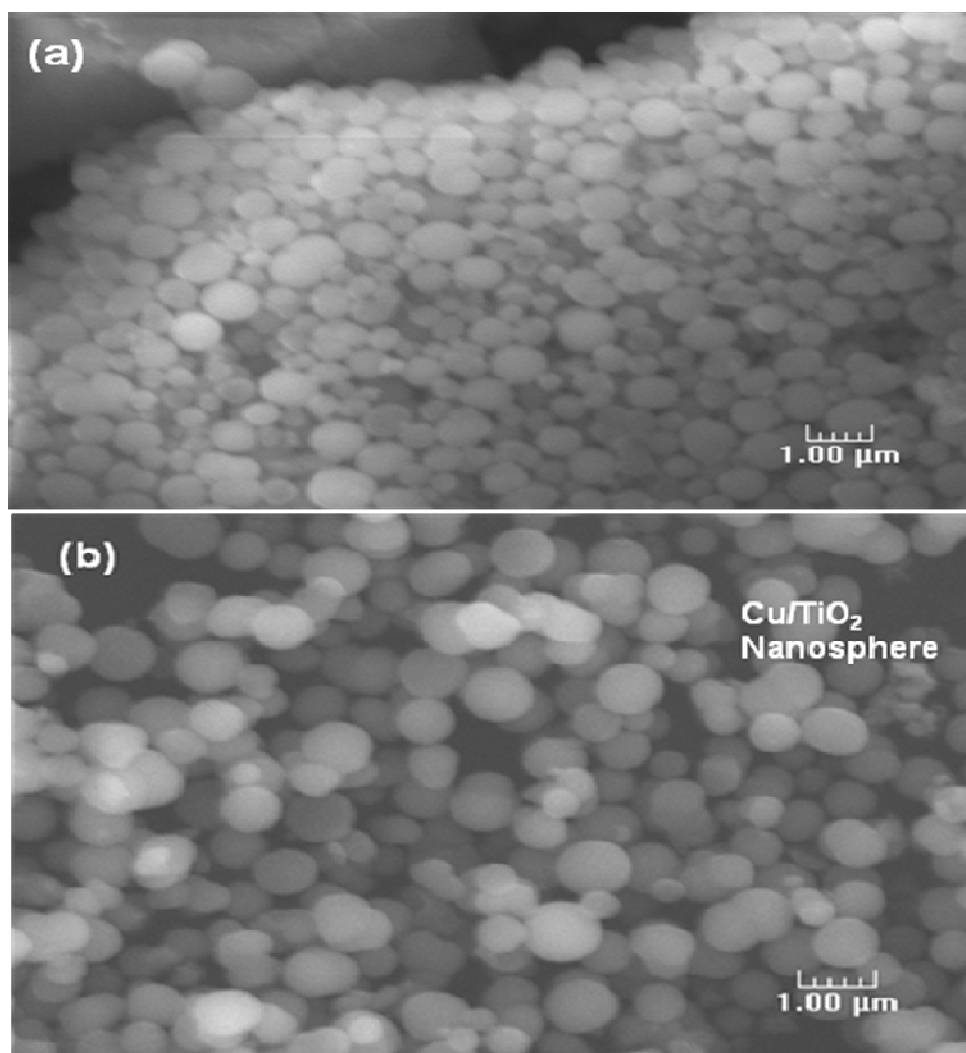
Figure 6.7 SEM images of (a, b) Cu^{+2} and CuO/TiO_2 nanosphere.
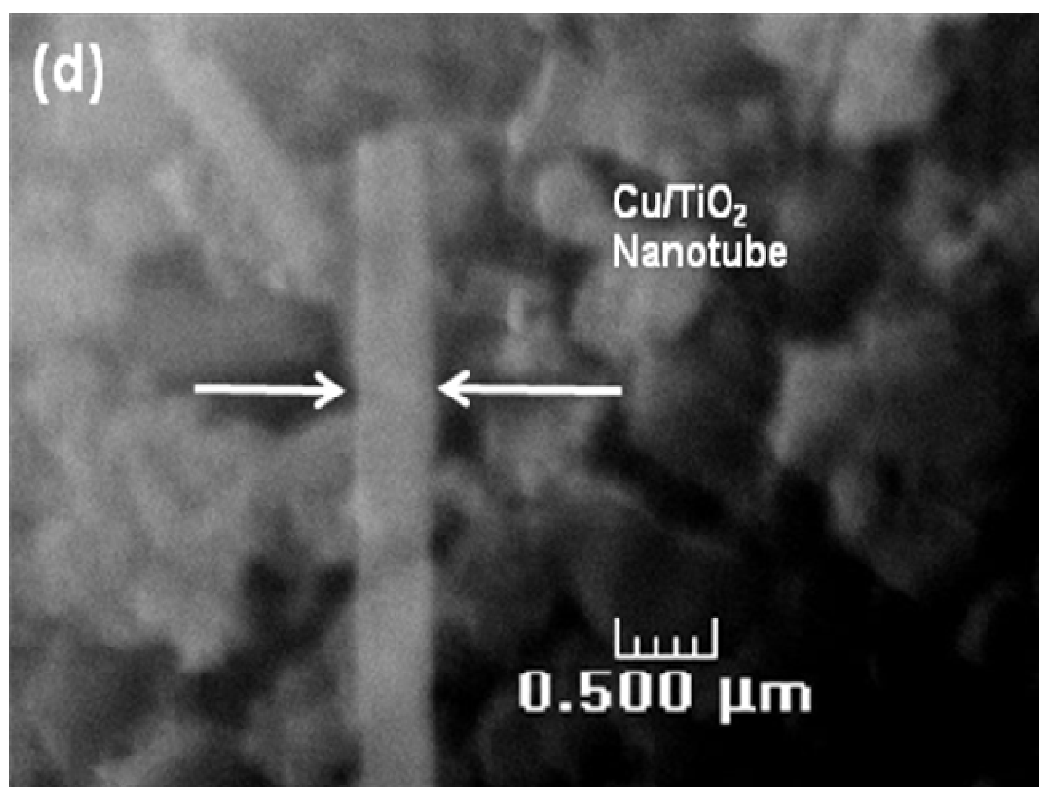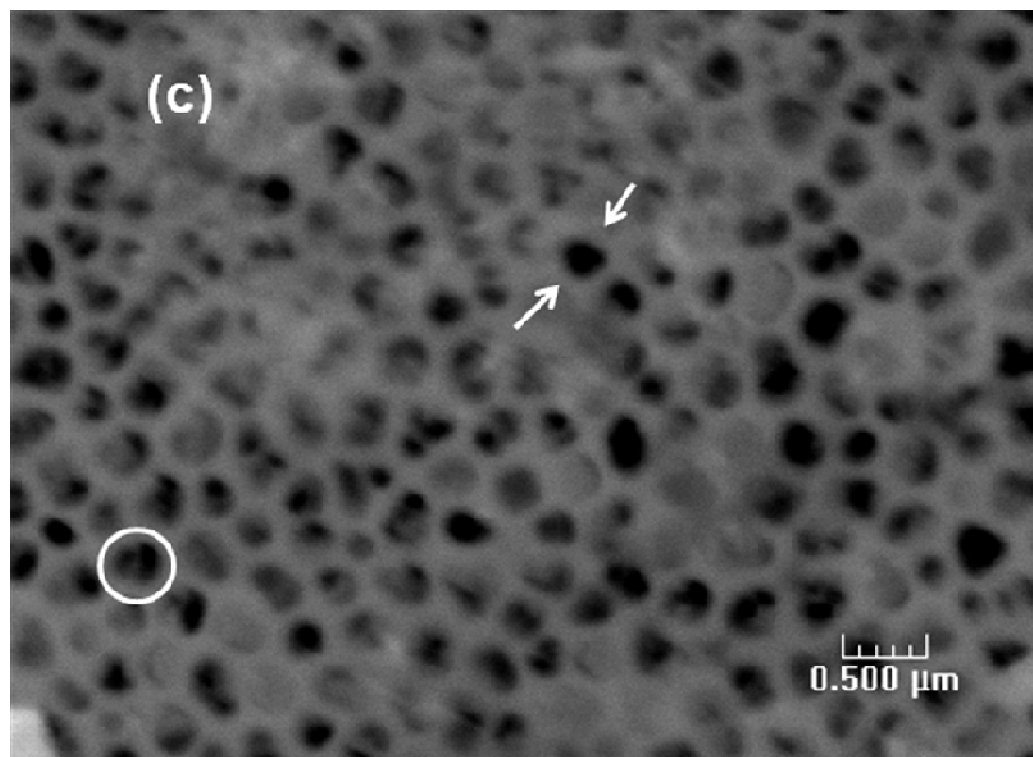
Figure 6.7 continued (c) the PAATM membrane pore size (d) Cu^{+2} and CuO/TiO_2 nanotube.
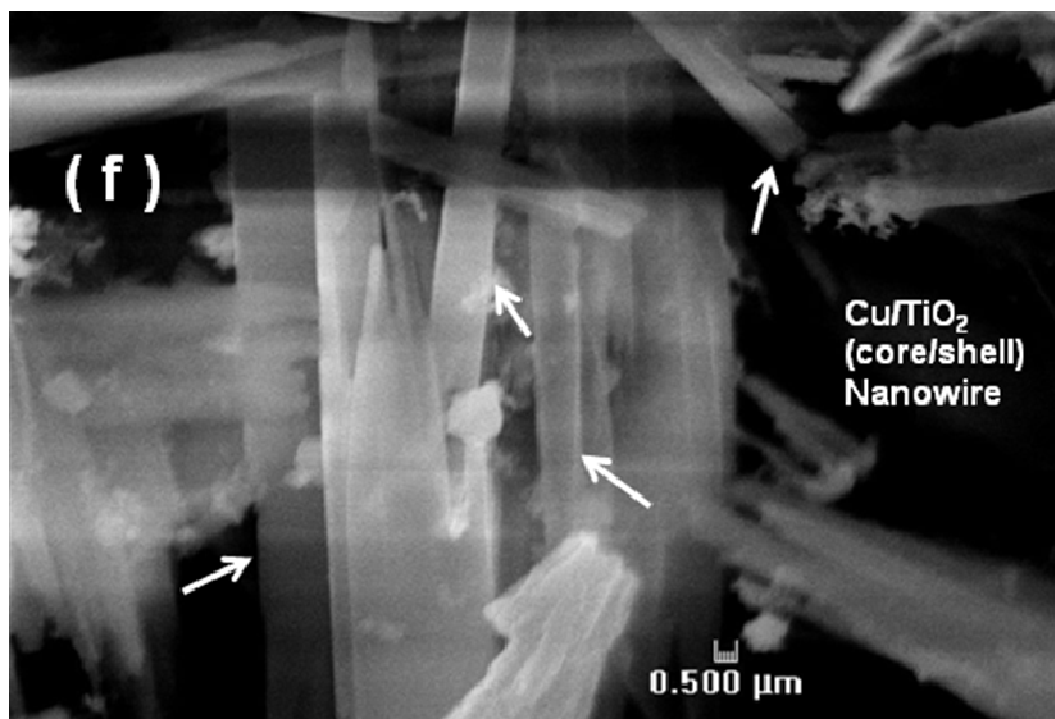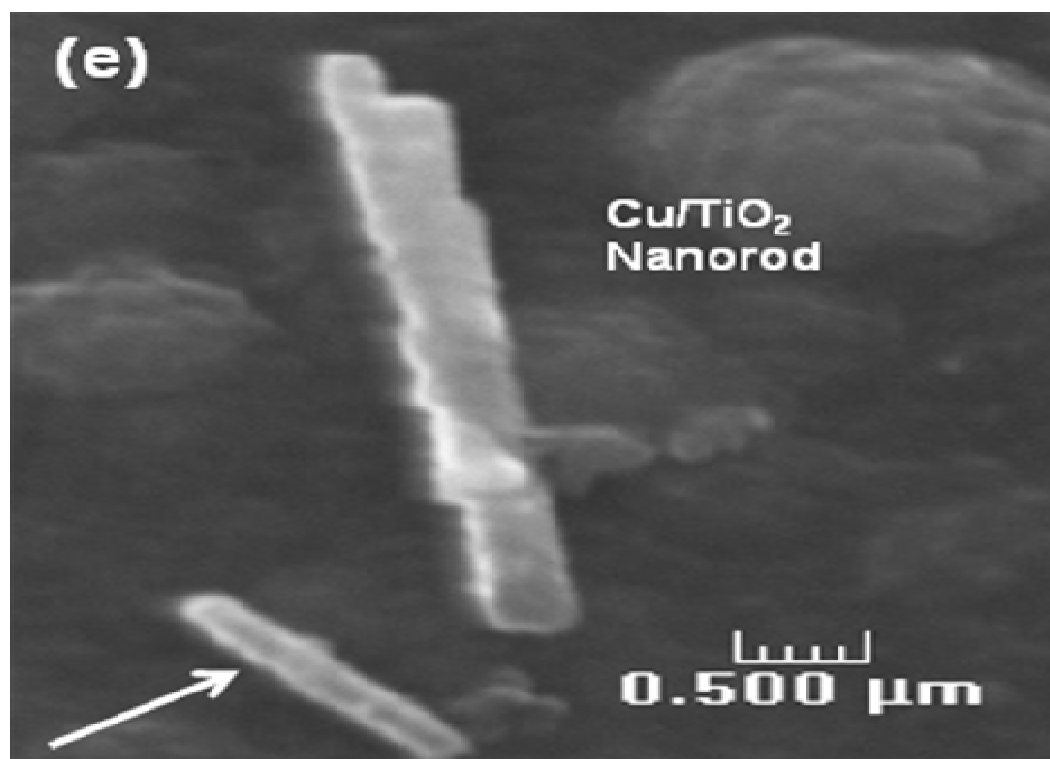
Figure 6.7 continued (e) Cu^{+2} and CuO/TiO_2 nanorod (f) Cu^{+2} and CuO/TiO_2 (core/shell) nanowire.
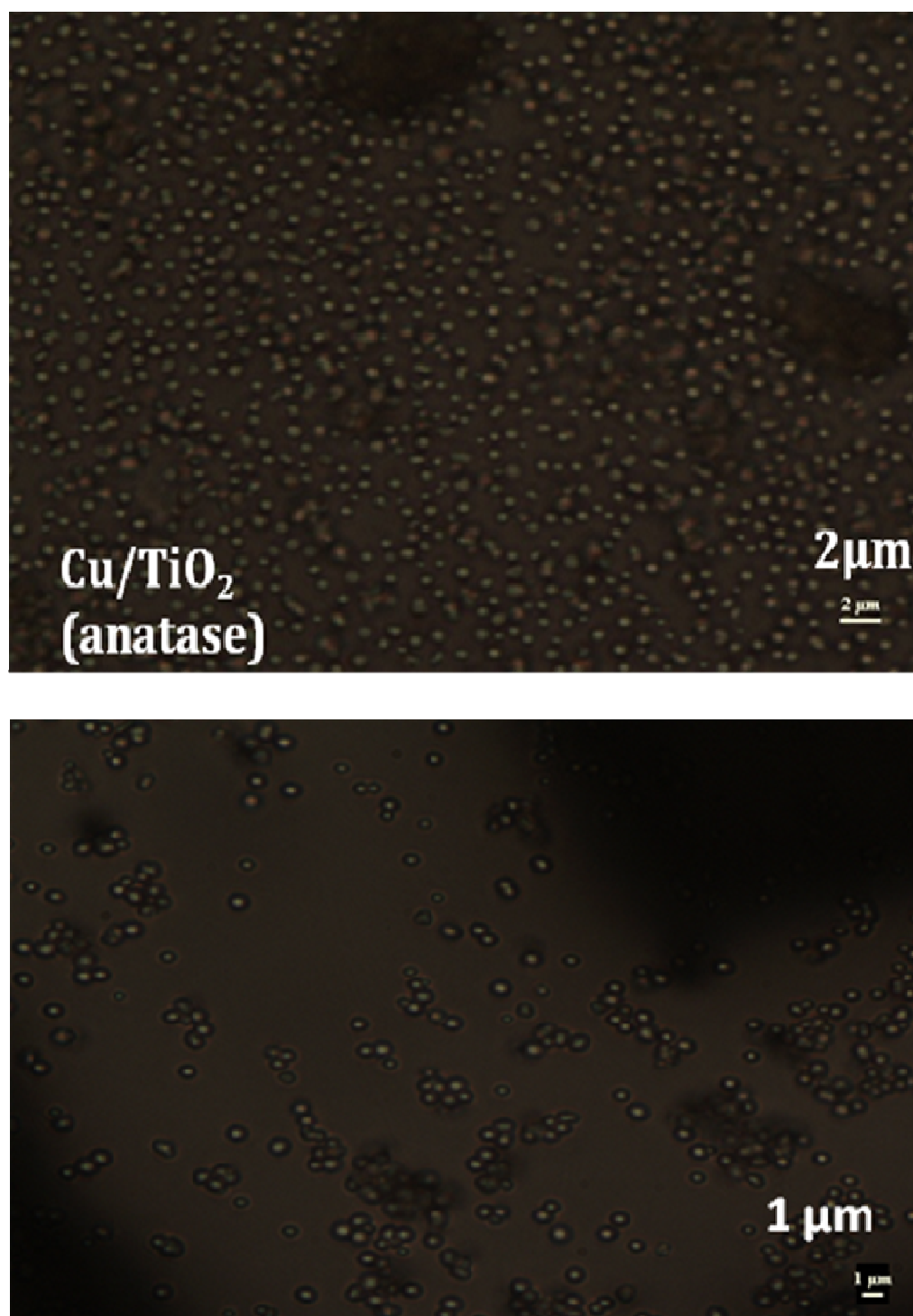
Figure 6.8 Optical microscopic images of Cu^{+2}/TiO_2 uniform nanosphere prepared by autoclave reactor.

Figure 6.9 Digital image of Cu^{+2} and CuO/TiO_2 nanoparticles prepared by sol-gel method [74] [85].

Table 6.1 Surface element analysis of Cu^{+2} and CuO/TiO_2 using EDS (a) nanosphere (b) nanotube (c) (core/shell) nanowire.

(a) Cu^{+2} and CuO/TiO_2 nanosphere

Element	keV	KRatio	Wt%	At%	At Prop	ChiSquared
Ti	4.510	0.7454	72.16	75.38	0.0	134.34
Cu	8.046	0.2417	25.26	19.89	0.0	1.10
Ru	2.558	0.0108	1.26	0.63	0.0	1.68
O	0.523	0.0020	1.31	4.10	0.0	3.38
Total		**1.0000**	**100.00**	**100.00**	**0.0**	**6.31**

Element	Gross (cps)	Z Corr	A Corr	F Corr
Ti	352.9	0.985	1.016	0.995
Cu	31.8	1.048	1.026	1.000
Ru	18.3	1.179	1.038	0.980
O	1.7	0.815	8.213	1.000
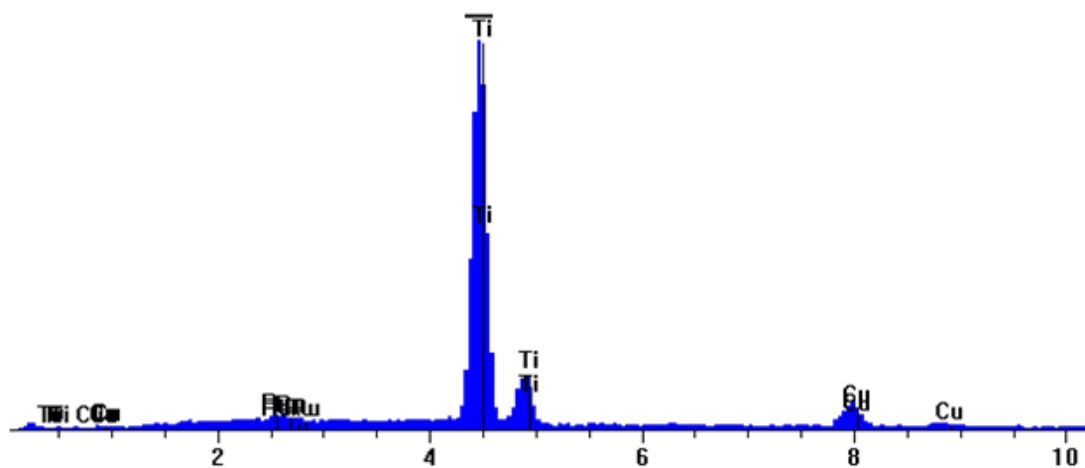
Table 6.1 continued. (b) Cu^{+2} and CuO/TiO_2 nanotube

Element	keV	KRatio	Wt%	At%	At Prop	ChiSquared
Ti	4.510	0.1682	15.12	16.22	0.0	52.55
Ru	2.558	0.0116	1.42	0.72	0.0	0.94
O	0.523	0.0007	0.17	0.54	0.0	0.58
Cu	8.046	0.7422	69.44	56.14	0.0	8.20
Al	1.487	0.0774	13.85	26.38	0.0	73.29
Total		**1.0000**	**100.00**	**100.00**	**0.0**	**10.76**

Element	Gross (cps)	Z Corr	A Corr	F Corr
Ti	170.0	0.971	1.046	0.984
Ru	24.3	1.161	1.172	0.997
O	6.2	0.803	3.381	0.998
Cu	159.7	1.033	1.006	1.000
Al	201.5	0.870	2.287	1.000
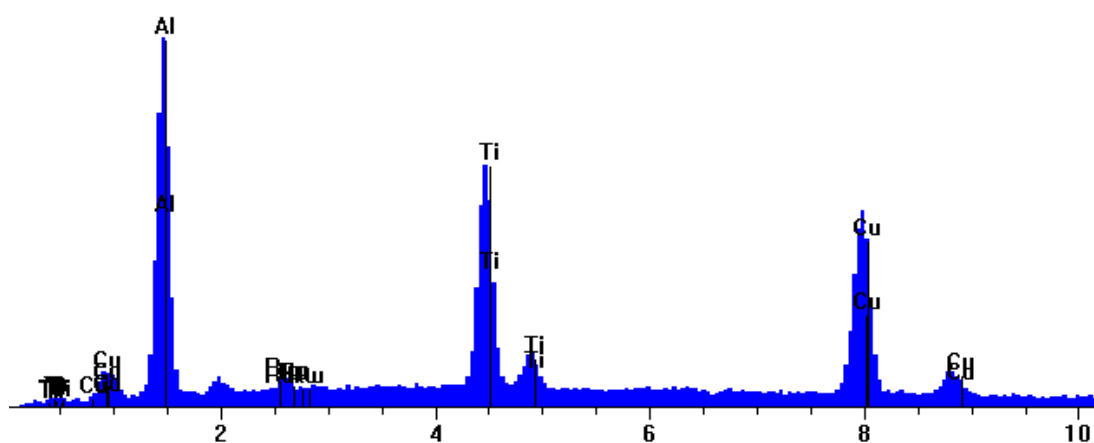
Table 6.1 continued. (c) Cu^{+2} and CuO/TiO_2 (core/shell) nanowire.

Element	keV	KRatio	Wt%	At%	At Prop	ChiSquared
Ti	4.510	0.2909	27.93	34.33	0.0	94.46
Ru	2.558	0.0272	3.43	2.00	0.0	2.34
O	0.523	0.0001	0.03	0.10	0.0	1.92
Cu	8.046	0.6818	68.62	63.58	0.0	4.75
Total		**1.0000**	**100.00**	**100.00**	**0.0**	**6.40**

Element	Gross (cps)	Z Corr	A Corr	F Corr
Ti	328.1	0.952	1.043	0.985
Ru	33.5	1.138	1.134	0.994
O	2.4	0.786	4.275	0.999
Cu	178.2	1.014	1.011	1.000
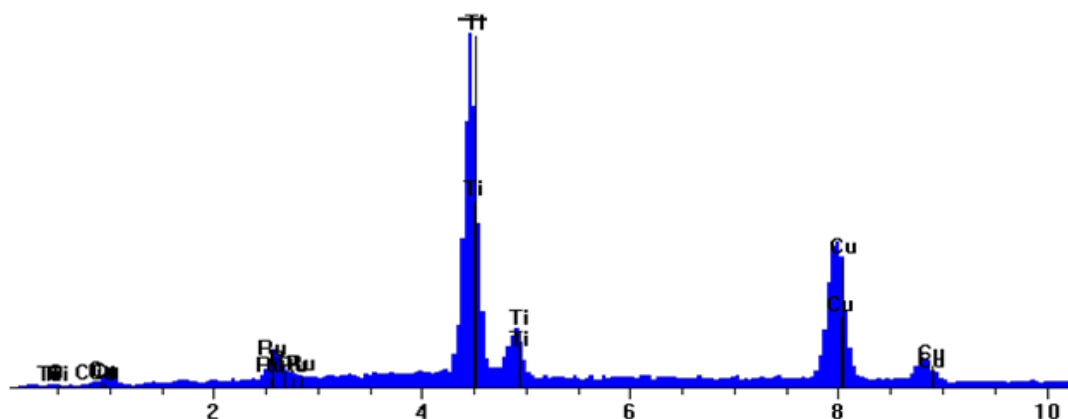
HIGH THROUGHPUT SCREENING PROCESS OF H_2 PRODUCTION MEASUREMENT

The procedure of hydrogen measurement was carried out as described in Chapter II. The experimental data is reported in appendix (E), under the following information:

Experiment	Run No.
Cu/TiO_2 nanosphere suspensions under UV light	43
Cu/TiO_2 nanosphere as film under UV light	44
Cu/TiO_2 nanosphere suspensions under sunlight	53
Cu/TiO_2 nanoparticles with dye in solution (0.018 g) under sunlight	13
Cu/TiO_2 nanoparticles with dye in solution (0.005 g) under sunlight	14
Cu/TiO_2 nanotube under UV light	66
Cu/TiO_2 nanorod under UV light	67
Cu/TiO_2 (core/shell) nanowire under UV light	68
Cu^{+2} and CuO/TiO_2 nanopowders under sunlight	12
Pure TiO_2 nanoparticles under sunlight	5

RESULTS AND DISCUSSION OF APPLICATION FOR H_2 PRODUCTION

The SEM images revealed that the averaged size of nanotube, nanorod, and (core/shell) nanowire was ≈ 200 nm which is the pore size of PAATM membrane. The EDS results showed the chemical compositions. The sample was coated with Ru element (by vapor coating) for better electron conductivity and better imaging. In order to investigate the nanostructure-properties relationship and their impact on solar to hydrogen conversion efficiency, several nanostructures TiO_2 doped with Cu were designed, synthesized, and tested for hydrogen production rate under same reaction conditions (Figures 6.10-6.19) and (Tables 6.2-6.11). Cu/TiO_2 as nanosphere, nanotube, nanorod, core/shell nanowire, and nanoparticles were tailored by various synthesis methods such as sol-gel, hydrothermal autoclave, (PAATM) Template membranes based. For Cu/TiO_2 (core/shell) nanowire, the copper diffuse inside the TiO_2 tube by capillary force and

pressure difference. The highest hydrogen production rate was observed for Cu/TiO_2 nanosphere suspension in water/methanol solution as 1797.3 ± 236.3 μmol/h/g. Significant results found in this study exhibited that the hydrogen production rate of Cu^{+2} and CuO/TiO_2 nanoparticles from water/methanol solution under natural sunlight as 24.88 ± 0.58 μmol/h/g. This indicated that the Cu^{+2} and CuO/TiO_2 nanoparticles response to certain range of wavelength longer than UV-spectrum ($\lambda < 400$ nm) which lies in the visible light spectrum range. The extremely low hydrogen production rate of pure TiO_2 under sunlight as 1.55 ± 0.1 μmol/h/g shows the importance role of the nanoparticles metal "Cu" and of metal oxide "CuO" to enhance the water reduction reaction by reduce the electron-hole recombination reaction. CuO formed due to Cu deposition technique conducted in the air is responsible of high activity under sunlight. Template membranes provide simple synthesis method to better control the size and morphology of nanotube, nanorod, and (core/shell) nanowire. Finally, the difference in hydrogen production activity observed for different nanostructure geometry of Cu/TiO_2 can be attributed to the following reasons: 1) the strength attachment between Cu and TiO_2 surface is changed depends on the structure of TiO_2. 2) The surface area and active sites that exposed to the light also different. 3) The electrode/electrolyte interface properties and interaction changed due to size effect whether suspension or aggregate. 4) Electrons mobility and transportation changed from 0- dimensional nanostructure such as nanosphere to 1-dimensional nanostructure such as nanotube, nanorod, and (core/shell) nanowire which has highly influence on charge carriers excitation and

separation/recombination. 5) Water species adsorption process on the TiO_2 surface also might be varied based on nanostructure and shape of TiO_2.

H_2 Production of Cu/TiO$_2$ Uniform Nanosphere under UV Light and Sunlight

Table 6.2 Results and conditions of Cu/TiO$_2$ nanosphere as film under UV light.

H_2 production (µmol/h)	H_2 production (µmol/h/g)	Effective Area, m^2	Energy Efficiency % @ x=0	Energy Efficiency % @ x=0.7
0.54 ± 0.01	180.1 ± 4.04	0.0001	0.106	0.355

Additives type and weight (g)	Photo catalyst type and weight (g)	Nano-structure and geometry	Photocatalyst Size, composition, Crystal structure	Water/ Methanol solution (1:1) Volume basis	Light Intensity If UV, (100 W/m^2) If Sunlight, ≈(240 W/m^2)
-	Cu^{+2} & CuO/TiO$_2$ (0.003)	Nanosphere, deposited on glass substrate as film	Cu (< 50 nm), TiO$_2$ (<100 nm, anatase)	10 ml (5 ml each)	UV
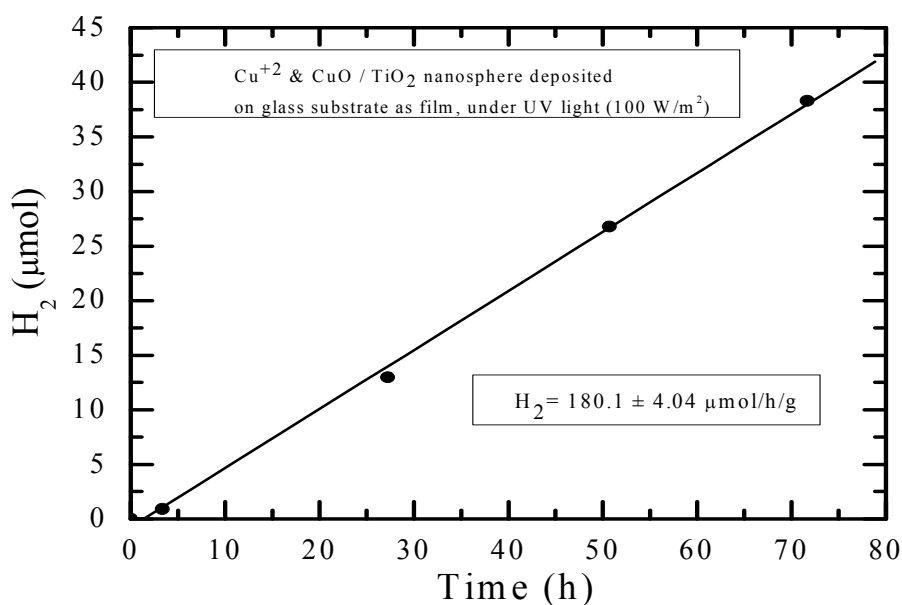
Figure 6.10 Hydrogen production rate of Cu/TiO$_2$ nanosphere as film under UV light.

Table 6.3 Results and conditions of Cu/TiO$_2$ nanosphere suspensions under sunlight.

H$_2$ production (μmol/h)	H$_2$ production (μmol/h/g)	Effective Area, m^2	Energy Efficiency % @ x=0	Energy Efficiency % @ x=0.7
0.35 ± 0.02	71.2 ± 4.2	0.000064	0.045	0.15

Additives type and weight (g)	Photo catalyst type and weight (g)	Nano-structure and geometry	Photocatalyst Size, composition, Crystal structure	Water/ Methanol solution (1:1) Volume basis	Light Intensity If UV, (100 W/m²) If Sunlight, ≈(240 W/m²)
-	Cu^{+2} & CuO/TiO$_2$ (0.005)	Nanosphere, suspension	Cu (<50 nm), TiO$_2$ (<100 nm, anatase)	10 ml (5 ml each)	Sunlight (Texas, College Station)

Figure 6.11 Hydrogen production rate of Cu/TiO$_2$ nanosphere suspensions under sunlight.

Table 6.4 Results and conditions of Cu/TiO$_2$ nanosphere suspensions under UV light.

H$_2$ production (μmol/h)	H$_2$ production (μmol/h/g)	Effective Area, m^2	Energy Efficiency % @ x=0	Energy Efficiency % @ x=0.7
3.59 ± 0.47	1797.3 ± 236.3	0.000064	1.108	3.69

Additives type and weight (g)	Photo catalyst type and weight (g)	Nano-structure and geometry	Photocatalyst Size, composition, Crystal structure	Water/ Methanol solution (1:1) Volume basis	Light Intensity If UV, (100 W/m²) If Sunlight, ≈(240 W/m²)
-	Cu^{+2} & CuO/TiO$_2$ (0.002)	Nanosphere, suspension	Cu (<50 nm), TiO$_2$ (<100 nm, anatase)	10 ml (5 ml each)	UV
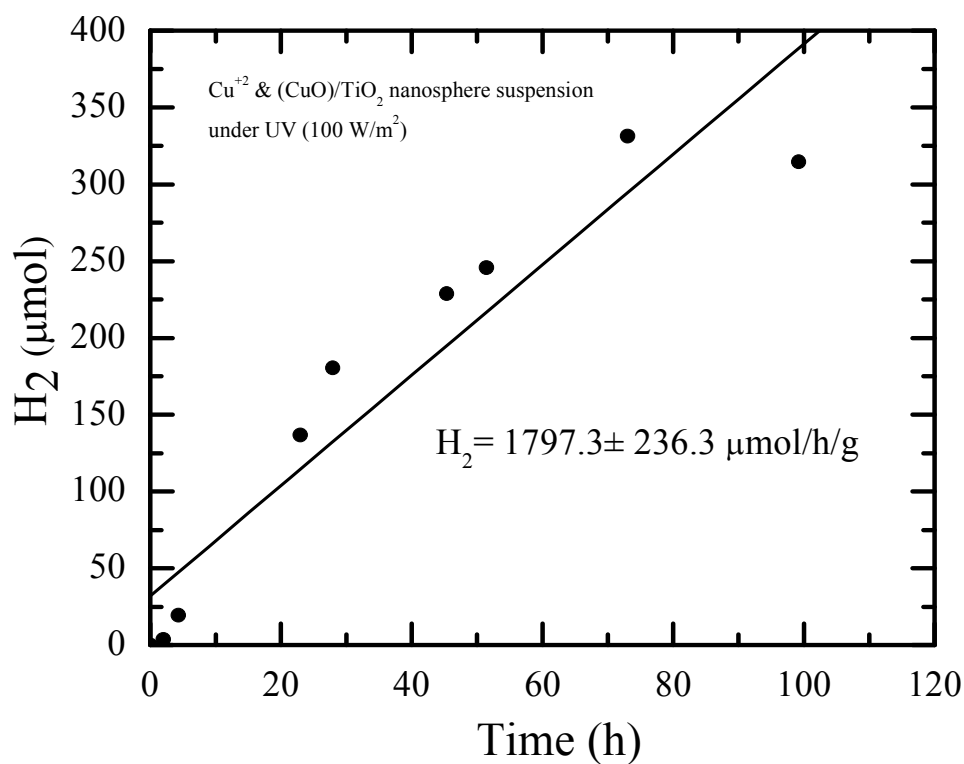
Figure 6.12 Hydrogen production rate of Cu/TiO$_2$ nanosphere suspensions under UV light.

H_2 Production of Cu^{+2} and CuO/TiO$_2$ Nanoparticles after Adding Dye to Solution under Sunlight

Table 6.5 Results and conditions of Cu/TiO$_2$ nanoparticles with dye (0.018 g) added to water/methanol solution under sunlight.

H_2 production (µmol/h)	H_2 production (µmol/h/g)	Effective Area, m^2	Energy Efficiency % @ x=0	Energy Efficiency % @ x=0.7
0.093 ± 0.006	0.42 ± 0.029	0.000081	0.0094	0.031

Additives type and weight (g)	Photo catalyst type and weight (g)	Nano-structure and geometry	Photocatalyst Size, composition, Crystal structure	Water/ Methanol solution (1:1) Volume basis	Light Intensity If UV, (100 W/m^2) If Sunlight, ≈ (240 W/m^2)
Dye (Rose Bengal Sodium) (0.018 g)	Cu^{+2} & CuO/TiO$_2$ (0.205)	Nanoparticles, Nano-composites	Cu (10 mol %, <30 nm), TiO$_2$ (<30 nm, anatase)	10 ml (5 ml each)	Sunlight (Texas, College Station)
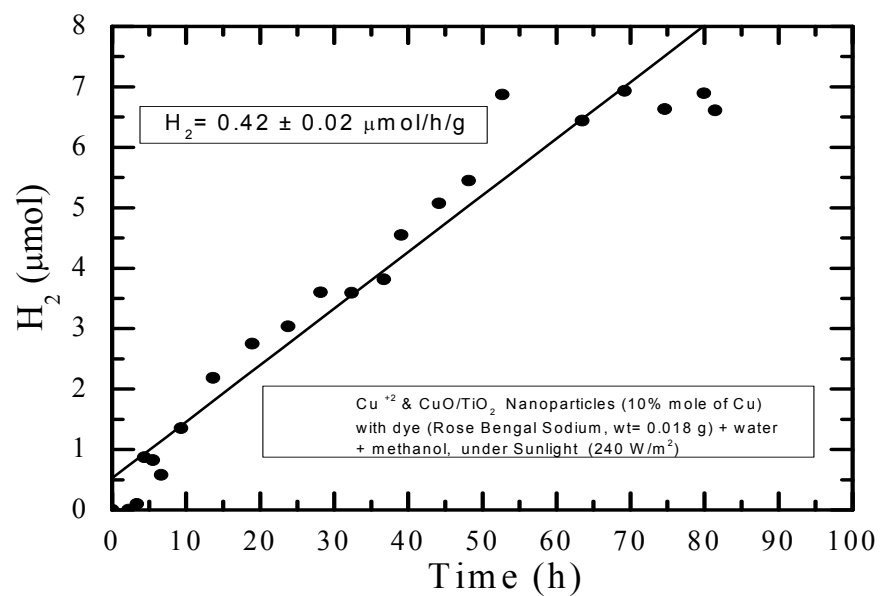
Figure 6.13 Hydrogen production rate of Cu/TiO$_2$ nanoparticles with dye (0.018 g) under sunlight.

Table 6.6 Results and conditions of Cu/TiO$_2$ nanoparticles with dye (0.005 g) added to water/methanol solution under sunlight.

H$_2$ production (μmol/h)	H$_2$ production (μmol/h/g)	Effective Area, m^2	Energy Efficiency % @ x=0	Energy Efficiency % @ x=0.7
0.13 ± 0.006	0.64 ± 0.029	0.000081	0.0132	0.044

Additives type and weight (g)	Photo catalyst type and weight (g)	Nano-structure and geometry	Photocatalyst Size, composition, Crystal structure	Water/ Methanol solution (1:1) Volume basis	Light Intensity If UV, (100 W/m²) If Sunlight, ≈ (240 W/m²)
Dye (Rose Bengal Sodium) (0.005 g)	Cu^{+2} & CuO/TiO$_2$ (0.2)	Nanoparticles, Nano-composites	Cu (10 mol %, <30 nm), TiO$_2$ (<30 nm, anatase)	10 ml (5 ml each)	Sunlight (Texas, College Station)
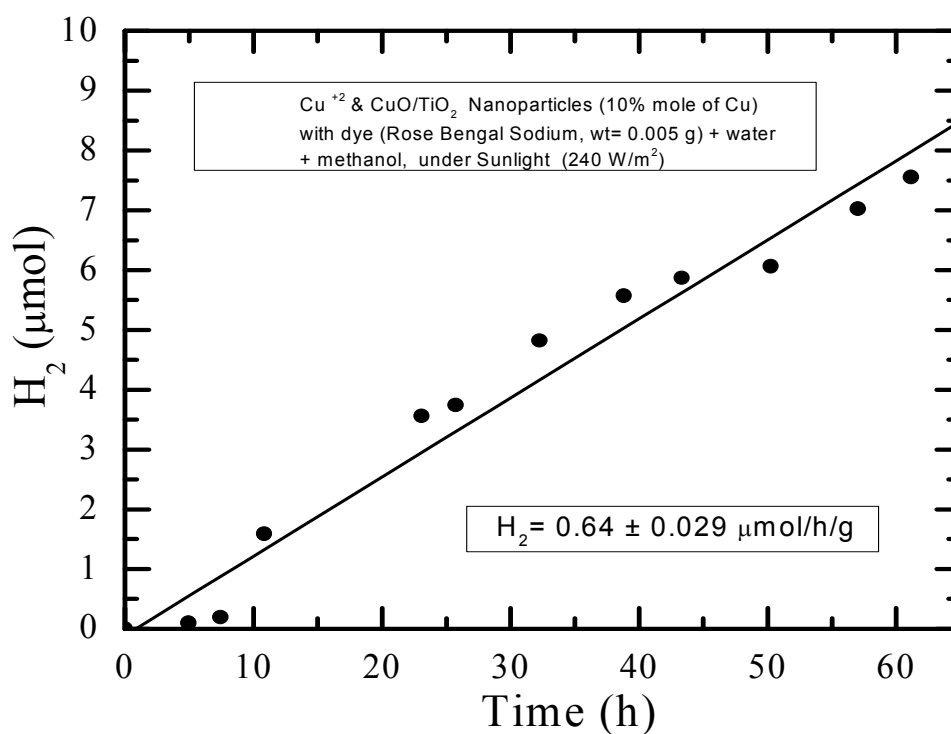
Figure 6.14 Hydrogen production rate of Cu/TiO$_2$ nanoparticles with dye (0.005 g) under sunlight.

H$_2$ Production of Cu/TiO$_2$ Nanotube and Nanorod under UV Light

Table 6.7 Results and conditions of Cu/TiO$_2$ nanotube under UV light.

H$_2$ production (μmol/h)	H$_2$ production (μmol/h/g)	Effective Area, m^2	Energy Efficiency % @ x=0	Energy Efficiency % @ x=0.7
0.29 ± 0.03	404 ± 47.3	0.000144	0.0398	0.132

Additives type and weight (g)	Photo catalyst type and weight (g)	Nano-structure and geometry	Photocatalyst Size, composition, Crystal structure	Water/ Methanol solution (1:1) Volume basis	Light Intensity If UV, (100 W/m^2) If Sunlight, ≈ (240 W/m^2)
-	Cu^{+2} & CuO/TiO$_2$ (0.00072)	Nanotube, by Template-Membrane based	Cu (< 50 nm), TiO$_2$ (d≈ 200 nm, anatase)	10 ml (5 ml each)	UV
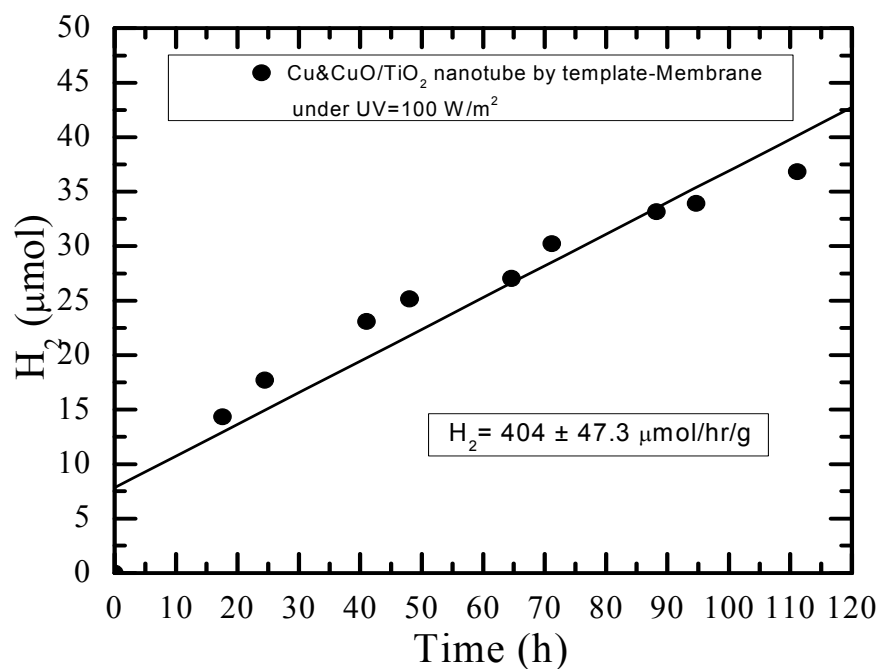
Figure 6.15 Hydrogen production rate of Cu/TiO$_2$ nanotube under UV light.

Table 6.8 Results and conditions of Cu/TiO$_2$ nanorod under UV light.

H$_2$ production (μmol/h)	H$_2$ production (μmol/h/g)	Effective Area, m^2	Energy Efficiency % @ x=0	Energy Efficiency % @ x=0.7
0.72 ± 0.03	128.6 ± 5.4	0.000144	0.0988	0.329

Additives type and weight (g)	Photo catalyst type and weight (g)	Nano-structure and geometry	Photocatalyst Size, composition, Crystal structure	Water/ Methanol solution (1:1) Volume basis	Light Intensity If UV, (100 W/m²) If Sunlight, ≈ (240 W/m²)
-	Cu^{+2} & CuO/TiO$_2$ (0.0056)	Nanorod, by Template-Membrane based	Cu (< 50 nm), TiO$_2$ (d≈ 200 nm, anatase)	10 ml (5 ml each)	UV
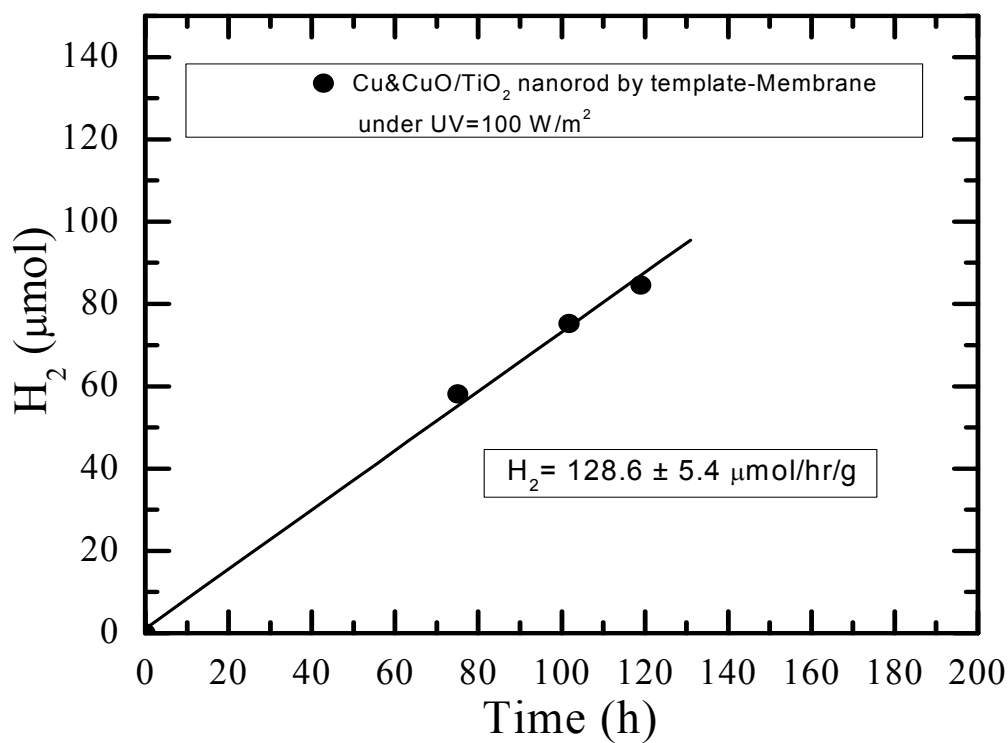
Figure 6.16 Hydrogen production rate of Cu/TiO$_2$ nanorod under UV light.

H₂ Production of Cu/TiO₂ (Core/Shell) Nanowire under UV Light

Table 6.9 Results and conditions of Cu/TiO₂ (core/shell) nanowire under UV light.

H₂ production (μmol/h)	H₂ production (μmol/h/g)	Effective Area, m²	Energy Efficiency % @ x=0	Energy Efficiency % @ x=0.7
0.17 ± 0.009	56.8 ± 3.0	0.000144	0.0233	0.0777

Photo catalyst type and weight (g)	Nano-structure and geometry	Photocatalyst Size , composition, Crystal structure	Water/ Methanol solution (1:1) Volume basis	Light Intensity If UV, (100 W/m²) If Sunlight , ≈ (240 W/m²)
Cu⁺² & CuO/TiO₂ (0.003)	Nanowire (core/shell) by template-Membrane based & chemical deposition	Cu (< 200 nm), TiO₂ (d< 200 nm, anatase)	10 ml (5 ml each)	UV
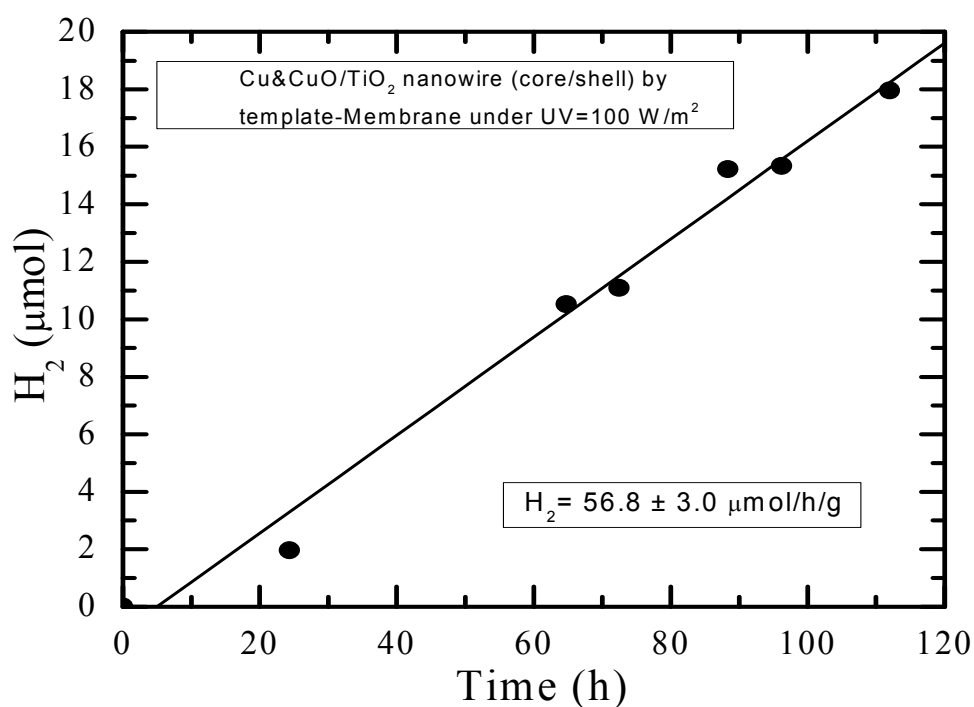
Figure 6.17 Hydrogen production rate of Cu/TiO₂ (core/shell) nanowire under UV light.

H_2 Production of Cu^{+2} and CuO/TiO_2 Nanopowders under Sunlight

Table 6.10 Results and conditions of Cu^{+2} and CuO/TiO_2 nanopowders under sunlight.

H_2 production ($\mu mol/h$)	H_2 production ($\mu mol/h/g$)	Effective Area, m^2	Energy Efficiency % @ x=0	Energy Efficiency % @ x=0.7
5.1 ± 0.12	24.88 ± 0.58	0.00008	0.51	1.72

Additives type and weight (g)	Photo catalyst type and weight (g)	Nano-structure and geometry	Photocatalyst Size, composition, Crystal structure	Water/ Methanol solution (1:1) Volume basis	Light Intensity If UV, (100 W/m²) If Sunlight, ≈ (240 W/m²)
-	Cu^{+2} & CuO/TiO_2 (0.205)	Nanopowders, Nanocomposites	Cu (10 mol %, <50 nm), TiO_2 (<500nm, anatase)	10 ml (5 ml each)	Sunlight (Texas, College Station, Latitude: 30.6277778 Longitude: -96.3341667)

Figure 6.18 Hydrogen production rate of Cu^{+2} and CuO/TiO_2 nanopowders under sunlight.

Table 6.11 Results and conditions of Pure TiO$_2$ nanoparticles under sunlight.

H$_2$ production (μmol/h)	H$_2$ production (μmol/h/g)	Effective Area, m^2	Energy Efficiency % @ x=0	Energy Efficiency % @ x=0.7
0.31 ± 0.02	1.55 ± 0.1	0.000081	0.031	0.105

Additives type and weight (g)	Photo catalyst type and weight (g)	Nano-structure and geometry	Photocatalyst Size, composition, Crystal structure	Water/ Methanol solution (1:1) Volume basis	Light Intensity If UV, (100 W/m²) If Sunlight, ≈ (240 W/m²)
-	TiO$_2$ (0.2)	Nanoparticles	Pure TiO$_2$ (<30 nm, anatase)	10 ml (5 ml each)	Sunlight (Texas, College Station)
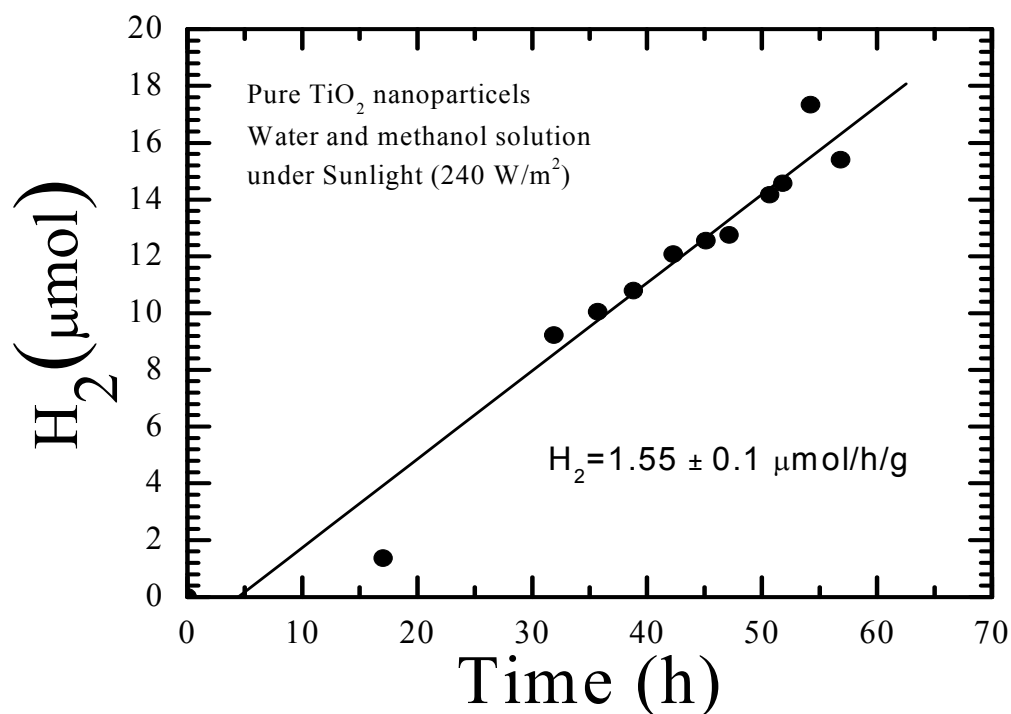
Figure 6.19 Hydrogen production rate of Pure TiO$_2$ nanoparticles under sunlight.

CONCLUSIONS

The effect of property (geometry) of nanostructure on the reactivity is due to two reasons. First, the surface area to volume ratio is significantly increases in nanostructures. Second, the surface energy dominates property of nanostructures. When the surface area to volume ratio increases, it means high surface energy and high stability. For instant, gold particles with size equal 2 cm, the surface energy is less than the gravity force. If the size extremely reduced to 2 nm, the surface energy will be more than the gravity force and it will be more stable with less weight. For TiO_2, the change in surface area to volume ratio leads to change the electrical conductivity due to large active sites availability (surface atoms) (Figure 6.20).

Photocatalyst	Surface area ,A	Volume ,V	A/V, ratio	Energy efficiency % @ x= 0.7
Cu/TiO$_2$ Nanorod	$2\,h\,\pi\,R$	$h\,\pi\,R^2$	2/R	0.329
Cu/TiO$_2$ Nanotube	$6\,h\,\pi\,r$	$3h\,\pi\,r^2$	4/R	0.132
Cu/TiO$_2$ Nanosphere	$4\,\pi\,R^2$	$(4/3)\,\pi\,R^3$	3/R	3.69
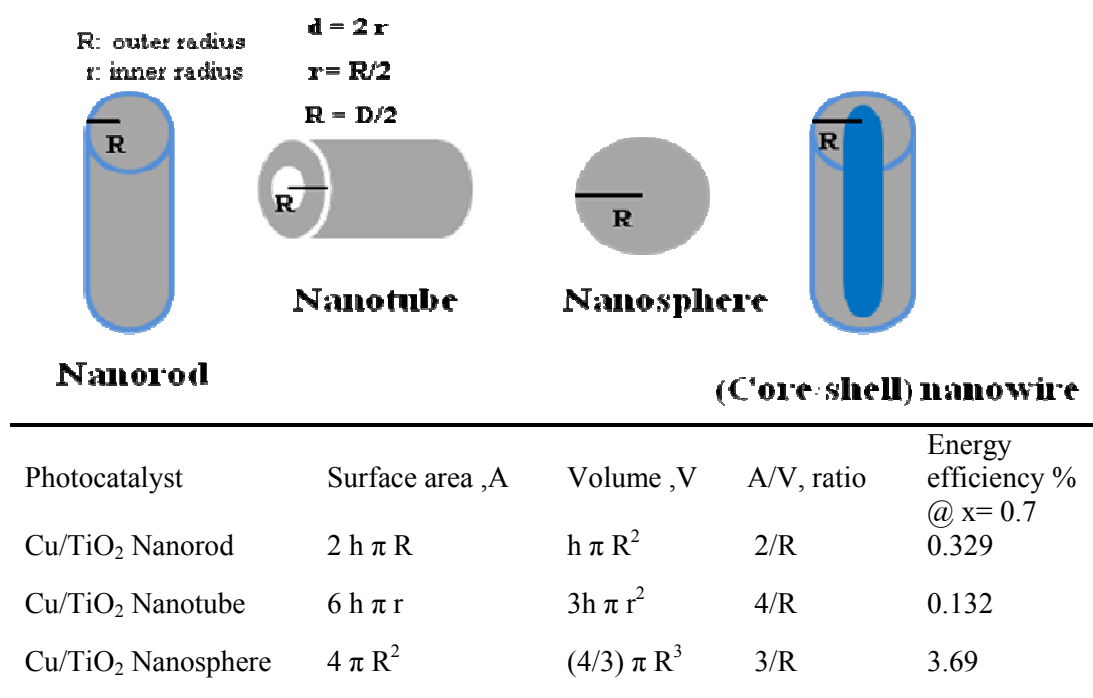
Figure 6.20 shows the surface area to volume ratio of different nanostructures and related energy efficiency %.

Significant results found in this study exhibited that the hydrogen production rate of Cu^{+2} and CuO/TiO_2 nanopowders from water/methanol solution under natural sunlight as 24.88 ± 0.58 µmol/h/g. This indicated that the Cu^{+2} and CuO/TiO_2 nanopowders response to certain range of wavelength longer than UV-spectrum ($\lambda<400$ nm) lies in the visible light spectrum range. The formation of CuO that has band gap 1.2 eV supposes to be the main reason of this significant observation. The CuO formed on the surface of TiO_2 because the Cu metal is not reduced after the conventional wet impregnation method used to deposit Cu on TiO_2 surface. Cu/TiO_2 nanosphere shows high performance than any Cu/TiO_2 nanostructure has and higher energy efficiency as 0.709 %. As 0D-dimentional nanostructure, nanosphere has larger surface area to volume ratio than 1D-dimentional nanostructure as nanotube, nanorod, and (core/shell) nanowire which attribute their activity and performance.

CHAPTER VII

NANOFIBERS AS EFFECTIVE SUPPORTER FOR TiO$_2$ NANOCOMPOSITES PHOTOCATALYST SYSTEM INCLUDING QUANTUM DOTS AND DYE SENSITIZATION

OVERVIEW

The design of nanostructure materials is crucial to the capture of solar energy. It is demonstrated here that nanofibers are valuable photocatalyst architecture for solar-hydrogen production. Several architectures have been designed, synthesized, characterized and evaluated for hydrogen production: (1) Ag/TiO$_2$ nanofibers (2) PVP nanofibers supported nanopowders of Cu+2 and CuO/TiO2 are (3) silica nanofiber supported nanopowders of Cu^{+2} and CuO/TiO$_2$ (4) silica nanofiber supported Fe^{+3}/TiO$_2$ nanoparticels (5) silica nanofibers supported integration photocatalyst of Ag/CuInS$_2$/Dye (R.B.S)/TiO$_{2-x}$.N$_x$, all are fabricated by electrospinning. The performance of photoelectrochemical hydrogen production from water splitting with methanol (as sacrificial reagents) was measured under UV irradiation (10 mW/cm^2, 365nm) and sunlight (240 W/m^2). Hydrogen production rate for Ag/TiO$_2$ nanofibers is 17.63±0.14 μmol/h/g and for Cu^{+2} and CuO/TiO$_2$ nanopowders on PVP nanofibers is 152.49±0.26 μmol/h/g. From the results observation, it is concluded that injection of metal/TiO$_2$ nanopowders into nanofibers is more effective than tailor metal/TiO$_2$ nanofiber "one-synthesis". Silica nanofiber is strong supporter due to its stability in aqueous solution. The size of nanopowders is significant for overall performance. Integration photocatalyst

system of nanostructure materials include quantum dots, dye, nitrogen doping to TiO_2 decorated with inexpensive metal that injected into silica nanofibers provide very promising photocatalyst for hydrogen production from water-splitting using solar energy.

INTRODUCTION

Titanium is a well known semiconductor for its high photocatalytic activity, photovoltaic, and high stability in aqueous solution [34]. It has an UV responsive band gap energy (Eg=3.2 eV for anatase crystal structure) with broad applications such as a photocatalyst for pollutants degradation, dye-sensitized solar cells, lithium batteries and gas sensors [35] [36] [34] [37] [38]. The band gap energy of TiO_2 can be modified to be responsive to visible solar spectrum by several approaches, such as noble metals loading, ions doping, dye and composite semiconductors sensitization [45]. Mutation of electronic structure and changes of electron confinement are achieved by defect and band gap engineering [45]. A number of method has been used to produce platforms of TiO_2 nanostructures and band gaps such as hydrothermal method [106], sol-gel method [107], and chemical vapor deposition [108,109]. The preparation method is of vital importance to control morphology that significantly governs the surface area. The architectures of geometry, size, compositions, crystal structure, and the metal-TiO_2 interconnection are essential factors need to be elucidated in order to understand the structure-properties relationship. Many fabrication methods have been already demonstrated to generate one-dimensional nanostructure such as wires, tubes, rods and spirals [110]. For instance,

the nanoneedle TiO_2 has been fabricated to harvest solar energy in dye-sensitized solar cell photovoltaic technology [111].

Nanofibers by Electrospinning

Electrospinning is one of these methods that was used to synthesize nanofibers with exceptional length, uniformity in diameter and diversified in compositions [110]. It is a simple and scalable mass production technique [112]. Electrospinning technique is worked based on electrostatics interactions [110] and on the uniaxial stretching or elongation; of a viscoelastic jet of polymer solutions or melts. The factors control the diameter and density of fibers are (1) the polymer solution properties such as viscosity and electrical conductivity, (2) the distance between spinneret and collector, (3) the feed flow rate of polymer solution [110].

Nanofibers have diverse applications such as in filtration and tissue engineering [113]. A very limited work have been published for applying nanofibers as photocatalyst towards solar-hydrogen production from water-splitting [109], [113], [114] and [115]. Nanofibers hold a great potential to improve the efficiency of hydrogen production due to large surface area and high porosity to provide for the reactions. In addition, as heterogeneous photocatalysts, the nanofiber structure can be easily handled, recycled and reused. Also, electrospinning, as a fabrication technique, is preferred due to better control of fine nanofiber dimensions, scalable mass production and simplicity [110]. As high porosity architecture, polymers nanofibers loaded with photocatalyst particles is a novel approach to be used as supported material holding the nanopowders and prevent aggregation. This approach will reduced the area losses (active sites) which is useful for light harvesting.

Solar-hydrogen production from water splitting have received extensive attention due to intense concerns about energy and environment problems [12]. Storing solar energy in hydrogen energy is alternative approach to the photovoltaic (PV) solar cells because of growing interest in hydrogen fuel cell [62]. This approach combines PV technology and water electrolysis method in a one-step process to reduce the cost. The state-of-art of this process is to discover high efficiency materials. The photocatalyst and additives play an important role to improve the quantum efficiency and consequently, the hydrogen generation. Since discovered by Fujishima and Honda in 1972 [66], the searching for advanced materials that efficient, stable in aqueous solution, abundant and low cost manufacture, and environmentally friendly [45] have attracted extensive attention.

To design and fabricate an efficient advanced material which met the criteria, gaining a better understanding of process mechanism and materials roles and functions is essential. Water reduction reactions at semiconductor's surface will successfully completed, if two protons transfer to react with two electrons to form hydrogen molecular. This reaction takes place on the surface of the catalytic metal. The methanol as the one of the strongest sacrificial reagent (hole scavenger) used in this reactions is oxidized by the hole to produce hydroxyl radical (OH^-) and oxygen anions (O^{-2}) [89][116]. To design a novel TiO_2 photocatalyst system for water cleavage, many key issues need to be understood and controlled (1) structure-properties relationship (2) The effective surface area and the electronic band gap are critical for photons harvesting and electron-hole pair separation. (3) metal-TiO_2 interconnection to suppress water recombination reactions [91].

Ag/TiO$_2$ Nanofibers, Cu^{+2} and CuO/TiO$_2$ Nanopowders @ (PVP) Nanofibers

In this study, we present the results of nanofibers structure of Ag/TiO$_2$ and nanofibers supported nanopowders of Cu^{+2} and CuO/TiO$_2$ as photocatalysts for hydrogen production from photoelectrochemical water-splitting. A very simple, powerful, and scalable electrospinning technique was used to synthesize these nanofibers. The anatase crystal structure of nanofibers and nanopowders are generated by annealing at 500°C for 5 hours [117]. Simple, accurate and high throughput screening technique used to monitor and evaluate the time course of hydrogen production rate for tested materials.

Fe^{+3}/TiO$_2$ Nanoparticles @ Silica Nanofiber

The enhancement of the photocatalytic and the photovoltaic properties of TiO$_2$,mainly, electronic structure such as bang gap and band edge positions, can be obtained modification of TiO$_2$ surface using noble metals loading or deposition as electron acceptor or scavengers. Also by cation and anion ions [92] The metal particles distribution on the surface of TiO$_2$ and related surface area will enhance the performance and the chemical photoreactivity by their ability to donate or accept photo generated electrons from conduction and valence bands. The functional properties of metal-TiO$_2$ photocatalyst and their ability to absorb longer wavelength light and succeed to do the reduction and oxidation reaction of water-splitting are highly related to the composition, structure, surface area, crystal structure, and surface and interface properties and interaction with electrolyte solution. Upon the metal ions doping, the incorporation into TiO$_2$ lattice and the impurity in the energy level in the band gap of TiO$_2$ occurred. The doping of metal ions should be near to the TiO$_2$ surface because the trapped electrons

and holes must be transferred to the surface for the redox reactions to be occurred. This also reduces the recombination reaction between charge carriers. However, the metal ions will be a recombination center for the pair of electron and hole, if they transfer to the interface in case of deep doping. As mentioned earlier, the metal ions band edge positions must be less negative than conduction band and less positive than valence band of the TiO_2 energy levels corresponding to the normal hydrogen electrode (NHE). Here, Fe^{+3} doping near to TiO_2 surface by conventional wet impregnation method will enhance the activity because the impurity energy level introduced to TiO_2 are near to the conduction and valence band of TiO_2 and also can trapped the electrons and holes at same time [45] [39]. Sticking the Fe^{+3}/TiO_2 onto Silica nanofiber architecture has many advantages. First, nanofiber provides tremendous surface area for loading nanoparticles. Second, it enhanced the interaction between these nanoparticles with electrolyte solution which important for the charges transfer and reactivity. Third, silica nanofiber is stable and not dissolved in water like PVP polymer.

Quantum Dots and Dye Sensitization Solar Cell (e.g. DSSC), Dye Sensitization onto Ag/TiO$_2$ Nanofiber and Quantum Dots "CuInS$_2$" Injected Inside Ag/TiO$_2$ Nanofiber

Dyes are very sensitive and able to absorb visible light due to their small band gap electronic structure. Therefore, they are used in dye sensitized solar cells (DSSC). DSSC is low cost class of solar cell as alternative to solid state devices with main objective to reduce the (cost/efficiency) ratio of solar to electrical energy conversion efficiency. Dyes can inject photoexcited electrons to the conduction band of wide band gap

semiconductor to initiate the catalytic reaction. The electron-hole recombination reaction time of dyes is in nanoseconds while the electrons injection time is in femtoseconds [45]. This means that the charges separation process is faster than the charges recombination process which leads to make dye-sensitized TiO_2 film efficient for solar to hydrogen energy conversion and. The process of electrons photoexcitation and transportation in the presence of dye sensitization on to TiO_2 photoelctrode are shown in Figure 7.1.
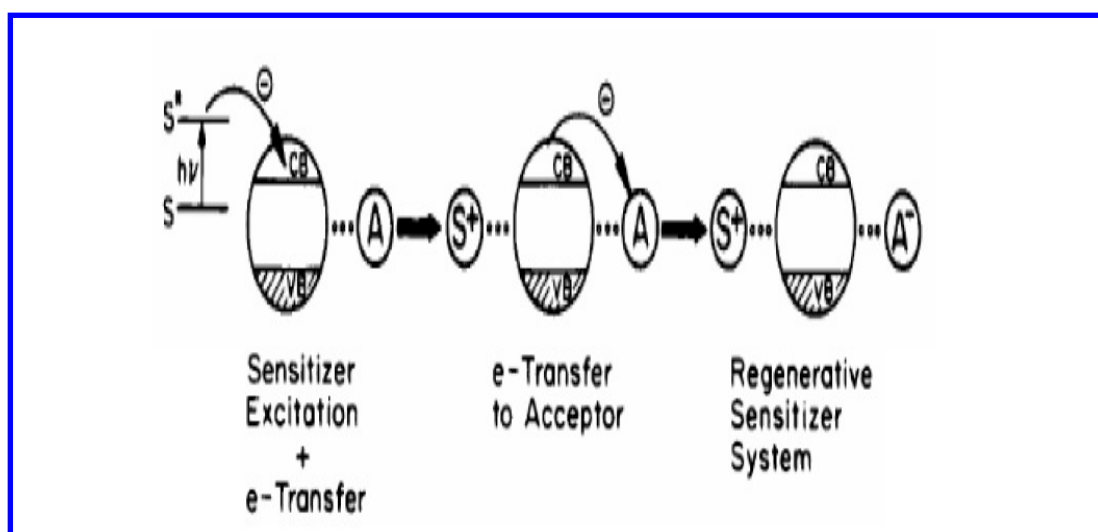
Figure 7.1 Electron photoexcitation and transfer using Dye sensitization [46][52].

DESIGN AND SYNTHESIS

Ag/ TiO₂ Nanofiber as "One-Step"

The synthesis procedure is described by [118][119][120][112][121]. Electrospinning is a common technique to generate scalable production of nanofibers [122]. To obtain mixture of titania and silver, silver nitrate was mixed with the initial precursor solution of TTIP (titanium

(IV) isopropoxide (Ti [OCH (CH$_3$)$_2$]4) (Sigma Aldrich), Polyvinylpyrrolidone, (PVP), MW= 1300000, (Sigma Aldrich), ethanol and acetic acid. The solution was made in batch by mixing 4.5 ml of TTIP with 6 ml ethanol and 6 ml acetic acid. The solution was placed on a stir plate in a closed glass container for 1 hour. Concurrently a solution of 22.5 ml ethanol and 1.35 grams PVP was mixed for an hour. Then 3.5 ml of the TTIP solution was mixed with 2.5 ml of the PVP solution and kept in a closed container on the stir plate, which resulted in a solution of (0.165 g/cm^3) TTIP and 0.025 g/cm^3 PVP. Then, 0.255 grams of AgNO$_3$ was added and stirred until the solution looked homogenous (~30 minutes). This yielded a solution with 42.5 mg/cm^3 AgNO$_3$ and 16.6 mg/cm^3 TTIP. This would result in nanofibers that contain 40% silver. The solution was then electrospun at a flow rate of (0.508 ml/hr) and at an electric field of (1.35 KV/cm), where the voltage and distance were set to 6.78 KV, and 5 cm respectively. Figure 7.2 showed the schematic diagram for fabrication procedure of nanofibers by electrospinning. Electrospinning set up to fabricate nanofibers from polymer solution is shown in Figure 7.3.
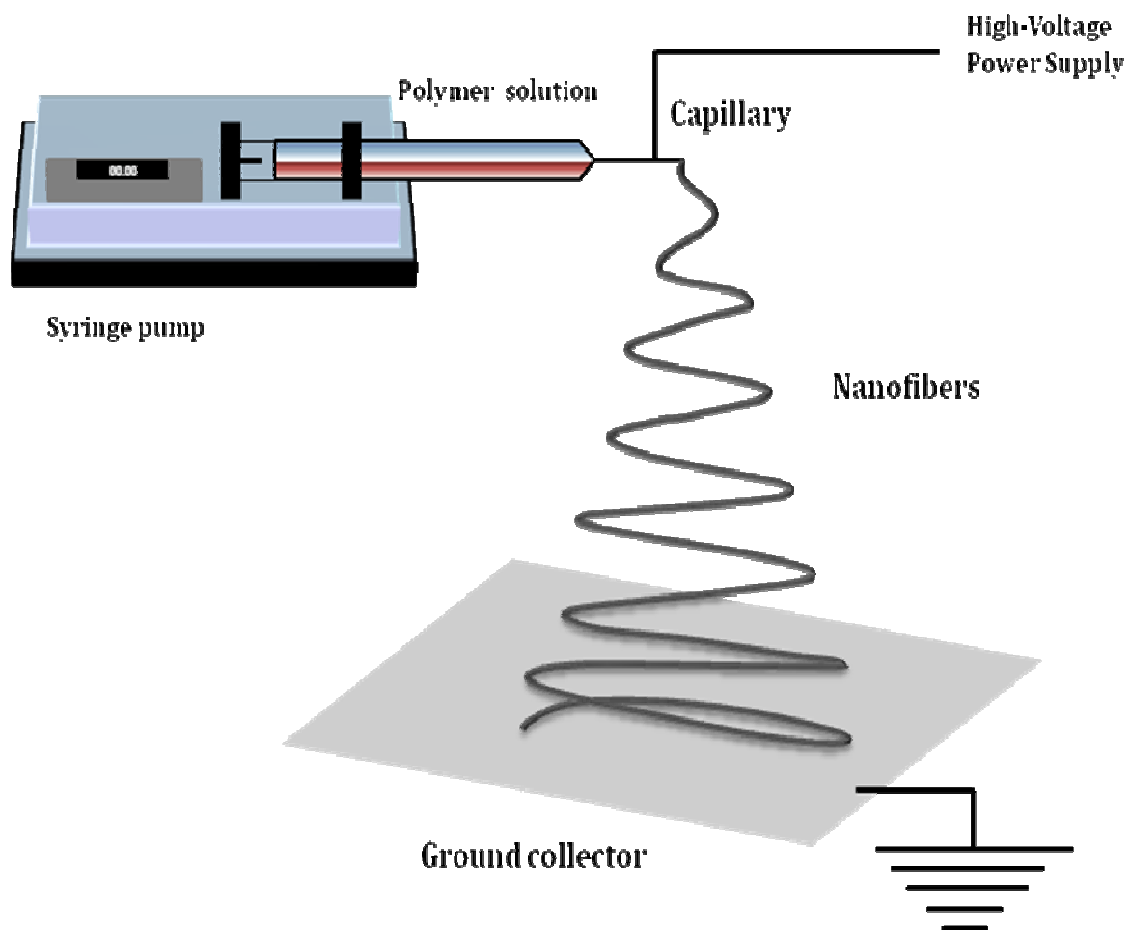
Figure 7.2 Schematic of electrospinning technique to prepare nanofibers from polymer solution. A high voltage difference between amplifier and ground creates the electrical charges and binding the polymer to generate nanofibers due to shear stress. Many factors affect the process such as flow rate, polymer or solution viscosity, electrical charges applied and distance between the ground and the tip of syringe.
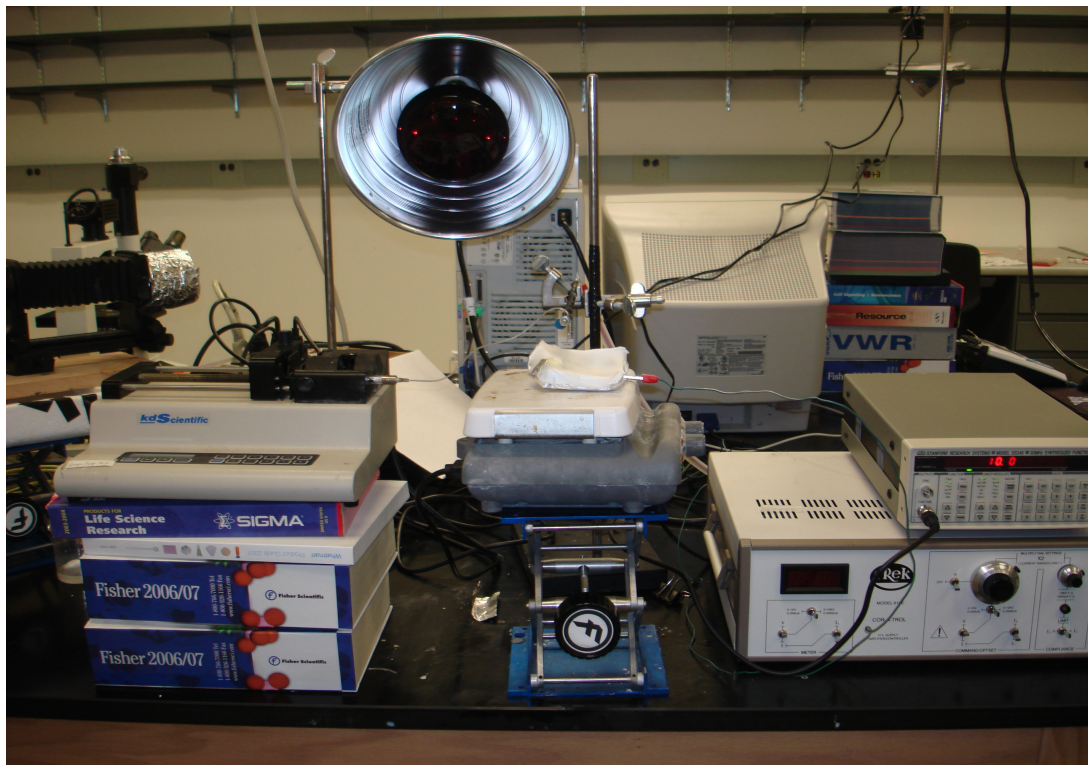
Figure 7.3 Electrospinning set up to fabricate nanofibers from polymer solution.

Cu^{+2} and CuO/TiO$_2$ Nanopowders inside PVP Nanofiber

0.1 g of Cu^{+2} and CuO /TiO$_2$ nanopowders (10 mol% of Cu) were prepared following the synthesis method reported by Jeon, et al. [74] and described in Chapter III, using the conventional sol-gel method. The sample has anatase crystal structure which obtained after 5 hours of annealing at 500°C. The nanoparticles will ground mechanically to form nanopowders. Then, it mixed with 0.31 g of Polyvinylpyrrolidone (PVP) (Mw=1300000) and 3 ml ethanol [118] [119] [121] to have the PVP nanofiber-support material of Cu^{+2} and CuO/TiO$_2$ nanopowders. The solution mixed and inserted to syringe pump to be ready

for electrospinning. The electrospinning conditions are: flow rate is (1 ml/hr), voltage is 10 KV, the distance between heat of the needle and collector is varied to collect nanofiber continuously, (usually is 5-10 cm). The idea developed to enhance the interaction of light, electrode surface, and water in order to have more interactions which lead to more water-splitting reactions and hydrogen production. The extremely small scale of Cu^{+2} and CuO /TiO_2 nanopowders (<100 nm) will be useful during electrospinning to fabricate nanofibers for two reasons. First, reduce the viscosity of the polymer solution. Second, reduce the electrical charge difference because of metal size.

Cu^{+2} and CuO/TiO_2 Nanopowders inside Silica Nanofiber and Cu^{+2} and CuO/TiO_2 Nanoparticles "One-Step" inside Silica Nanofiber

PVP nanofiber holding nanopowders are dissolving after certain time of immersion in the water, therefore, it loss their advantage to support nanopowders in water/methanol solution. Due to instability of PVP nanofiber they replace with silica nanofiber. Silica used is spin-on glass (SOG) intermediate coating solution (IC1-200, Futurrex) [123]. The diameters of electrospun fibers range from micrometers to nanometers, depending on parameters such as the selection of polymers, electric-field strength, and pumping rates. Metal or semiconductor oxide fibers can also be electrospun by adding oxide precursors to the polymer solutions and removing the polymer parts by calcination [123].

To synthesized Cu^{+2} and CuO/TiO_2 nanopowders inside silica nanofiber, the solution prepared is 1.24 g of PVP, 3 ml ethanol, 8 ml of silica (IC1-200, Futurrex), and 0.1 g of Cu^{+2} and CuO/TiO_2 nanopowders (10 mol% of Cu, the method used to make it mentioned in Chapter III), all these chemicals are mixing for more than 24 hours to form

gray polymer solution and then inserted into syringe pump. The electrospinning conditions as follows; flow rate is (1 ml/hr), DC voltage is 10 KV, and the distance between heat of the needle and collector is varied to collect nanofiber continuously, (usually is 5-10 cm) [121]. The collector used is aluminum foil. After making the nanocomposites silica nanofiber, it is heated to 550°C for 12 hours to remove the PVP nanofiber and keep silica nanofiber as only supporter materials. Final structure is rigid and soft silica nanofiber with Cu^{+2} and CuO/TiO_2 nanopowders inside it.

To synthesized Cu^{+2} and CuO/TiO_2 nanopowders in "one-step" inside silica nanofiber, the solution prepared is 1.24 g of PVP, 3 ml ethanol, 8 ml of silica, 1 ml of acetic acid, 0.5 g of TTIP, 0.05 g of Cu $(NO_3)_2$.2.5 H_2O (10% mole of Cu), all these chemicals are mixing for more than 24 hours to form blue polymer solution and then inserted into syringe pump. The electrospinning conditions as follows; flow rate is (1 ml/hr), DC voltage is 10 KV, and the distance between heat of the needle and collector is varied to collect nanofiber continuously, (usually is 5-10 cm) [121]. The collector used is aluminum foil. After making the nanocomposites silica nanofiber, it is heated to 550°C for 12 hours to remove the PVP nanofiber and keep silica nanofiber as only supporter materials. Final structure is rigid and soft silica nanofiber with Cu^{+2} and CuO/TiO_2 nanopowders prepared together inside it.

Ag/CuInS$_2$/Dye (R.B.S)/TiO$_{2-x}$.N$_x$ Injected into Silica Nanofiber

An integration photocatalyst system include silica nanofiber supporting TiO$_2$ nanocomposites doped by nitrogen, and loaded with Rose Bengal dye, CuInS$_2$ nanoparticels, and silver dots. The photocatalysts system of nanocomposites TiO$_2$ injected into silica nanofiber as stable supporter. The combination of all these materials is due to their effective optical properties and potential to enhance the light absorption responding to visible spectrum. In typical preparation method, the solution prepared is 0.675 g of PVP, 6 ml ethanol, 8 ml of silica, 3 ml of acetic acid, 2.25 g of TTIP, 1 ml of Triethylamine, 0.11 g of Ag (NO$_3$) (10% Wt. of Ag), 0.0005 CuInS$_2$ nanoparticels, 0.006 Rose Bengal Sodium dye powders, all these chemicals are mixing for more than 24 hours to form red polymer solution and then inserted into syringe pump. The electrospinning conditions as follows; flow rate is (0.508 ml/hr), DC voltage is 6.78 KV, and the distance between heat of the needle and collector is varied to collect nanofiber continuously, (usually is 5-10 cm) [124]. The collector used is aluminum foil. After making the nanocomposites silica nanofiber, it is heated to 550°C for 12 hours to remove the PVP nanofiber and keep silica nanofiber as only supporter materials. Final structure is Ag/CuInS$_2$/Dye (R.B.S)/TiO$_{2-x}$.N$_x$ injected into silica nanofiber.

Fe^{+3}/TiO$_2$ Nanoparticles inside Silica Nanofiber

The synthesis procedures of Fe^{+3}/TiO$_2$ nanoparticles are as the one used to prepare Cu^{+2} and CuO/TiO$_2$. The only difference is by using a chemical precursor of Fe^{+3}. In typical synthesis, the solution prepared is 1.24 g of PVP, 3 ml ethanol, 8 ml of silica, 1 ml of acetic acid, 0.5 g of TTIP, 0.01 g of FeCl$_3$.6H$_2$O (Sigma Aldrich, FW=270.3) (1.45 %

Wt. of Fe), all these chemicals are mixing for more than 24 hours to form yellow polymer solution and then inserted into syringe pump. The electrospinning conditions as follows; flow rate is (1 ml/hr), DC voltage is 10 KV, and the distance between heat of the needle and collector is varied to collect nanofiber continuously, (usually is 5-10 cm) [121]. The collector used is aluminum foil. After making the nanocomposites silica nanofiber, it is heated to 550°C for 12 hours to remove the PVP nanofiber and keep silica nanofiber as only supporter materials. Final structure is Fe^{+3}/TiO_2 nanoparticles injected into silica nanofiber.

CHARACTERIZATION

After synthesis, photographs have been taken for nanofiber (Figure 7.4). Also, nanofiber are characterized using optical microscopic images (Figures 7.5-7.14). Scanning Electron Microscopy (SEM) images (Figure 7.15) and Energy dispersive X-ray spectroscopy (EDS) (Table 7.1) were taken for nanofiber samples using JEOL JSM-6400. Figure 7.16 shows the solutions to make silica nanofiber.
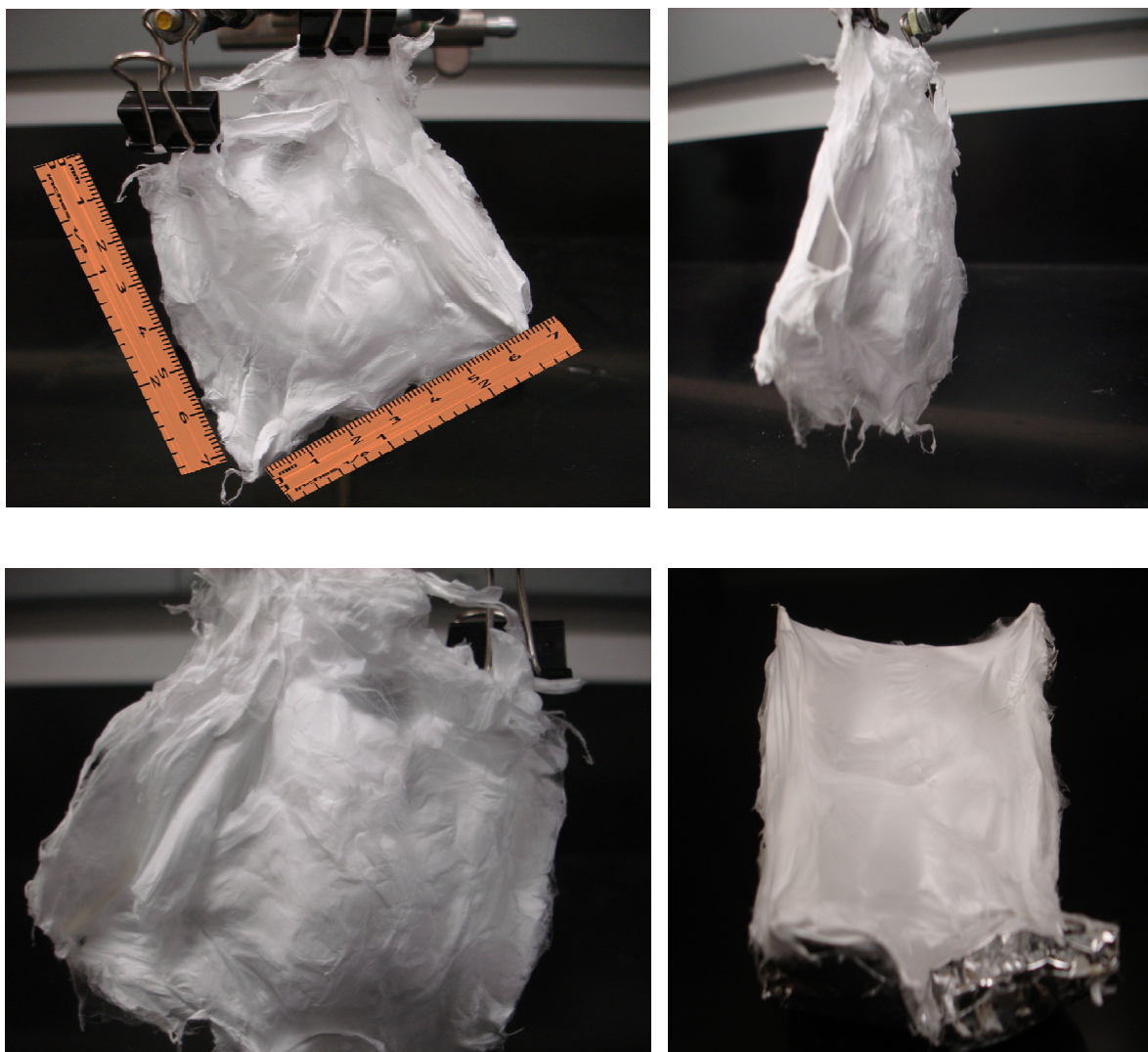
Figure 7.4 Photographs of "TiO$_2$+ PVP" nanofibers. For one of the samples, the size is about 7cm × 7cm.
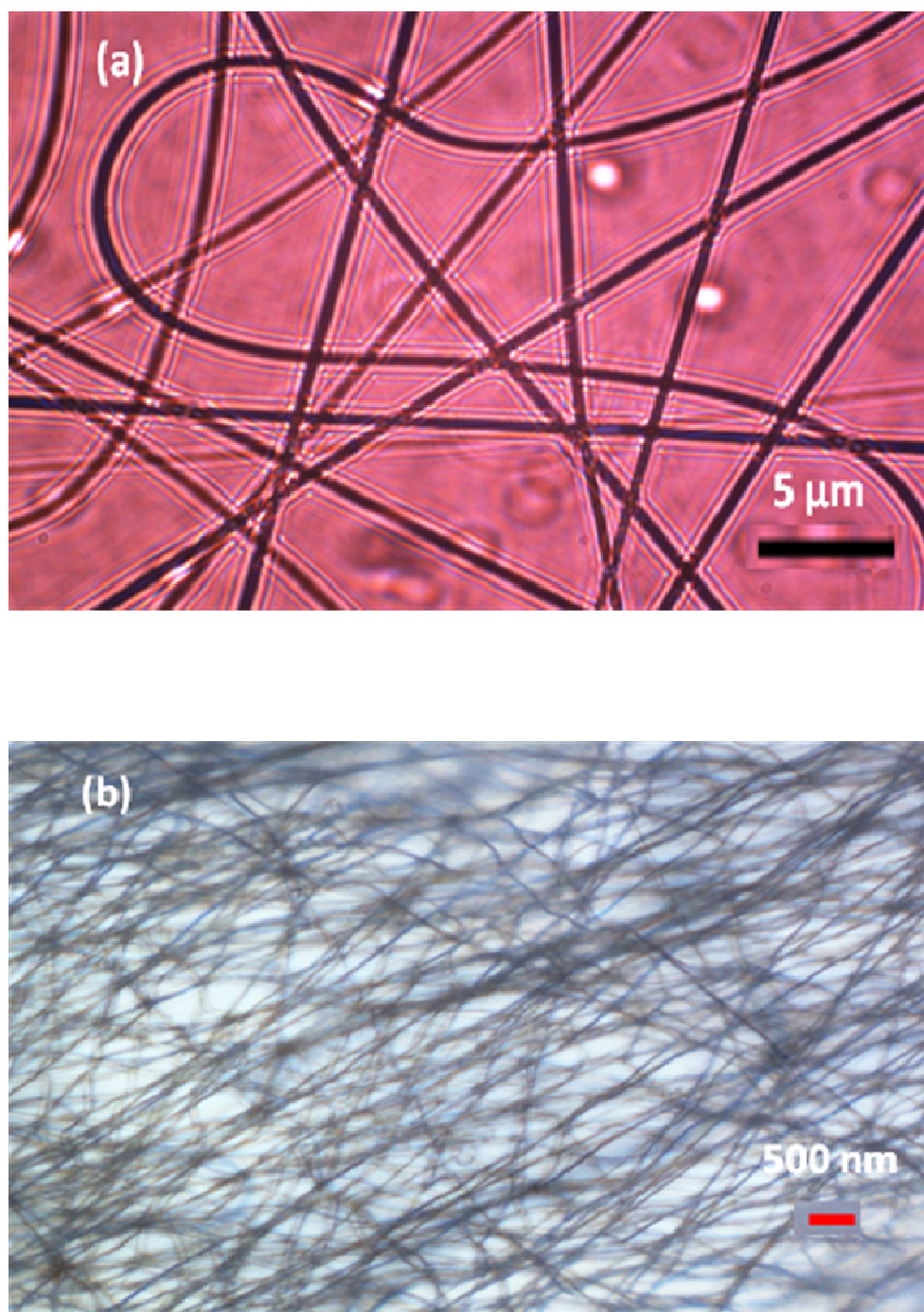
Figure 7.5 (a) Optical microscope image of nanofibers synthesized by electrospinning before annealing. The average diameter is about 800 nm. (b) Optical microscope image of Ag/TiO$_2$ nanofibers after annealing at 500°C for 5 hours. The average diameter is about 200 nm.
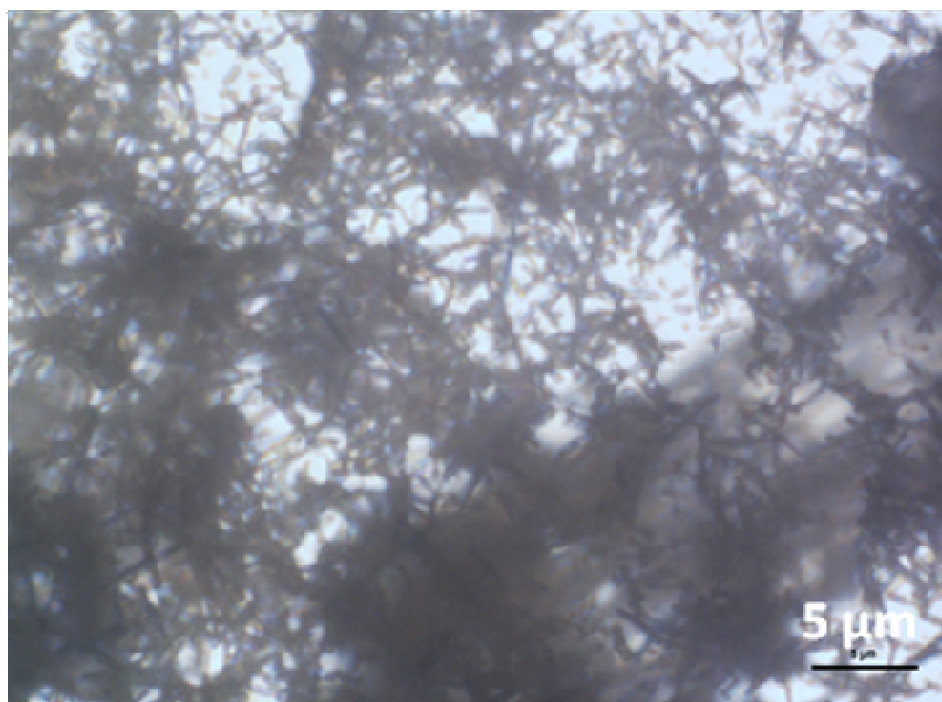
Figure 7.6 Optical microscope image of Ag/TiO$_2$ nanofibers.
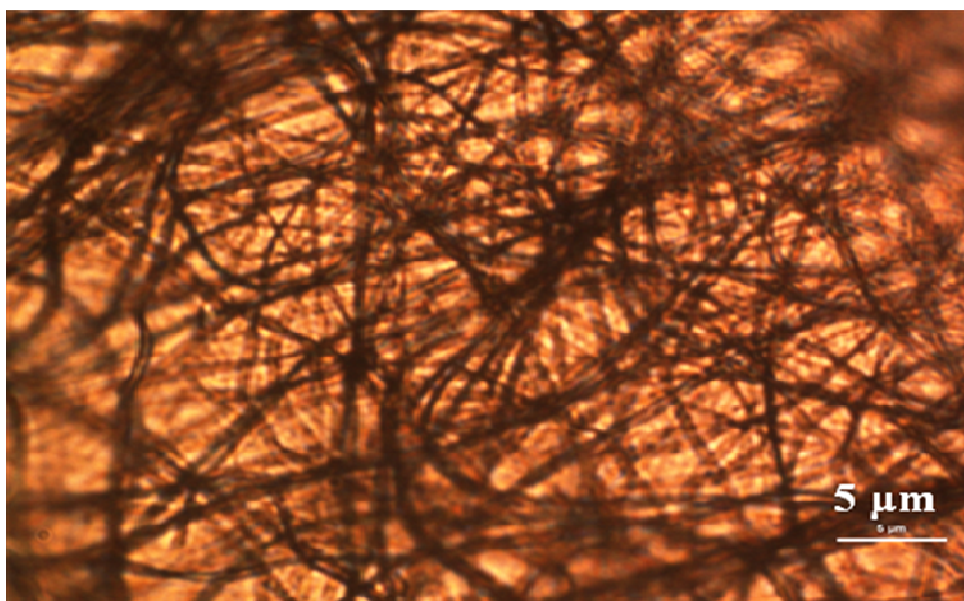
Figure 7.7 Optical microscope image of Ag/TiO$_2$ nanofibers after calcinations.
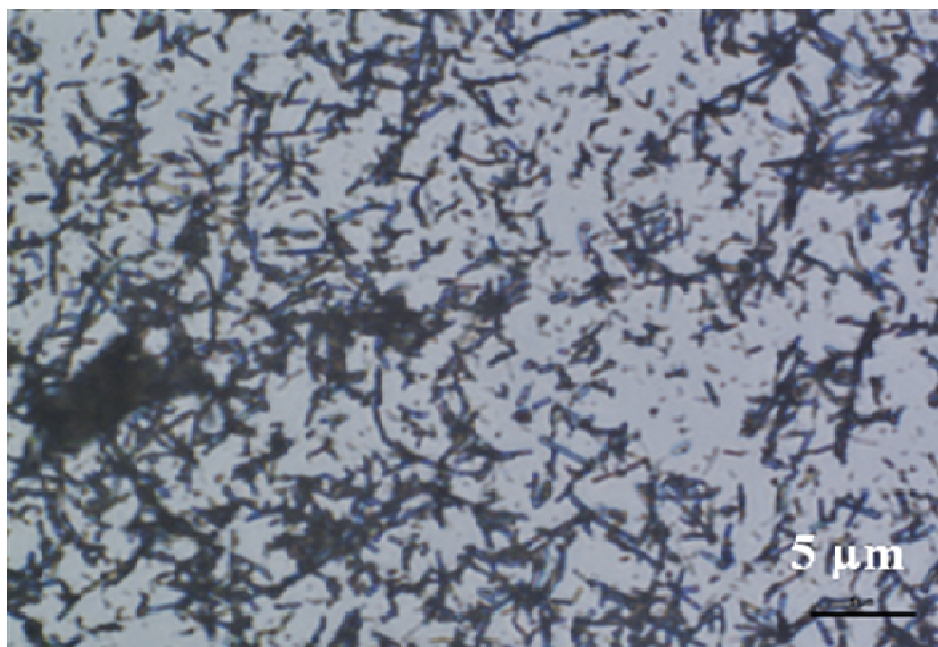
Figure 7.8 Optical microscope image of Ag/TiO$_2$ nanorods from ground mechanically the nanofibers (after calcinations).
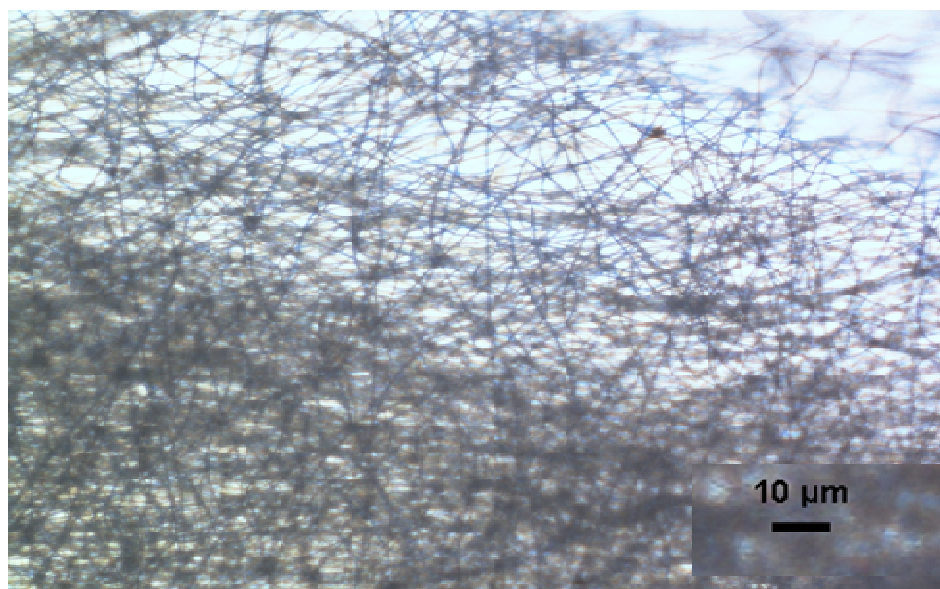
Figure 7.9 Optical microscope image of TiO$_2$ nanofibers.
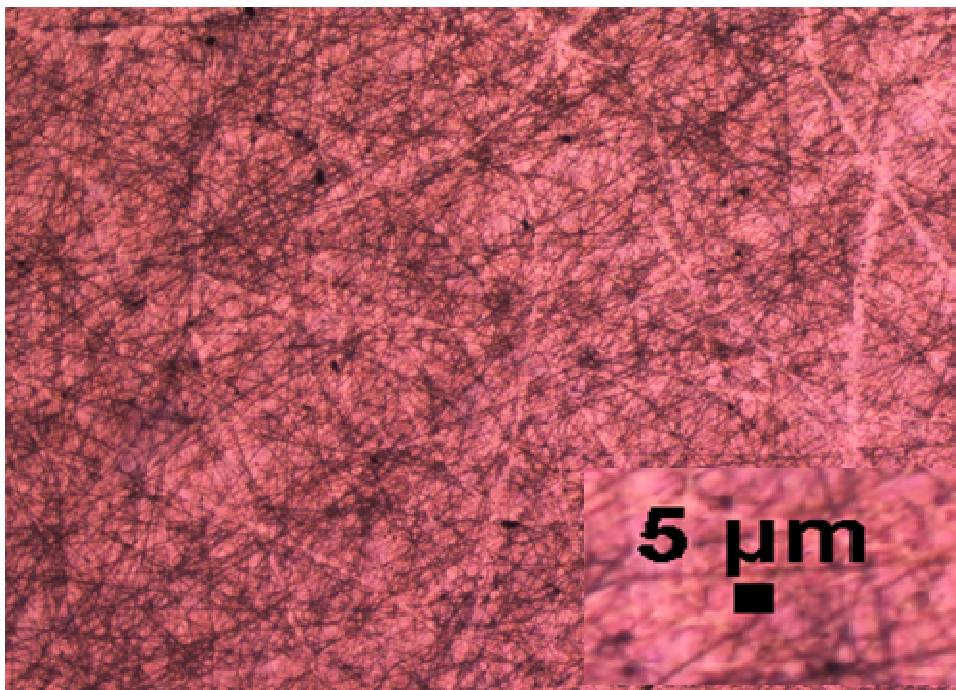
Figure 7.10 Optical microscope image of Cu^{+2} and CuO/TiO_2 nanopowders @ silica nanofiber.
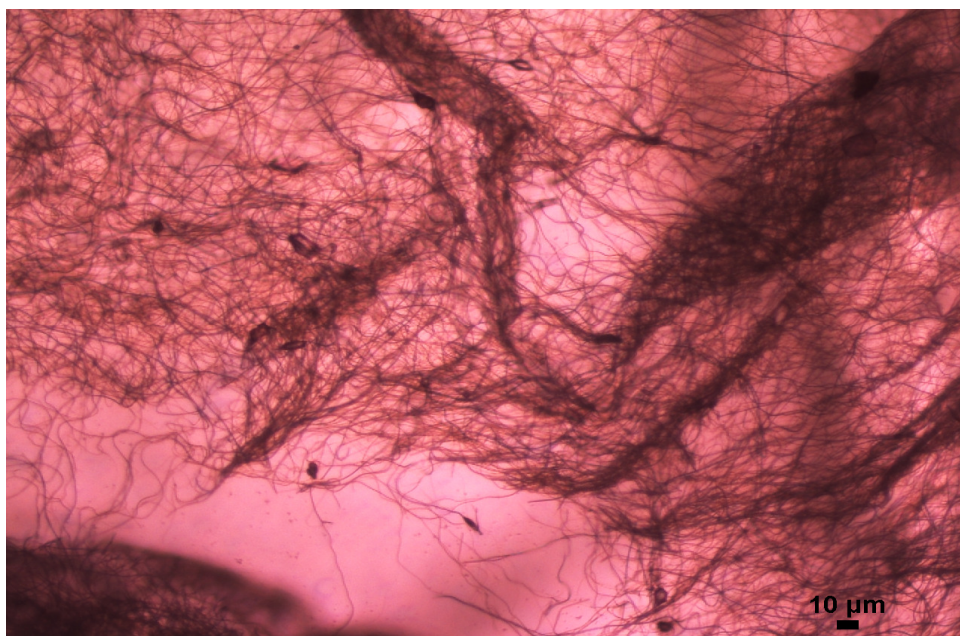
Figure 7.11 Optical microscope image of $Ag/CuInS_2/Dye$ (R.B.S)/$TiO_{2-x}.N_x$ @ silica nanofiber.
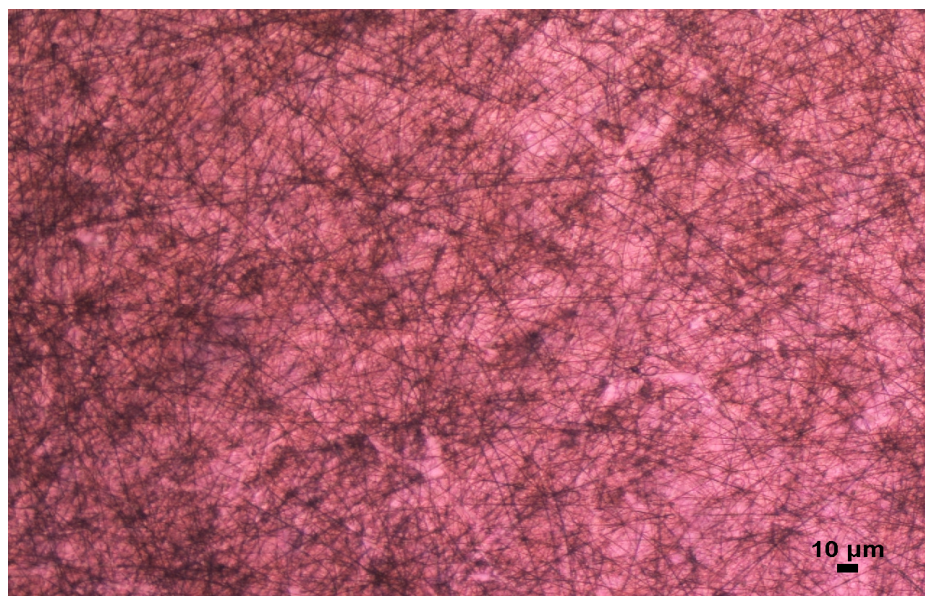
Figure 7.12 Optical microscope image of Fe^{+3}/TiO_2 nanoparticels @ silica nanofibers.
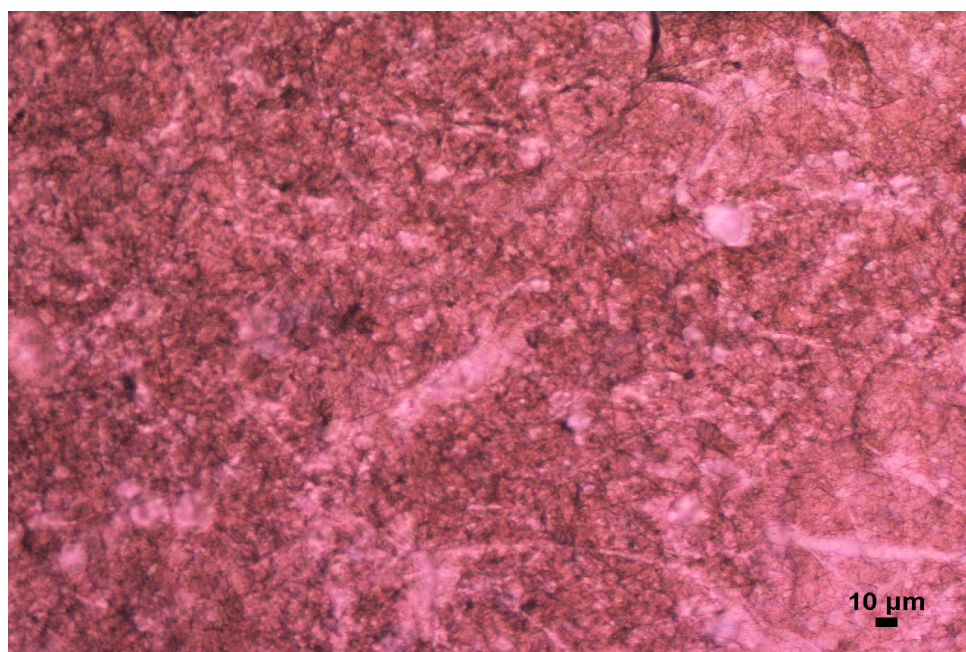
Figure 7.13 Optical microscope image of Cu^{+2} and CuO/TiO_2 nanoparticles "one-step" @ silica nanofiber.
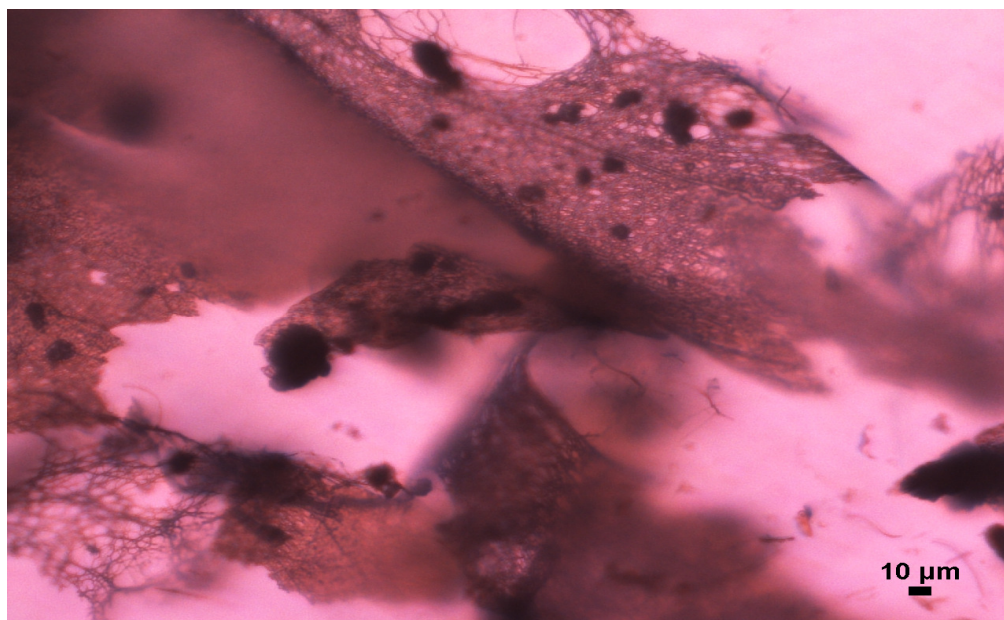
Figure 7.14 Optical microscope image of Cu^{+2} and CuO/TiO_2 nanoparticles "one-step" @ silica nanofiber after annealing at 550°C for 12 hours.
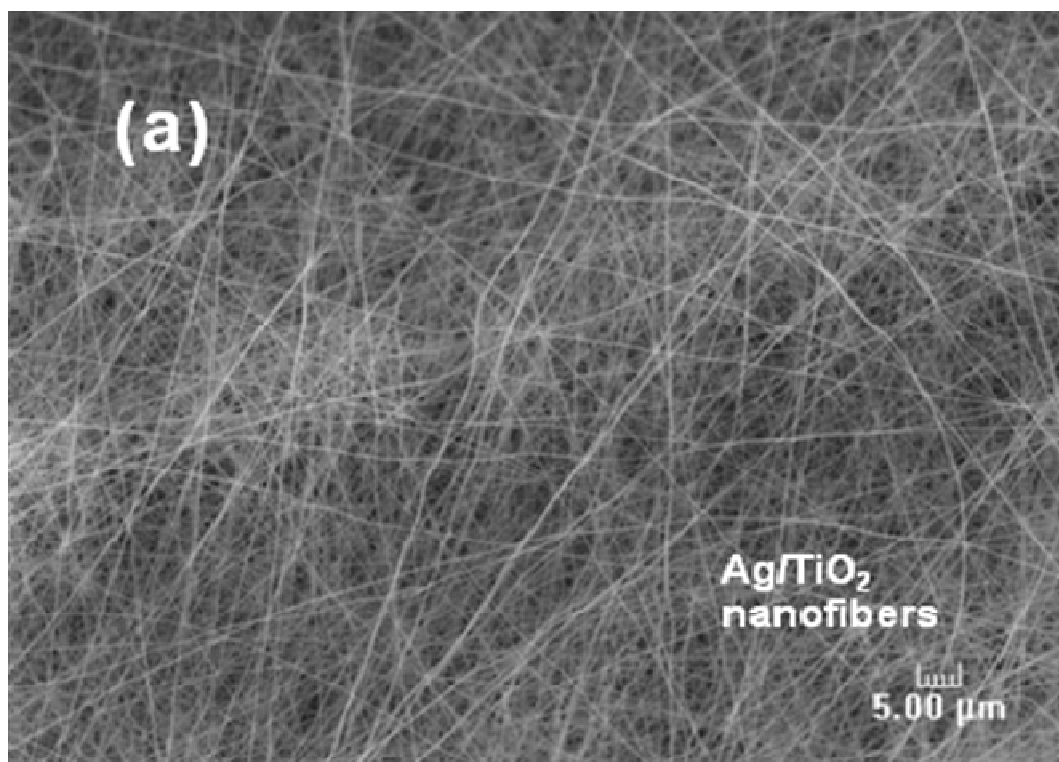
Figure 7.15 SEM images (a) Ag/TiO_2 nanofibers after annealing.
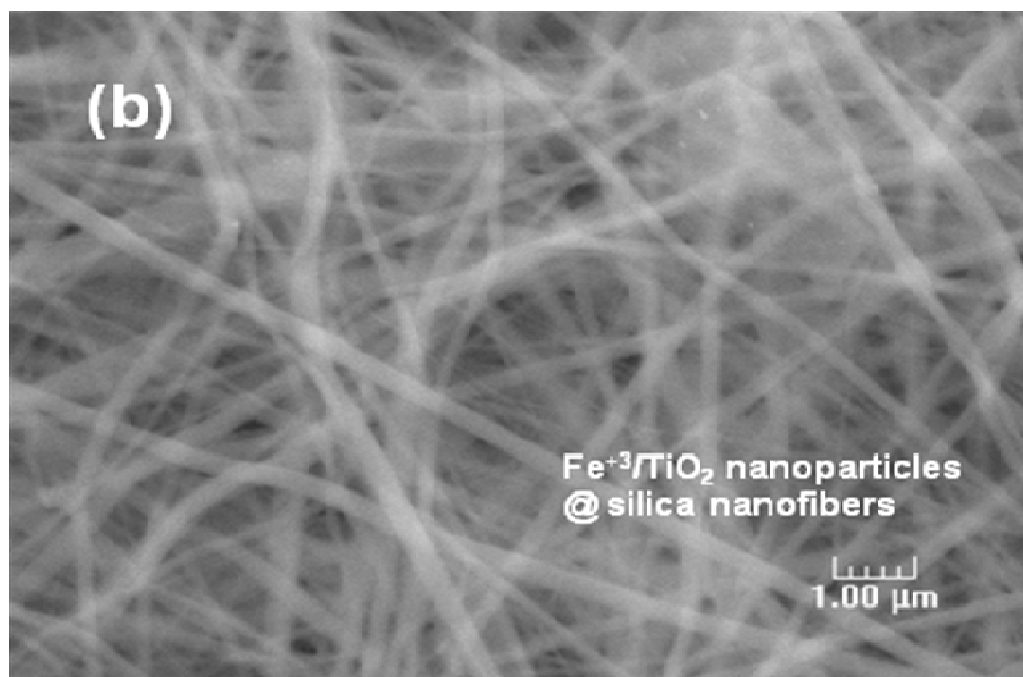
Figure 7.15 continued (b) Fe^{+3}/TiO_2 nanoparticles @ silica nanofibers before annealing. (c) $Ag/CuInS_2/Dye$ (R.B.S)$/TiO_{2-x}.N_x$ @ silica nanofiber after annealing.

Table 7.1 Surface element analysis using EDS (a) Cu^{+2} and CuO/TiO_2 nanoparticles "one-step" @ silica nanofiber.

Element	keV	KRatio	Wt%	At%	At Prop	ChiSquared
Ti	4.510	0.5760	53.19	46.96	0.0	116.23
Cu	8.046	0.2199	21.43	14.26	0.0	0.21
Ru	2.558	0.0077	0.91	0.38	0.0	2.32
O	0.523	0.0026	1.36	3.59	0.0	38.77
Si	1.740	0.1938	23.12	34.81	0.0	63.87
Total		**1.0000**	**100.00**	**100.00**	**0.0**	**10.31**

Element	Gross (cps)	Z Corr	A Corr	F Corr
Ti	228.3	1.010	1.031	0.996
Cu	28.1	1.073	1.020	1.000
Ru	11.9	1.210	1.111	0.988
O	2.4	0.838	6.940	0.999
Si	206.2	0.920	1.460	0.998
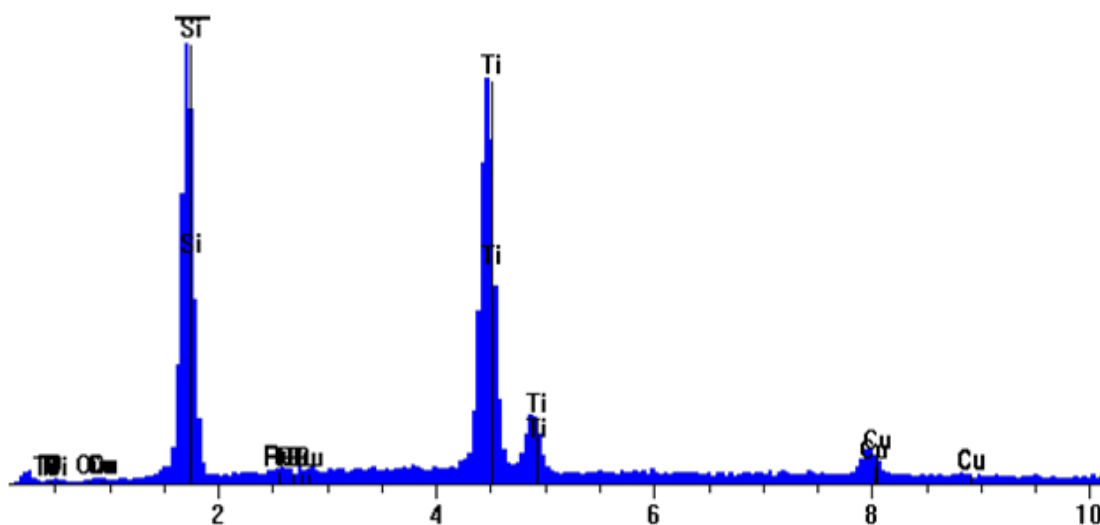
Table 7.1. continued. (b) Ag/TiO$_2$ nanofibers.

Element	keV	KRatio	Wt%	At%	At Prop	ChiSquared
Ti	4.510	0.7088	67.66	77.50	0.0	22.63
Ru	2.558	0.1273	13.06	7.09	0.0	2.39
O	0.523	0.0027	1.92	6.57	0.0	
Ag	2.984	0.1612	17.37	8.83	0.0	1.50
Total		**1.0000**	**100.00**	**100.00**	**0.0**	**1.59**

Element	Gross (cps)	Z Corr	A Corr	F Corr
Ti	72.9	0.952	1.083	1.000
Ru	16.5	1.139	0.996	0.977
O	1.2	0.786	9.753	1.000
Ag	20.1	1.160	1.030	0.976
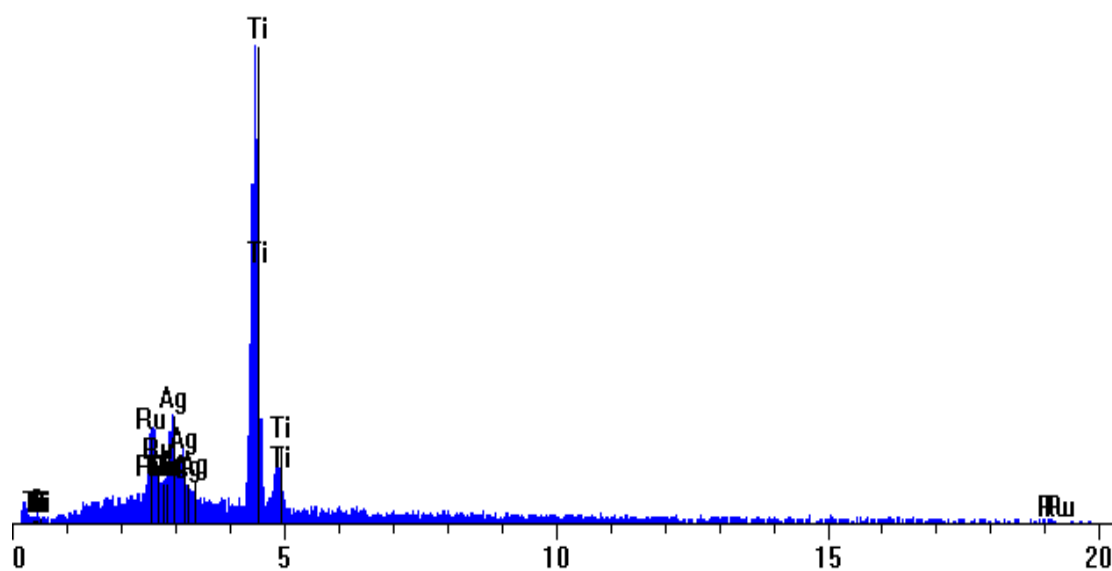
Table 7.1 continued. (c) Cu^{+2} and CuO/TiO_2 nanopowders @ silica nanofiber.

Element	keV	KRatio	Wt%	At%	At Prop	ChiSquared
Ti	4.510	0.4351	40.79	31.16	0.0	32.03
Ru	2.558	0.0000	0.00	0.00	0.0	3.07
O	0.523	0.0008	0.36	0.82	0.0	
Cu	8.046	0.1223	11.87	6.84	0.0	0.98
Si	1.740	0.4418	46.98	61.19	0.0	40.43
Total		**1.0000**	**100.00**	**100.00**	**0.0**	**6.37**

Element	Gross (cps)	Z Corr	A Corr	F Corr
Ti	132.8	1.038	1.044	0.998
Ru	8.8	1.244	1.175	0.992
O	1.6	0.862	6.283	0.999
Cu	19.8	1.101	1.016	1.000
Si	328.2	0.946	1.298	0.998
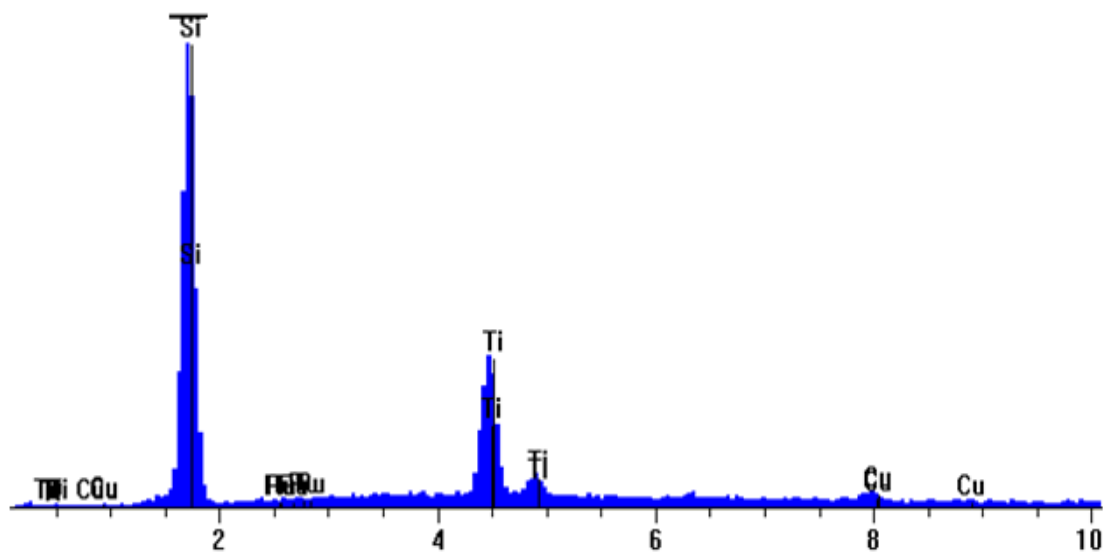
Table 7.1 continued. (d) Fe^{+3}/TiO_2 nanoparticles @ silica nanofibers.

Element	keV	KRatio	Wt%	At%	At Prop	ChiSquared
Ti	4.510	0.8866	84.56	76.05	0.0	117.62
Ru	2.558	0.0231	2.58	1.10	0.0	3.11
O	0.523	0.0034	2.72	7.34	0.0	1.08
Si	1.740	0.0866	10.10	15.49	0.0	16.02
Fe	6.403	0.0002	0.02	0.02	0.0	0.53
Total		**1.0000**	**100.00**	**100.00**	**0.0**	**10.71**

Element	Gross (cps)	Z Corr	A Corr	F Corr
Ti	175.1	1.011	1.014	1.000
Ru	11.7	1.211	1.016	0.976
O	1.6	0.838	10.210	1.000
Si	51.8	0.921	1.367	0.995
Fe	5.9	1.049	1.078	1.000
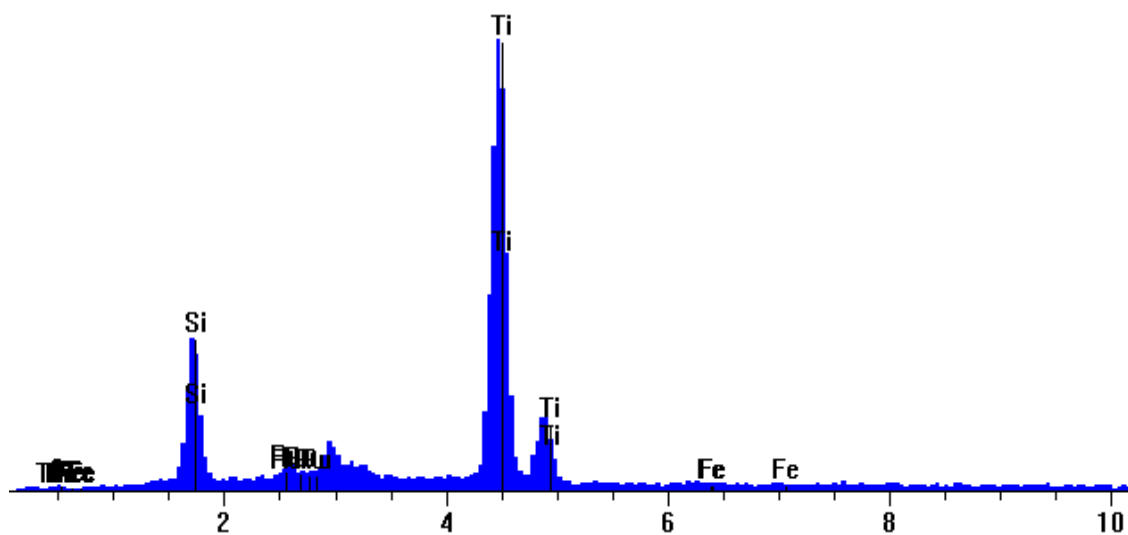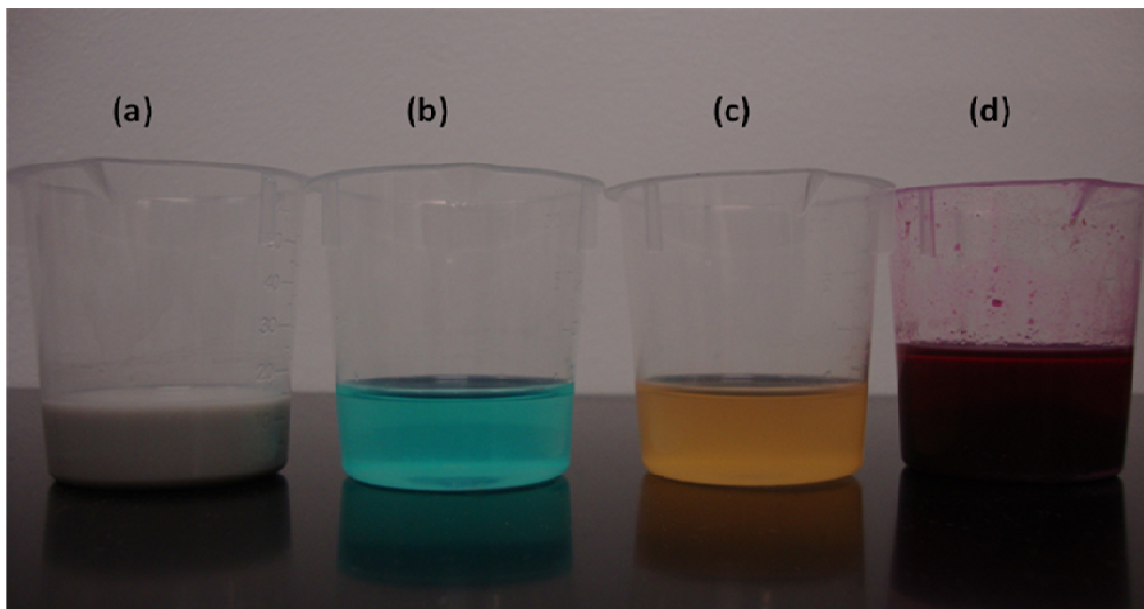
Figure 7.16 All polymer solutions have PVP initially (a) Cu^{+2} and CuO/TiO_2 nanopowders @ silica nanofiber (b) Cu^{+2} and CuO/TiO_2 nanoparticles "one-step" @ silica nanofiber. (c) Fe^{+3}/TiO_2 nanoparticles @ silica nanofibers (d) $Ag/CuInS_2/Dye$ (R.B.S)/$TiO_{2-x}.N_x$ @ silica nanofiber.

HIGH THROUGHPUT SCREENING PROCESS OF H_2 PRODUCTION MEASUREMENT

The procedure of hydrogen measurement was carried out as described in Chapter II. The experimental data is reported in appendix (F), under the following information:

Experiment	Run No.
Ag/ TiO_2 nanofiber as "one-step" under UV light	23
Cu^{+2} and CuO/TiO_2 nanopowders @ PVP nanofiber under UV light	25
Cu^{+2} and CuO/TiO_2 nanopowders @ PVP nanofiber under sunlight	55
Cu^{+2} and CuO/TiO_2 nanopowders @ silica nanofiber under sunlight	62
$Ag/CuInS_2/Dye(R.B.S)/TiO_{2-x}.N_x$ @ silica nanofiber under Sunlight	63
Fe^{+3}/TiO_2 nanoparticels @ silica nanofibers under sunlight	64
Cu^{+2} and CuO/TiO_2 nanoparticles "one-step" @ silica nanofiber under sunlight	65

RESULTS AND DISCUSSIONS OF APPLICATION FOR H_2 PRODUCTION

The SEM images taken for nanofiber shows the network architecture that provide large surface area to deposit nanoparticles inside the nanofiber. The EDS analysis shows chemical compositions. Prior to do the SEM and EDS, the samples were coated with Ru element (by vapor coating) for better electron conductivity and better imaging. Also the silica nanofibers as rigid and soft materials enhance the stability in aqueous solution. Nanofibers are valuable photocatalyst architecture for solar-hydrogen production. It exhibited higher activity of composite nanostructure material of nanofiber supported nanopowders from photoelectrochemical water-splitting. The high porosity and high surface area which allow better surface deposition of nanopowders is the reasons of this improvement.

Figure 7.17 and Table 7.2 showed that the hydrogen production rate of Ag/TiO$_2$ nanofiber is 17.63±0.14 µmol/h/g. The stability trend of hydrogen production was more than Ten days. Significant improvement was observed for Cu^{+2} and CuO /TiO$_2$ nanopowders loaded on polymer nanofibers to 152.49±0.26 µmol/h/g (Figure 7.18 and Table 7.3). This could be explained by nanofibers architecture as supported material for Cu^{+2} and CuO/TiO$_2$ nanopowders. Better connection, better tunable junction between CuO and TiO$_2$, and large distribution throughout the nanofibers network are elucidated the higher activity.

Electrospinning method as versatile technique is suitable for making such kind composite nanofibers with mass production. Controlling the feed flow rate and electrical charges are important for the uniformity of nanofibers. During the experiments, the

distance between the spinneret and the collector was changed to avoid losses and collect more fibers. In addition, we have noticed that the spinneret or tip head is blocked many times; enough heat (infrared heat lamp) was exposure to the syringe and tube to reduce the polymer solution viscosity and facilitate the flow. For Ag/TiO_2 nanofibers, the electrical conductivity of Ag particles effect on the electrostatic charges difference which effect on the size of nanofibers diameter. A static sound also can be heard which refers to the electrical charges difference between metal and high voltage amplifier. For the polymer solution mixed with Cu^{+2} and CuO/TiO_2 nanopowders, the nanopowders are fouled around the syringe wall and need to be well mixed again to avoid blocking of the spinneret and ensure the distribution through the polymer solution. For these reasons, the performance of Ag/TiO_2 nanofibers was low comparing to Cu^{+2} and CuO/TiO_2 nanopowders loaded on polymer nanofibers. The tunable junction between the silver nanoparticles and TiO_2 nanofibers (few numbers of atoms that connected to the surface) inhibits the electronic transport because they were not completely doped on the surface of TiO_2 nanofibers. This is might ascribed to the electrospinning technique limitation conditions. Also, the surface chemistry is not in acidic or basic conditions well.

Figures 7.19-7.23 and Tables 7.4-7.8 shows the results of hydrogen production rate of different nanofibers photocatalyst and at different reaction conditions.

H$_2$ Production of Ag/ TiO$_2$ Nanofiber as "One-Step" under UV Light

Table 7.2 Results and conditions of Ag/ TiO$_2$ nanofiber as "one-step" under UV light.

H$_2$ production (μmol/h)	H$_2$ production (μmol/h/g)	Effective Area, m^2	Energy Efficiency % @ x=0	Energy Efficiency % @ x=0.7
0.49 ± 0.004	17.6 ± 0.14	0.000081	0.119	0.398

Photocatalyst type and weight (g)	Nano-structure and geometry	Photocatalyst Size, composition, Crystal structure	Water/ Methanol solution (1:1) Volume basis	Light Intensity If UV, (100 W/m^2) If Sunlight, ≈(240 W/m^2)
Ag / TiO$_2$ (0.028)	Nanofibers	Ag (4 wt %, <20 nm), TiO$_2$ nanofibers (<200 nm, anatase) [one-step electrospinning]	10 ml (5 ml each)	UV
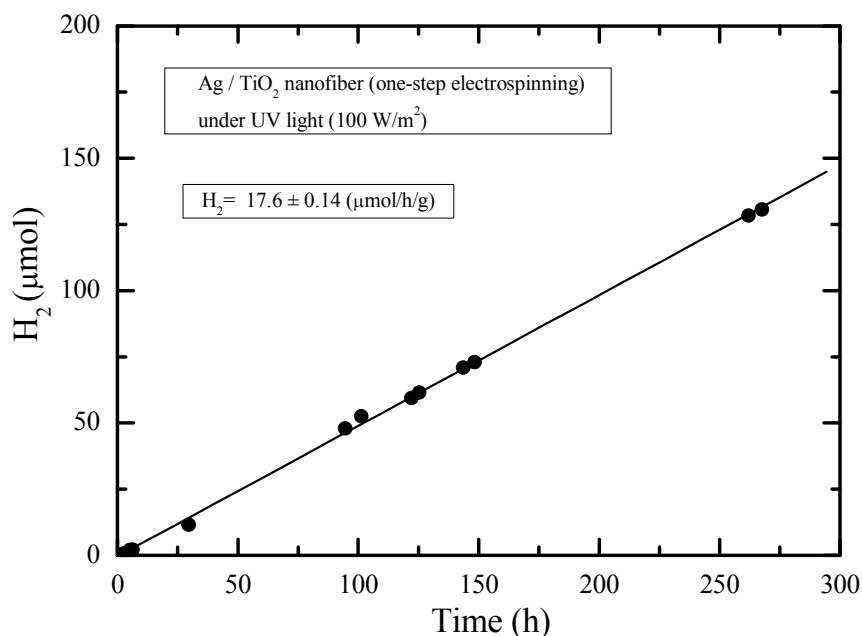
Figure 7.17 Time course of hydrogen production of Ag/TiO$_2$ nanofiber under UV light (100 W/m^2), from water/methanol solution (1:1 v/v). The weight of photocatalyst is estimated to be 28 mg. Hydrogen production rate is 17.63±0.14 μmol/h/g. The linear trend expresses the stability of hydrogen production over 250 hours.

H₂ Production of Cu⁺² and CuO/TiO₂ Nanopowders inside PVP Nanofiber under UV Light and Sunlight

Table 7.3 Results and conditions of Cu^{+2} and CuO/TiO_2 nanopowders @ PVP nanofiber under UV light.

H₂ production (μmol/h)	H₂ production (μmol/h/g)	Effective Area, m²	Energy Efficiency % @ x=0	Energy Efficiency % @ x=0.7
0.545 ± 0.0009	152.49 ± 0.26	0.000081	0.1329	0.443

Photocatalyst type and weight (g)	Nano-structure and geometry	Photocatalyst Size, composition, Crystal structure	Water/ Methanol solution (1:1) Volume basis	Light Intensity If UV, (100 W/m²) If Sunlight, ≈ (240 W/m²)
Cu⁺² & CuO/TiO₂ (0.00358)	Nanopowders @ PVP Nanofibers (as support)	Cu (10 mol %, (<30 nm), TiO₂ (<30 nm, anatase), PVP nanofibers (d< 500 nm)	10 ml (5 ml each)	UV
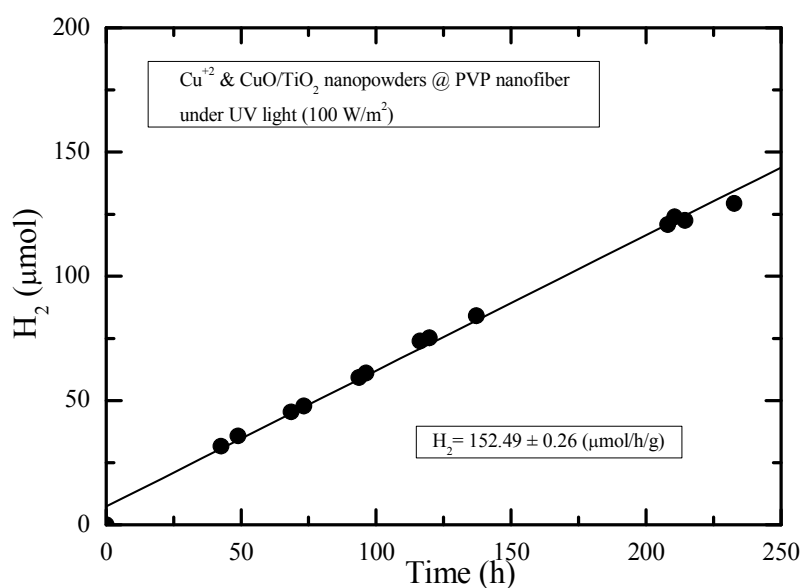
Figure 7.18 Time course of hydrogen production of nanofibers polymers loaded with Cu^{+2} and CuO /TiO_2 nanopowders under UV light (100 W/m²), from water/methanol solution (1:1 v/v). The weight of photocatalyst is estimated to be 3.58 mg. Hydrogen production rate is 152.49±0.26 μmol/h/g. The linear trend expresses the stability of hydrogen production over 250 hours.

Table 7.4 Results and conditions of Cu^{+2} and CuO/TiO_2 nanopowders @ PVP nanofiber under sunlight.

H_2 production (μmol/h)	H_2 production (μmol/h/g)	Effective Area, m^2	Energy Efficiency % @ x=0	Energy Efficiency % @ x=0.7
0.18 ± 0.01	625.2 ± 36.8	0.000081	0.0183	0.061

Photocatalyst type and weight (g)	Nano-structure and geometry	Photocatalyst Size, composition, Crystal structure	Water/ Methanol solution (1:1) Volume basis	Light Intensity If UV, (100 W/m²) If Sunlight, ≈ (240 W/m²)
Cu^{+2} & CuO/TiO_2 (0.000289)	Nanopowders @ Nanofibers (as support)	Cu (10 mol %, <50 nm), TiO_2 (<100 nm, anatase), PVP nanofibers (d< 1μm)	10 ml (5 ml each)	Sunlight (Texas, College Station)
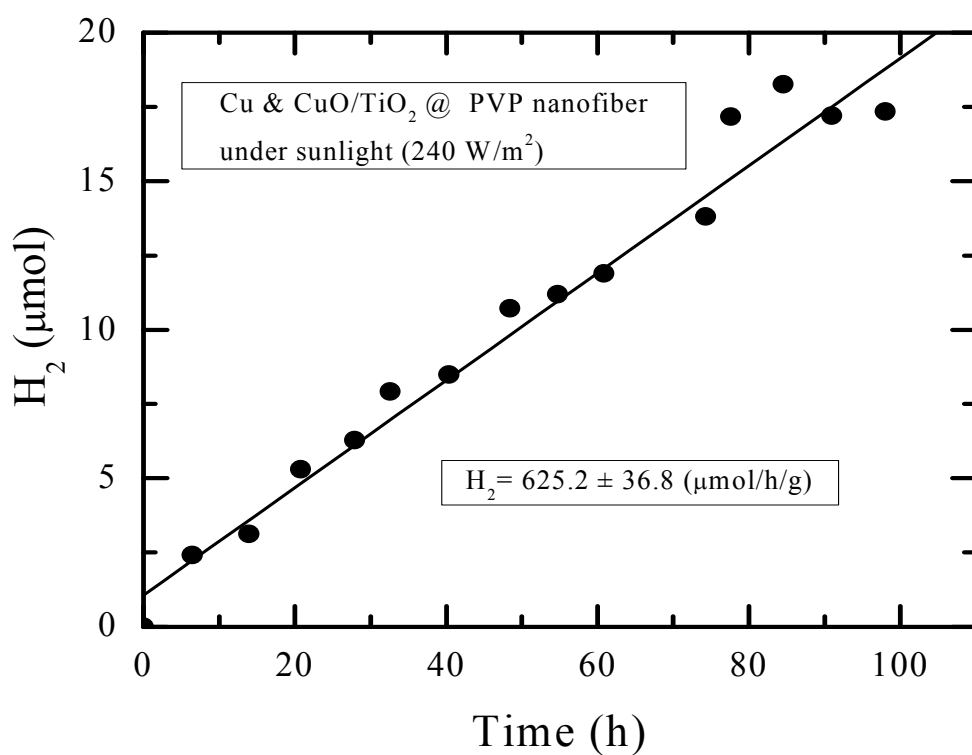
Figure 7.19 hydrogen production rate of Cu^{+2} and CuO/TiO_2 nanopowders @ PVP nanofiber under sunlight.

H$_2$ Production of Cu^{+2} and CuO/TiO$_2$ Nanopowders inside Silica Nanofiber under Sunlight

Table 7.5 Results and conditions of Cu^{+2} and CuO/TiO$_2$ nanopowders @ silica nanofiber under sunlight

H$_2$ production (μmol/h)	H$_2$ production (μmol/h/g)	Effective Area, m^2	Energy Efficiency % @ x=0	Energy Efficiency % @ x=0.7
0.36 ± 0.01	64.9 ± 1.8	0.000081	0.0366	0.122

Photocatalyst type and weight (g)	Nano-structure and geometry	Photocatalyst Size , composition, Crystal structure	Water/ Methanol solution (1:1) Volume basis	Light Intensity If UV, (100 W/m^2) If Sunlight, ≈(240 W/m^2)
Cu^{+2} & CuO/TiO$_2$ (0.0056)	Nanopowders @ Silica Nanofibers (as support)	Cu (10 mol %, <50 nm), TiO$_2$ (<100 nm, anatase), Silica nanofibers (d< 1μm)	10 ml (5 ml each)	Sunlight (Texas, College Station)
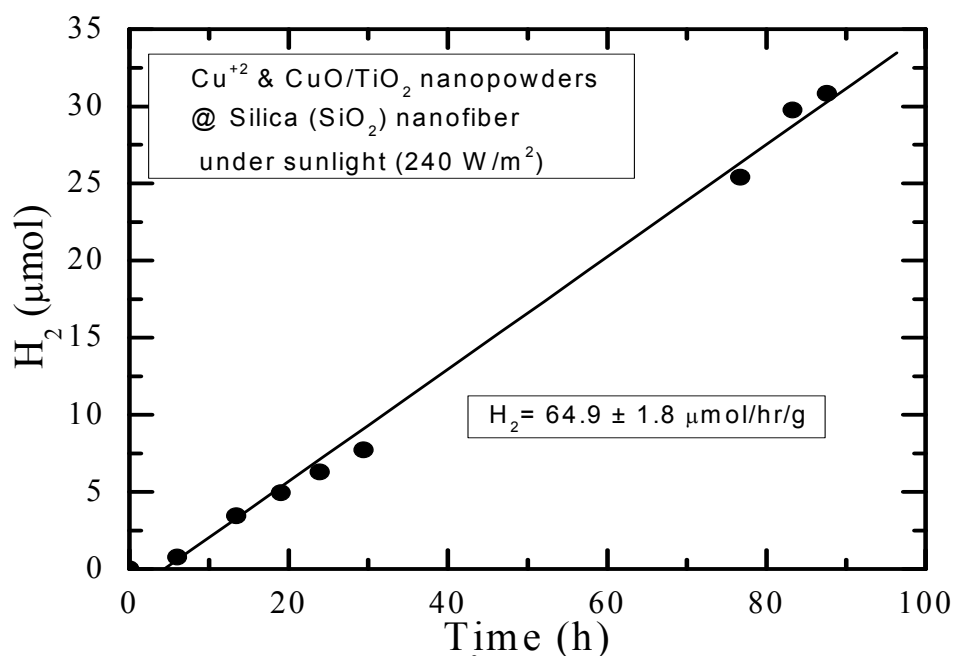
Figure 7.20 Hydrogen production rate of Cu^{+2} and CuO/TiO$_2$ nanopowders @ silica nanofiber under sunlight.

H$_2$ Production of Ag/CuInS$_2$/Dye (R.B.S)/TiO$_{2-x}$.N$_x$ inside Silica Nanofiber under Sunlight

Table 7.6 Results and conditions of Ag/CuInS$_2$/Dye (R.B.S)/TiO$_{2-x}$.N$_x$ @ silica nanofiber under Sunlight.

H$_2$ production (μmol/h)	H$_2$ production (μmol/h/g)	Effective Area, m^2	Energy Efficiency % @ x=0	Energy Efficiency % @ x=0.7
1.19 ± 0.07	34.0 ± 2.2	0.000081	0.1209	0.4033

Photocatalyst type and weight (g)	Nano-structure and geometry	Photocatalyst Size , composition, Crystal structure	Water/ Methanol solution (1:1) Volume basis	Light Intensity If UV, (100 W/m^2) If Sunlight , ≈ (240 W/m^2)
Ag/dye/CuInS$_2$/ TiO$_{2-x}$.N$_x$ (0.035)	Nanopowders @ Silica Nanofibers (as support)	Ag (10 wt %, <50 nm), TiO$_2$ (<100 nm, anatase), Silica nanofibers (d< 1μm)	10 ml (5 ml each)	Sunlight (Texas, College Station)
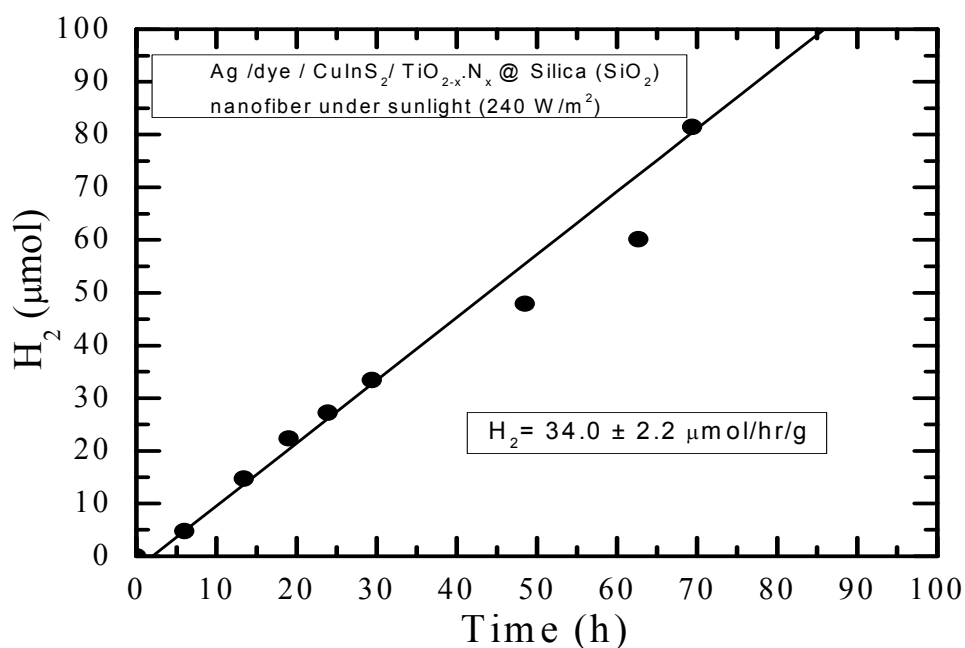
Figure 7.21 Hydrogen production rate of Ag/CuInS$_2$/Dye (R.B.S)/TiO$_{2-x}$.N$_x$ @ silica nanofiber under Sunlight.

H$_2$ Production of Fe^{+3}/TiO$_2$ Nanoparticles inside Silica Nanofibers under Sunlight

Table 7.7 Results and conditions of Fe^{+3}/TiO$_2$ nanoparticles @ silica nanofibers under sunlight.

H$_2$ production (µmol/h)	H$_2$ production (µmol/h/g)	Effective Area, m^2	Energy Efficiency % @ x=0	Energy Efficiency % @ x=0.7
0.11 ± 0.002	15.7 ± 0.03	0.000081	0.0111	0.0372

Photocatalyst type and weight (g)	Nano-structure and geometry	Photocatalyst Size, composition, Crystal structure	Water/ Methanol solution (1:1) Volume basis	Light Intensity If UV, (100 W/m²) If Sunlight, ≈(240 W/m²)
Fe^{+3}/TiO$_2$ (0.007)	Nanopowders @ Silica Nanofibers (as support)	Fe^{+3}(<50 nm), TiO$_2$ (<100 nm, anatase), Silica nanofibers (d< 1µm)	10 ml (5 ml each)	Sunlight (Texas, College Station)
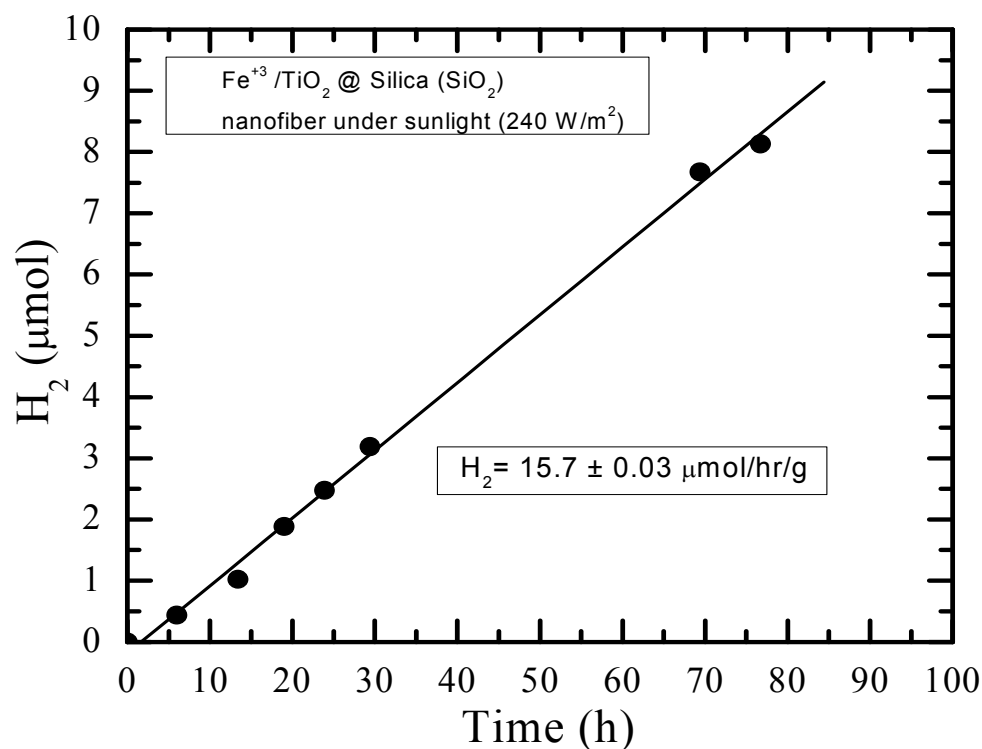
Figure 7.22 Hydrogen production rate of Fe^{+3}/TiO$_2$ nanoparticles @ silica nanofibers under sunlight.

H_2 Production of Cu^{+2} and CuO/TiO_2 Nanopowders "One-Step" inside Silica Nanofiber under Sunlight

Table 7.8 Results and conditions of Cu^{+2} and CuO/TiO_2 nanoparticles "one-step" @ silica nanofiber under sunlight.

H_2 production (µmol/h)	H_2 production (µmol/h/g)	Effective Area, m^2	Energy Efficiency % @ x=0	Energy Efficiency % @ x=0.7
0.018±0.007	2.35 ± 0.09	0.000081	0.00183	0.0061

Photocatalyst type and weight (g)	Nano-structure and geometry	Photocatalyst Size , composition, Crystal structure	Water/ Methanol solution (1:1) Volume basis	Light Intensity If UV, (100 W/m²) If Sunlight , ≈(240 W/m²)
Cu^{+2} & CuO/TiO_2 (0.008)	Colloids (one-step) @ Nanofibers (as support)	Cu (10 mol %) , TiO_2 (<30 nm, anatase), Silica nanofibers (d< 500 nm)	10 ml (5 ml each)	Sunlight (Texas, College Station)
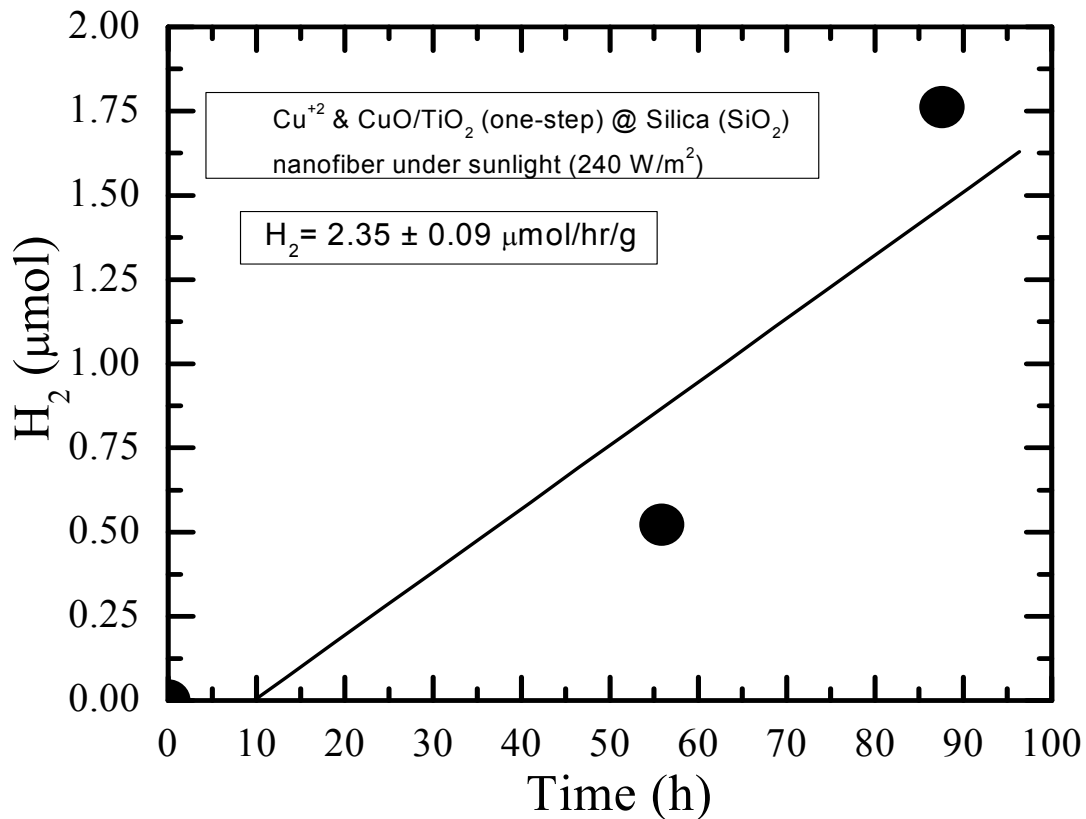
Figure 7.23 Hydrogen production rate of Cu^{+2} and CuO/TiO_2 nanoparticles "one-step" @ silica nanofiber under sunlight.

CONCLUSIONS

We demonstrated the feasibility of using composite nanofibers with nanopowders as photocatalyst architecture for photoelectrochemical reactions to produce hydrogen from water/methanol decomposition. Hydrogen production rate for Ag/TiO_2 nanofibers is 17.63 ± 0.14 µmol/h/g and for Cu^{+2} and CuO/TiO_2 on polymer nanofibers is 152.49 ± 0.26 µmol/h/g. The new architecture reduces the aggregation phenomena of nanopowders allowing for high surface area and high porosity of composite nanofibers with nanopowders materials. As the results indicated, it is valuable and effective

photocatalytic materials for solar-hydrogen production from water-splitting. Silica nanofiber is strong supporter due to its stability in aqueous solution. Integration photocatalyst system of nanostructure materials include quantum dots, dye, nitrogen doping to TiO_2 decorated with inexpensive metal that injected into silica nanofibers provide cost-effective and very promising photocatalyst for hydrogen production from water-splitting using solar energy.

The highest energy efficiency reached from nanofibers system is $\approx$ 0.13%. It is important to mention that energy efficiency (%) calculated assuming that all sunlight power was absorbed. This assumption made because of inability to measure the light passing through photocatalyst and being wasted. Accordingly, this assumption was lead to inaccurate and weak solar to hydrogen conversion efficiency. Also, the quantum efficiency which means two times the hydrogen molecular produced over total number of photons absorbed will be very low based on this assumption. When light transmission assumed to be 70% and only 30% was absorbed, the highest energy efficiency reached from nanofibers system is $\approx$ 0.44%. The maximum energy efficiency can be achieved for water-splitting using solar energy is around 30 % due to the fact that the minimum energy required to split water is $\approx$ 1.23 to 1.5 eV, including the thermodynamic losses. The portion of photons energy or sun power that can be reached to earth and effectively absorbed from sunlight which has the same or larger energy than 1.5 eV is limited to $\approx$ 30 %. This means the photons wavelength from sunlight that should be harvest is equal or less than $\approx$ 1008 nm.

CHAPTER VIII

COMPARISON OF RESULTS

In this chapter, a comparison of results and data analyzed in order to find the most promising photocatalyst system for solar-hydrogen production from water splitting either under UV light or sunlight. Table 8.1 & Table 8.2 show the summary of comparison of results results.

Table 8.1 Summary of the results shows the effect of additives on solar-hydrogen production from photoelectrochemical water-splitting.

Photocatalyst Cu^{+2} and CuO/TiO$_2$ Nanoparticles (0-D) [Additives type]	Light Source UV ≈100 W/m^2 Sunlight ≈240 W/m^2	Effective area, m^2	H$_2$ production (μmol/h/g)	Energy Efficiency (%) @ x= 0	Energy Efficiency (%) @ x= 0.7
NaCl (weight=0.175g) (3.5 wt %)	UV	0.00008	63.3 ± 0.0069	3.089	10.29
	Sunlight	-	-	-	-
*Seawater (Gulf of Mexico)	UV	0.00008	16.65 ± 0.67	0.81	2.7
	Sunlight	0.00008	5.4 ± 1.3	0.054	0.18
*Pure water	UV	0.00008	62.8 ± 0.01	3.06	10.22
	Sunlight	0.00008	24.88 ± 0.58	0.51	1.72
Electron relay (MV^{+2}) (weight=0.027g)	UV	0.00008	16.38 ± 1.00	0.123	0.413
	Sunlight	-	-	-	-
Iodide anion (KI) (weight=0.0166g)	UV	0.00008	25.2 ± 2.8	0.307	1.02
	Sunlight	-	-	-	-
Carbonate Salt (NaHCO$_3$) (weight=0.0144g)	UV	0.00008	43.5 ± 2.0	0.529	1.76
	Sunlight	-	-	-	-
**Dye (Rose Bengal Sodium)	UV	-	-	-	-
	Sunlight	0.000081	0.64 ± 0.029	0.0132	0.044

*Mixed with methanol in equal volume basis (total volume of the solution is 10 ml).
** Weight of dye= 0.005 g, the dye is suspended in the water/methanol solution.

Notes (1) all other additives listed in Table 8.1 were mixed with equal volume of pure water (deionized) and methanol in the presence of same photocatalyst. The weight of photocatalyst was changed based on each experiment. (2) Methanol, pure water, and seawater are expected to generate no hydrogen when they are used individually under either UV light or sunlight in the presence of same photocatalyst and same reaction conditions. Hydrogen can be only generated from the mixture of pure water/methanol or seawater/methanol solutions due to the nature of experimental set-up used here (single photoelectrochemical cell), which has no oxidation co-catalyst, only methanol added to water to stop oxygen production. Therefore, the activity tests for methanol, pure water, and seawater individually under either UV light or sunlight in the presence of same photocatalyst and same reaction conditions were not conducted as in other cases. The primary objectives of this study was to investigate the following (1) The structure-properties relationship through testing quantum dots, nanocomposites thin film, nanofibers, nanorods, nanowires (core/shell), nanotubes, nanopowders, nanoparticles, nanospheres of TiO_2 decorated with metals, dye sensitization, and nitrogen-doping. (2) The role of adding electron donors/relays to solution and their effect on semiconductor surface-electrolyte interface under constant conditions such as KI, Mv^{+2}, NaCl, NaHCO$_3$, sea and pure water. (3) Band gap and defect engineering by cation and anion doping. (4) Quantum dots and dye sensitization effect. The nanomaterials activity evaluated based on observed hydrogen production rate (μmol/h/g) experimentally and based on the energy efficiency (%) calculation.

Table 8.2 Summary of the results shows the effect of nanostructures shape, quantum dots and dye sensitization, metals doping, and nitrogen doping on solar-hydrogen production from photoelectrochemical water-splitting.

Design Nanocomposites Photocatalyst	Light Source UV ≈ 100 W/m^2 Sunlight ≈ 240 W/m^2	Effective area, m^2	H_2 production (μmol/h/g)	Energy Efficiency (%) @ x= 0	Energy Efficiency (%) @ x= 0.7
Ag/TiO$_2$ nanocomposites thin film (2-D)	UV	0.0001	147.9 ± 35.5	0.016	0.056
	Sunlight	-	-	-	-
Cu/TiO$_2$ nanotube (1-D)	UV	0.000144	404 ± 47.3	0.0398	0.132
	Sunlight	-	-	-	-
Cu/TiO$_2$ nanorod (1-D)	UV	0.000144	128.6 ± 5.4	0.0988	0.329
	Sunlight	-	-	-	-
Cu/TiO$_2$ (core/shell) nanowire (1-D)	UV	0.000144	56.8 ± 3.0	0.0233	0.0777
	Sunlight	-	-	-	-
Ag/TiO$_2$ nanofiber (2-D)	UV	0.000081	17.6 ± 0.14	0.119	0.398
	Sunlight	-	-	-	-
Cu/TiO$_2$ nanopowder @ PVP nanofiber	UV	0.000081	152.49 ± 0.26	0.1329	0.443
	Sunlight	0.000081	625.2 ± 36.8	0.0183	0.061
Cu/TiO$_2$ nanopowder @ silica nanofiber	UV	-	-	-	-
	Sunlight	0.000081	64.9 ± 1.8	0.0366	0.122
Cu/TiO$_2$ nanosphere suspension (0-D)	UV	0.000064	1797.3 ± 236.3	1.108	3.69
	Sunlight	0.000064	71.2 ± 4.2	0.045	0.15
Metal doping Ag/CuInS$_2$/TiO$_{2-x}$. N$_x$ film	UV	-	-	-	-
	Sunlight	0.000121	57.1 ± 9.2	0.019	0.063
Quantum dots sensitization Ag/CuInS$_2$/CdS/TiO$_{2-x}$.N$_x$ film	UV	-	-	-	-
	Sunlight	0.000121	21.6 ± 1.6	0.014	0.047
Cu and CuO/TiO$_2$ nanopowders (0-D)	UV	0.00008	62.8 ± 0.01	3.06	10.22
	Sunlight	0.000081	24.88 ± 0.58	0.518	1.72
Cu/TiO$_{2-x}$. N$_x$ (Nitrogen-doping) Nanocolloids (nanoparticles)	UV	-	-	-	-
	Sunlight	0.000064	20.8 ± 11.1	0.00797	0.0265
Dye sensitization @ nanofiber Ag/CuInS$_2$/Dye/TiO$_{2-x}$. N$_x$	UV	-	-	-	-
	Sunlight	0.000081	34.0 ± 2.2	0.1209	0.4033

The solar to hydrogen energy conversion efficiency (%) is calculated based on that all UV light or sunlight exposed to photocatalyst is absorbed (x = 0). On other assumption, only 30% of light is absorbed and 70% is transmitted (x = 0.7). It is important to know the energy efficiency % corresponding to light transmission or light harvesting efficiency because the ultimate goal is to split seawater using sunlight for hydrogen production. Table 3.10 which show the hydrogen production rate from seawater/methanol under sunlight using nanopowders of Cu^{+2} and CuO/TiO_2. Figure 8.1 shows the energy efficiency % verses "X" (portion of sunlight transmitted without absorption).
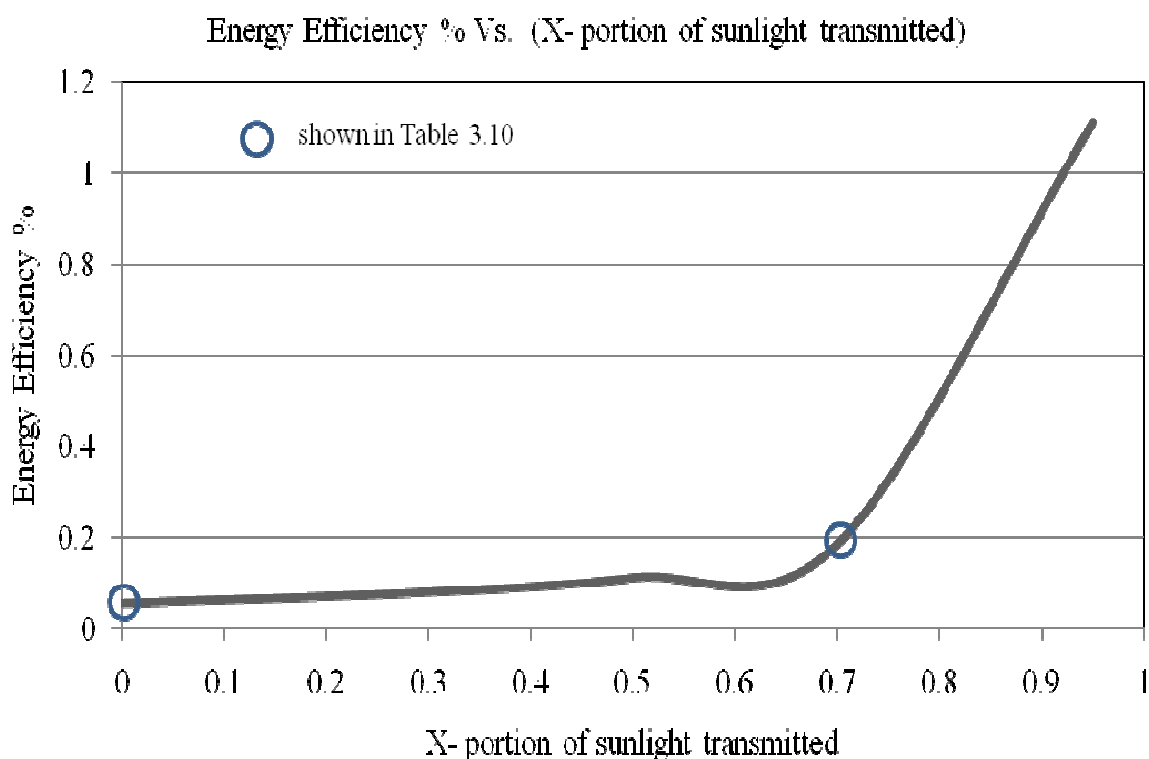
Figure 8.1 Solar to hydrogen energy conversion efficiency (%) Vs. X- portion of sunlight transmitted without absorption for hydrogen production by seawater splitting under sunlight.

The nanomaterials synthesized/fabricated in matter that alter their main parameters such as size, shape/geometry, crystal structure, internal and external chemical compositions. Controlling over these nanomaterials parameters will allowed modifying and promoting their properties, flexibility, behavior, and interaction with solid and liquid surfaces and interfaces.

Accordingly, the nanomaterials properties such as photocatalytic, photovoltaic, stability, and reactivity will be enhanced. In specific, thermal, optical, electrical, and chemical properties are targeted to improve. Several multifunctional TiO_2 nanocomposites photocatalyst designed and prepared to obtain the following: (1) Enhance the solar energy harvesting by extend the absorption to longer wavelength photons that lies in visible spectrum of sunlight (largest portion of sun radiation). (2) Convert the photons energy to electrical energy by photoexcitation charge carriers, more electron-hole pair per single photon, reduce recombination of electron-hole pair, and enhance quantum efficiency. (3) Convert electrical energy (electrons and holes) to chemical energy by catalyze the water reduction and oxidation reaction for hydrogen production. (4) Stability (photoresistance and resistance to corrosion in water solutions). The alteration of nanostructure of TiO_2 and varies nanocomposites deposited on the surface was reflected on hydrogen production rate and energy efficiency %. As final conclusion statement, nanostructure TiO_2 sensitized with quantum dots, dye, doped with nitrogen, loaded with low cost metals such as Ag & Cu is a powerful photocatalyst system can be used and improved for hydrogen production from photoelectrochemical water-splitting using solar energy.

This research was dedicated to investigate the nanoscience and nanotechnology application to the renewable energy production in order to participate in the progress efforts to find solutions of energy and environment challenges. Also it is oriented to encourage engineers and scientists to tackle more promising, sustainable, clean and renewable energy production technologies. Sea (water) and sunlight as natural resources is the best resource ever that can be utilized to generate energy source/carriers because they are clean, abundant, and permanent. Moreover, the concept to generate energy from sun and seawater is quite simple which means simple and cost-effective technology or process could be used. Specifically, nanomaterials and quantum dots were used as photocatalytic materials to catalyze the water-splitting reaction using solar energy for hydrogen production. The research was conducted by design, synthesis, characterization and application of these nanomaterials for water-splitting reaction in the presence of electron donor (to prevent oxygen evolution) under UV light and natural sunlight. Green, simple, low cost and effective synthesis methods of nanomaterials were used. In addition high throughput screening process to test the nanomaterials for water-splitting reaction in the laboratory or under natural sunlight was established. The process is also simple, inexpensive, safe, and flexible to test large numbers of nanomaterials. An effective experimental schedule was used to collect samples regularly and measure hydrogen evolution using gas chromatography.

CHAPTER IX

CONCLUSIONS

Hydrogen production by water-splitting using solar energy and nanostructure photocatalysts is very promising as renewable, efficient, environmentally clean technology. The key is to reduce the cost of hydrogen production as well as increase the solar-to-hydrogen conversion efficiency by searching for cost-effective photocatalytic materials.

In this dissertation, energy efficiency calculations were carried out based on hydrogen production observation to evaluate the nanomaterials activity. The results are important to gain better understanding of water-splitting reaction mechanism to develop the technology. Design, synthesis, characterization/properties and application of these nanomaterials was the road-map to achieve the research objectives.

The design of TiO_2 is selected based on superb photocatalytic and photovoltaic properties and high stability in aqueous solution. Various structures of nanocomposites TiO_2 were designed according to their characteristics and potential activity. TiO_2 with quantum dots, nanocomposites thin film, nanofibers, nanorods, (core/shell) nanowires, nanotubes, nanopowders, nanoparticles, and nanosphere decorated with metals, dye sensitization, and doped with nitrogen are designed. Green physical and chemical synthesis methods such as sol-gel techniques, autoclave, microwave, electrospinning, wet impregnation, hydrothermal, chemical vapor deposition, template-based fabrication (anodic aluminium oxide membrane), drop casting, dip coating, wet coating were used to

synthesize and fabricate the nanomaterials and quantum dots. Several characterization techniques such as XRD, XPS, EDS, SEM, UV-visible spectra, and optical microscopic and digital camera were also obtained to characterize the properties. The application or processing to test the activity of these nanomaterials for hydrogen production by water-splitting was conducted through extensive experimental program. It was carried out in a one photo-single column experimental set-up to detect hydrogen evolution.

A high throughput screening process to evaluate single photo reduction catalysts was established here for simplicity, safety, cost-effective and flexibility of testing nanomaterials for water photoreduction reactivity and hydrogen generation. Therefore, methanol as electron donor or oxidation agent was mixed with water in equal volume ratio in order to prevent the oxygen evolution and only measured the time course of hydrogen production.

Major findings in this dissertation are (1) a high throughput screening process to evaluate single photoreduction catalysts for solar-hydrogen production by water-splitting was established. (2) Among all tested nanomaterials, nanofibers structure of TiO_2 doped with nitrogen, sensitized with dye (Rose Bengal Sodium) and quantum dots ($CuInS_2$), and decorated with metals (Ag) showed the high solar-to-hydrogen conversion efficiency and high hydrogen production rate (3) Simple, safe, inexpensive, robust, efficient and green physical and chemical synthesis methods were used to prepare the nanomaterials and quantum dots. (4) Gaining insight and better understanding of water-splitting reaction mechanism by (a) Studying the structure-properties relationship of nanomaterials (b) Studying the role of additives on surface-interface chemistry of

semiconductor and electrolyte (c) Knowing how to reduce the electron-hole recombination reactions to enhance quantum efficiency (d) Extending the absorption of nanomaterials to harness the visible light of solar energy by doping and defect chemistry.

Finally, the conclusion statements as follows:

- The most promising results found is when using Cu^{+2} and CuO/TiO_2 nanopowders as photocatalyst to produce hydrogen from water/methanol solution or water/methanol with NaCl (3.5 wt%) under UV light (100 W/m^2), the energy effiency % @ x= 0.7 reached up to 10%.

- For seawater/methanol equal volume solution under sunlight, the energy efficiency % was about 0.18%, this value is encouraging research towards splitting seawater using sunlight as renewable and clean energy source in presence of photocatalytic nanomaterials.

- Cu/TiO_2 nanosphere suspension in water/methanol equal volume solution also showed a promising hydrogen production rate with 3.69 % energy efficiency under UV light. The Cu/TiO_2 nanosphere shows better performance than nanotube and nanowire, and nanorod.

- Cu/TiO_2 nanopowders injected inside silica nanofiber structure have energy efficiency of 0.122% under sunlight suggesting that nanofiber network is a very effective support soft material for nanomaterials photocatalyst.

Quantum dots sensitization to TiO_2 thin film with Ag and nitrogen doping showed unexpected results with only 0.063% of energy efficiency. However, an integeration photocatalyst system of $Ag/CuInS_2/Dye/TiO_{2-x}.N_x$ exhibited a better performance as 0.4033% energy efficiency.

Dye sensitization, quantum dots sensitization, and nitrogen doping to TiO_2 were used to harvest visible light from the sun. However, it needs further investigation and improvement.

REFERENCES

1   Spath, P. L., and Mann, M.K. *Life Cycle Assessment of Hydrogen Production via Natural Gas Steam Reforming.* Technical Report, National Renewable Energy Laboratory (Golden, CO, 2001).

2   Bossel, U., Eliasson, B., and Taylor, G. . The future of the hydrogen economy: rright or bleak? *Proc. Eur. Fuel Cell Forum, www.efcf.com/reports,* (2003).

3   Yacobucci, B. D. & Curtright, A. E. A *Hydrogen Economy and Fuel Cells: An Overview.* CRS Report for Congress. Congressional Research Service, (The Library of Congress, 2004).

4   Jain, I. P. Hydrogen: the fuel for 21st century. *International Journal of Hydrogen Energy* **34**, 7368-7378, doi:DOI 10.1016/j.ijhydene.2009.05.093 (2009).

5   Prakasam, H. E. *Towards Highly Efficient Water Photoelectrolysis* Doctor of Philosophy thesis, (The Pennsylvania State University, 2008).

6   Rosen, M. A. & Scott, D. S. Comparative efficiency assessments for a range of hydrogen production processes. *International Journal of Hydrogen Energy* **23**, 653-659 (1998).

7   Hassmann, K. & Kuhne, H. M. Primary energy-sources for hydrogen-production. *International Journal of Hydrogen Energy* **18**, 635-640 (1993).

8   New York State Energy Research and Development Authority, N., Hydrogen fact sheet. Hydrogen Production-Steam Methane Reforming (SMR), www.nyserda.org. (Accessed October, 22, 2010).

9   International Clearinghouse for Hydrogen Commerce, http://www.ch2bc.org/index2.;htm (Accessed October 22, 2010).

10   Vayssieres, L. *On Solar Hydrogen & Nanotechnology* (John Wiley & Sons (Asia) Pte Ltd., 2009).

11   Zou, Z., Ye, J., Sayama, K. & Arakawa, H. Direct splitting of water under visible light irradiation with an oxide semiconductor photocatalyst. *Nature* **414**, 625-627 (2001).

12   Osterloh, F. E. Inorganic materials as catalysts for photochemical splitting of water. *Chemistry of Materials* **20**, 35-54, doi:Doi 10.1021/Cm7024203 (2008).

13   Maeda, K. & Domen, K. New non-oxide photocatalysts designed for overall water splitting under visible light. *Journal of Physical Chemistry C* **111**, 7851-7861, doi:Doi 10.1021/Jp070911w (2007).

14   Shet, S., Ahn, K. S., Deutsch, T., Wang, H. L., Ravindra, N. *et al.* Synthesis and characterization of band gap-reduced ZnO:N and ZnO:(Al,N) films for photoelectrochemical water splitting. *Journal of Materials Research* **25**, 69-75, doi:DOI 10.1557/Jmr.2010.0017 (2010).

15   Wang, H. L., Deutsch, T. & Turner, J. A. Direct water splitting under visible light with nanostructured hematite and WO3 photoanodes and a GaInP2 photocathode. *Journal of the Electrochemical Society* **155**, F91-F96, doi:Doi 10.1149/1.2888477 (2008).

16   Turner, J. A. & Kocha, S. S. Photoelectrochemical water-splitting systems. *Solar '95 - Proceedings of the 1995 American Solar Energy Society Annual Conference*, 38-41436 (1995).

17   Yan, Y., Ahn, K. S., Shet, S., Deutsch, T., Huda, M. *et al.* Band gap reduction of ZnO for photoelectrochemical splitting of water - art. no. 66500H. *Solar Hydrogen and Nanotechnology II* **6650**, H6500-H65006210, doi:Artn 66500h Doi 10.1117/12.734950 (2007).

18   Arakawa, H. & Sayama, K. Solar hydrogen production. Significant effect of Na2CO3 addition on water splitting using simple oxide semiconductor photocatalysts. *Catalysis Surveys from Japan* **4**, 75-80 (2000).

19   Arakawa, H. & Sayama, K. Oxide semiconductor materials for solar light energy utilization. *Research on Chemical Intermediates* **26**, 145-152 (2000).

20   Ohno, T., Fujihara, K., Sarukawa, K., Tanigawa, E. & Matsumura, M. Splitting of water by combining two photocatalytic reactions through a quinone compound dissolved in an oil phase. *Zeitschrift Fur Physikalische Chemie-International Journal of Research in Physical Chemistry & Chemical Physics* **213**, 165-174 (1999).

21   Zhang, Y. J., Wu, Y. P., Wang, Z. H. & Hu, Y. R. Preparation of CdS/TiO2NTs nanocomposite and its activity of photocatalytic hydrogen production. *Rare Metal Materials and Engineering* **38**, 1514-1517 (2009).

22   Wu, R. J., Ju, Y. D. & Jeng, C. C. Promotion of generation of hydrogen by splitting of water by CNT over Pt/TiO2 catalysts. *Journal of Nanoscience and Nanotechnology* **10**, 4213-4220, doi:DOI 10.1166/jnn.2010.2941 (2010).

23   Deguchi, S., Shibata, N., Takeichi, T., Furukawa, Y. & Isu, N. Photocatalytic hydrogen production from aqueous solution of various oxidizing sacrifice agents. *Journal of the Japan Petroleum Institute* **53**, 95-100 (2010).

24   Fang, J., Shi, F. C., Bu, J., Ding, J. J., Xu, S. T. *et al.* One-step synthesis of bifunctional TiO2 catalysts and their photocatalytic activity. *Journal of Physical Chemistry C* **114**, 7940-7948, doi:Doi 10.1021/Jp100519q (2010).

25   Fei, H. H., Yang, Y. C., Rogow, D. L., Fan, X. J. & Oliver, S. R. J. Polymer-templated nanospider TiO2 thin films for efficient photoelectrochemical water splitting. *ACS Applied Materials & Interfaces* **2**, 974-979, doi:Doi 10.1021/Am100087b (2010).

26   Tode, R., Ebrahimi, A., Fukumoto, S., Iyatani, K., Takeuchi, M. *et al.* Photocatalytic decomposition of water on double-layered visible light-responsive TiO2 thin films prepared by a magnetron sputtering deposition method. *Catalysis Letters* **135**, 10-15, doi:DOI 10.1007/s10562-010-0262-y (2010).

27   Aryal, K., Pantha, B. N., Li, J., Lin, J. Y. & Jiang, H. X. Hydrogen generation by solar water splitting using p-InGaN photoelectrochemical cells. *Applied Physics Letters* **96**, -, doi:Artn 052110 Doi 10.1063/1.3304786 (2010).

28   Youngblood, W. J., Lee, S. H. A., Maeda, K. & Mallouk, T. E. Visible light water splitting using dye-sensitized oxide semiconductors. *Accounts of Chemical Research* **42**, 1966-1973, doi:Doi 10.1021/Ar9002398 (2009).

29   Wu, K. R., Yeh, C. W., Hung, C. H., Cheng, L. H. & Chung, C. Y. Photoelectrochemical properties of nitrogen-doped indium tin oxide thin films prepared by reactive DC magnetron sputtering. *Thin Solid Films* **518**, 1581-1584, doi:DOI 10.1016/j.tsf.2009.09.056 (2009).

30   Bak, T., Nowotny, J., Rekas, M. & Sorrell, C. C. Photo-electrochemical hydrogen generation from water using solar energy. Materials-related aspects. *International Journal of Hydrogen Energy* **27**, 991-1022, doi:Pii S0360-3199(02)00022-8 (2002).

31   Hanna, M. C. & Nozik, A. J. Solar conversion efficiency of photovoltaic and photoelectrolysis cells with carrier multiplication absorbers. *Journal of Applied Physics* **100**, -, doi:Artn 074510 Doi 10.1063/1.2356795 (2006).

32   Khaselev, O. & Turner, J. A. A monolithic photovoltaic-photoelectrochemical device for hydrogen production via water splitting. *Science* **280**, 425-427 (1998).

33   Mor, G. K., Shankar, K., Paulose, M., Varghese, O. K. & Grimes, C. A. Enhanced photocleavage of water using titania nanotube arrays. *Nano Letters* **5**, 191-195, doi:Doi 10.1021/Nl048301k (2005).

34   Hirano, M. & Matsushima, K. Photoactive and adsorptive niobium-doped anatase (TiO2) nanoparticles: Influence of hydrothermal conditions on their morphology, structure, and properties. *Journal of the American Ceramic Society* **89**, 110-117, doi:DOI 10.1111/j.1551-2916.2005.00648.x (2006).

35   Chou, C. S., Yang, R. Y., Yeh, C. K. & Lin, Y. J. Preparation of TiO2/nano-metal composite particles and their applications in dye-sensitized solar cells. *Powder Technology* **194**, 95-105, doi:DOI 10.1016/j.powtec.2009.03.039 (2009).

36   Kavan, L., Kalbac, M., Zukalova, M., Exnar, I., Lorenzen, V. *et al.* Lithium storage in nanostructured TiO2 made by hydrothermal growth. *Chemistry of Materials* **16**, 477-485, doi:Doi 10.1021/Cm035046g (2004).

37   Sobana, N., Muruganadham, M. & Swaminathan, M. Nano-Ag particles doped TiO2 for efficient photodegradation of Direct azo dyes. *Journal of Molecular Catalysis a-Chemical* **258**, 124-132, doi:DOI 10.1016/j.molcata.2006.05.013 (2006).

38   Park, J. A., Moon, J., Lee, S. J., Kim, S. H., Zyung, T. *et al.* Structure and CO gas sensing properties of electrospun TiO2 nanofibers. *Materials Letters* **64**, 255-257, doi:DOI 10.1016/j.matlet.2009.10.052 (2010).

39   Li, Y. & Zhang, J. Z. Hydrogen generation from photoelectrochemical water splitting based on nanomaterials. *Laser & Photonics Reviews* **4**, 517-528, doi:DOI 10.1002/lpor.200910025 (2010).

40   Currao, A. Photoelectrochemical water splitting. *CHIMIA International Journal for Chemistry* **61**, 815-819 (2007).

41   Wilhelm, E. & Fowler, M. A Technical and economic review of solar hydrogen production technologies. *Bulletin of Science Technology Society* **26**, 278-287, doi:10.1177/0270467606290306 (2006).

42   Bao, N., and Domen, K. . Development of photocatalysts for water splitting under visible light. *Chinese-American Chemical Society* **2**, 10-14 (2008).

43   Moon, S. C., Mametsuka, H., Tabata, S. & Suzuki, E. Photocatalytic production of hydrogen from water using TiO2 and B/TiO2. *Catalysis Today* **58**, 125-132 (2000).

44   Hoffmann, M. R., Martin, S. T., Choi, W. Y. & Bahnemann, D. W. Environmental applications of semiconductor photocatalysis. *Chemical Reviews* **95**, 69-96 (1995).

45   Ni, M., Leung, M. K. H., Leung, D. Y. C. & Sumathy, K. A review and recent developments in photocatalytic water-splitting using TiO2 for hydrogen production. *Renewable and Sustainable Energy Reviews* **11**, 401-425 (2007).

46   Chen, X. *Synthesis and Investigation of Novel Nanomaterials for Improved Photocatalysis.* Doctor of Philosophy, thesis, (Case Western Reserve University, 2005).

47   Aprile, C., Corma, A. & Garcia, H. Enhancement of the photocatalytic activity of TiO2 through spatial structuring and particle size control: from subnanometric to submillimetric length scale. *Physical Chemistry Chemical Physics* **10**, 769-783, doi:Doi 10.1039/B712168g (2008).

48   Kitano, M., Takeuchi, M., Matsuoka, M., Thomas, J. A. & Anpo, M. Photocatalytic water splitting using Pt-loaded visible light-responsive TiO2 thin film photocatalysts. *Catalysis Today* **120**, 133-138, doi:DOI 10.1016/j.cattod.2006.07.043 (2007).

49   Matsuoka, M., Kitano, M., Takeuchi, M., Tsujimaru, K., Anpo, M. *et al.* Photocatalysis for new energy production - Recent advances in photocatalytic water splitting reactions for hydrogen production. *Catalysis Today* **122**, 51-61, doi:DOI 10.1016/j.cattod.2007.01.042 (2007).

50   Park, J. H. & Bard, A. J. Unassisted water splitting from bipolar Pt/dye-sensitized TiO2 photoelectrode arrays. *Electrochemical and Solid State Letters* **8**, G371-G375 (2005).

51   Hirano, K., Suzuki, E., Ishikawa, A., Moroi, T., Shiroishi, H. *et al.* Sensitization of TiO2 particles by dyes to achieve H-2 evolution by visible light. *Journal of Photochemistry and Photobiology a-Chemistry* **136**, 157-161 (2000).

52   Chen, X. & Mao, S. S. Titanium dioxide nanomaterials: Synthesis, properties, modifications, and applications. *Chemical Reviews* **107**, 2891-2959, doi:Doi 10.1021/Cr0500535 (2007).

53   Elhajj, J. *Electrosynthesis of TiO$_2$-Au Composites for Water Splitting Applications and Their Photoelectrochemical Characterization* M.Sc., thesis, (Northeastern University, 2008).

54   Linsebigler, A. L., Lu, G. Q. & Yates, J. T. Photocatalysis on TiO2 surfaces - principles, mechanisms, and selected results. *Chemical Reviews* **95**, 735-758 (1995).

55   Nowotny, J., Bak, T., Nowotny, M. K. & Sheppard, L. R. Titanium dioxide for solar-hydrogen I. Functional properties. *International Journal of Hydrogen Energy* **32**, 2609-2629, doi:DOI 10.1016/j.ijhydene.2006.09.004 (2007).

56   Connexions, The early history of nanotechnology. http://cnx.org/content/m14504/latest/, (Accessed October 22, 2010).

57   Buchman, A., Campoverde, J. & Dean, D., Nanoparticles as catalysts in chemical reaction, http://test.che.tamu.edu/orgs/groups/Seminario/materials/G02_nanoCatalyst.pdf., (Accessed October 22, 2010.

58   Chen, K. C., Materials engineering, National Center for Learning and Teaching in NanoscaleScience and Engineering, <http://www.nanoed.org/seminar/docs/Nano%20World_kathychen_121405.pdf> (Accessed October 22, 2010.

59   Lewis, N. S. Basic research needs for solar energy utilization. Report on the Basic Energy Sciences Workshop on Solar Energy Utilization. http://www.sc.doe.gov/bes/reports/files/SEU_rpt.pdf., <> (2005).

60   Pandit, A. & Holzarth, A. Harnessing solar energy for the production of clean fuels. www.ssnmr.leidenuniv.nl/files/ssnmr/CleanSolarFuels.pdf. (Accessed October 22, 2010).

61   Ye, Z. X., Liu, H. D., Schultz, I., Wu, W. H., Naugle, D. G. *et al.* Template-based fabrication of nanowire-nanotube hybrid arrays. *Nanotechnology* **19**, doi:Artn 325303 (3pp) Doi 10.1088/0957-4484/19/32/325303 (2008).

62   Dunn, S. Hydrogen futures: toward a sustainable energy system. *International Journal of Hydrogen Energy* **27**, 235-264 (2002).

63   Dougherty, W., Kartha, S., Rajan, C., Lazarus, M., Bailie, A. *et al.* Greenhouse gas reduction benefits and costs of a large-scale transition to hydrogen in the USA. *Energy Policy* **37**, 56-67 (2009).

64   Kikuchi, E., Nemoto, Y., Kajiwara, M., Uemiya, S. & Kojima, T. Steam reforming of methane in membrane reactors: comparison of electroless-plating and CVD membranes and catalyst packing modes. *Catalysis Today* **56**, 75-81 (2000).

65   Nowotny, J., Bak, T., Nowotny, M. K. & Sheppard, L. R. Titanium dioxide for solar-hydrogen II. Defect chemistry. *International Journal of Hydrogen Energy* **32**, 2630-2643, doi:DOI 10.1016/j.ijhydene.2006.09.005 (2007).

66   Fujishima, A. & Honda, K. Electrochemical photolysis of water at a semiconductor electrode. *Nature* **238**, 37-38 (1972).

67   Murphy, A. B., Barnes, P. R. F., Randeniya, L. K., Plumb, I. C., Grey, I. E. *et al.* Efficiency of solar water splitting using semiconductor electrodes. *International Journal of Hydrogen Energy* **31**, 1999-2017, doi:DOI 10.1016/j.ijhydene.2006.01.014 (2006).

68   Steinfeld, A. Solar hydrogen production via a two-step water-splitting thermochemical cycle based on Zn/ZnO redox reactions. *International Journal of Hydrogen Energy* **27**, 611-619, doi:Pii S0360-3199(01)00177-X (2002).

69   Licht, S., Wang, B., Mukerji, S., Soga, T., Umeno, M. *et al.* Over 18% solar energy conversion to generation of hydrogen fuel; theory and experiment for efficient solar water splitting (Reprinted from J. Phys. Chem. B, vol 104, pg 8920-8924, 2000). *Int. J. Hydrogen Energy* **26**, 653-659 (2001).

70   Kudo, A. Development of photocatalyst materials for water splitting. *International Journal of Hydrogen Energy* **31**, 197-202, doi:DOI 10.1016/j.ijhydene.2005.04.050 (2006).

71   Shah, A., Torres, P., Tscharner, R., Wyrsch, N. & Keppner, H. Photovoltaic technology: the case for thin-film solar cells. *Science* **285**, 692-698, doi:10.1126/science.285.5428.692 (1999).

72   Kitano, M., Takeuchi, M., Matsuoka, M., Thomas, J. M. & Anpo, M. Preparation of visible light-responsive TiO_2 thin film photocatalysts by an RF magnetron sputtering deposition method and their photocatalytic reactivity. *Chemistry Letters* **34**, 616-617 (2005).

73   Arabatzis, I. M., Stergiopoulos, T., Bernard, M. C., Labou, D., Neophytides, S. G. *et al.* Silver-modified titanium dioxide thin films for efficient photodegradation of methyl orange. *Applied Catalysis B: Environmental* **42**, 187-201 (2003).

74   Choi, H.-J. & Kang, M. Hydrogen production from methanol/water decomposition in a liquid photosystem using the anatase structure of Cu loaded TiO_2. *International Journal of Hydrogen Energy* **32**, 3841-3848 (2007).

75   (<http://upload.wikimedia.org/wikipedia/en/5/56/Relative_abundance_of

elements.pn>), O., 22, 2010. (Accessed on October 22, 2010).

76   Liao, W. S., Yang, T. L., Castellana, E. T., Kataoka, S. & Cremer, P. S. A rapid prototyping approach to ag nanoparticle fabrication in the 10-100 nm range. *Advanced Materials (Weinheim, Germany)* **18**, 2240-+, doi:DOI 10.1002/adma.200600589 (2006).

77   Castellana, E. T., Kataoka, S., Albertorio, F. & Cremer, P. S. Direct writing of metal nanoparticle films inside sealed microfluidic channels. *Analytical Chemistry* **78**, 107-112, doi:Doi 10.1021/Ac051288j (2006).

78   Liao, W. S., Chen, X., Yang, T. L., Castellana, E. T., Chen, J. X. *et al.* Benchtop chemistry for the rapid prototyping of label-free biosensors: Transmission localized surface plasmon resonance platforms. *Biointerphases* **4**, 80-85, doi:Doi 10.1116/1.3284738 (2009).

79   Kato, K., Tsuzuki, A., Taoda, H., Torii, Y., Kato, T. *et al.* Crystal structures of TiO2 thin coatings prepared from the alkoxide solution via the dip-coating technique affecting the photocatalytic decomposition of aqueous acetic acid. *Journal of Materials Science* **29**, 5911-5915 (1994).

80   Maeda, T., Vardar, G., Self, W. & Wood, T. Inhibition of hydrogen uptake in Escherichia coli by expressing the hydrogenase from the cyanobacterium Synechocystis sp. PCC 6803. *BMC Biotechnology* **7**, 25 (2007).

81   Maeda, T., Sanchez-Torres, V. & Wood, T. K. Enhanced hydrogen production from glucose by metabolically engineered Escherichia coli. *Applied Microbiology and Biotechnology* **77**, 879-890, doi:DOI 10.1007/s00253-007-1217-0 (2007).

82   Varghese, O. K. & Grimes, C. A. Appropriate strategies for determining the photoconversion efficiency of water photo electrolysis cells: A review with examples using titania nanotube array photoanodes. *Solar Energy Materials and Solar Cells* **92**, 374-384, doi:DOI 10.1016/j.solmat.2007.11.006 (2008).

83   Yan, H. J., Yang, J. H., Ma, G. J., Wu, G. P., Zong, X. *et al.* Visible-light-driven hydrogen production with extremely high quantum efficiency on Pt-PdS/CdS photocatalyst. *Journal of Catalysis* **266**, 165-168, doi:DOI 10.1016/j.jcat.2009.06.024 (2009).

84   Ge, L., Xu, M. X. & Fang, H. B. Photo-catalytic degradation of methyl orange and formaldehyde by Ag/InVO$_4$-TiO$_2$ thin films under visible-light irradiation. *Journal of Molecular Catalysis a-Chemical* **258**, 68-76, doi:DOI 10.1016/j.molcata.2006.05.026 (2006).

85   Jeon, M. K., Park, J. W. & Kang, M. Hydrogen production from methanol/water decomposition in a liquid photosystem using the anatase and rutile forms of Cu-TiO$_2$. *Journal of Industrial and Engineering Chemistry* **13**, 84-91 (2007).

86   Zhu, J. F. & Zach, M. Nanostructured materials for photocatalytic hydrogen production. *Current Opinion in Colloid & Interface Science* **14**, 260-269, doi:DOI 10.1016/j.cocis.2009.05.003 (2009).

87   Watanabe, T. & Honda, K. Measurement of the extinction coefficient of the methyl viologen cation radical and the efficiency of Its formation by semiconductor photocatalysis. *Journal of Physical Chemistry* **86**, 2617-2619 (1982).

88   Gurunathan, K., Maruthamuthu, P. & Sastri, M. V. C. Photocatalytic hydrogen production by dye-sensitized Pt/SnO2 and Pt/SnO2/RuO2 in aqueous methyl viologen solution. *International Journal of Hydrogen Energy* **22**, 57-62 (1997).

89   Lin, W. C., Yang, W. D., Huang, I. L., Wu, T. S. & Chung, Z. J. Hydrogen Production from Methanol/Water Photocatalytic Decomposition Using Pt/TiO2-xNx Catalyst. *Energy & Fuels* **23**, 2192-2196, doi:Doi 10.1021/Ef801091p (2009).

90   Luı́sa Andrade, R. C., Helena Aguilar Ribeiro, Adé́lio Mendes. Impedance characterization of dye-sensitized solar cells in a tandem arrangement for hydrogen production by water splitting. *International Journal of Hydrogen Energy* **35**, 8876-8883 (2010).

91   Yerga, R. M. N., Galvan, M. C. A., del Valle, F., de la Mano, J. A. V. & Fierro, J. L. G. Water splitting on semiconductor catalysts under visible-light irradiation. *Chemsuschem* **2**, 471-485, doi:DOI 10.1002/cssc.200900018 (2009).

92   Nowotny, M. K., Sheppard, L. R., Bak, T. & Nowotny, J. Defect chemistry of titanium dioxide. application of defect engineering in processing of TiO2-based photocatalysts. *Journal of Physical Chemistry C* **112**, 5275-5300, doi:Doi 10.1021/Jp077275m (2008).

93   Yang, X., Wolcottt, A., Wang, G., Sobo, A., Fitzmorris, R. C. *et al.* Nitrogen-doped ZnO nanowire arrays for photoelectrochemical water splitting. *Nano Letters* **9**, 2331-2336, doi:Doi 10.1021/Nl900772q (2009).

94   Burda, C., Lou, Y. B., Chen, X. B., Samia, A. C. S., Stout, J. *et al.* Enhanced nitrogen doping in TiO2 nanoparticles. *Nano Letters* **3**, 1049-1051, doi:Doi 10.1021/Nl034332o (2003).

95   Bensebaa, F., Durand, C., Aouadou, A., Scoles, L., Du, X.,Wang, D., Page, Y.L. A new green synthesis method of CuInS$_2$ and CuInSe$_2$ nanoparticles and their integration into thin films. *J Nanopart Res* doi:DOI 10.1007/s11051-009-9752-5 (2009).

96   Lee, Y. L., Chi, C. F. & Liau, S. Y. CdS/CdSe Co-sensitized TiO2 photoelectrode for efficient hydrogen generation in a photoelectrochemical cell. *Chemistry of Materials* **22**, 922-927, doi:Doi 10.1021/Cm901762h (2010).

97   Martínez-Castañón, G. A., Sánchez-Loredo, M.G., Martínez-Mendoza, J.R., and Ruiz, F. Synthesis of CdS nanoparticles: a simple method in aqueous media *Azojomo Journals of Materials Online* **1**, AZojomo (ISSN 1833-1122X), , doi:DOI: 10.2240/azojomo00170 (2005).

98   Knol. The effects of global warming on the hydrologic cycle. http://knol.google.com (Accessed October 22, 2010).

99   Shang, H. M., Wang, Y. & Cao, G. Z. Growth of oxide nanorod, nanotube and nanocable arrays through template-based sol electrophoretic deposition. *High-Performance Ceramics IV, Pts 1-3* **336-338**, 2122-21272698 (2007).

100   Law, M., Greene, L. E., Johnson, J. C., Saykally, R. & Yang, P. D. Nanowire dye-sensitized solar cells. *Nature Materials* **4**, 455-459, doi:Doi 10.1038/Nmat1387 (2005).

101   U.S. Department of Energy, B. L., Lawrence Berkeley National Laboratory , Getting to the hydrogen highway via the nano road, http://newscenter.lbl.gov/feature-stories/2009/04/20/hydrogen-highway-nano-road/. (Accessed October 22, 2010).

102   Tanaka, S., Nogami, D., Tsuda, N. & Miyake, Y. Synthesis of highly-monodisperse spherical titania particles with diameters in the submicron range. *Journal of Colloid and Interface Science* **334**, 188-194, doi:DOI 10.1016/j.jcis.2009.02.060 (2009).

103   Huczko, A. Template-based synthesis of nanomaterials. *Applied Physics A-Materials Science & Processing* **70**, 365-376 (2000).

104   Koo, H. J., Kim, Y. J., Lee, Y. H., Lee, W. I., Kim, K. *et al.* Nano-embossed hollow spherical TiO2 as bifunctional material for high-efficiency dye-sensitized solar cells. *Advanced Materials* **20**, 195-+, doi:DOI 10.1002/adma.200700840 (2008).

105   Sigma-Aldrich. Product detail. http://www.sigmaaldrich.com/catalog (Accessed October 22, 2010.

106   Chen, Y. F., Lee, C. Y., Yeng, M. Y. & Chiu, H. T. Preparing titanium oxide with various morphologies. *Materials Chemistry and Physics* **81**, 39-44, doi:Doi 10.1016/S0254-0584(03)00100-7 (2003).

107   Kamiya, K., Tanimoto, K. & Yoko, T. Preparation of TiO2 fibers by hydrolysis and polycondensation of Ti(O-I-C3h7)4. *Journal of Materials Science Letters* **5**, 402-404 (1986).

108   Chen, X. B. & Mao, S. S. Synthesis of titanium dioxide (TiO2) nanomaterials. *Journal of Nanoscience and Nanotechnology* **6**, 906-925, doi:Doi 10.1166/Jnn.2006.160 (2006).

109   Chuangchote, S., Jitputti, J., Sagawa, T. & Yoshikawa, S. Photocatalytic activity for hydrogen evolution of electrospun TiO2 nanofibers. *ACS Applied Materials & Interfaces* **1**, 1140-1143, doi:Doi 10.1021/Am9001474 (2009).

110   Li, D. & Xia, Y. N. Electrospinning of nanofibers: Reinventing the wheel? *Advanced Materials* **16**, 1151-1170, doi:DOI 10.1002/adma.200400719 (2004).

111   Liu, J. W., Kuo, Y. T., Klabunde, K. J., Rochford, C., Wu, J. *et al.* Novel dye-sensitized solar cell architecture using TiO2-coated vertically aligned carbon nanofiber arrays. *ACS Applied Materials & Interfaces* **1**, 1645-1649, doi:Doi 10.1021/Am900316f (2009).

112   Li, D., McCann, J. T. & Xia, Y. N. Electrospinning: A simple and versatile technique for producing ceramic nanofibers and nanotubes. *Journal of the American Ceramic Society* **89**, 1861-1869, doi:DOI 10.1111/j.1551-2916.2006.00989.x (2006).

113   Fang, J., Niu, H. T., Lin, T. & Wang, X. G. Applications of electrospun nanofibers. *Chinese Science Bulletin* **53**, 2265-2286, doi:DOI 10.1007/s11434-008-0319-0 (2008).

114   Formo, E., Lee, E., Campbell, D. & Xia, Y. N. Functionalization of electrospun TiO2 nanofibers with Pt nanoparticles and nanowires for catalytic applications. *Nano Letters* **8**, 668-672, doi:Doi 10.1021/Nl073163v (2008).

115   Madhugiri, S., Sun, B., Smirniotis, P. G., Ferraris, J. P. & Balkus, K. J. Electrospun mesoporous titanium dioxide fibers. *Microporous and Mesoporous Materials* **69**, 77-83, doi:DOI 10.1016/j.micromeso.2003.12.023 (2004).

116   Galinska, A. & Walendziewski, J. Photocatalytic water splitting over Pt-TiO2 in the presence of sacrificial reagents. *Energy & Fuels* **19**, 1143-1147 (2005).

117   Alves, A. K., Berutti, F. A., Clemens, F. J., Graule, T. & Bergmann, C. P. Photocatalytic activity of titania fibers obtained by electrospinning. *Materials Research Bulletin* **44**, 312-317, doi:DOI 10.1016/j.materresbull.208.06.001 (2009).

118   Lee, S. H. & Sigmund, W. M. Synthesis of anatase-silver nanocomposite fibers via electrospinning. *Journal of Nanoscience and Nanotechnology* **6**, 554-557, doi:Doi 10.1166/Jnn.2006.127 (2006).

119   Lee, S. H., Tekmen, C. & Sigmund, W. M. Three-point bending of electrospun TiO2 nanofibers. *Materials Science and Engineering a-Structural Materials Properties Microstructure and Processing* **398**, 77-81, doi:DOI 10.1016/j.msea.2005.03.014 (2005).

120   Lee, S., Jeon, C. & Park, Y. Fabrication of TiO2 tubules by template synthesis and hydrolysis with water vapor. *Chemistry of Materials* **16**, 4292-4295, doi:Doi 10.1021/Cm049466x (2004).

121   Fujihara, K., Kumar, A., Jose, R., Ramakrishna, S. & Uchida, S. Spray deposition of electrospun TiO2 nanorods for dye-sensitized solar cell. *Nanotechnology* **18**, -, doi:Artn 365709
Doi 10.1088/0957-4484/18/36/365709 (2007).

122   Zhang, Y. Z., Wu, L. H., Xie, E. Q., Duan, H. G., Han, W. H. *et al.* A simple method to prepare uniform-size nanoparticle TiO2 electrodes for dye-sensitized solar cells. *Journal of Power Sources* **189**, 1256-1263, doi:DOI 10.1016/j.jpowsour.2009.01.023 (2009).

123   Tsou, P. H., Chou, C. K., Saldana, S. M., Hung, M. C. & Kameoka, J. The fabrication and testing of electrospun silica nanofiber membranes for the detection of proteins. *Nanotechnology* **19**, -, doi:Artn 445714 Doi 10.1088/0957-4484/19/44/445714 (2008).

124   Goldstein, P. J. *Electrospinning of Ceramic and Nanocomposite Nanofibers* M.Sc., thesis, (University of Florida, 2004).

APPENDIX A

EXPERIMENTAL DATA OF CHAPTER II

There are some points should be mentioned to understand how the experimental data collected and then analyzed, these points are listed below:

1. START and END times are in the 24-hours time format.
2. Net H_2 = H_2 measurement at time (X_i)- H_2 measurement at time (0)
3. Prior to start all reaction times, reaction cell (flask) purged with nitrogen for at least half-hour to remove all air and oxygen species dissolved in solution, then hydrogen will be measured after completion of nitrogen purging step and considered as H_2 concentration at time (0) and all other hydrogen data are subtracted from this point.
4. Reaction time (X_i) = [hours + (minutes/60)] + Reaction time (X_{i-1})
5. Gas Chromatography used for H2 measurement has the following conditions:
   - Retention time = 0.4 minutes.
   - Temperature= 100˚C.
   - Pressure= 15 psi.
   - Flow rate= 21 ml/min.
   - Oven Temperature= 70˚C.
6. Several commissioning runs were conducted for the following purposes:
   - To test the experimental set-up.
   - To test the leakage from the flask.
   - To evaluate the nonmaterial initial, medium, and final activity.
   - To investigate the stability or life-time by extension of run duration.
   - To confirm the Gas Chromatography detection and measurements accuracy.
7. Hydrogen produced was calculated using the following formula after measure the H_2 peak.
   H_2 production = [H_2 peak*0.000246*(((V-10)*(1000))/ (50))]
   H_2 peak = area under the curve at the retention time of hydrogen gas (0.4 minutes) measured using Gas Chromatography.
   Syringe volume = 50 µl
   V= volume of the flask (reaction cell), V-10 = head volume (H.V.)
   Two types of flasks used, Quartz flask obtained from (Chemglass Life Sciences, V= 194 ml, transparence to visible light); Pyrex flask with different volume (V= 108 ml, 109 ml, 276.5 ml, 282.5 ml).

Run 10: started on May 28, 2009 and completed on June 11, 2009

Sample No.	START	END	Date	Reaction time (h)	H$_2$ Production (µmol)	
0				0	1.2915	Net H$_2$
1	11:20	13:15	28-May-09	1.916666667	1.3776	0.0861
2	13:26	16:39	28-May-09	5.133333333	1.3776	0.0861
3	16:51	12:21	28-May/01-Jun-09	96.55	0.9471	-
4	12:23	14:58	1-Jun-09	99.13333333	1.1193	-
5	15:12	9:39	01/02-Jun-09	117.5833333	1.4637	0.1722
6	9:53	13:50	2-Jun-09	121.5333333	1.5498	0.2583
7	14:01	11:16	02/03-Jun-09	142.7833333	2.0664	0.7749
8	11:27	14:04	3-Jun-09	145.4	2.4108	1.1193
9	14:15	18:01	3-Jun-09	149.1666667	2.0664	-
10	18:09	8:57	03/04-Jun-09	163.9666667	2.2386	0.9471
11	9:11	17:09	4-Jun-09	171.9333333	2.583	1.2915
12	17:36	13:30	04/05-Jun-09	191.8333333	3.7023	2.4108
13	13:48	16:20	5-Jun-09	194.3666667	3.7023	2.4108
14	16:40	15:15	05/06-Jun-09	216.95	3.8745	2.583
15	15:45	15:20	06/08-Jun-09	264.3666667	5.50179	4.21029
16	15:38	16:14	08/09-Jun-09	288.9666667	6.1992	4.9077
17	16:28	15:35	09/10-Jun-09	312.0833333	7.35294	6.06144
18	15:51	15:58	10/11-Jun-09	336.2	8.24838	6.95688

Run 4: started on Aril 18, 2009 and completed on April 29, 2009

Sample No.	START	END	Date	Reaction time (h)	H$_2$ Production (μmol)	
0				0	0.67035	Net H$_2$
1	9:35	11:50	19-Apr-09	3.25	2.01105	1.3407
2	12:00	13:50	19-Apr-09	5.25	0.67035	0
3	14:05	16:15	19-Apr-09	7.583333333	2.6814	2.01105
4	16:35	10:40	19/20-Apr-09	26.05	3.08361	2.41326
5	10:55	15:30	20-Apr-09	31.66666667	2.6814	2.01105
6	16:05	17:35	20-Apr-09	33.6	3.21768	2.54733
7	17:45	13:20	20/21 -Apr-09	53.58333333	3.75396	3.08361
8	14:10	18:05	21-Apr-09	57.21666667	4.0221	3.35175
9	18:20	10:10	21/22 -Apr-09	71.18333333	4.0502547	3.3799047
10	10:50	13:35	22-Apr-09	74.05	4.451124	3.780774
11	13:55	11:05	22/24 -Apr-09	118.9666667	6.220848	5.550498
12	11:32	11:20	24/29 -Apr-09	238.7666667	8.285526	7.615176

Run 9: started on May 18, 2009 and completed on May 28, 2009

Sample No.	START	END	Date	Reaction time (h)	H$_2$ Production (μmol)	
0				0	2.6814	Net H$_2$
1	9:27	10:35	19-May-09	1.133333333	-	-
2	10:44	11:55	19-May-09	2.316666667	-	-
3	12:03	13:28	19-May-09	3.733333333	-	-
4	13:40	14:54	19-May-09	4.966666667	-	-
5	15:07	17:08	19-May-09	7.016666667	-	-
6	17:37	10:40	19/20-May-09	24.06666667	-	-
7	10:48	10:00	20/21-May-09	47.26666667	2.94954	0.26814
8	10:09	10:00	21/22-May-09	71.11666667	3.35175	0.67035
9	10:15	10:02	22/26-May-09	161.8166667	3.0983577	0.4169577
10	10:21	9:53	26/27-May-09	185.35	4.69245	2.01105
11	10:06	14:34	27-May-09	189.8166667	4.6562511	1.9748511
12	14:45	16:48	27-May-09	191.8666667	4.69245	2.01105
13	17:02	9:05	27/28-May-09	207.9166667	5.1911904	2.5097904

Run 15: started on June 24, 2009 and completed on July 06, 2009

Sample No.	START	END	Date	Reaction time (h)	H₂ Production (µmol)	
0				0	2.01105	Net H₂
1	13:35	14:37	24-Jun-09	1.033333333	2.14512	0.13407
2	14:48	15:39	24-Jun-09	1.883333333	2.14512	0.13407
3	15:45	16:51	24-Jun-09	2.983333333	2.01105	0
4	17:03	17:33	24-Jun-09	4.483333333	2.14512	0.13407
5	17:43	10:53	24/25-Jun-09	21.65	2.6814	0.67035
6	11:02	14:21	25-Jun-09	24.96666667	2.54733	0.53628
7	14:29	16:40	25-Jun-09	27.15	2.81547	0.80442
8	16:59	11:17	25/26-Jun-09	45.45	2.81547	0.80442
9	11:29	15:17	26-Jun-09	49.25	3.35175	1.3407
10	15:25	16:28	26-Jun-09	50.3	3.21768	1.20663
11	16:47	11:16	26/29-Jun-09	116.7833333	6.6981372	4.6870872
12	11:56	16:42	29-Jun-09	121.55	6.783942	4.772892
13	17:02	11:11	29/30-Jun-09	139.7	7.26538737	5.25433737
14	11:30	14:58	30-Jun-09	143.1666667	8.4303216	6.4192716
15	15:34	11:09	30-Jun/1-Jul-09	152.75	8.6770104	6.6659604
16	11:24	14:22	1-Jul-09	155.7166667	8.7976734	6.7866234
17	14:33	16:46	1-Jul-09	157.9333333	8.9518539	6.9408039
18	16:54	12:59	1/2-Jul-09	178.0166667	9.2669184	7.2558684
19	13:20	15:17	2-Jul-09	179.9666667	9.4090326	7.3979826
20	15:26	16:41	2-Jul-09	181.2166667	9.2682591	7.2572091
21	16:53	11:51	2/3-Jul-09	200.1833333	11.0554122	9.0443622
22	12:00	14:24	3-Jul-09	202.5833333	10.59153	8.58048
23	14:39	16:31	3-Jul-09	204.45	10.90686264	8.89581264
24	16:39	16:27	3/6-Jul-09	276.25	23.1016017	21.0905517

Run 21: started on September 25, 2009 and completed on November 07, 2009

Sample No.	START	END	Date	Reaction time (h)	H$_2$ Production (µmol)	
0				0	2.27919	Net H$_2$
1	15:28	16:28	25-Sep-09	1	2.27919	0
2	16:38	17:47	25-Sep-09	2.15	2.27919	0
3	17:54	18:50	25-Sep-09	3.05	2.41326	0.13407
4	19:03	10:26	25/28-Sep-09	66.43333333	16.4316192	14.1524292
5	10:36	12:20	28-Sep-09	68.16666667	15.68619	13.407
6	12:31	13:58	28-Sep-09	69.61666667	15.243759	12.964569
7	14:09	16:04	28-Sep-09	71.53333333	15.444864	13.165674
8	16:19	17:49	28-Sep-09	73.03333333	15.41805	13.13886
9	18:05	15:48	28/29-Sep-09	94.75	20.325012	18.045822
10	15:58	14:03	29/30-Sep-09	117.6666667	24.186228	21.907038
11	14:14	14:24	30-Sep/1-Oct-09	141.8333333	26.14365	23.86446
12	14:37	16:29	1-Oct-09	143.7	25.540335	23.261145
13	16:44	16:41	1/2-Oct-09	167.65	25.969359	23.690169
15	17:08	13:45	2/5-Oct-09	236.2666667	25.33923	23.06004
16	15:12	15:29	5/6-Oct-09	260.55	27.75249	25.4733
17	15:40	13:58	6/7-Oct-09	282.85	30.70203	28.42284
18	14:10	14:23	7/8-Oct-09	307.0666667	34.120815	31.841625
19	14:32	12:48	8/9-Oct-09	329.3333333	34.831386	32.552196
20	13:03	17:00	9-Oct-09	333.2833333	35.595585	33.316395
21	17:06	13:53	9/12-Oct-09	402.0666667	42.205236	39.926046
22	14:05	14:11	12/13-Oct-09	426.1666667	44.993892	42.714702
23	14:26	14:20	13/14-Oct-09	450.1	47.219454	44.940264
24	14:44	15:03	14/15-Oct-09	474.4166667	51.563322	49.284132
25	15:14	16:41	15/16-Oct-09	499.8666667	55.437945	53.158755
26	16:54	11:36	16/19-Oct-09	566.5666667	60.19743	57.91824
27	11:47	13:21	19/20-Oct-09	592.1333333	62.128038	59.848848
28	13:32	14:18	20/21-Oct-09	616.9	65.359125	63.079935
29	14:48	14:59	21/22-Oct-09	641.0833333	68.214816	65.935626
30	15:12	15:09	22/23-Oct-09	665.0333333	68.9776743	66.6984843
31	15:20	15:05	23/24-Oct-09	688.7833333	73.094964	70.815774
32	15:16	13:56	24/26-Oct-09	735.45	76.15176	73.87257
33	14:06	13:00	26/27-Oct-09	758.35	81.045315	78.766125
34	13:08	13:46	27/28-Oct-09	782.9833333	67.57128	65.29209
35	14:04	13:54	28/29-Oct-09	806.8166667	55.23684	52.95765
36	14:12	14:44	29-Oct/4-Nov-09	951.35	103.2339	100.95471
37	14:55	14:24	4/5-Nov-09	974.8333333	120.12672	117.84753
38	14:44	14:36	5/6-Nov-09	998.7	111.5851203	109.3059303
39	14:50	15:00	6/7-Nov-09	1022.866667	115.487898	113.208708

Run 22: started on November 10, 2009 and completed on November 18, 2009

Sample No.	START	END	Date	Reaction time (h)	H$_2$ Production (μmol)	
0				0	2.94954	Net H$_2$
1	15:09	16:11	10-Nov-09	1.033333333	3.08361	0.13407
2	16:19	17:20	10-Nov-09	2.05	3.512634	0.563094
3	17:32	18:37	10-Nov-09	3.133333333	3.21768	0.26814
4	18:52	10:52	10/11-Nov-09	19.13333333	4.518159	1.568619
5	11:00	15:16	11-Nov-09	23.4	4.69245	1.74291
6	15:26	16:50	11-Nov-09	24.8	4.82652	1.87698
7	16:58	11:47	11/15-Nov-09	115.4833333	11.93223	8.98269
8	12:00	15:14	15-Nov-09	118.85	11.328915	8.379375
9	15:33	10:29	15/16-Nov-09	137.65	13.755582	10.806042
10	10:38	13:04	16-Nov-09	140.0833333	14.21142	11.26188
11	13:15	16:48	16-Nov-09	143.6333333	13.00479	10.05525
12	17:03	11:58	16/17-Nov-09	162.55	15.01584	12.0663
13	12:14	16:17	17-Nov-09	166.6	14.238234	11.288694
14	16:34	14:26	17/18-Nov-09	188.5666667	15.5293281	12.5797881

Run 36: started on April 05, 2010 and completed on April 10, 2010

Sample No.	START	END	Date	Reaction time (h)	H_2 Production (µmol)	
0				0	2.62236	Net H_2
1	16:42	17:27	5-Apr-10	0.75	3.60312264	0.98076264
2	17:38	11:00	5/6-Apr-10	18.11666667	7.09872852	4.47636852
3	11:12	16:56	6-Apr-10	23.85	8.99993952	6.37757952
4	17:05	10:07	6/7-Apr-10	40.88333333	10.8041232	8.1817632
5	10:16	17:09	7-Apr-10	47.76666667	11.98549638	9.36313638
6	17:18	9:44	7/8-Apr-10	64.2	11.3744865	8.7521265
7	9:52	18:23	8-Apr-10	72.71666667	11.6760579	9.0536979
8	18:31	11:28	8/9-Apr-10	89.66666667	12.68304414	10.06068414
9	11:41	18:13	9-Apr-10	96.2	11.25516912	8.63280912
10	18:30	13:57	9/10-Apr-10	115.65	10.93130766	8.30894766

Run 37: started on November 10, 2009 and completed on November 18, 2009

Sample No.	START	END	Date	Reaction time (h)	H_2 Production (µmol)	
0				0	2.491242	Net H_2
1	17:51	14:53	12/13-Apr-10	19.03333333	9.88498602	7.39374402
2	15:06	15:17	13/14-Apr-10	43.21666667	10.92606294	8.43482094
3	15:27	13:38	14/15-Apr-10	65.4	11.75735106	9.26610906
4	13:48	16:31	15/16-Apr-10	92.11666667	14.87009238	12.37885038
5	16:41	11:42	16/19-Apr-10	159.1333333	16.44481956	13.95357756
6	11:54	12:31	19/20-Apr-10	183.4333333	18.95835162	16.46710962

Run 38: started on April 20, 2010 and completed on April 22, 2010

Sample No.	START	END	Date	Reaction time (h)	H2 Production (μmol)	
0				0	2.360124	Net H2
1	14:21	17:58	20-Apr-10	3.616666667	4.22593314	1.86580914
2	18:10	16:04	20/21-Apr-10	25.51666667	4.4055648	2.0454408
3	16:15	13:01	21/22-Apr-10	46.28333333	3.409068	1.048944

Run 47: started on May 17, 2010 and completed on May 21, 2010

Sample No.	START	END	Date	Reaction time (h)	H_2 Production (μmol)	
0				0	1.96677	Net H_2
1	13:08	17:31	17-May-10	4.383333333	6.17303544	4.20626544
2	17:42	17:17	17/18-May-10	27.8	6.57819006	4.61142006
3	17:29	17:31	18/19-May-10	51.83333333	7.96017378	5.99340378
4	17:43	16:27	19/20-May-10	74.56666667	8.00606508	6.03929508
5	16:42	17:45	20/21-May-10	99.61666667	6.20450376	4.23773376

Run 54: started on July 03, 2010 and completed on July 12, 2010

Sample No.	START	END	Date	Reaction time (h)	H$_2$ Production (µmol)	
0				0	1.96677	Net H$_2$
1	9:28	16:59	5-Jul-10	7.516666667	10.92999648	8.96322648
2	17:13	11:10	5/6-Jul-10	25.46666667	44.1146511	42.1478811
3	11:20	16:53	6-Jul-10	31.01666667	51.00883554	49.04206554
4	17:09	10:23	6/7-Jul-10	48.25	86.84338494	84.87661494
5	10:31	17:24	7-Jul-10	55.13333333	94.75635624	92.78958624
6	17:34	14:35	7/8-Jul-10	76.15	118.166164	116.199394
7	14:50	17:17	8-Jul-10	78.6	127.2054389	125.2386689
8	17:26	13:08	8/9-Jul-10	98.3	170.0062876	168.0395176
9	13:21	10:51	9/12-Jul-10	167.8	244.3606831	242.3939131

APPENDIX B

EXPERIMENTAL DATA OF CHAPTER III

Run 26: started on January 11, 2010 and completed on January 19, 2010

Sample No.	START	END	Date	Reaction time (h)	H$_2$ Production (µmol)	
0				0	2.753478	Net H$_2$
1	14:49	17:26	12-Jan-10	2.616666667	15.5112594	12.7577814
2	17:37	13:35	12/13-Jan-10	22.58333333	340.6576758	337.9041978
3	13:44	17:13	13-Jan-10	26	399.844341	397.090863
4	17:24	11:36	13/14-Jan-10	44.2	641.7177156	638.9642376
5	11:50	17:35	14-Jan-10	49.95	708.955026	706.201548
6	17:42	10:37	14/15-Jan-10	66.86666667	938.9622216	936.2087436
7	10:49	17:29	15-Jan-10	73.38333333	1019.029428	1016.27595
8	17:38	11:33	15/19-Jan-10	163.3	2103.853869	2101.100391
9	11:41	16:55	19-Jan-10	168.5333333	2142.782803	2140.029325

Run 27: started on January 19, 2010 and completed on January 25, 2010

Sample No.	START	END	Date	Reaction time (h)	H$_2$ Production (µmol)	
0				0	2.491242	Net H$_2$
1	9:29	11:37	20-Jan-10	2.133333333	13.71100926	11.21976726
2	11:45	15:12	20-Jan-10	5.583333333	52.93495896	50.44371696
3	15:20	17:42	20-Jan-10	7.95	83.87697131	81.38572931
4	17:51	9:57	20/21-Jan-10	24.05	339.5287498	337.0375078
5	10:07	14:04	21-Jan-10	28	399.4300081	396.9387661
6	14:26	17:34	21-Jan-10	31.2	433.2820534	430.7908114
7	17:44	12:32	21/22-Jan-10	50	714.6455472	712.1543052
8	12:40	17:05	22-Jan-10	54.41666667	753.1155684	750.6243264
9	17:13	11:34	22/25-Jan-10	120.7666667	1477.541207	1475.049965

Run 28: started on January 25, 2010 and completed on February 01, 2010

Sample No.	START	END	Date	Reaction time (h)	H₂ Production (μmol)	
0				0	2.62236	Net H₂
1	11:24	14:55	26-Jan-10	3.516666667	9.1585923	6.5362323
2	15:03	17:50	26-Jan-10	6.3	20.75466822	18.13230822
3	17:58	10:12	26/27-Jan-10	22.53333333	123.5734703	120.9511103
4	10:24	13:26	27-Jan-10	25.56666667	142.6747405	140.0523805
5	13:36	18:01	27-Jan-10	29.98333333	166.7348935	164.1125335
6	18:15	10:28	27/28-Jan-10	46.2	243.3589415	240.7365815
7	11:15	14:22	28-Jan-10	49.31666667	272.3635543	269.7411943
8	14:40	17:45	28-Jan-10	52.4	302.5246279	299.9022679
9	17:57	12:07	28/29-Jan-10	70.56666667	437.0556294	434.4332694
10	12:20	18:03	29-Jan-10	76.28333333	480.1921402	477.5697802
11	18:14	11:29	29-Jan/1-Feb-10	141.5333333	872.5457099	869.9233499

Run 29: started on February 01, 2010and completed on February 08, 2010

Sample No.	START	END	Date	Reaction time (h)	H$_2$ Production (µmol)	
0				0	2.884596	Net H$_2$
1	12:14	14:27	2-Feb-10	2.216666667	6.91778568	4.03318968
2	14:41	16:29	2-Feb-10	4.016666667	16.68607668	13.80148068
3	16:38	18:00	2-Feb-10	5.383333333	27.6134508	24.7288548
4	18:07	11:02	2/3-Feb-10	22.3	241.4013498	238.5167538
5	12:20	15:38	3-Feb-10	25.6	273.7861846	270.9015886
6	17:27	10:29	3/4-Feb-10	42.63333333	469.5728934	466.6882974
7	10:37	13:30	4-Feb-10	45.51666667	496.6474492	493.7628532
8	13:37	17:03	4-Feb-10	48.95	568.8580654	565.9734694
9	17:13	10:34	4/5-Feb-10	66.3	758.124276	755.23968
10	10:46	15:07	5-Feb-10	70.65	829.4537792	826.5691832
11	15:22	10:25	5/8-Feb-10	135.6833333	1596.288224	1593.403628

Run 30 (C): started on February 15, 2010 and completed on February 17, 2010

Sample No.	START	END	Date	Reaction time (h)	H$_2$ Production (µmol)	
22				0	2.62236	Net H$_2$
23	17:58	10:42	15/16-Feb-10	16.73333333	57.7378113	55.1154513
24	10:52	13:49	16-Feb-10	20.68333333	55.99000836	53.36764836
25	14:06	10:06	16/17-Feb-10	40.68333333	55.64516802	53.02280802
26	10:18	14:34	17-Feb-10	44.95	55.25705874	52.63469874

Run 30 (D): started on February 17, 2010 and completed on February 22, 2010

Sample No.	START	END	Date	Reaction time (h)	H₂ Production (µmol)	
34				0	2.62236	Net H₂
35	16:21	15:02	17/18-Feb-10	21.41666667	8.92389108	6.30153108
36	15:13	14:24	18/19-Feb-10	44.6	12.09170196	9.46934196
37	14:36	16:54	19/21-Feb-10	94.9	11.7875082	9.1651482
38	17:06	11:17	21/22-Feb-10	113.0833333	11.94878334	9.32642334

Run 31: started on February 22, 2010 and completed on March 02, 2010

Sample No.	START	END	Date	Reaction time (h)	H₂ Production (µmol)	
0				0	2.62236	Net H₂
1	15:16	18:48	23-Feb-10	3.533333333	20.35738068	17.73502068
2	19:11	12:03	23/24-Feb-10	20.4	186.042019	183.419659
3	12:16	17:02	24-Feb-10	25.16666667	219.6672301	217.0448701
4	17:13	11:46	24/25-Feb-10	43.71666667	362.4455539	359.8231939
5	11:58	17:08	25-Feb-10	48.88333333	373.7675932	371.1452332
6	17:20	13:32	25/26-Feb-10	69.08333333	522.0148487	519.3924887
7	13:42	16:37	26-Feb-10	72	513.195852	510.573492
8	16:49	9:42	26-Feb/1-Mar-10	136.8833333	879.9486322	877.3262722
9	9:53	10:38	1/2-Mar-10	161.6333333	1091.972994	1089.350634

Run 32: started on March 01, 2010 and completed on March 09, 2010

Sample No.	START	END	Date	Reaction time (h)	H₂ Production (µmol)	
0				0	2.62236	Net H₂
1	13:23	17:56	2-Mar-10	4.55	18.5204175	15.8980575
2	18:13	14:00	2/3-Mar-10	24.33333333	113.613747	110.991387
3	14:08	18:13	3-Mar-10	28.41666667	123.0804666	120.4581066
4	18:22	10:58	3/4-Mar-10	45.01666667	178.7898824	176.1675224
5	11:09	18:00	4-Mar-10	51.86666667	196.4829454	193.8605854
6	18:08	12:29	4/5-Mar-10	70.21666667	275.2389721	272.6166121
7	12:38	13:07	5/8-Mar-10	142.7	670.8757364	668.2533764
8	13:41	13:30	8/9-Mar-10	166.5166667	827.9485445	825.3261845

Run 33: started on March 08, 2010 and completed on March 15, 2010

Sample No.	START	END	Date	Reaction time (h)	H₂ Production (µmol)	
0				0	2.62236	Net H₂
1	15:53	17:04	9-Mar-10	1.183333333	3.409068	0.786708
2	17:13	10:35	9/10-Mar-10	18.55	101.0080625	98.38570248
3	10:45	17:05	10-Mar-10	24.88333333	139.8806159	137.2582559
4	17:38	11:49	10/11-Mar-10	43.06666667	270.2171527	267.5947927
5	12:05	17:14	11-Mar-10	47.68333333	294.9302733	292.3079133
6	18:20	10:34	11/12-Mar-10	63.91666667	373.0149758	370.3926158
7	12:34	17:10	12-Mar-10	68.51666667	389.8492159	387.2268559
8	19:19	17:04	12/14-Mar-10	114.2666667	583.7137348	581.0913748
9	17:39	10:28	14/15-Mar-10	131.0833333	700.4664467	697.8440867
10	10:37	15:50	15-Mar-10	136.3	721.9514422	719.3290822

Run 34: started on March 20, 2010 and completed on March 29, 2010

Sample No.	START	END	Date	Reaction time (h)	H$_2$ Production (µmol)	
0				0	2.62236	Net H$_2$
1	12:07	15:52	22-Mar-10	3.75	5.1594933	2.5371333
2	16:01	17:34	22-Mar-10	5.3	9.41689476	6.79453476
3	17:45	10:44	22/23-Mar-10	22.28333333	118.741772	116.119412
4	10:54	14:00	23-Mar-10	25.38333333	137.9676043	135.3452443
5	14:10	18:00	23-Mar-10	29.21666667	158.8337228	156.2113628
6	18:08	17:14	23/24-Mar-10	52.11666667	288.7834615	286.1611015
7	17:23	10:26	24/25-Mar-10	69.16666667	374.1911043	371.5687443
8	10:35	14:51	25-Mar-10	73.43333333	394.3439409	391.7215809
9	15:01	18:26	25-Mar-10	76.85	407.1279459	404.5055859
10	18:34	11:08	25/26-Mar-10	93.41666667	483.0085549	480.3861949
11	11:17	13:35	26-Mar-10	95.71666667	498.9564372	496.3340772
12	14:01	18:03	26-Mar-10	99.75	508.2055009	505.5831409
13	18:12	9:35	26/29-Mar-10	163.1333333	803.6012431	800.9788831

Run 35: started on March 29, 2010 and completed on April 05, 2010

Sample No.	START	END	Date	Reaction time (h)	H$_2$ Production (µmol)	
0				0	2.62236	Net H$_2$
1	11:06	14:41	30-Mar-10	3.583333333	7.81987752	5.19751752
2	14:52	17:56	30-Mar-10	6.65	16.80801642	14.18565642
3	18:17	14:30	30/31-Mar-10	26.86666667	102.075363	99.453003
4	14:39	17:46	31-Mar-10	29.98333333	109.024617	106.402257
5	17:55	9:57	31-Mar/1-Apr-10	46.01666667	207.3500052	204.7276452
6	10:07	13:23	1-Apr-10	49.28333333	210.2293565	207.6069965
7	13:33	18:19	1-Apr-10	54.05	235.4249914	232.8026314
8	18:26	10:34	1/2-Apr-10	70.18333333	328.1804869	325.5581269
9	10:44	18:04	2-Apr-10	77.51666667	377.4297189	374.8073589
10	18:19	12:40	2/3-Apr-10	95.86666667	481.4272718	478.8049118
11	12:51	10:56	3/5-Apr-10	141.95	816.369514	813.747154

Run 39: started on April 23, 2010 and completed on April 27, 2010

Sample No.	START	END	Date	Reaction time (h)	H$_2$ Production (µmol)	
0				0	2.491242	Net H$_2$
1	13:13	16:10	23-Apr-10	2.95	4.06859154	1.57734954
2	16:21	18:13	23/24-Apr-10	28.81666667	55.32655128	52.83530928
3	18:20	10:25	24/26-Apr-10	68.9	138.1419913	135.6507493
4	10:35	16:54	26-Apr-10	75.21666667	155.1794642	152.6882222
5	17:02	9:53	26/27-Apr-10	92.06666667	209.7507758	207.2595338

Run 40: started on April 27, 2010 and completed on May 01, 2010

Sample No.	START	END	Date	Reaction time (h)	H$_2$ Production (µmol)	
0				0	2.62236	Net H$_2$
1	16:17	9:39	27/28-Apr-10	17.36666667	15.05365758	12.43129758
2	9:46	14:35	28-Apr-10	22.18333333	19.9823832	17.3600232
3	14:44	10:00	28/29-Apr-10	41.45	19.78701738	17.16465738
4	10:09	18:08	29-Apr-10	49.43333333	56.96028156	54.33792156
5	18:21	10:12	29/30-Apr-10	65.28333333	82.35390462	79.73154462
6	10:24	17:22	30-Apr-10	72.25	91.28041806	88.65805806
7	17:32	16:20	30-Apr/1-May-10	95.05	112.9030874	110.2807274

Run 41: started on May 01, 2010 and completed on May 05, 2010

Sample No.	START	END	Date	Reaction time (h)	H$_2$ Production (µmol)	
0				0	2.229006	Net H$_2$
1	18:12	15:45	1/2-May-10	21.55	12.40245162	10.17344562
2	15:56	14:30	2/3-May-10	44.11666667	20.77302474	18.54401874
3	14:38	17:47	3-May-10	47.26666667	23.30491332	21.07590732
4	17:55	11:08	3/4-May-10	64.48333333	37.85770014	35.62869414
5	11:19	16:40	4-May-10	69.83333333	36.9949437	34.7659377
6	17:27	16:53	4/5-May-10	93.26666667	47.98132092	45.75231492

Run 42: started on May 04, 2010 and completed on May 05, 2010

Sample No.	START	END	Date	Reaction time (h)	H$_2$ Production (µmol)	
0				0	1.81056	Net H$_2$
1	13:22	16:46	4-May-10	3.4	1.81056	0
2	10:10	16:42	5-May-10	9.933333333	1.81056	0

Run 52: started on May 27, 2010 and completed on May 31, 2010

Sample No.	START	END	Date	Reaction time (h)	H$_2$ Production (µmol)	
0				0	2.097888	Net H$_2$
1	14:38	17:52	28-May-10	3.233333333	2.229006	0.131118
2	18:07	14:07	28/29-May-10	23.23333333	2.360124	0.262236
3	15:09	17:12	29/31-May-10	73.28333333	2.491242	0.393354

Run 6: started on June 11, 2010 and completed on June 17, 2010

Sample No.	START	END	Date	Reaction time (h)	H₂ Production (µmol)	
0				0	1.442298	Net H2
1	11:48	17:56	11-Jun-10	6.133333333	7.6179558	6.1756578
2	18:08	14:26	11/12-Jun-10	26.43333333	49.80910584	48.36680784
3	14:39	17:11	12/14-Jun-10	76.96666667	272.8172226	271.3749246
4	17:34	16:46	14/15-Jun-10	100.1666667	334.0768634	332.6345654
5	17:04	16:33	15/16-Jun-10	123.65	396.7827357	395.3404377
6	16:46	16:47	16/17-Jun-10	147.6666667	471.3206963	469.8783983

Run 11: started on June 11, 2010 and completed on June 16, 2010

Sample No.	START	END	Date	Reaction time (h)	H₂ Production (µmol)	
0				0	1.086336	Net H2
1	13:37	17:53	11-Jun-10	4.266666667	6.18939936	5.10306336
2	10:10	14:22	12-Jun-10	8.466666667	11.47080288	10.38446688
3	11:09	17:09	14-Jun-10	14.46666667	15.62241696	14.53608096
4	9:47	16:49	15-Jun-10	21.5	17.33430144	16.24796544
5	10:03	16:28	16-Jun-10	27.91666667	16.21718592	15.13084992

APPENDIX C

EXPERIMENTAL DATA OF CHAPTER IV

Run 48: started on May 24, 2010 and completed on May 29, 2010

Sample No.	START	END	Date	Reaction time (h)	H$_2$ Production (µmol)	
0				0	0.771456	Net H$_2$
1	11:07	16:42	24-May-10	5.583333333	4.194792	3.423336
2	10:08	17:00	25-May-10	12.45	3.8621016	3.0906456
3	10:11	16:27	26-May-10	18.71666667	5.18659512	4.41513912
4	9:33	18:18	27-May-10	27.46666667	4.56460872	3.79315272
5	10:11	17:48	28-May-10	35.08333333	4.74541872	3.97396272
6	10:01	14:57	29-May-10	40.01666667	4.39054896	3.61909296

Run 49: started on May 24, 2010 and completed on May 29, 2010

Sample No.	START	END	Date	Reaction time (h)	H₂ Production (µmol)	
0				0	1.448448	Net H₂
1	13:10	16:42	24-May-10	3.533333333	2.082144	0.633696
2	10:08	17:00	25-May-10	10.4	2.534784	1.086336
3	10:11	16:27	26-May-10	16.66666667	3.2771136	1.8286656
4	9:33	18:18	27-May-10	25.41666667	3.43644288	1.98799488
5	10:11	17:48	28-May-10	33.03333333	3.75781728	2.30936928
6	10:01	14:57	29-May-10	37.96666667	4.12173984	2.67329184

Run 50: started on May 24, 2010 and completed on May 27, 2010

Sample No.	START	END	Date	Reaction time (h)	H₂ Production (µmol)	
0				0	2.229006	Net H₂
1	13:12	16:46	24-May-10	3.566666667	2.360124	0.131118
2	17:03	17:04	24/25-May-10	27.58333333	2.229006	0
3	17:16	17:37	25/26-May-10	51.8	2.491242	0.262236
4	17:53	11:09	26/27-May-10	69.06666667	2.491242	0.262236

APPENDIX D

EXPERIMENTAL DATA OF CHAPTER V

Run 59: started on August 5, 2010 and completed on August 25, 2010

Sample No.	START	END	Date	Reaction time (h)	H$_2$ Production (µmol)	
0				0	0.535788	Net H$_2$
1	11:24	16:27	6-Aug-10	5.05	0.584496	0.048708
2	13:12	16:39	7-Aug-10	8.5	0.779328	0.24354
3	10:20	17:12	9-Aug-10	15.36666667	0.73062	0.194832
4	9:15	17:00	10-Aug-10	23.11666667	0.876744	0.340956
5	9:43	17:27	11-Aug-10	30.85	1.022868	0.48708
6	10:35	17:14	12-Aug-10	37.5	1.266408	0.73062
7	10:27	17:06	13-Aug-10	44.15	1.412532	0.876744
8	10:40	16:57	16-Aug-10	50.43333333	1.70478	1.168992
9	10:06	16:06	17-Aug-10	56.43333333	2.18796336	1.65217536
10	10:25	17:00	18-Aug-10	63.85	2.4670602	1.9312722
11	11:30	17:07	19-Aug-10	69.46666667	2.68234956	2.14656156
12	12:20	17:13	20-Aug-10	74.35	2.9127384	2.3769504
13	11:49	17:19	21-Aug-10	79.85	3.18160656	2.64581856
14	9:48	16:55	23-Aug-10	98.96666667	2.47387932	1.93809132
15	9:49	17:10	24-Aug-10	106.3166667	4.05347976	3.51769176
16	10:10	16:59	25-Aug-10	113.1333333	3.61510776	3.07931976

Run 46: started on May 17, 2010 and completed on May 21, 2010

Sample No.	START	END	Date	Reaction time (h)	H₂ Production (μmol)	
0				0	1.086336	Net H₂
1	11:34	17:26	17-May-10	5.866666667	2.172672	1.086336
2	10:02	17:02	18-May-10	12.86666667	5.26239264	4.17605664
3	9:37	17:26	19-May-10	20.68333333	8.37202944	7.28569344
4	9:48	17:41	21-May-10	28.56666667	8.31771264	7.23137664

Run 51: started on May 27, 2010 and completed on June 02, 2010

Sample No.	START	END	Date	Reaction time (h)	H₂ Production (μmol)	
0				0	0.819672	Net H₂
1	13:30	17:48	28-May-10	4.3	1.350048	0.530376
2	10:01	14:57	29-May-10	9.233333333	1.91224656	1.09257456
3	10:24	17:14	31-May-10	16.06666667	2.07232368	1.25265168
4	11:32	17:11	1-Jun-10	21.71666667	2.59257432	1.77290232
5	11:04	17:05	2-Jun-10	27.73333333	3.10366392	2.28399192

Run 56: started on August 05, 2010 and completed on August 25, 2010

Sample No.	START	END	Date	Reaction time (h)	H_2 Production (μmol)	
0				0	0.535788	Net H_2
1	11:24	16:27	6-Aug-10	5.05	0.73062	0.194832
2	13:12	16:39	7-Aug-10	8.5	0.828036	0.292248
3	10:20	17:12	9-Aug-10	15.36666667	1.120284	0.584496
4	9:15	17:00	10-Aug-10	23.11666667	1.607364	1.071576
5	9:43	17:27	11-Aug-10	30.85	2.10369852	1.56791052
6	10:35	17:14	12-Aug-10	37.5	2.60052012	2.06473212
7	10:27	17:06	13-Aug-10	44.15	2.87474616	2.33895816
8	10:40	16:57	16-Aug-10	50.43333333	3.27366468	2.73787668
9	10:06	16:06	17-Aug-10	56.43333333	3.57906384	3.04327584
10	10:25	17:00	18-Aug-10	63.85	3.95362836	3.41784036
11	11:30	17:07	19-Aug-10	69.46666667	4.12946424	3.59367624
12	12:20	17:13	20-Aug-10	74.35	4.25854044	3.72275244
13	11:49	17:19	21-Aug-10	79.85	4.34134404	3.80555604
14	9:48	16:55	23-Aug-10	98.96666667	4.74951708	4.21372908
15	9:49	17:10	24-Aug-10	106.3166667	5.10313716	4.56734916
16	10:10	16:59	25-Aug-10	113.1333333	3.62338812	3.08760012

Run 57: started on August 05, 2010 and completed on August 25, 2010

Sample No.	START	END	Date	Reaction time (h)	H$_2$ Production (µmol)	
0				0	0.48708	Net H$_2$
1	11:24	16:27	6-Aug-10	5.05	0.584496	0.097416
2	13:12	16:39	7-Aug-10	8.5	0.73062	0.24354
3	10:20	17:12	9-Aug-10	15.36666667	1.022868	0.535788
4	9:15	17:00	10-Aug-10	23.11666667	3.628746	3.141666
5	9:43	17:27	11-Aug-10	30.85	6.49326348	6.00618348
6	10:35	17:14	12-Aug-10	37.5	5.6476926	5.1606126
7	10:27	17:06	13-Aug-10	44.15	6.99105924	6.50397924
8	10:40	16:57	16-Aug-10	50.43333333	8.11670112	7.62962112
9	10:06	16:06	17-Aug-10	56.43333333	7.81178904	7.32470904
10	10:25	17:00	18-Aug-10	63.85	7.85319084	7.36611084
11	11:30	17:07	19-Aug-10	69.46666667	7.52392476	7.03684476
12	12:20	17:13	20-Aug-10	74.35	8.46398916	7.97690916
13	11:49	17:19	21-Aug-10	79.85	8.60085864	8.11377864
14	9:48	16:55	23-Aug-10	98.96666667	2.25420624	1.76712624
15	9:49	17:10	24-Aug-10	106.3166667	8.20145304	7.71437304
16	10:10	16:59	25-Aug-10	113.1333333	4.82501448	4.33793448

Run 58: started on August 05, 2010 and completed on August 25, 2010

Sample No.	START	END	Date	Reaction time (h)	H_2 Production (µmol)	
0				0	0.584496	Net H_2
1	11:24	16:27	6-Aug-10	5.05	0.73062	0.146124
2	13:12	16:39	7-Aug-10	8.5	0.633204	0.048708
3	10:20	17:12	9-Aug-10	15.36666667	1.022868	0.438372
4	9:15	17:00	10-Aug-10	23.11666667	0.97416	0.389664
5	9:43	17:27	11-Aug-10	30.85	2.20744656	1.62295056
6	10:35	17:14	12-Aug-10	37.5	1.56742344	0.98292744
7	10:27	17:06	13-Aug-10	44.15	1.71062496	1.12612896
8	10:40	16:57	16-Aug-10	50.43333333	2.72375136	2.13925536
9	10:06	16:06	17-Aug-10	56.43333333	2.66140512	2.07690912
10	10:25	17:00	18-Aug-10	63.85	2.63899944	2.05450344
11	11:30	17:07	19-Aug-10	69.46666667	3.6457938	3.0612978
12	12:20	17:13	20-Aug-10	74.35	4.01305212	3.42855612
13	11:49	17:19	21-Aug-10	79.85	4.20788412	3.62338812
14	9:48	16:55	23-Aug-10	98.96666667	3.60585324	3.02135724
15	9:49	17:10	24-Aug-10	106.3166667	3.6433584	3.0588624
16	10:10	16:59	25-Aug-10	113.1333333	3.0539916	2.4694956

Run 59: started on August 05, 2010 and completed on August 25, 2010

Sample No.	START	END	Date	Reaction time (h)	H₂ Production (μmol)	
						Net H₂
0				0	0.535788	Net H₂
1	11:24	16:27	6-Aug-10	5.05	0.584496	0.048708
2	13:12	16:39	7-Aug-10	8.5	0.779328	0.24354
3	10:20	17:12	9-Aug-10	15.36666667	0.73062	0.194832
4	9:15	17:00	10-Aug-10	23.11666667	0.876744	0.340956
5	9:43	17:27	11-Aug-10	30.85	1.022868	0.48708
6	10:35	17:14	12-Aug-10	37.5	1.266408	0.73062
7	10:27	17:06	13-Aug-10	44.15	1.412532	0.876744
8	10:40	16:57	16-Aug-10	50.43333333	1.70478	1.168992
9	10:06	16:06	17-Aug-10	56.43333333	2.18796336	1.65217536
10	10:25	17:00	18-Aug-10	63.85	2.4670602	1.9312722
11	11:30	17:07	19-Aug-10	69.46666667	2.68234956	2.14656156
12	12:20	17:13	20-Aug-10	74.35	2.9127384	2.3769504
13	11:49	17:19	21-Aug-10	79.85	3.18160656	2.64581856
14	9:48	16:55	23-Aug-10	98.96666667	2.47387932	1.93809132
15	9:49	17:10	24-Aug-10	106.3166667	4.05347976	3.51769176
16	10:10	16:59	25-Aug-10	113.1333333	3.61510776	3.07931976

Run 60: started on August 05, 2010 and completed on August 25, 2010

Sample No.	START	END	Date	Reaction time (h)	H$_2$ Production (µmol)	
0				0	0.535788	Net H$_2$
1	11:24	16:27	6-Aug-10	5.05	0.97416	0.438372
2	13:12	16:39	7-Aug-10	8.5	1.315116	0.779328
3	10:20	17:12	9-Aug-10	15.36666667	1.607364	1.071576
4	9:15	17:00	10-Aug-10	23.11666667	2.2990176	1.7632296
5	9:43	17:27	11-Aug-10	30.85	3.27756132	2.74177332
6	10:35	17:14	12-Aug-10	37.5	4.3885908	3.8528028
7	10:27	17:06	13-Aug-10	44.15	4.237596	3.701808
8	10:40	16:57	16-Aug-10	50.43333333	4.92730128	4.39151328
9	10:06	16:06	17-Aug-10	56.43333333	4.38323292	3.84744492
10	10:25	17:00	18-Aug-10	63.85	4.8683646	4.3325766
11	11:30	17:07	19-Aug-10	69.46666667	5.20055316	4.66476516
12	12:20	17:13	20-Aug-10	74.35	5.18545368	4.64966568
13	11:49	17:19	21-Aug-10	79.85	5.51325852	4.97747052
14	9:48	16:55	23-Aug-10	98.96666667	4.63018248	4.09439448
15	9:49	17:10	24-Aug-10	106.3166667	4.83232068	4.29653268
16	10:10	16:59	25-Aug-10	113.1333333	3.64481964	3.10903164

Run 61: started on August 05, 2010 and completed on August 25, 2010

Sample No.	START	END	Date	Reaction time (h)	H₂ Production (µmol)	
0				0	0.48708	Net H₂
1	11:24	16:27	6-Aug-10	5.05	4.822092	4.335012
2	13:12	16:39	7-Aug-10	8.5	6.672996	6.185916
3	10:20	17:12	9-Aug-10	15.36666667	7.46011728	6.97303728
4	9:15	17:00	10-Aug-10	23.11666667	8.73285732	8.24577732
5	9:43	17:27	11-Aug-10	30.85	11.91982176	11.43274176
6	10:35	17:14	12-Aug-10	37.5	11.21696532	10.72988532
7	10:27	17:06	13-Aug-10	44.15	13.82771412	13.34063412
8	10:40	16:57	16-Aug-10	50.43333333	16.13062836	15.64354836
9	10:06	16:06	17-Aug-10	56.43333333	16.38878076	15.90170076
10	10:25	17:00	18-Aug-10	63.85	17.1184266	16.6313466
11	11:30	17:07	19-Aug-10	69.46666667	17.45986968	16.97278968
12	12:20	17:13	20-Aug-10	74.35	18.55579968	18.06871968
13	11:49	17:19	21-Aug-10	79.85	18.41990436	17.93282436
14	9:48	16:55	23-Aug-10	98.96666667	17.72143164	17.23435164
15	9:49	17:10	24-Aug-10	106.3166667	11.1127302	10.6256502
16	10:10	16:59	25-Aug-10	113.1333333	8.01100476	7.52392476

APPENDIX E

EXPERIMENTAL DATA OF CHAPTER VI

Run 12: started on June 4, 2009 and completed on June 30, 2009

Sample No.	START	END	Date	Reaction time (h)	H_2 Production (µmol)	
0				0	0.578592	Net H_2
1	9:44	11:57	5-Jun-09	2.216666667	1.398264	0.819672
2	12:26	13:32	5-Jun-09	3.316666667	6.412728	5.834136
3	13:44	14:45	5-Jun-09	4.333333333	13.789776	13.211184
4	15:15	16:25	5-Jun-09	5.5	14.9807112	14.4021192
5	16:42	17:49	5-Jun-09	6.616666667	14.127288	13.548696
6	12:30	15:13	6-Jun-09	9.333333333	39.9807072	39.4021152
7	10:57	15:16	8-Jun-09	13.65	47.396328	46.817736
8	10:54	16:11	9-Jun-09	18.93333333	68.4618984	67.8833064
9	11:05	15:55	11-Jun-09	23.76666667	78.0279528	77.4493608
10	10:53	15:16	12-Jun-09	28.15	145.8100056	145.2314136
11	12:41	16:52	15-Jun-09	32.33333333	124.5226416	123.9440496
12	10:43	15:06	16-Jun-09	36.71666667	155.4966	154.918008
13	12:34	14:54	17-Jun-09	39.05	175.86786	175.289268
14	10:54	16:00	18-Jun-09	44.15	208.3789445	207.8003525
15	11:45	15:46	19-Jun-09	48.16666667	256.701984	256.123392
16	11:23	15:55	22-Jun-09	52.7	359.0983032	358.5197112
17	10:58	16:04	23-Jun-09	57.8	429.218832	428.64024
18	11:07	16:47	24-Jun-09	63.46666667	324.5370744	323.9584824
19	10:47	16:31	25-Jun-09	69.2	348.8765112	348.2979192
20	11:01	16:26	26-Jun-09	74.61666667	374.6913576	374.1127656
21	11:19	16:37	29-Jun-09	79.91666667	397.9213442	397.3427522
22	11:07	12:37	30-Jun-09	81.41666667	385.3851842	384.8065922

Run 5: started on April 18, 2009 and completed on May 07, 2009

Sample No.	START	END	Date	Reaction time (h)	H₂ Production (μmol)	
0				0	0.675024	Net H₂
1	13:52	18:03	22-Apr-09	4.183333333	-	-
2	9:20	20:42	23-Apr-09	15.55	-	-
3	9:15	10:45	24-Apr-09	17.05	2.0443584	1.3693344
4	11:39	19:43	24-Apr-09	25.11666667	-	-
5	10:00	16:47	27-Apr-09	31.9	9.8916846	9.2166606
6	10:45	14:34	4-May-09	35.71666667	10.72010313	10.04507913
7	14:59	18:05	4-May-09	38.81666667	11.4696885	10.7946645
8	10:05	13:32	5-May-09	42.26666667	12.7444931	12.0694691
9	13:56	16:48	5-May-09	45.13333333	13.22144712	12.54642312
10	9:48	11:48	6-May-09	47.13333333	13.420407	12.745383
11	12:19	15:52	6-May-09	50.68333333	14.841549	14.166525
12	16:10	17:17	6-May-09	51.8	15.2397369	14.5647129
13	9:41	12:07	7-May-09	54.23333333	18.0176673	17.3426433
14	12:30	15:06	7-May-09	56.83333333	16.074993	15.399969

Run 14: started on July 13, 2009 and completed on July 29, 2009

Sample No.	START	END	Date	Reaction time (h)	H$_2$ Production (µmol)	
0				0	0.96432	Net H$_2$
1	11:39	12:39	13-Jul-09	1	0.867888	-
2	12:52	13:56	13-Jul-09	2.066666667	0.819672	-
3	14:06	16:59	13-Jul-09	4.95	1.060752	0.096432
4	10:30	12:58	14-Jul-09	7.416666667	1.157184	0.192864
5	13:11	16:35	14-Jul-09	10.81666667	2.555448	1.591128
6	12:18	17:29	16-Jul-09	23.06666667	4.5178392	3.5535192
7	14:19	16:59	21-Jul-09	25.73333333	4.70443512	3.74011512
8	10:22	16:54	22-Jul-09	32.26666667	5.7835092	4.8191892
9	10:38	17:10	23-Jul-09	38.8	6.5356788	5.5713588
10	12:34	17:05	24-Jul-09	43.31666667	6.83606448	5.87174448
11	10:11	17:16	27-Jul-09	50.23333333	7.02651768	6.06219768
12	9:55	16:42	28-Jul-09	57.01666667	7.98987336	7.02555336
13	11:12	15:20	29-Jul-09	61.15	8.51590992	7.55158992

Run 43: started on May 06, 2010 and completed on May 09, 2010

Sample No.	START	END	Date	Reaction time (h)	H$_2$ Production (µmol)	
0				0	2.097888	Net H$_2$
1	13:36	16:56	6-May-10	3.333333333	3.015714	0.917826
2	17:11	17:04	6/7-May-10	27.21666667	15.07070292	12.97281492
3	17:13	16:42	7/8-May-10	50.7	28.89578484	26.79789684
4	16:57	14:27	8/9-May-10	71.7	40.41187878	38.31399078

Run 44: started on May 06, 2010 and completed on May 11, 2010

Sample No.	START	END	Date	Reaction time (h)	H$_2$ Production (μmol)	
0				0	1.538976	Net H$_2$
1	12:25	17:00	6-May-10	4.583333333	2.353728	0.814752
2	11:05	16:23	7-May-10	9.883333333	5.34296256	3.80398656
3	12:20	16:45	8-May-10	14.3	6.54698496	5.00800896
4	10:45	15:04	10-May-10	18.61666667	7.92029472	6.38131872
5	10:08	14:35	11-May-10	23.06666667	9.46379712	7.92482112

Run 13: started on June 4, 2009 and completed on June 30, 2009

Sample No.	START	END	Date	Reaction time (h)	H$_2$ Production (µmol)	
						Net H$_2$
0				0	0.626808	Net H$_2$
1	9:44	11:57	5-Jun-09	2.216666667	0.626808	0
2	12:26	13:32	5-Jun-09	3.316666667	0.72324	0.096432
3	13:44	14:45	5-Jun-09	4.333333333	1.494696	0.867888
4	15:15	16:25	5-Jun-09	5.5	1.44648	0.819672
5	16:42	17:49	5-Jun-09	6.616666667	1.2054	0.578592
6	12:30	15:13	6-Jun-09	9.333333333	1.976856	1.350048
7	10:57	15:16	8-Jun-09	13.65	2.81195712	2.18514912
8	10:54	16:11	9-Jun-09	18.93333333	3.37367352	2.74686552
9	11:05	15:55	11-Jun-09	23.76666667	3.66296952	3.03616152
10	10:53	15:16	12-Jun-09	28.15	4.2285432	3.6017352
11	12:41	16:52	15-Jun-09	32.33333333	4.2189	3.592092
12	10:43	15:06	16-Jun-09	36.71666667	4.44165792	3.81484992
13	12:34	14:54	17-Jun-09	39.05	5.17646976	4.54966176
14	10:54	16:00	18-Jun-09	44.15	5.69961336	5.07280536
15	11:45	15:46	19-Jun-09	48.16666667	6.07666248	5.44985448
16	11:23	15:55	22-Jun-09	52.7	7.49951664	6.87270864
17	10:58	16:08	23-Jun-09	57.8	8.98601592	8.35920792
18	11:07	16:47	24-Jun-09	63.46666667	7.06750128	6.44069328
19	10:47	16:31	25-Jun-09	69.2	7.55882232	6.93201432
20	11:01	16:26	26-Jun-09	74.61666667	7.2613296	6.6345216
21	11:19	16:37	29-Jun-09	79.91666667	7.52024952	6.89344152
22	11:07	12:37	30-Jun-09	81.41666667	7.23673944	6.60993144

Run 53: started on June 28, 2010 and completed on July 02, 2010

Sample No.	START	END	Date	Reaction time (h)	H₂ Production (µmol)	
0				0	2.62236	Net H₂
1	12:46	14:46	28-Jun-10	2	6.35135592	3.72899592
2	14:56	17:15	28-Jun-10	4.316666667	22.12485132	19.50249132
3	17:26	12:07	28/29-Jun-10	23	139.3967905	136.7744305
4	12:17	17:13	29-Jun-10	27.93333333	183.0276162	180.4052562
5	17:21	10:47	29/30-Jun-10	45.36666667	231.292152	228.669792
6	10:55	17:00	30-Jun-10	51.45	248.3807609	245.7584009
7	17:08	14:44	30-Jun/1-Jul-10	73.03333333	333.9732802	331.3509202
8	14:53	17:05	1/2-Jul-10	99.23333333	317.1075718	314.4852118

Run 66: started on August 21, 2010 and completed on August 27, 2010

Sample No.	START	END	Date	Reaction time (h)	H$_2$ Production (µmol)	
0				0	1.31118	Net H$_2$
1	16:18	9:55	22/23-Aug-10	17.61666667	15.65024448	14.33906448
2	10:00	16:51	23-Aug-10	24.46666667	19.01604354	17.70486354
3	17:18	9:53	23/24-Aug-10	41.05	24.38008092	23.06890092
4	10:05	17:03	24-Aug-10	48.01666667	26.46223476	25.15105476
5	17:38	10:13	24/25-Aug-10	64.6	28.35033396	27.03915396
6	10:20	16:55	25-Aug-10	71.18333333	31.52863428	30.21745428
7	17:22	10:26	25/26-Aug-10	88.25	34.46043276	33.14925276
8	10:33	17:00	26-Aug-10	94.7	35.2248507	33.9136707
9	17:18	9:44	26/27-Aug-10	111.1333333	38.14615974	36.83497974

Run 67: started on August 21, 2010 and completed on September 01, 2010

Sample No.	START	END	Date	Reaction time (h)	H$_2$ Production (µmol)	
0				0	1.31118	Net H$_2$
1	9:57	16:55	27-Aug-10	6.966666667	1.442298	0.131118
2	17:14	8:54	27/30-Aug-10	70.63333333	40.19160054	38.88042054
3	9:11	13:38	30-Aug-10	75.08333333	59.3767863	58.0656063
4	13:55	17:38	30-Aug-10	78.8	34.50501288	33.19383288
5	17:46	12:02	30/31-Aug-10	97.06666667	53.50794462	52.19676462
6	12:15	16:59	31-Aug-10	101.8	76.48244058	75.17126058
7	17:08	10:24	31-Aug /1-Sep-10	119.0666667	85.88753472	84.57635472

Run 68: started on September 02, 2010 and completed on September 08, 2010

Sample No.	START	END	Date	Reaction time (h)	H_2 Production (μmol)	
0				0	1.442298	Net H_2
1	16:23	16:42	3/4-Sep-10	24.31666667	3.409068	1.96677
2	16:55	9:18	4/6-Sep-10	64.7	11.96713986	10.52484186
3	9:34	17:18	6-Sep-10	72.43333333	12.53225844	11.08996044
4	17:27	9:21	6/7-Sep-10	88.33333333	16.66903134	15.22673334
5	9:32	17:23	7-Sep-10	96.18333333	16.78048164	15.33818364
6	17:31	9:17	7/8-Sep-10	111.95	19.40415282	17.96185482

Run 69: started on September 02, 2010 and completed on September 08, 2010

Sample No.	START	END	Date	Reaction time (h)	H_2 Production (μmol)	
0				0	1.086336	Net H_2
1	9:45	16:04	3-Sep-10	6.316666667	3.35315712	2.26682112
2	10:14	16:36	4-Sep-10	12.68333333	4.34353344	3.25719744
3	9:21	13:35	6-Sep-10	16.91666667	5.36559456	4.27925856
4	12:02	14:48	8-Sep-10	19.68333333	8.40824064	7.32190464

APPENDIX F

EXPERIMENTAL DATA OF CHAPTER VII

Run 23: started on November 19, 2009 and completed on November 30, 2009

Sample No.	START	END	Date	Reaction time (h)	H_2 Production (µmol)	
0				0	2.62236	Net H_2
1	10:11	11:16	19-Nov-09	1.1	2.884596	0.262236
2	11:26	13:28	19-Nov-09	3.016666667	3.27795	0.65559
3	13:36	15:48	19-Nov-09	5.216666667	4.5956859	1.9733259
4	15:59	17:05	19-Nov-09	6.316666667	4.720248	2.097888
5	17:17	16:36	19/20-Nov-09	29.63333333	14.029626	11.407266
6	16:47	9:41	20/23-Nov-09	94.53333333	50.5197654	47.8974054
7	9:53	16:40	23-Nov-09	101.3166667	55.1482308	52.5258708
8	16:54	13:41	23/24-Nov-09	122.1	61.9270314	59.3046714
9	13:56	17:12	24-Nov-09	125.3666667	64.0773666	61.4550066
10	17:23	11:32	24/25-Nov-09	143.5166667	73.5703098	70.9479498
11	11:42	16:25	25-Nov-09	148.2333333	75.523968	72.901608
12	16:34	10:22	25/30-Nov-09	262.0333333	131.0131056	128.3907456
13	10:43	16:17	30-Nov-09	267.6	133.2683352	130.6459752

Run 62: started on August 16, 2010 and completed on August 30, 2010

Sample No.	START	END	Date	Reaction time (h)	H_2 Production (µmol)	
0				0	0.72324	Net H_2
1	10:06	16:06	17-Aug-10	6	1.494696	0.771456
2	10:25	17:00	18-Aug-10	13.41666667	4.1634516	3.4402116
3	11:30	17:07	19-Aug-10	19.03333333	5.66489784	4.94165784
4	12:20	17:13	20-Aug-10	23.91666667	7.01012424	6.28688424
5	11:49	17:19	21-Aug-10	29.41666667	8.45322912	7.72998912
6	9:48	16:55	23-Aug-10	48.53333333	9.83461752	9.11137752
7	9:49	17:10	24-Aug-10	55.88333333	7.05834024	6.33510024
8	10:10	16:59	25-Aug-10	62.7	15.0168732	14.2936332
9	10:23	17:05	26-Aug-10	69.4	6.97492656	6.25168656
10	9:41	17:00	27-Aug-10	76.71666667	26.12198232	25.39874232
11	10:19	16:55	28-Aug-10	83.31666667	30.48553032	29.76229032
12	9:17	13:34	30-Aug-10	87.6	31.5621936	30.8389536

Run 63: started on August 16, 2010 and completed on August 30, 2010

Sample No.	START	END	Date	Reaction time (h)	H$_2$ Production (µmol)	
0				0	0.72324	Net H$_2$
1	10:06	16:06	17-Aug-10	6	5.4749268	4.7516868
2	10:25	17:00	18-Aug-10	13.41666667	15.46913928	14.74589928
3	11:30	17:07	19-Aug-10	19.03333333	23.071356	22.348116
4	12:20	17:13	20-Aug-10	23.91666667	27.96720864	27.24396864
5	11:49	17:19	21-Aug-10	29.41666667	34.14078528	33.41754528
6	9:48	16:55	23-Aug-10	48.53333333	48.64608672	47.92284672
7	9:49	17:10	24-Aug-10	55.88333333	19.49517528	18.77193528
8	10:10	16:59	25-Aug-10	62.7	60.84232392	60.11908392
9	10:23	17:05	26-Aug-10	69.4	82.16874288	81.44550288
10	9:41	17:00	27-Aug-10	76.71666667	46.5356724	45.8124324
11	10:19	16:55	28-Aug-10	83.31666667	109.2246691	108.5014291
12	9:17	13:34	30-Aug-10	87.6	107.2087582	106.4855182

Run 64: started on August 16, 2010 and completed on August 30, 2010

Sample No.	START	END	Date	Reaction time (h)	H$_2$ Production (µmol)	
0				0	0.681912	Net H$_2$
1	10:06	16:06	17-Aug-10	6	1.120284	0.438372
2	10:25	17:00	18-Aug-10	13.41666667	1.70478	1.022868
3	11:30	17:07	19-Aug-10	19.03333333	2.56739868	1.88548668
4	12:20	17:13	20-Aug-10	23.91666667	3.15335592	2.47144392
5	11:49	17:19	21-Aug-10	29.41666667	3.86887644	3.18696444
6	9:48	16:55	23-Aug-10	48.53333333	4.29068772	3.60877572
7	9:49	17:10	24-Aug-10	55.88333333	7.00128792	6.31937592
8	10:10	16:59	25-Aug-10	62.7	5.69104272	5.00913072
9	10:23	17:05	26-Aug-10	69.4	8.35731864	7.67540664
10	9:41	17:00	27-Aug-10	76.71666667	8.81566092	8.13374892
11	10:19	16:55	28-Aug-10	83.31666667	8.86826556	8.18635356
12	9:17	13:34	30-Aug-10	87.6	5.66766288	4.98575088

Run 65: started on August 16, 2010 and completed on August 30, 2010

Sample No.	START	END	Date	Reaction time (h)	H₂ Production (μmol)	
0				0	0	Net H₂
1	10:06	16:06	17-Aug-10	6	-	-
2	10:25	17:00	18-Aug-10	13.41666667	-	-
3	11:30	17:07	19-Aug-10	19.03333333	-	-
4	12:20	17:13	20-Aug-10	23.91666667	-	-
5	11:49	17:19	21-Aug-10	29.41666667	-	-
6	9:48	16:55	23-Aug-10	48.53333333	-	-
7	9:49	17:10	24-Aug-10	55.88333333	1.30099068	0.52166268
8	10:10	16:59	25-Aug-10	62.7	-	-
9	10:23	17:05	26-Aug-10	69.4	-	-
10	9:41	17:00	27-Aug-10	76.71666667	1.37453976	0.59521176
11	10:19	16:55	28-Aug-10	83.31666667	2.6959878	1.9166598
12	9:17	13:34	30-Aug-10	87.6	2.54109636	1.76176836

Run 25: started on December 12, 2009 and completed on December 24, 2009

Sample No.	START	END	Date	Reaction time (h)	H$_2$ Production (µmol)	
0				0	2.753478	Net H$_2$
1	15:57	10:32	12/14-Dec-09	42.58333333	34.352916	31.599438
2	10:45	17:03	14-Dec-09	48.88333333	38.4306858	35.6772078
3	17:17	12:58	14/15-Dec-09	68.56666667	48.0940824	45.3406044
4	13:08	17:46	15-Dec-09	73.2	50.4542064	47.7007284
5	17:56	14:23	15/16-Dec-09	93.65	62.0319258	59.2784478
6	14:34	17:14	16-Dec-09	96.31666667	63.723348	60.96987
7	17:30	13:26	16/17-Dec-09	116.25	76.638471	73.884993
8	13:36	17:07	17-Dec-09	119.7666667	77.9365392	75.1830612
9	17:18	10:39	17/18-Dec-09	137.1166667	86.8525632	84.0990852
10	10:48	9:43	18/21-Dec-09	208.0333333	123.578715	120.825237
11	10:03	12:34	21-Dec-09	210.6	126.6730998	123.9196218
12	12:53	16:39	21-Dec-09	214.3666667	125.21769	122.464212
13	17:03	11:22	21/22-Dec-09	232.6833333	132.0620496	129.3085716
14	11:40	17:04	22-Dec-09	238.0833333	136.034925	133.281447
15	17:20	13:33	22/23-Dec-09	258.2666667	132.7097725	129.9562945
16	13:55	16:18	23-Dec-09	260.65	132.2049682	129.4514902
17	16:36	10:40	23/24-Dec-09	278.7166667	127.6237053	124.8702273
18	10:55	16:55	24-Dec-09	284.7166667	125.6792254	122.9257474

Run 55: started on July 15, 2010 and completed on August 04, 2010

Sample No.	START	END	Date	Reaction time (h)	H$_2$ Production (μmol)	
0				0	1.720032	Net H$_2$
1	9:44	16:12	16-Jul-10	6.466666667	4.13169792	2.41166592
2	9:47	17:14	19-Jul-10	13.91666667	4.84505856	3.12502656
3	9:42	16:32	20-Jul-10	20.75	7.01773056	5.29769856
4	10:21	17:29	21-Jul-10	27.88333333	7.99724352	6.27721152
5	11:01	15:44	22-Jul-10	32.6	9.64440048	7.92436848
6	10:02	17:47	23-Jul-10	40.35	10.21065312	8.49062112
7	9:37	17:42	26-Jul-10	48.43333333	12.43221024	10.71217824
8	9:45	16:03	27-Jul-10	54.73333333	12.91110336	11.19107136
9	9:58	14:05	28-Jul-10	60.85	13.6199376	11.8999056
10	10:01	16:08	29-Jul-10	66.96666667	11.93973792	10.21970592
11	10:03	17:22	30-Jul-10	74.28333333	15.52184035	13.80180835
12	11:41	15:01	31-Jul-10	77.61666667	18.89047776	17.17044576
13	10:30	17:24	2-Aug-10	84.51666667	19.98767712	18.26764512
14	10:52	17:18	3-Aug-10	90.95	18.920352	17.20032
15	9:58	17:03	4-Aug-10	98.03333333	19.06248096	17.34244896

VITA

Name: Naser D. Alenzi

Address: Kuwait Institute for Scientific Research
                   P.O.Box 24885
                   Safat, 13109
                   Kuwait

Email: eng_nasser1973@yahoo.com

Education: M.Sc., Chemical Engineering, Kuwait University, Kuwait, 2001

                   B.Sc., Chemical Engineering, Kuwait University, Kuwait, 1997